Electrocaloric Effect of Ferroelectrics and Relaxors

Zur Erlangung des akademischen Grades Doktor-Ingenieur (Dr.-Ing.)
vorgelegte Dissertation von M.Sc. Yang-Bin Ma aus Henan, China
Darmstadt 2017

1. Gutachter: Prof. Dr. Bai-Xiang Xu & Prof. Dr. rer. nat. Karsten Albe, TU Darmstadt
2. Gutachter: Prof. Dr. rer. nat. Peter Entel, University of Duisburg-Essen

TECHNISCHE
UNIVERSITÄT
DARMSTADT

Fachbereich
Material- und Geowissenschaften
Mechanik Funktionaler Materialien

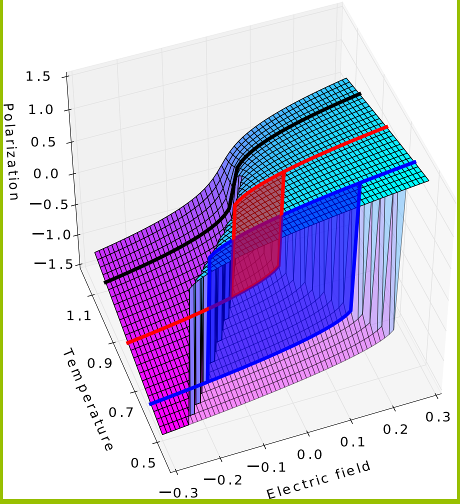

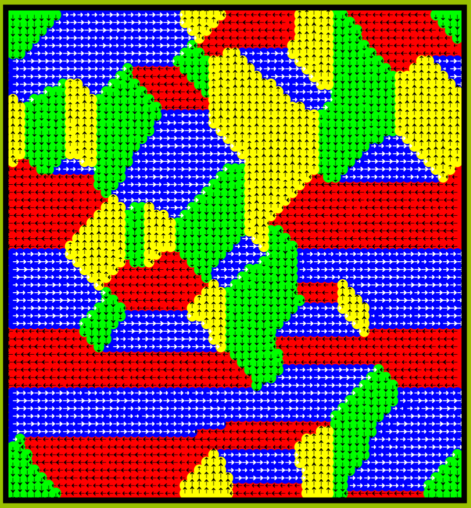

Electrocaloric Effect of Ferroelectrics and Relaxors

Vorgelegte Dissertation von M.Sc. Yang-Bin Ma aus Henan, China

1. Gutachter: Prof. Dr. Bai-Xiang Xu & Prof. Dr. rer. nat. Karsten Albe, TU Darmstadt
2. Gutachter: Prof. Dr. rer. nat. Peter Entel, University of Duisburg-Essen

Tag der mündlichen Prüfung: 16.10.2017

Jahr der Veröffentlichung der Dissertation auf TUprints: 2018

Bitte zitieren Sie dieses Dokument als:
URN: urn:nbn:de:tuda-tuprints-75079
URL: http://tuprints.ulb.tu-darmstadt.de/7507

Erklärung zur Dissertation

Hiermit versichere ich, die vorliegende Dissertation ohne Hilfe Dritter nur mit den angegebenen Quellen und Hilfsmitteln angefertigt zu haben. Alle Stellen, die aus Quellen entnommen wurden, sind als solche kenntlich gemacht. Diese Arbeit hat in gleicher oder ähnlicher Form noch keiner Prüfungsbehörde vorgelegen.

Darmstadt, den 22. Juni 2018

(Yang-Bin Ma)

Acknowledgement

First and foremost, Prof. Bai-Xiang Xu and Prof. Karsten Albe are sincerely appreciated for their kind supervising. They provided me with comprehensive instructions, lightened my scientific path with their fruitful knowledge, and corrected my manuscript patiently. It will be my precious memory in all my life. I am grateful to all my cooperation partners. Sincere thanks are given to Dr. Anna Grünebohm in University of Duisburg-Essen and Dr. Kai-Christian Meyer in TU Darmstadt for their help in understanding ferroelectrics theory. I express my gratitude to Prof. Jürgen Rödel, Dr. Nikola Novak and Dr. Jurij Koruza in TU Darmstadt for their experimental contributions and fruitful discussion. Moreover, the helpful discussion with Prof. Tongqing Yang initiated also part of this thesis. Many thanks should be also given to Christian Molin, Dr. Sylvia Gebhardt in Fraunhofer Institute for Ceramic Technologies and Systems, and Dr. Vladimir V. Shvartsman, Prof. Doru C. Lupascu in University of Duisburg-Essen for our cooperation on $BaZr_xTi_{1-x}O_3$. In addition, I would like to thank Dr. Melanie Gröting, Na Liu, Dr. Matias Acosta, Dr. Yuri Genenko, Dr. Hairui Liu in TU Darmstadt, Prof. Jo Wook in Ulsan National Institute of Science and Technology, Prof. George Rossetti in University of Connecticut, Dr. Yinan Zuo in RWTH Aachen and Prof. Inna Ponomareva in University of South Florida, for the insightful discussions. Simultaneously, I am fairly thankful to all the members in my host group (Mechanics of Functional Materials) for their kind help and the wonderful working atmosphere. Especially, I am sincerely grateful to Yangyiwei Yang, Dr. Min Yi, Shuai Wang, Dr. Peter Stein, Dr. Ying Zhao, Dr. Habib Pouriayevali, Dagmar Eder-Goy, Ziqi Zhou, Yang Bai, Yao Liu, and Qihua Gong due to their friendly assistance. Additionally, I attended the group seminar of Nonmetallic-Inorganic Materials lead by Prof. Jürgen Rödel frequently, and become almost an unofficial member of this group. I had many wonderful discussions with them, learned a plenty of useful knowledge in this process, and I was delightful to be together with all the Nonmetallic-Inorganic Materials members. Also I thank Prof. Peter Entel in University of Duisburg-Essen sincerely for sacrificing his valuable time acting as the co-referee.

I dedicate this work to my lovely wife Jingnan Shi and my parents. They are always my backbone to kicking out the stumbling block in front of me so that I am fearless. During my PhD student life the birth of my son, Yueran Ma, is a priceless gift from the heaven, and I enjoy the life with him greatly.

The funding of Deutsche Forschungsgemeinschaft through project within the Priority Program ‘Caloric Effects in Ferroic Materials: New Concepts for Cooling’ (SPP 1599) is gratefully acknowledged for supporting me to pursue my PhD degree. Competence Center of High Performance Computing in Hesse is appreciated for the calculation resources, which provided reliable facilities to carry out my research.

Abstract

Since the discovery of the giant electrocaloric effect in $PbZr_{0.95}Ti_{0.05}O_3$ [1], the electrocaloric effect of ferroelectrics has received increasing research interest and has been demonstrated to have great potential for cooling application. For successful implementation and commercialization of electrocaloric refrigeration, it is necessary to reveal the mechanism and the factors influencing the electrocaloric effect.

The general goal of this thesis is to develop computational methods for evaluating and understanding the electrocaloric effect in complex ferroelectric materials and to derive optimization strategies with respect to the caloric cycle and the materials.

For evaluating the electrocaloric effect, two methods are developed. One is based on a thermodynamical analytical model with the entropy analysis using the Landau theory and the work loss associated with irreversibility. This allows for a quick calculation of the temperature change on the basis of thermodynamics. The other method is based on the strict enforcement of energy conservation under adiabatic conditions and is implemented in the framework of lattice-based Monte-Carlo microcanonical simulations using a novel Ginzburg-Landau type effective Hamiltonian. Using this method the electrocaloric effect in complex materials can be explicitly interpreted on the domain structure level, and by adjusting the Hamiltonian it can be applied to study complex materials such as relaxors and ferroelectrics with defect dipoles.

Based on Monte-Carlo simulations and experimental measurements, an improved thermodynamic cycle is validated, where the cooling effect is enhanced by applying a reversed electric field. In comparison with conventional adiabatic cooling by on-off cycles of the external electric field, applying a reversed field can enhance the cooling efficiency by more than 20% in standard ferroelectrics and also relaxor ferroelectrics, like $Pb(Mg_{1/3}/Nb_{2/3})_{0.71}Ti_{0.29}O_3$. The optimal reversed field corresponds to the shoulder of the P-E loop, which is thermodynamically explained and quantitatively determined by the analytical model based on the entropy calculation. It signifies in general the importance of considering irreversible process in the electrocaloric cycles.

By considering oxygen vacancy-acceptor associates by fixed local dipoles, simulation results demonstrate that defect dipoles have a significant influence on the electrocaloric effect in acceptor doped $BaTiO_3$. In particular, defect dipoles anti-parallel to the external field can lead to abnormal electrocaloric features like inverse effect and double peaks, which stem from the delicate interplay of internal and external fields and are systematically explained by the domain structure evolution and related entropy analysis. The results are in good agreement to those from Molecular-Dynamics simulations employing an ab initio based effective Hamiltonian. By making use of the inverse electrocaloric effect in the presence of defect dipoles, improved electrocaloric cycles are proposed with enhanced cooling effect.

Generic effective Hamiltonian models are presented for relaxors based on the random field theory, and the corresponding direct electrocaloric calculations reveal that the presence of random fields reduces the entropy variation in an electrocaloric cycle by pinning local polarization. With increasing strength or density of the random fields, the electrocaloric peak shifts to a lower temperature. The effective temperature range becomes wider, but the temperature variation is reduced. The dielectric and electrocaloric properties of the model solid solution $BaZr_xTi_{1-x}O_3$ are also simulated by a composition-sensitive effective Hamiltonian, which differentiates the polar Ti-occupied sites from the nonpolar Zr-occupied sites. The model is verified by corresponding experimental measurements. Based on systematic simulations, distinct regimes of ferroelectrics, relaxors, polar clusters, and paraelectric phases are identified sequentially as the Zr-concentration increases. The correlation between the internal random fields induced by the composition fluctuation and the state regimes demonstrates the fundamental role of random fields in relaxors.

Abstract

Seit der Entdeckung des riesigen elektrokalorischen Effektes in $PbZr_{0.95}Ti_{0.05}O_3$ [1] hat der elektrokalorische Effekt in ferroelektrischen Materialien zunehmend Interesse geweckt und sein hohes Potenzial für Kühlanwendungen ist erwiesen. Für eine erfolgreiche Implementierung und Kommerzialisierung von elektrokalorischer Kühlung ist es notwendig den Mechanismus des elektrokalorischen Effektes und beeinflussenden Faktoren deutlich zu machen.

Das allgemeine Ziel dieser Arbeit ist die Entwicklung von Simulationsmethoden zur Bestimmung und zum Verständnis des elektrokalorischen Effektes in ferroelektrischen Materialien sowie die Ableitung von Optimierungsstrategien des zugrunde liegend thermodynamischen Kreisprozesses und der Materialien.

Zwei Methoden werden entwickelt um den elektrokalorischen Effekt zu bestimmen. Die eine Methode basiert auf einem thermodynamischen analytischen Modell bei dem für die Analyse der Entropie die Landau-Theorie genutzt wird und Irreversibilität und die zugehörige Dissipation berücksichtigt werden. Dies erlaubt eine schnelle Berechnung der Temperaturänderung auf thermodynamischer Basis. Die andere Methode basiert auf der strikten Energieerhaltung unter adiabatischen Bedingungen und wird mittels gitterbasierten, mikrokanonischen Monte-Carlo Simulationen implementiert, die einen neuen effektiven Hamiltonian vom Ginzburg-Landau-Typ benutzen. Auf diese Weise kann der elektrokalorische Effekt in komplexen Materialien explizit auf der Ebene der Domänenstruktur interpretiert werden und es ist möglich durch die Anpassung des Hamiltonians komplexe Materialien wie Relaxoren und Ferroelektrika mit Dipoldefekten zu untersuchen.

Mittels Monte-Carlo-Simulationen und experimentellen Messungen wird ein verbesserter thermodynamischer Kreisprozess bestätigt, bei dem der Kühleffekt durch das Anlegen eines umgekehrten elektrischen Feldes verstärkt wird. Im Vergleich zur konventionellen adiabatischen Kühlung mit Ein-Aus-Prozessen, kann das Anlegen eines umgekehrten Feldes, sowohl an gewöhnliche als auch an Relaxor-Ferroelektrika, wie z.B. $Pb(Mg_{1/3}/Nb_{2/3})_{0.71}Ti_{0.29}O_3$, die Kühleffizienz um 20% verbessern. Das optimale umgekehrte Feld entspricht der Schulter der P-E Schleife. Dies kann durch das analytische Model, welches auf der Berechnung der Entropie basiert, thermodynamisch erklärt und quantitativ bestimmt werden und betont wie wichtig es im Allgemeinen ist irreversible Prozesse in elektrokalorischen Prozessen zu berücksichtigen.

Betrachtet man Sauerstoffleerstellen-Akzeptor-Paare als lokale unveränderliche Dipole, zeigen die Simulation, dass Defektdipole einen signifikanten Einfluß auf den elektrokalorischen Effekt im Akzeptor-dotierten $BaTiO_3$ haben. Insbesondere können zum externen Feld antiparallele Defektdipole zu anormalen elektrokalorischen Eigenschaften, wie z.B. einem negativen Effekt und Doppelpeaks, führen, die ihren Ursprung im filigranen Wechselspiel zwischen internem und externen elektrischen Feldern haben und systematisch durch die Entwicklung der Domänenstruktur und der damit verbundenen Entropie analyisert werden. Die Ergebnisse stehen in guter Übereinstimmung mit den Ergebnissen von Molekulardynamiksimulationen, die einen auf *ab-initio*-Rechnungen basierten effektiven Hamiltonian nutzen. Der negative elektrokalorische Effekt in Gegenwart von Defektdipolen erlaubt es, einen verbesserten elektrokalorischen Kreisprozess mit höherer Kühleffizienz aufzustellen. Für Relaxoren werden, basierend auf der Zufallsfeldtheorie, allgemeine effektive Hamiltonianmodelle aufgestellt. Die entsprechenden direkt berechneten kalorischen Antworten zeigen, dass die Zufallsfelder die Entropieänderung in einem elektrokalorischen Kreisprozess durch das Pinning der lokalen Polarisation verringern. Mit wachsender Stärke oder Dichte der Zufallsfeder werden die elektrokalorischen Peaks zu niedrigeren Temperaturen verschoben. Der effektive Temperaturbereich wird verbreitert, aber die Temperaturänderung wird reduziert. Außerdem werden die dielektrischen und elektrokalorischen Eigenschaften des Modellsystems $BaZr_xTi_{1-x}O_3$ berechnet. Der hierzu benutzte konzentrationsabhängige effektiven Hamiltonian unterscheidet zwischen den polaren, von Titan besetzten, und den nichtpolaren, von Zirkon besetzten, Gitterplätzen. Dieses Model wird durch entsprechende experimentelle Messungen bestätigt. Mittels systematischer Rechnungen lassen sich bei steigender Zr-Konzentration zunächst ein ferroelektrischer Bereich, dann ein Bereich mit Relaxoreigenschaften, dann ein Bereich mit polaren Clustern und schließlich eine paraelektrische Phase deutlich unterscheiden. Die Korrelation zwischen internen Zufallsfeldern, die durch Kompositionsschwankungen induziert werden, und den unterschiedlichen Bereichen demonstriert die Bedeutung der Zufallsfelder in Relaxoren.

Contents

Chapter 1

Motivation

Refrigeration technology has a great importance for modern society, e.g., for food and medical industry, electronic applications and aerospace engineering. Table 1.1 summarizes several most used or investigated refrigeration technologies [2–4]. In addition to the traditional vapor compression, the eco-friendly solid refrigeration develops significantly, including thermoelectric, magnetocaloric, and electrocaloric coolers. Vapor compression utilizes the liquid-gas phase transition, and has a high energy conversion efficiency (40%-50%). However, the corresponding devices give rise to noise, and environmentally unfriendly matters, e.g., halofluorocarbon. The thermoelectric effect makes use of the Peltier effect, but has a low efficiency. The magnetocaloric effect has a fairly high energy conversion efficiency (60%-70%), large temperature change, and high potential for commercialization. Nevertheless, the price of magnets is high, and it is necessary to equip large magnets to achieve considerable temperature changes. The electrocaloric effect has a similar mechanism as the magnetocaloric effect. More exactly, the ordering of ferroelectric domain structures can be altered through application or removal of an electric field. It leads to a change of the dipolar entropy and thus the variation of the vibrational entropy under adiabatic condition, represented as the temperature change of the sample. This is the fundamental mechanism of the electrocaloric effect [5]. In Fig. 1.1 a typical electrocaloric cycle is shown. The red and blue arrows represent the heating and cooling processes, respectively. Process **i** is an adiabatic process from state (a) with temperature T to (b) with $T + \Delta T$, which decreases the dipolar entropy and increases the temperature by application of field. Process **ii** is

TABLE 1.1 *Efficiency of energy conversion in different cooling technologies, taken from Refs. [2–4].*

Novel or existing technology	Efficiency (%)	Comments
Conventional fridge (vapor compression cycle)	40-50	Everything is optimized, no growth in this market
Thermoelectric cooler or power generator	10	More than 60 years of extensive research has not yet delivered a practical and efficient device
Magnetocaloric cooler	60-70	Requires large magnetic field and therefore large magnets
Electrocaloric cooler / pyroelectric power generator	60-70	Small effect in bulk materials Large effect in thin films

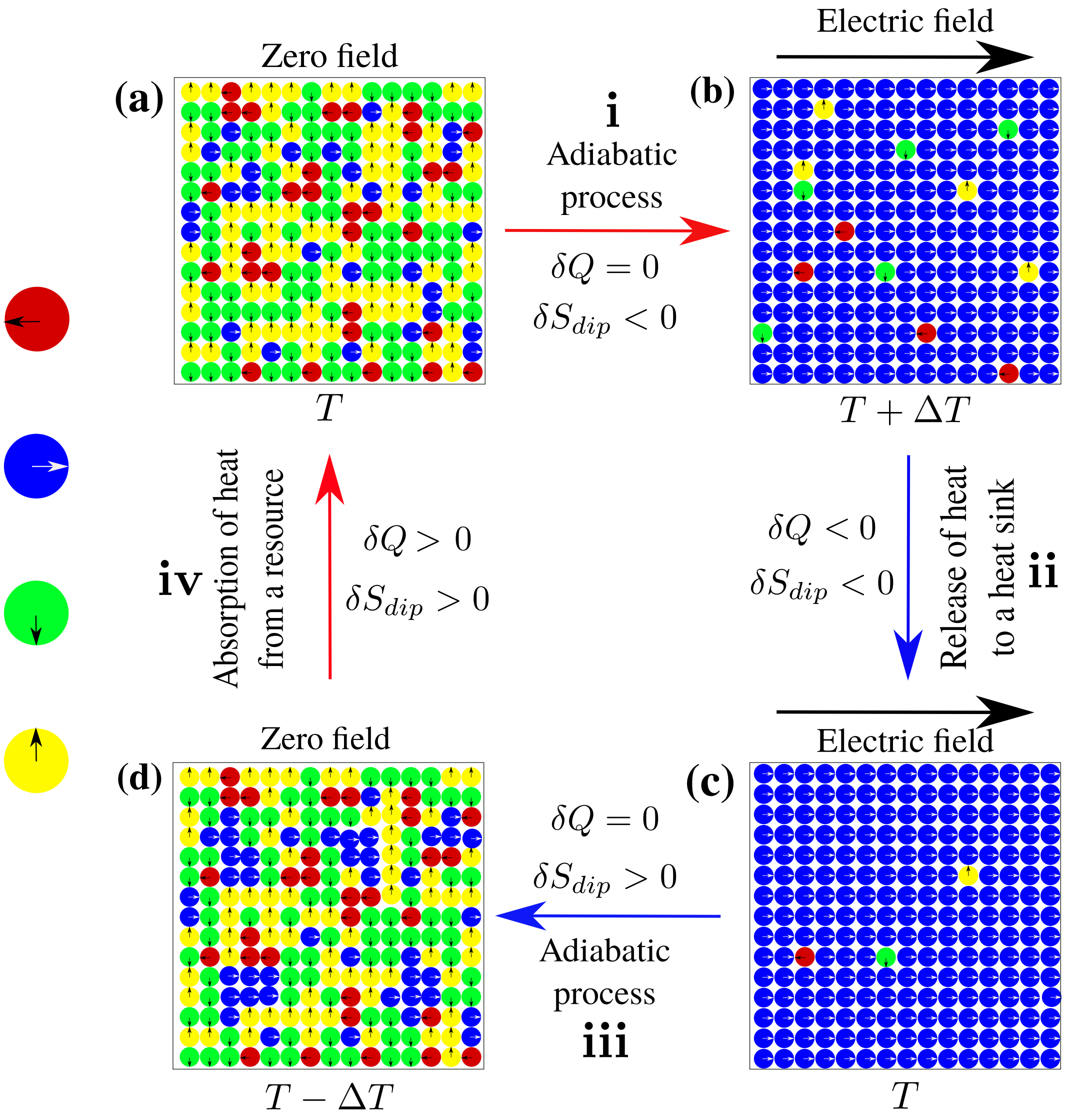

Figure 1.1 *Conventional electrocaloric cycle. The conventional cycle involves four processes, namely, a-b-c-d-a. under adiabatic conditions ($\Delta Q = 0$) a field is applied rapidly, taking the initial state (a) at T to a state (b) at $T + \Delta T$, and reducing the lower dipolar entropy ($\Delta S_{dip} < 0$). By transferring heat to a heat sink ($\Delta Q < 0$), the state (b) transforms to the state (c) at T, and the dipolar entropy decreases further ($\Delta S_{dip} < 0$). Removing the field rapidly under adiabatic conditions ($\Delta Q = 0$), from state (c) the system is cooled to state (d) at $T - \Delta T$, and the dipolar entropy increases ($\Delta S_{dip} > 0$). Finally, by absorbing heat from a heat resource ($\Delta Q > 0$), the system warms up to the state (a), and the dipolar entropy slightly increases ($\Delta S_{dip} > 0$). Adapted from Ref. [5].*

a process from stage (b) to (c) with T, in which the temperature decreases by releasing the heat to a heat sink. Process **iii** from state (c) to (d) with $T - \Delta T$ is again an adiabatic process. In process **iii** the dipolar entropy increases by removal of the field. Process **iv** from state (d) to (a) is a process, in which the temperature increases through adsorption of heat from a heat source.

Experimentally, Kobeko and Kurtschatov [6] carried out the first investigation on the electrocaloric effect of Rochelle salt. Afterwards, however, the electrocaloric effect was of little interest to the researchers for quite a long period, since the temperature change was extremely tiny if compared with its counterpart, the magnetocaloric effect [7]. Strikingly, in 2006 Mischenko *et al.* [1] reported a giant electrocaloric effect of a value 12 K under 48 $\mathrm{kV\,mm^{-1}}$ at the initial temperature 499.15 K in $\mathrm{PbZr_{0.95}Ti_{0.05}O_3}$ thin films with 350 nm thickness. After this discovery, the electrocaloric effect has attracted increasing research interests in the last decade, and experimental and fundamental investigations began to surge. Many researchers focus on exploring materials exhibiting large electrocaloric effects, as reviewed in Refs. [5, 7, 8]. For instance, Neese *et al.* [9] found that a large electrocaloric effect can be realized in the ferroelectric poly(vinylidene fluoride-trifluoroethylene) (P(VDF-TrFE)) copolymer at temperatures above the ferroelectric-paraelectric transition (above 293 K), where an isothermal entropy change of more than 55 $\mathrm{J\,kg^{-1}\,K^{-1}}$, and an adiabatic temperature change of more than 12 K were observed. Meanwhile, much effort is devoted to developing device concepts or constructing devices, as reviewed in Refs. [10–12]. For example, by integrating a silicon chip to the electrocaloric effect thin film cooling device, Kar-Narayan and Mathur [13, 14] managed to reduce the operation voltage further down to 5 V. This technique brings the electrocaloric effect one step closer to commercialization. The electrocaloric effect can be further optimized by morphology design with efficient heat change, e.g., cellular structure of polymeric ferroelectrics [15] and multilayer ferroelectric devices [13].

Thus, the merits of the electrocaloric effect are the high energy conversion efficiency (60%-70%), cheap device components, and the adaptivity to miniaturization. All these features make the electrocaloric refrigeration very attractive to, e.g., refrigerant-free devices in satellites and microelectronic device cooling [15]. Moreover, as an environmental-friendly technique, the electrocaloric effect can reduce $\mathrm{CO_2}$ emission and avoid the use of halofluorocarbon. But for the successful implementation and commercialization of electrocaloric refrigeration, it is indispensable to reveal the mechanism and the factors influencing this effect. For this purpose, theoretical and computational studies can serve as an efficient and flexible tool.

There exist already a number of theoretical studies on the electrocaloric effect in ferroelectrics and relaxor ferroelectrics. The main techniques utilized for the study of ferroelectrics include the phenomenological thermodynamic Landau theory [16–26], phase-field simulations [27–35], and Monte-Carlo/Molecular-Dynamics simulations using the first-principles based effective Hamiltonians [36–41].

For instance, a thermodynamic analysis of the electrocaloric effect in $BaTiO_3$ thin film was carried out by Akcay *et al.* [17]. They explained how the initial applied field and the misfit strain between the film and the substrate influence the electrocaloric effect. Pirc *et al.* [42] calculated the electrocaloric effect induced by first and second order phase transitions, using a modified phenomenological Landau approach on the basis of the spherical random bond-random field theory with temperature-dependent Landau coefficients, while the gradient energy or the dipole-dipole interaction energy was ignored. Dunne *et al.* [43] applied a matrix treatment of an one-dimensional lattice model to study the characteristics of relaxor ferroelectrics under varying electric field and pressure by Monte-Carlo simulations. They incorporated the configurational energy and found that the dual-peak behavior of the electrocaloric effect is due to the presence of polar nanoregions. Cao and Li [44] modified a transverse Ising model [45] to calculate the electrocaloric effect in $BaTiO_3$ thin films and found that the electrocaloric effect strongly depends on the four-spin interaction and the quantum fluctuation.

However, in all studies mentioned above the electrocaloric effect was calculated using the indirect method, which is based on the Maxwell relation

$$\Delta T = -\int_{E_1}^{E_2} \frac{T}{C(E,T)\rho} \left(\frac{\partial P(E,T)}{\partial T} \right)_E dE, \qquad (1.1)$$

where the external field varies from E_1 to E_2, $C(E,T)$ is the heat capacity, and ρ is the mass density. This method evaluates the temperature change from field- and temperature-dependent polarization data, is convenient and has been applied widely both in experimental and theoretical work. The accuracy of the results based on the indirect method is, however, under doubt, due to the involved numerical integration and the challenges to determine $P(E,T)$, $\frac{\partial P(E,T)}{\partial T}$, and $C(E,T)$ precisely [46]. Due to the lack of information, C is usually treated as a constant, which might cause some serious unexpected deviations from the reality. Moreover, since the Maxwell relation is valid only for reversible processes, the indirect method is in principle not applicable to materials/processes with strong irreversibility, e.g. relaxor ferroelectrics, antiferroelectrics and processes involving 1st order phase transitions in general. Therefore, there is increasing interest in developing the direct method.

Experimentally, one can determine the adiabatic temperature change by using a thermocouple, differential scanning calorimeter, infra-red camera, scanning thermal microscopy, or specifically designed calorimeters [46]. In theoretical studies, there are again two methods. One is based on entropy calculation, which was proposed by Pirc et al. [42] in their analytical study based on the Landau theory, where a reversible process was assumed. However, this deviates the fact that the total entropy is not constant in the process involving irreversibility. In this thesis, the analytical model is further developed with consideration of irreversibility by separating the polarization into reversible and irreversible parts. The other type is based on the assumption of constant total energy. For example, Axelsson *et al.* [47] modeled the electrocaloric effect by directly evaluating the entropy from the partition function of a one-dimensional lattice model and showed how the field applied along a particular lattice direction induces an inverse electrocaloric effect. According to their model the sign reversal of the electrocaloric effect occurs when two phase transition temperatures are close. Lisenkov and Ponomareva [36, 48] studied the electrocaloric effect in $Ba_{0.5}Sr_{0.5}TiO_3$ using a first-principles based effective Hamiltonian in combination with a microcanonical Monte-Carlo algorithm. Similarly, Nishimatsu [38] used an effective Hamiltonian approach in microcanonical Molecular-Dynamics simulation to simulate the electrocaloric effect in $BaTiO_3$ and demonstrated the influence of the magnitude of external fields and the crystal anisotropy. Rose and Cohen [39] used Molecular-Dynamics with a first-principles based shell model potential to study $LiNbO_3$. They revealed that a line of maximum electrocaloric effect passes through the zero field ferroelectric transition, continuing along a Widom line at high temperatures with increasing fields. However, the first-principles based simulations require delicate parameterization and the computation is expensive. In this thesis, we develop a statistical lattice-based Monte-Carlo model using a Ginzburg-Landau type effective Hamiltonian, and a canonical and microcanonical multi-demon algorithm [48–50]. This model can represent the ferroelectric behavior and allow to study the electrocaloric effect by changing the parameters flexibly. In this sense, the factors influencing the electrocaloric effect are revealed more straightforwardly

In short, to study the electrocaloric effect involving the irreversible processes, e.g., for the field reversal case, the defect engineering and the relaxors, both methods, including the thermodynamical analytical model of entropy changes and the statistical model by strict enforcement of the adiabatic condition using the lattice-based Monte-Carlo simulations, are revisited and extended.

Chapter 2

Fundamentals of Ferroelectrics and Relaxors

Capturing the key features of ferroelectrics and relaxors is a prerequisite for modeling the electrocaloric effect properly. Therefore, from Sec. 2.1 to 2.3 background information on ferroelectric materials and their properties for the main interest of this thesis is presented. After a short summary of the major features of conventional ferroelectrics, defect engineered ferroelectrics and relaxor ferroelectrics (relaxors) are introduced, along with a brief literature review. Meanwhile, existing studies on the electrocaloric effects of engineered ferroelectrics and relaxors are commented.

2.1 Ferroelectrics

Rochelle salt was firstly synthesized in 1665 by Seignette, and ferroelectricity was firstly discovered by Valasek in 1920 showing the dielectric hysteresis in Rochelle salt [51]. Since then it is gradually accepted that ferroelectrics are a group of materials, which not only have the piezoelectric, and pyroelectric effect, but also, more importantly, possess some other intrinsic properties [52]. Three of these intrinsic properties are summarized in the following. More details can be found in Refs. [53–61].

Firstly, the spontaneous polarization is temperature-dependent. An illustration is shown in Fig. 2.1 for a typical perovskite-structure ferroelectric material ABO_3, e.g., $BaTiO_3$ and $PbTiO_3$. Above T_C, the crystal structure is cubic, and there is no spontaneous polarization. Correspondingly, no domain structure exists, as illustrated in the right panel of Fig. 2.2. By contrast, below the Curie temperature T_C, the crystal structure becomes tetragonal, and there are offsets of the B ion and oxygen ions away from their center positions. As illustrated in Fig. 2.1 the B ion shifts downwards, and oxygen ions shift upwards, which leads to a spontaneous polarization. In barium titanate ($BaTiO_3$) Mason and Matthias [62] obtained the spontaneous polarization as function of temperature from experimental data, and a sharp change of the polarization was observed at the phase transition temperature.

In order to minimize the high energy density due to the field-induced by surface charges, a domain structure appears (see the left inset of Fig. 2.2). Depending on the type of material, the temperature and the boundary conditions, different angles between the domains can be observed, e.g., 71°, 90°, 109°, 120°, 180°. Matthias and Von Hippel [63] observed domains and domain walls (originally described as domain boundaries), and investigated the influence

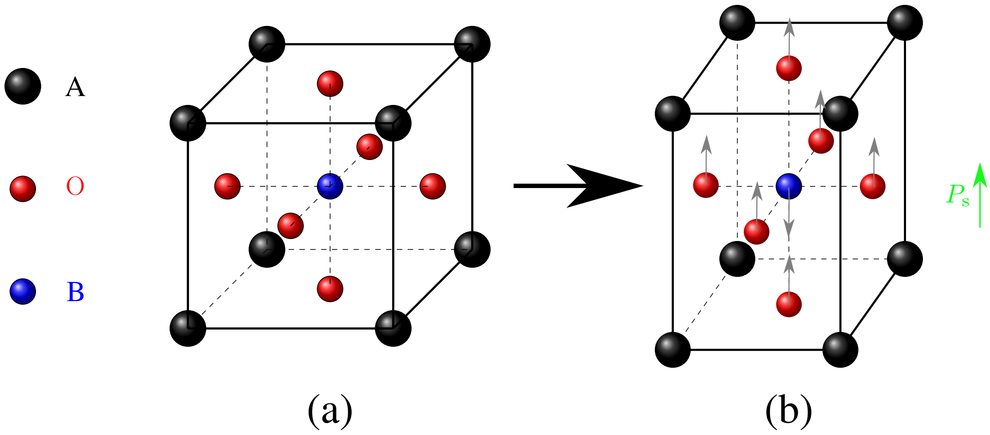

FIGURE 2.1 *Exhibition of the spontaneous polarization for a typical perovskite-structure ferroelectric material ABO_3. (a) Above the Curie temperature T_C it is a cubic structure, and there is no spontaneous polarization. (b) Below T_C, it is a tetragonal phase, and the spontaneous polarization appears.*

of temperature and electric fields on the domain structure. They revealed that the domain structure appears below the Curie temperature, and that the domain size varies under external electric fields. Experimentally, many methods can be applied to observe the domain structures, e.g., surface etching, almost nondestructive surface decoration, polarized light microscopy, scanning force microscopy, and transmission electron microscopy. It should be noted that the domain structure has significant influence on the material properties, including hysteresis, electrocaloric effect, and degradation mechanisms [61].

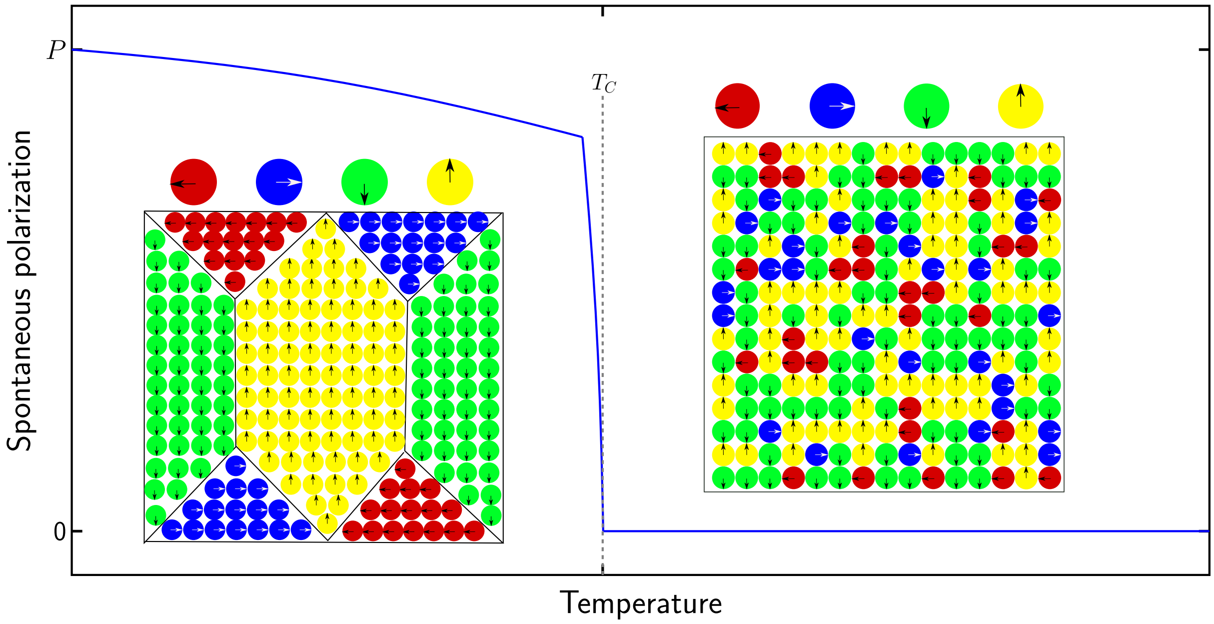

FIGURE 2.2 *Spontaneous polarization and the domain structure vs. temperature. Usually ferroelectrics in the polar state exhibit a domain structure below the Curie temperature T_C, while the nonpolar state shows no domain structures above T_C. The schematic plots of the domain structure are adapted from Ref. [64].*

Secondly, the polarization can be reversed under the external field (see Fig. 2.3). Below T_C, a hysteresis loop exists (see the left inset of Fig. 2.3). The hysteresis becomes slimmer as the temperature increases. Above T_C, the hysteresis loop diminishes (see the right inset of Fig. 2.3). When the temperature is far above T_C, it degenerates to a straight line due to the piezoelectric effect.

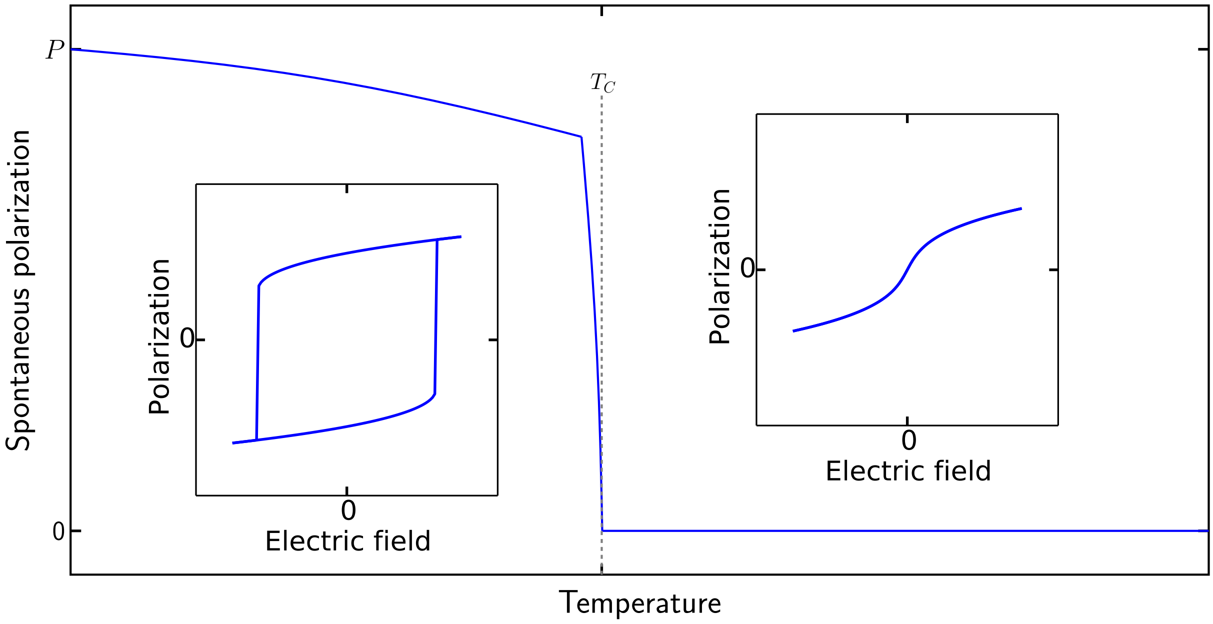

FIGURE 2.3 *Spontaneous polarization and the hysteresis vs. the temperature. In ferroelectrics, the hysteresis appears below the Curie temperature T_C, and usually diminishes above T_C.*

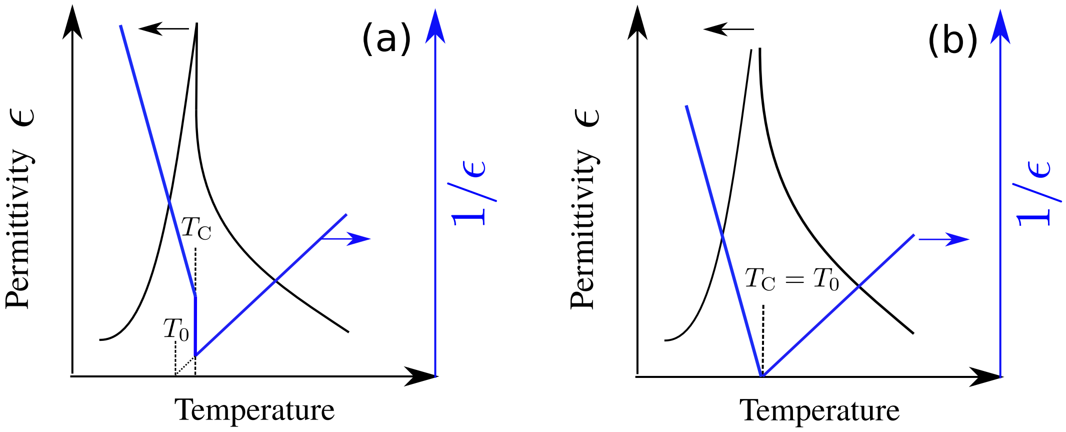

FIGURE 2.4 *Temperature dependence of the dielectric permittivity in ferroelectrics with (a) the first order phase transition and (b) the second order phase transition. As can be seen, at the Curie temperature T_C the dielectric peak is sharp and the width is relatively narrow. Above T_C the temperature dependence of the dielectric constant obeys the Curie-Weiss law. Adapted from Ref. [65].*

Thirdly, there is an anomaly of the permittivity, as shown in Fig. 2.4. The permittivity at the Curie-Weiss temperature T_0 exhibits a sharp peak, and no frequency-dependent permittivity can be observed. Far away from T_0, the permittivity can be lower than the peak value by one or two orders of magnitude. Specially, above T_0, the dielectric behavior follows the well-known Curie-Weiss law

$$\epsilon = \frac{1}{a_0(T - T_0)} , \tag{2.1}$$

where a_0 is the Curie-Weiss constant. For a second order phase transition, the two temperatures T_0 and T_C are equal, and the theoretical dielectric constant below T_C is equal to $-1/[2a_0(T - T_C)]$.

Moreover, the spontaneous polarization, the hysteresis loop, and the permittivity have also anomalies around other phase transition temperatures. For instance, $BaTiO_3$ experiences the cubic to tetragonal phase transition around 401 K, the tetragonal to orthorhombic phase transition around 285 K, and the orthorhombic to rhombohedral phase transition around 196 K [66]. Changes are also observed in the spontaneous polarization, hysteresis and permittivities at these phase transition temperatures.

In addition to inorganic crystals (e.g., perovskite oxides), ferroelectricity can be found in many other groups of materials, such as the polymeric materials (e.g., Polyvinylidene fluoride) and the liquid crystals (e.g., p-decyloxybenzylidene p-amino 2-methylbutyl cinna-mate) [60, 67].

This thesis deals directly with ferroelectrics and relaxors based on perovskite oxides. One aim is to develop a computational model for evaluating the electrocaloric effect. Hence, the developed models and the results should cover general features of ferroelectrics. These are the temperature-dependent spontaneous polarization with the evolution of the domain structures, the switchable spontaneous polarization under the electric field, and the permittivity anomaly at the phase-transition temperature. The former two features are successfully captured by our model in Chap. 4 for the benchmark test of $BaTiO_3$, which validates the model and promises further investigation of the electrocaloric effect for ferroelectrics.

Current studies on ferroelectrics mainly focus on the electrocaloric effect close to the phase-transition temperature. For a 1st order phase-transition a large latent heat is involved. Hence, a large temperature change can be achieved. For instance, Bai *et al.* [68, 69] showed that $BaTiO_3$ prepared from hydrothermally synthesized nano-sized powders has a strong ECE effect up to 1.4 K, around the tetragonal-cubic phase transition temperature, ranging from 395 K to 404 K, while thin films of $BaTiO_3$ exhibit a ECE of $\Delta T = 7.1$ K. Also in the theoretical study of $LiNbO_3$ using Molecular-Dynamics with a first-principles based shell model potential, Rose and Cohen reported that a temperature change of more than 22 K can be obtained around the phase transition temperature when the polarization varies sharply [39]. However, we should note that around the phase-transition temperature the thermal hysteresis is not negligible, which deteriorates the electrocaloric effect during cycling.

In short, more effort is needed to explore materials with large electrocaloric effects around the phase transition temperatures and to design optimized device concepts. In this sense, one can raise the question whether the electrocaloric effect can be improved in the ferroelectric phase.

Also the maximization of the electrocaloric cooling by adjusting the cycle loading has only been hardly addressed. In a conventional electrocaloric cycle unipolar loading is applied, i.e., the cooling/heating effect is obtained by removing/applying an electric field. The principle idea of the electrocaloric effect lies in changing the vibrational entropy by varying the dipolar entropy. In this context, one can ask whether a sesquipolar loading can lead to larger electrocaloric effect, since the polarization can be further altered if a reversed field is considered. Nevertheless, the irreversible contribution is expected to be more prominent during field reversal, and the total entropy can increase. Combined with experimental results, comprehensive theoretical and computational studies are presented in this thesis to show the impact of a reversed field and to determine the optimal reversed field. Our results imply that an enhancement of temperature change by 20% can be achieved by employing the optimal sesquipolar loading.

2.2 Defect Engineering in Ferroelectrics

Dopants are usually introduced in perovskite ferroelectrics in order to improve or design their properties, e.g., the electro-strain effect [70]. For example, in acceptor doped $BaTiO_3$, Ba or Ti ions are substituted by ions with a lower valence [71]. These ions can be Mn, Cu, Fe or others. Charge neutrality is typically obtained by compensating oxygen vacancies, e.g., as shown in Fig. 2.5. Acceptor doped materials, which are also referred to as hard doped, are difficult to polarize, and exhibit high coercive fields as well as small strains [72]. It is well-established that in acceptor doped material reactions between dopants and oxygen vacancies can occur. For $BaTiO_3$ it was demonstrated that $(\mathrm{Mn}''_{\mathrm{Ti}} - \mathrm{V}_{\mathrm{O}}^{\bullet\bullet})^{\times}$ associates with preferred orientation parallel to the spontaneous polarization are present in crystals annealed in a reducing atmosphere [74].

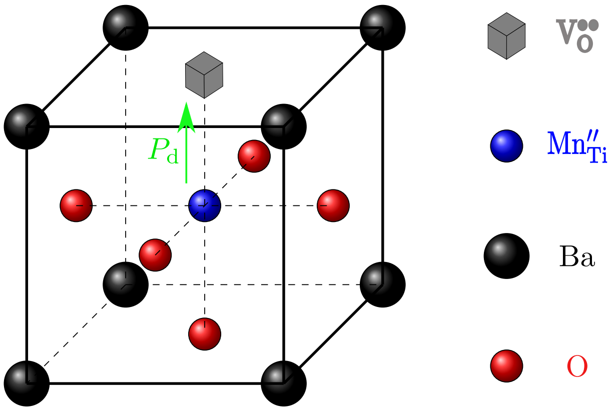

FIGURE 2.5 *Lattice structure of Mn-doped* $BaTiO_3$. *The defect associates* $(\mathrm{Mn}''_{\mathrm{Ti}} - \mathrm{V}_{\mathrm{O}}^{\bullet\bullet})^{\times}$ *induce the polarization* P_{d}*, which produces an internal field. Adapted from Ref. [73].*

Since the re-orientation of defect dipoles is kinetically hindered by the activation barrier for the oxygen vacancy migration, such defect complexes cannot immediately follow the polarization switching [73]. Non-switchable defect dipoles impose a restoring force for reversible

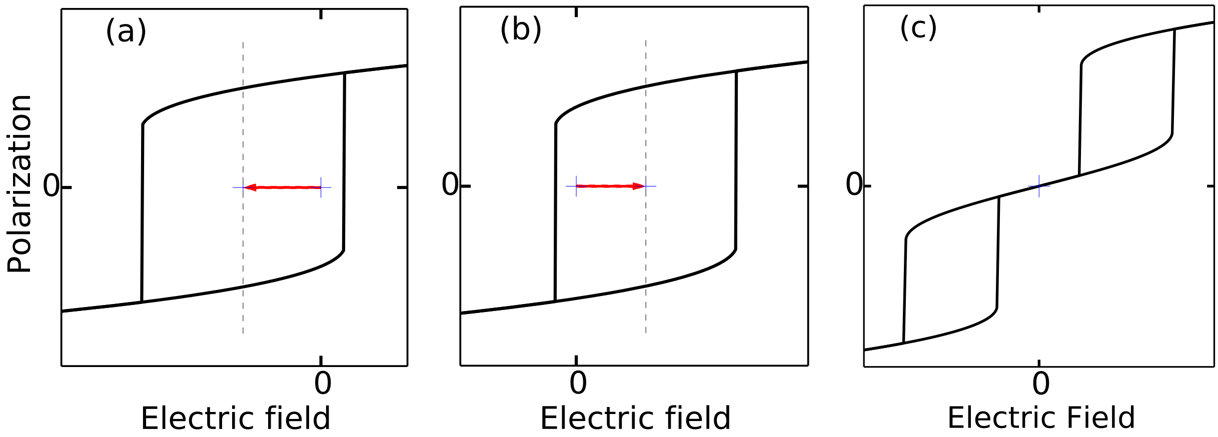

Figure 2.6 *Hysteresis for ferroelectrics with (a) parallel defect dipoles, (b) anti-parallel defect dipoles, and (c) mixture of defect dipoles. Hereby mixed defects means that defect dipoles are ordered over large regions, but the polarization of these different regions are anti-parallel to each other. Adapted from Ref. [59].*

domain switching, and the defect-associated polarization P_d affects the materials behavior significantly [70]. There exit a number of studies, revealing the influence of defect dipoles on the material properties and degradation mechanisms [71, 75–80].

Particularly, experimental observations have revealed that the dielectric hysteresis can be shifted or pinched by defect dipoles [57, 70, 81–100]. Throughout the whole sample, when defect dipoles orient to the same direction, the P-E loops can be shifted. Depending on the direction of the applied field, the center of the hysteresis loop can be shifted to the left or right as shown in Figs. 2.6(a) and (b). However, when defect dipoles are ordered in several large regions, while the polarization in these different regions are anti-parallel to each other, it represents a pinched hysteresis as shown in Fig. 2.6(c), which is similar to that of the antiferroelectric materials. In this thesis, only samples with parallel and anti-parallel defects are studied, namely the cases shown in Figs. 2.6(a) and (b).

Since defect dipoles can change the ferroelectric domain evolution significantly, they potentially can have a large impact on the electrocaloric effect. In fact, the possibility to enhance and control the electrocaloric effect in dielectric materials by the presence of internal dipoles was formulated by Van Vechten [101] in an US-patent in the late seventies of the last century. However, recently Grünebohm *et al.* [41] have shown by means of Molecular-Dynamics simulations based on an effective Hamiltonian approach that the electrocaloric effect can switch from conventional to inverse in the presence of fixed defect dipoles. While the influence of phase transitions on the electrocaloric effect in ferroelectrics is widely studied, the possibility to tune the electrocaloric effect by defect dipoles has not been investigated in much detail. Simulation results in Chap. 6 show that the delicate interplay of the external field and the internal field-induced by defect dipoles results in an inverse electrocaloric effect, which can be utilized for the optimization of the caloric cycle.

2.3 Relaxors

Relaxors show large electromechanical coupling and were first studied by Smolenskii [102] using $PbMg_{1/3}Nb_{2/3}O_3$ (PMN) and some other PMN based materials. Compared with ferroelectrics, relaxors are described as a class of crystals possessing peculiar structures and properties. The compositional fluctuation is one of the essential characteristics of relaxors. Disordered distribution of different ions on the equivalent lattice sites is one extreme case for chemical fluctuations. More details can be found in the review articles [65, 103–109].

Several macroscopic properties that can distinguish relaxors from ferroelectrics can be summarized as follows (see Fig. 2.7). Firstly, at low temperature, compared with ferroelectrics discussed in Fig. 2.3, the remnant polarization is significantly smaller, and the hysteresis loop is slimmer in relaxors as shown in Fig. 2.7(a) [65, 103]. Secondly, the temperature-dependence of polarization is different from ferroelectrics. Above T_m the polarization in relaxors remains finite even at rather high temperatures [110]. Hereby, T_m is the temperature where the permittivity is maximum.

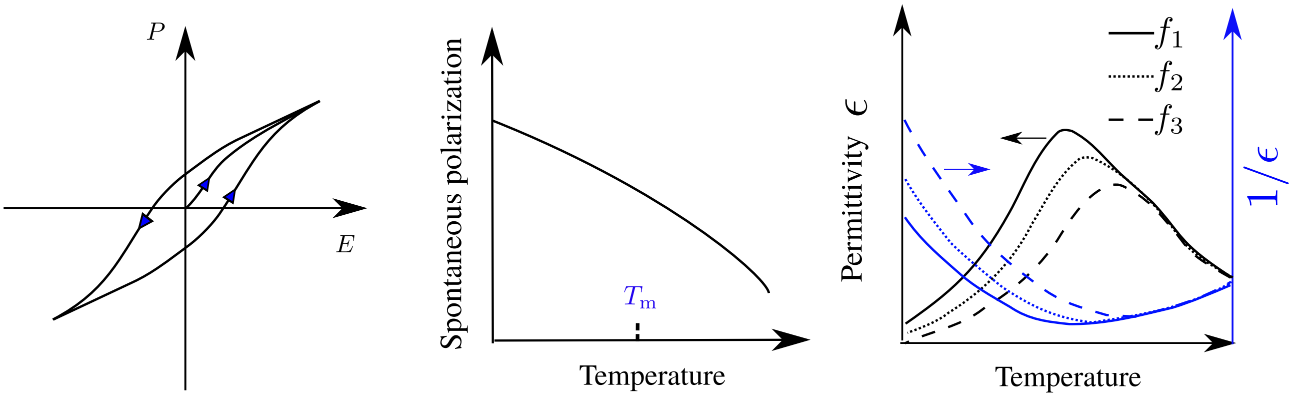

(a) (b) (c)

Figure 2.7 *(a) The hysteresis, (b) the temperature dependence of the spontaneous polarization, and (c) that of the dielectric permittivity in the relaxors. T_m is the temperature where the permittivity is maximum. Adapted from Ref. [65].*

Moreover, the permittivity exhibits a rounded peak around T_m, and demonstrates a highly frequency-dependent dispersion while in ferroelectrics the permittivity does not depend on the frequency [111].

Depending on the type of material, relaxors can be classified into two categories [105]. The first category is the canonical relaxors, e.g., $Pb(Mg_{1/3}\,Nb_{2/3})O_3$. As shown in Fig. 2.8(a) three different ranges can be distinguished by two characteristic temperatures: the freezing temperature T_f and the Burns temperature T_B. Below T_f, the nonergodic state exists, where the relaxation time of the dipoles becomes infinite so that the polar nanoregions are almost "frozen". Experimentally, the freezing temperature T_f can be approximated as the Vogel-Fulcher temperature T_VF, which satisfies the well-known Vogel-Fulcher relation:

$$f_\mathrm{m} = f_0 \exp\left(\frac{-E_\mathrm{a}}{T_\mathrm{m} - T_\mathrm{VF}}\right) , \tag{2.2}$$

where f_m is the frequency of the permittivity peak, while f_0 and E_a stand for the characteristic frequency and the activation energy of the dipole reorientation, respectively [112, 113]. Between T_f and T_B, the ergodic state appears, and the polar nanoregions are relatively mobile. In this temperature range, various formulas are utilized by different researchers to describe the dielectric behavior (see review in Ref. [108]), and one type of the formulas can be expressed as:

$$\frac{1}{\epsilon} = \frac{1}{\epsilon_\mathrm{A}} + \frac{(T - T_\mathrm{A})^2}{B} , \tag{2.3}$$

where ϵ_A, T_A and B are the fitting parameters.

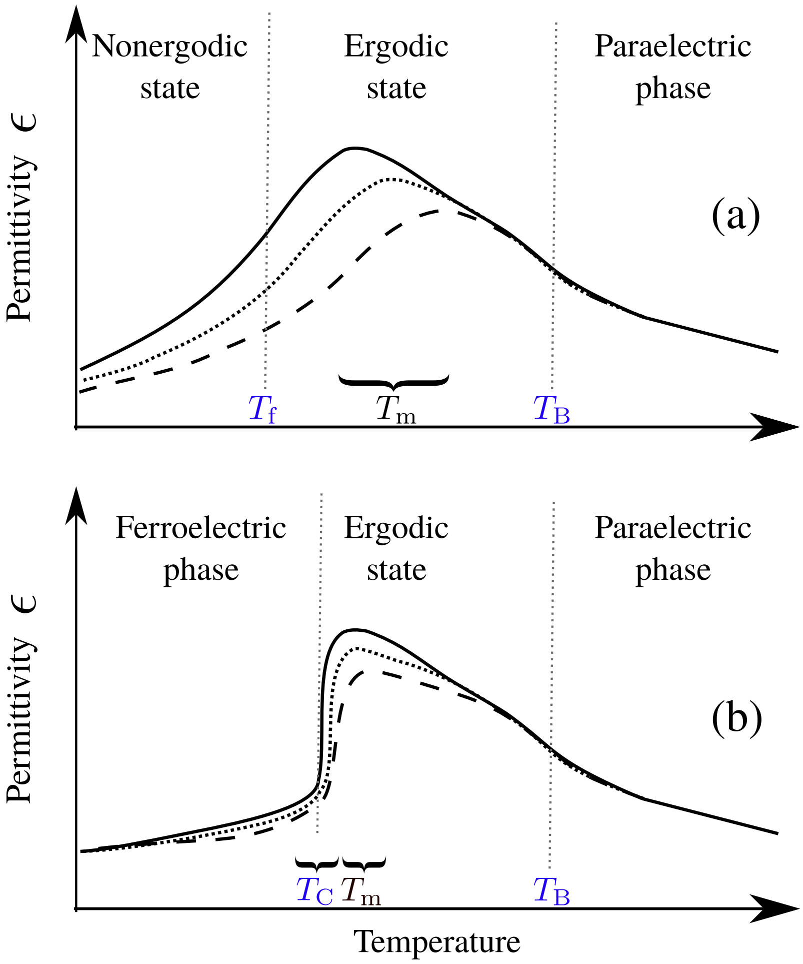

FIGURE 2.8 *Different phases at different temperatures for (a) canonical relaxors with transition from the nonergodic state to the ergodic state and (b) relaxors with transition from ferroelectric phase to the ergodic state. Adapted from Ref. [105].*

Above T_B, there exist no polar nanoregions and the material behaves like a paraelectric phase. In this high temperature range, similar to ferroelectrics, the dielectric behavior obeys the Curie-Weiss law:

$$\epsilon = \frac{1}{a_0(T - T_B)} \ . \tag{2.4}$$

Classified into the second category, as shown in Fig. 2.8(b), relaxors exhibit a temperature-induced spontaneous transition from the ferroelectric phase below the Curie temperature T_C to the ergodic state above T_C, e.g., for $(1-x)\mathrm{Pb(Fe_{1/3}Nb_{2/3})O_3}$-$x$ and $(1-x)\mathrm{Pb(Zn_{1/3}Nb_{2/3})O_3}$-$x\mathrm{PbTiO_3}$. Hereby, a diffuse phase transition with T_C depending on the frequency is demonstrated. However, this temperature-induced transition can be also sharp, when T_C is independent of the frequency. It should be noted that T_m exists within the ergodic state, and T_m can be either bigger or equal to T_C.

There are some specific characters for the canonical relaxors. As illustrated in Fig. 2.9, the relaxor phase can transform to the ferroelectric phase, if a large enough electric field is applied [114, 115]. Below T_f this field-induced transition is irreversible, and after field removal the ferroelectric phase cannot transform back to the nonergodic state. By contrast, above T_f, this phase transition induced by the field is reversible. After removing the field the ferroelectric phase disappears and the ergodic state appears.

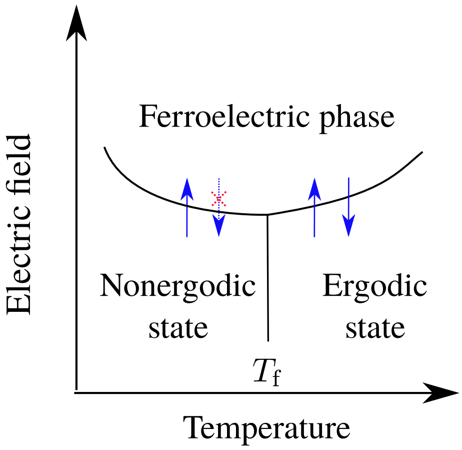

FIGURE 2.9 *Electric field-induced ferroelectrics in the relaxors. This transition is irreversible below T_f, while reversible above T_f. Adapted from Ref. [115].*

Albeit it has been more than half a century since the discovery of relaxors, the fundamental mechanisms governing in relaxors are still unclear. Various models have been proposed to explain the relaxor behavior in different materials. They include polar nanoregions, [105] the dipole-glass model, [102] the random field model, [116, 117] and the spherical random bond-random field model [118].

Experiments have indicated the existence of polar nanoregions in relaxors, e.g., elastic diffuse neutron and X-ray scattering around the reciprocal points [105] and ^{207}Pb Nuclear Magnetic

Resonance spectra [119]. To explain the microscopic aspects of polar nanoregions, two major classes of theories were proposed, as the schematic illustrations show in Fig. 2.10. In the first class, polar nanoregions are embedded into a cubic matrix with unchanged symmetry, whereas in the second one, polar nanoregions are separated by domain walls.

Grouped into the second concept, the random field model was firstly developed by Westphal and Kleemann [116] referring to the original idea of Imry and Ma [120]. It was proposed that the relaxor behavior of $PbMg_{1/3}Nb_{2/3}O_3$ is due to quenched random electric fields [116]. These quenched fields can originate from compositional fluctuations, and the experimental results of the linear birefringence supported this theory [116]. Similarly, Glinchuk and Farhi [117] described relaxors as systems with random sites and orientations of dipoles, lattice defects and unavoidable impurities embedded into the paraelectric phase.

The origin of relaxors is strongly material dependent and under debate. But from a phenomenological point of view, what all models have in common is the randomness of local fields. In a generic sense, random fields can be introduced into ferroelectrics and lead to relaxor-like-features.

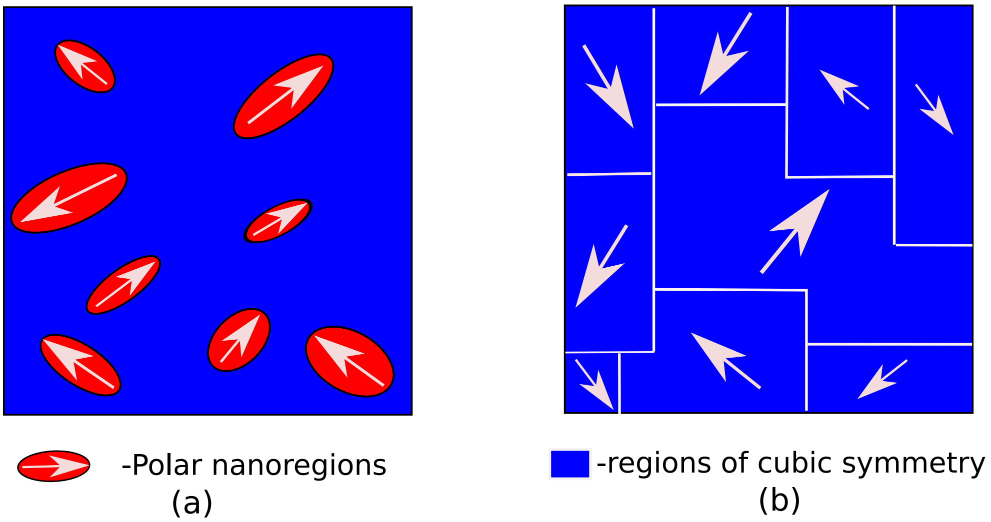

(a)

(b)

FIGURE 2.10 *Schematic representation of two different concepts for relaxors. Adapted from Ref. [105].*

Based on the above theories, plenty of numerical simulations were carried out. Using phase-field simulations, Semenovskaya and Khachaturyan [121] proposed that the coefficient of the quadratic terms in Landau multi-well potential should be a function of the concentration of the randomly distributed static defects and the critical instability temperature. This concept was utilized in Monte-Carlo simulations by Liu et at. [90]. Pirc *et al.* [42] also modified the quadratic term coefficient in their spherical random bond-random field model. Besides, according to the phase field model by Wang *et al.* [122], the effect associated with a random polarization field can include two parts: (a) the local field effect, and (b) the global temperature transition effect that influences the coefficient of the quadratic term of Landau energy.

As computing power has greatly increased, more expensive computations, e.g., first-principles calculations and the simulations based on effective Hamiltonians, are explored to reveal the origin of relaxor behaviors on the atomistic level. For instance, Gröting *et al.* [123] investigated $Na_{0.5}Bi_{0.5}TiO_3$ by means of first-principles calculations based on density functional theory and explored the influence of chemical order on the thermodynamic stability and local structure. They revealed that chemically ordered local areas can act as nucleation sites for polar nanoregions, which could explain the experimentally observed relaxor behavior of $Na_{0.5}Bi_{0.5}TiO_3$. Burton *et al.* [124] studied the influence of random field in $PbSc_{0.5}Nb_{0.5}O_3$ and $PbMg_{1/3}Nb_{2/3}O_3$ by effective Hamiltonian simulations. Nishimatsu [125, 126] developed an Open Source fast Molecular-Dynamics simulator, named 'feram', for bulk and thin-film ferroelectrics and relaxors.

In short, different from ferroelectrics, relaxors exhibit abnormal properties: slimmer hysteresis, nanosize polar domains persisting well above the permittivity peak temperature T_m, and the permittivity dispersion. Especially, in canonical relaxors, e.g., $Pb(Mg_{1/3}\,Nb_{2/3})O_3$, there are nonergodic and ergodic states. More details about these special features can be found in the aforementioned context. No investigations were performed on the permittivity. Other features, e.g., the behavior of the hysteresis, polarization and ergodic-nonergodic transition, are represented by our models in Chaps. 7 and 8. Researchers utilized different models to explain the unclear origin of the relaxors, which are summarized in this section. Within these models the random field model is utilized in this thesis to explain the relaxor behavior in a generic sense.

Relaxors show a few advantages over conventional ferroelectrics in terms of their electrocaloric effects. Relaxors have a broader phase transition range than ferroelectrics [110], which can broaden the operating temperature range for the electrocaloric effect. By adjusting the composition, it is possible to tailor the phase transition temperature and thus to control the peak position of the electrocaloric effect, which may allow considerable cooling at room temperature. Moreover, a giant electrocaloric effect has been observed in some relaxor materials. $(1-x)[Pb(Mg_{1/3}Nb_{2/3})O_3]-x[PbTiO_3]$ (PMN-PT) is one of the widely investigated relaxor system both in study of bulk ceramics and thin films. [7]) At the morphotropic phase boundary of PMN-PT, for 0.65PMN-0.35PT with 350 nm thickness, using indirect measurements Saranya *et al.* [127] concluded that a large temperature change 31.0 K under an electric field of $74.7\,\mathrm{kV\,mm^{-1}}$ can be achieved. The broad application temperature range in relaxors was also verified. For example, in experiments on $PbSc_{0.5}Ta_{0.5}O_3$, Correia *et al.* [128] revealed that there is still considerable electrocaloric effect within the operating temperature range from 1°C to 127°C.

Theoretically, it is challenging to study the electrocaloric effect in relaxors. First of all, the origin of relaxor ferroelectrics remains unclear, and the abnormal domain structure and dynamics are not well understood. The compositional fluctuations associated with the heterovalent substitutions on A or B sites is widely recognized to be responsible for the relaxor features, but the mechanisms how the chemical fluctuation influences the domain structure remain controversial. Moreover, since relaxors experience strong dissipation processes, the indirect method of evaluating electrocaloric effect using the Maxwell relation is technically unjustified. In this thesis, a generic Ginzburg-Landau type potential energy including the random fields resultant from the compositional fluctuation is proposed and combined with canonical and microcanonical ensembles to simulate the polarization switching and evaluate directly the electrocaloric effect in relaxors.

As one of the most simple relaxor ferroelectric materials, the solid solution system $BaZr_xTi_{1-x}O_3$ has attracted great interest [105, 109, 129–140]. $BaZr_xTi_{1-x}O_3$ can be considered as a solid solution through substituting certain percentage of Ti with Zr, as depicted in Fig. 2.11. It is believed that the small size-difference between Ti^{4+} and Zr^{4+} ions induces random strain fields, which are much weaker than in other relaxors with heterovalent cation substitution [107, 131, 138, 140]. Hence random strain fields may be not responsible for the relaxor behavior of $BaZr_xTi_{1-x}O_3$. However, the long-range Ti-O-Ti-O bonds that give rise to the dipolar correlation are broken through the substitution of Ti^{4+} by non-off-center Zr^{4+} [140]. This mechanism was used to explain the domain patterns in $BaZr_xTi_{1-x}O_3$. On the other hand, the first-principles calculations were performed to study different properties of $BaZr_xTi_{1-x}O_3$ [141–143]. Recently, Padurariu et al. [144] simulated the relaxor behavior of $BaM_xTi_{1-x}O_3$ (M=Zr, Sn, Hf) using a lattice-based model. They incorporated permanent dipoles due to Ti ions, O-related induced dipoles and nonpolar cells containing M ions to calculate the local field, and found that the correlation time around the Curie temperature increases, reflecting the increasing stability of some polar nanoregions in relaxors in comparison with ferroelectrics.

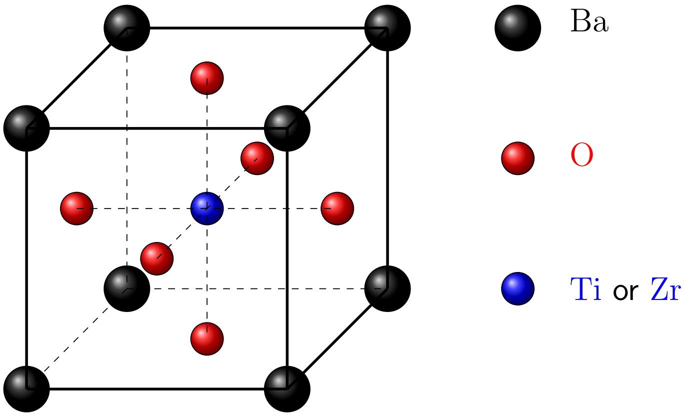

Figure 2.11 *Lattice structure of the solid solution* $BaZr_xTi_{1-x}O_3$*. Zr atom can substitute Ti atom (see the blue dots) with certain probability.*

As an environment-friendly lead-free relaxor, $BaZr_xTi_{1-x}O_3$ covers ferroelectrics, the relaxors, the polar clusters, and the paraelectrics with increasing the Zr content [136]. Hence, it is meaningful to investigate such group of material for understanding the fundamentals of the relaxor behavior and the corresponding electrocaloric effect. Experimentally, Qian *et al.* [145] measured the electrocaloric effect of $BaZr_{0.2}Ti_{0.8}O_3$ samples and reported a large temperature variation of 4.5 K under 14.5 kV mm^{-1} with a operating temperature range of 30 K, which is wider than that in $BaTiO_3$. Ye *et al.* [139] studied the same kind of material and published an even higher temperature variation of $\Delta T = 7$ K under 19.5 kV mm^{-1}. These observations suggest that $BaZr_xTi_{1-x}O_3$ might be a promising candidate for the electrocaloric cooling. Nevertheless, the origin of the relaxor behavior and that of the electrocaloric effect in $BaZr_xTi_{1-x}O_3$ is still under debate, and deserves further investigations both experimentally and theoretically. In this thesis, by describing Ti/Zr occupied lattice sites with Landau double/single wells and giving the composition-dependent dipole-dipole interaction strength, the hysteresis, domain structures, spontaneous polarizations and the electrocaloric effect are studied.

Chapter 3

Specific Questions and Outline

3.1 Specific Questions to Be Answered

In this section the questions raised in the previous chapter are collected, for which we pursue the answers in this thesis.

1) What methods should we choose to evaluate the electrocaloric effect theoretically? What are the benefits and drawbacks of the utilized methods?

2) Can we improve the electrocaloric effect, by varying the domain wall energy, adjusting the cycles, or applying defect engineering?

3) How can we describe irreversible processes in the framework of Landau theory?

4) What is the influence of field reversal on the electrocaloric effect?

5) Does the maximal cooling appear when the polarization becomes zero? If not, where does it appear and how can this phenomenon be explained in terms of energy and entropies?

6) How does the presence of defect dipoles influence the electrocaloric effect? How do microscopic domains and entropies change?

7) Can the electrocaloric effect be improved through defect engineering?

8) How can we simulate the material behavior of $BaZr_xTi_{1-x}O_3$? How do hysteresis, polarization, domain structure and local random fields evolve? What are the relations between theses factors and the electrocaloric effect?

9) How can we develop a generic model representing the relaxor behavior?

10) How does the electrocaloric effect change when varying the random fields or random-defects-induced fields?

3.2 Goal and Outline

The general goal of the thesis is to develop direct methods for evaluating and understanding the electrocaloric effect in complex ferroelectric materials and to derive thereafter optimization strategies with respect to the caloric cycle and the materials. On one hand, an analytical model based on entropy analysis is successfully extended to include the total entropy change associated with irreversible processes. It allows to study the enhancement of the caloric cooling by field reversal and the determination of the optimal reversed field with and without defect dipoles. On the other hand, a lattice-based Monte-Carlo simulation technique is developed, which makes use of a Ginzburg-Landau type effective Hamiltonian and a multi-demon microcanonical algorithm. This method is applied to study the dielectric property and the electrocaloric effect in ferroelectrics with defect dipoles and relaxor ferroelectrics. Note that even though the theoretical investigations in this thesis are performed on single crystals, the obtained knowledge can be applicable to ceramics and polymer ferroelectrics. The thesis is outlined in the following.

Chap. 2 presents the basic knowledge and known characteristics about ferroelectric perovskites, defect engineered ferroelectrics and relaxors.

In Chap. 4 the Landau theory for modeling ferroelectrics is first presented, which is one of the basic ingredients of the analytical model based on entropy change analysis in Chaps. 5 and 6. In the rest of the chapter, the direct method based on the lattice-based Monte-Carlo simulations is described. Thereby, a Ginzburg-Landau type effective Hamiltonian is presented, which allows convenient parameter studies on the domain structure level. By using this Hamiltonian and the microcanonical ensemble based on the multi-demon algorithms is introduced and enables the direct evaluation of the temperature change under strict adiabatic condition. By utilizing the developed Hamiltonian and algorithm, the conventional ferroelectrics $BaTiO_3$ is first simulated as validation. Details on the numerical implementation and convergence test are provided. The simulation of $BaTiO_3$ also serves as a basis for the various models used in the following Chaps. 5 to 8 to study the influence of defect dipoles and relaxors.

In Chap. 5 an improved thermodynamic cycle for ferroelectric single crystals is validated, where the cooling effect is enhanced by applying a reversed electric field. In contrast to the conventional adiabatic heating or cooling by on-off cycles of the external electric field, applying a reversed field significantly improves the cooling efficiency, since the variation in configurational entropy is increased. Both results from Monte-Carlo simulations by the direct method based on energy conservation and experiments using direct electrocaloric measurements show that the electrocaloric cooling efficiency can be enhanced by more than 20% in standard ferroelectrics and also relaxor ferroelectrics, like $Pb(Mg_{1/3}/Nb_{2/3})_{0.71}Ti_{0.29}O_3$. Moreover, the optimal reversed field corresponds to the shoulder of the P-E loop, instead of the zero-polarization position. This phenomenon cannot be explained if a constant total entropy is assumed under adiabatic conditions. To reveal the physics behind, a thermodynamical analytical model of entropy changes based on work loss is proposed, which takes the entropy contribution of the irreversible process into account. The optimal reversed field determined by this approach agrees with the experimental observations. It signifies the importance of considering irreversible process in the electrocaloric cycles.

Defect dipoles, which widely exist in doped and aged ferroelectrics, can influence the domain evolution significantly, and thus also the electrocaloric effect. In Chap. 6 the influence of defect dipoles on the electrocaloric effect in acceptor doped $BaTiO_3$ is studied by both methods. Thereby, oxygen vacancy-acceptor associates are described by fixed local dipoles with orientation parallel or anti-parallel to the external field. It is systematically investigated how the density of defect dipoles and the strength of the external field influence the electrocaloric effect. Results reveal that in the case of anti-parallel defect dipoles the electrocaloric effect can be conventional or inverse depending on the dipole density. Abnormal electrocaloric features, such as inverse effect and double peaks can appear. This stems from the delicate interplay of internal and external fields and can be explained by the domain structure evolution and related field-induced entropy changes. The results are in good agreement with those obtained by Molecular-Dynamics simulations employing an ab initio based effective Hamiltonian. Based on these results, improved electrocaloric cycles are proposed by making use of the inverse electrocaloric effect in the presence of defect dipoles.

A systematic study on the relation of the electrocaloric effect and the relaxor state transition of $BaZr_xTi_{1-x}O_3$ is given in Chap. 7. The results are obtained from canonical and microcanonical lattice-based Monte-Carlo simulations with a Ginzburg- Landau-type Hamiltonian. Thereby, a Ginzburg-Landau multi-well energy term is used for unit cells containing Ti, and a single-well energy term for unit cells occupied by Zr-ions. Results are compared with measurements of $BaZr_xTi_{1-x}O_3$ ($x = 0.12$ and 0.2) samples. Particularly, direct electrocaloric measurements at various temperatures, domain patterns by piezoresponse force microscopy at room temperature, and P-E loops. Distinct regimes depending on the Zr-concentration can be identified: the system experiences a sequence of ferroelectric, relaxor, and the paraelectric behavior as the Zr-concentration increases. Results reveal that BZT with a Zr-concentration of $x = 0.3$ exhibits a relatively large electrocaloric effect in a wide temperature range at rather low temperature. In addition, the correlation between the internal random field-induced by the composition fluctuation and the regimes is discussed.

A generic model for relaxors based on the random field theory is presented in Chap. 8, in order to explicitly examine the impact of random fields on the dielectric and electrocaloric effect. The direct method using canonical and microcanonical Monte-Carlo simulations is applied, and particularly the electrostatic energy contribution by the static random field is included. Results show that, if the strength or the density of the random fields increases, the electrocaloric peak shifts to lower temperature, but the temperature variation is reduced. On the contrary, if the domain-wall energy increases, the peak shifts to higher temperature and the electrocaloric effect becomes stronger. The maximal temperature change happens at the freezing temperature, where the nonergodic-to-ergodic transition takes place. Results imply that the presence of random fields reduces the entropy variation in an electrocaloric cycle by pinning local polarization. For comparison, a similar generic model based on the random defect dipoles is presented and compared with the generic model of the random field. The defect dipole configuration is quantitatively correlated with the random field, and it demonstrates that the random field plays a fundamental role. At the end selected results are summarized in Chap. 9, along with the outlook on the future work and comments on potential challenges.

Chapter 4

Theory and Model Development

Parts of this Chapter are based on the publication “Y.-B. Ma, K. Albe, and B.-X. Xu, Phys. Rev. B 91, 184108 (2015)”.

This chapter gives an introduction to the model used in the following chapters. The typical Landau-Devonshire theory is summarized in Sec. 4.1, which is needed for the calculation of dipolar entropy in Chaps. 5 and 6. In the rest of this chapter, the lattice-based Monte-Carlo simulation approach is detailed, with benchmark tests on the prototype ferroelectric $BaTiO_3$. This serves as a basis for various models used in the results presented in Chaps. 5 to 8.

4.1 Landau Theory

Devonshire applied the Landau theory [146–148] to ferroelectrics, and expanded the elastic Gibbs free energy density as a function of polarization, temperature, and stress [53, 149–151]. Placing the sample under stress-free conditions with constant temperature and assuming that the polarization is directed along one of the crystallographic axes only, the dipolar mean field Helmholtz free energy density F_{bulk} in a bulk material with spatially uniform-distributed polarization together with the electrostatic energy F_{ele} can be expressed as

$$F = F_{\text{bulk}} + F_{\text{ele}} = \left[F_0 + \frac{1}{2}aP^2 + \frac{1}{4}bP^4 + \frac{1}{6}cP^6 + \ldots \right] - EP, \tag{4.1}$$

where F_0 is the field-independent part, a, b and c are temperature-dependent phenomenological coefficients, P is the total macroscopic polarization, and E is the external electric field. Setting the first derivative of the Landau free energy density $\partial F/\partial P$ to be zero, one obtains a relation between the polarization and the electric field:

$$E \quad = \quad aP + bP^3 + cP^5. \tag{4.2}$$

The coefficient a can be determined from the dielectric permittivity ϵ above the Curie temperature by differentiating Eq. 4.2 with respect to P:

$$\frac{1}{\epsilon} \quad = \quad \frac{\partial E}{\partial P} \quad = \quad a \quad . \tag{4.3}$$

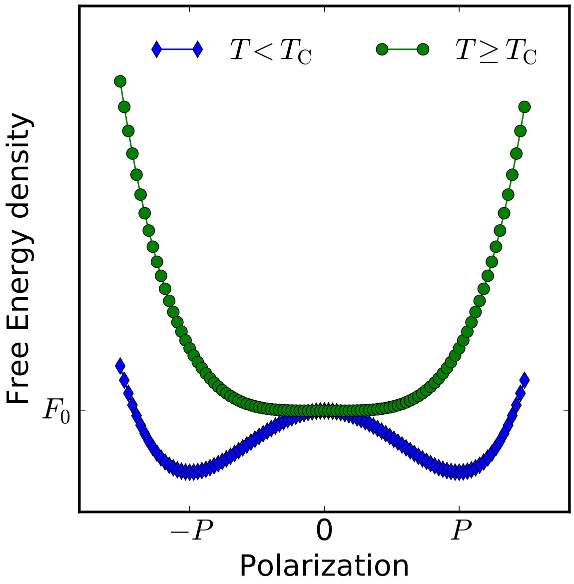

FIGURE 4.1 *The free energy density F vs polarization for a second order phase transition with no external field. For* $T \geq T_C$*, F has one single minimum, and the paraelectric phase exists. For* $T < T_C$*, F has two minima, and the ferroelectric phase exists.*

By recalling Eq. 2.1, one arrives at $a = a_0(T - T_C)$. When $b < 0$, a first order phase transition occurs at T_C, while for $b > 0$, it is a second order phase transition. In all ferroelectrics, the coefficient c is positive.

For the entropy analysis in the current thesis, the second order phase transition is of interest, i.e., with $b > 0$. As shown in Fig. 4.1, by setting $E = 0$, two distinctive curves can be observed for $T \geq T_C$ and $T < T_C$, respectively. When the temperature is above or equal to T_C, according to Eq. 4.2 the free energy density has one single minimum when the polarization is 0, and the material is in the paraelectric phase. However, below T_C, the free energy density has two minima with nonzero $\pm P$, and the material is in the ferroelectric phase. As illustrated in Fig. 4.2, in the ferroelectric phase with $T < T_C$, the polarization varies with respect to the external electric field. Clearly, when the external field is not large enough (e.g., E_1 and E_2), F has two minima, corresponding to two polarizations in the hysteresis loop. After applying a large enough electric field (e.g., E_3), F has only one minimum, and the polarization reaches saturation.

The Landau-Devonshire theory is well suited to describe a sample with spatially uniform-distributed polarization. For analytical solutions, in order to simplify the mathematical treatment, it is appropriate to use the above simple Landau-Devonshire theory, as it is done in Chap. 5 and 6 to evaluate the dipolar entropy.

However, in a realistic case the polarization always has some spatial variations, and this phenomenon can be described by the Ginzburg-Landau theory. Due to the presence of the

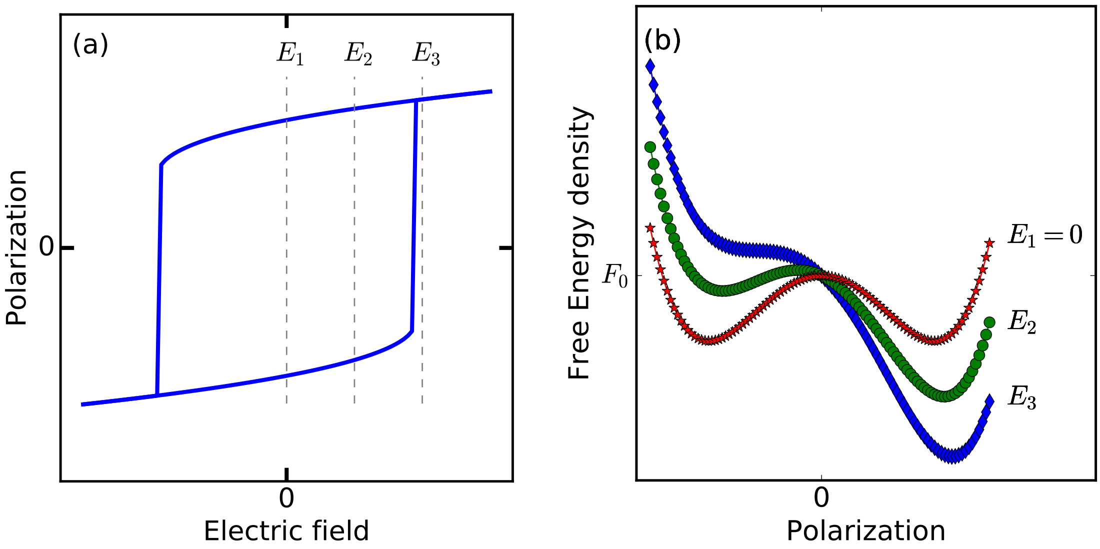

FIGURE 4.2 *Polarization vs the external field with $T < T_C$ and the corresponding free energy density F. When F has two minima, there is a hysteresis loop. When F has one single minimum, the polarization is saturated.*

polarization variations, i.e., the polarization gradient ∇P, one additional gradient term $F_{gra} = S_J|\nabla P|^2$ was added to the free energy density: [60, 152]

$$F = F_{bulk} + F_{gra} + F_{elec} = \left[F_0 + \frac{1}{2}aP^2 + \frac{1}{4}bP^4 + \frac{1}{6}cP^6 + \dots\right] + S_J|\nabla P|^2 - EP, \tag{4.4}$$

where S_J is a gauge coefficient for the gradient term. In the phase-field theory, the above free energy can be used to formulate the kinetic model of domain structure evolution, according to a Longevin-type equation. The formation of free energy can also be argued by the dipole-dipole interaction, which should be highly responsible for the formation of anti-parallel arrangements of dipoles at the neighboring domains. Hlinka and Márton [153] assumed that there is no depolarization field associated with the overall polarization of the sample and utilized a soluble equation to evaluate the depolarization field. By doing this, they acquired quantitative predictions for the domain wall profile and width.

By combining the phase-field theory and the Maxwell relation, the electrocaloric effect under the influence of a domain structure can be indirectly evaluated [28, 30–34], which is, however, not the purpose of this thesis.

4.2 Ginzburg-Landau Type Effective Hamiltonian

In order to exploit directly the influence of domain structure on dielectric and caloric properties in ferroelectrics and relaxors, a Ginzburg-Landau type effective Hamiltonian is proposed and used in lattice-based canonical and microcanonical Monte-Carlo calculations. The Ginzburg-Landau type effective Hamiltonian consists of a ground-state Landau-type term, a dipole-dipole interaction term, a gradient term penalizing the domain wall formation, and an electrostatic energy. By adjusting the parameters involved in the energy terms, the domain structure can be varied directly. The details of the effective Hamiltonian for conventional ferroelectrics are given in this section, whereas on this basis modifications are made accordingly in the following chapters for the specific materials and problems.

The potential energy H is given by the Ginzburg-Landau type effective Hamiltonian which includes four contributions: the Landau term H_{D}, the dipole-dipole interaction energy H_{dip}, the domain wall energy H_{gr} arising from short-range and elastic interactions [126] and the electrostatic energy H_{e}:

$$H = H_{\mathrm{D}} + H_{\mathrm{dip}} + H_{\mathrm{gr}} + H_{\mathrm{e}}. \tag{4.5}$$

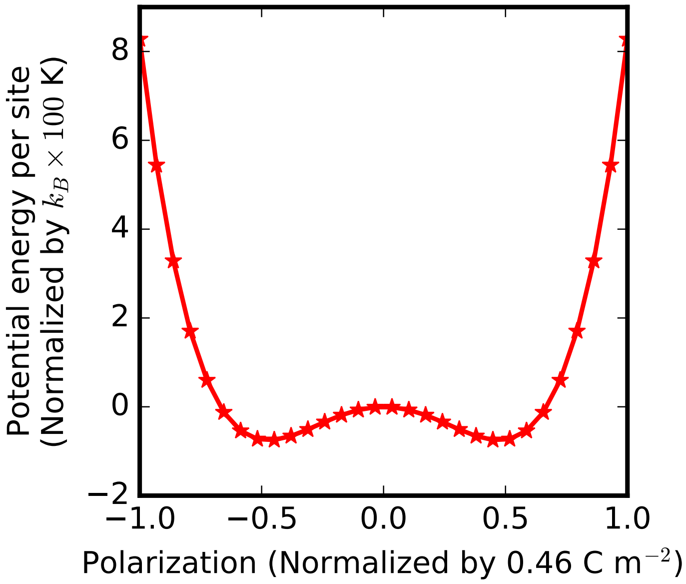

FIGURE 4.3 *Schematic illustration of the double-well Landau type energy for BaTiO$_3$.*

$$H_{\mathrm{D}} = V_0 \sum_i \Big[-\frac{a}{2}(P_x^2(\mathbf{r}_i) + P_y^2(\mathbf{r}_i)) + \frac{b}{4}(P_x^4(\mathbf{r}_i) + P_y^4(\mathbf{r}_i)) \Big], \tag{4.6}$$

The Landau term H_{D} describes the bulk contribution, if the system has a uniform distribution of polarization [60]. As it is well established, H_{D} is given by an even polynomial function with respect to the polarization. For 2D simulations the following sixth-order polynomial can be applied, where $V_0 = l_0^3$ is the volume of a lattice site, l_0 is the lattice constant, a, b are coefficients, $\mathbf{r}_i$ is the coordinate of site i, and $P_x(\mathbf{r}_i)$, $P_y(\mathbf{r}_i)$ are the Cartesian components of the polarization vector $\mathbf{P}(\mathbf{r}_i)$ at site i. The coefficients a, b ensure the multi-well character of the Landau term and are material-dependent. Different from the case in the Ising model, [45] the magnitude of the polarization is allowed to change, and its equilibrium value is determined by the minima of the Landau energy. Since in our case the entropy contributions are sampled by

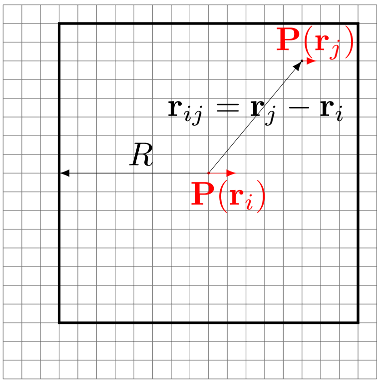

FIGURE 4.4 *Illustration of the long-range dipole-dipole interaction.*

the Monte-Carlo algorithm, the Landau-type energy describes a static ground state energy only. A typical ground Landau-type energy for $BaTiO_3$ is schematically illustrated in Fig. 4.3.

In ferroelectric materials, a homogeneous polarization distribution can lead to a large depolarization field and thus high electrostatic energy. Domain structures with multidomain variants are expected, even in ideal single crystals. To reproduce this heterogeneous feature, it is essential to add the long-range dipole-dipole interaction energy H_{dip} [60], as typically done in many phase-field simulations [154, 155], Monte-Carlo simulations [156–158], and first-principles based effective Hamiltonians [126, 159, 160]. The dipole-dipole interaction energy describes in principle the electrostatic energy of a dipole sitting in the electric field generated by its neighboring dipoles. The dipole vector at site i is equal to $V_0\mathbf{P}(\mathbf{r}_i)$, and is located at the center of site i. In the thesis a thin layer of dipoles in a 2D planar arrangement is regarded, but the electric field generated by the dipoles is still a 3D case. Therefore, the following expression is used [157, 158, 161, 162]:

$$H_{\text{dip}} = -\frac{1}{2}V_0\sum_i \mathbf{E}_\mathbf{i}\mathbf{P}(\mathbf{r}_\mathbf{i}), \tag{4.7}$$

$$\mathbf{E}_\mathbf{i} = V_0\frac{1}{4\pi\epsilon_0\epsilon_r}\sum_j\left[\frac{3\mathbf{r}_\mathbf{ij}[\mathbf{P}(\mathbf{r}_j)\cdot\mathbf{r}_\mathbf{ij}]}{|\mathbf{r}_\mathbf{ij}|^5} - \frac{\mathbf{P}(\mathbf{r}_j)}{|\mathbf{r}_\mathbf{ij}|^3}\right], \tag{4.8}$$

where $\mathbf{r}_\mathbf{ij} = \mathbf{r}_\mathbf{i} - \mathbf{r}_\mathbf{j}$, ϵ_0 is the vacuum permittivity and ϵ_r is the relative high-frequency permittivity.

The dipole-dipole interaction energy tends to introduce as many domains as possible in order to lower that contribution to the system and to form an anti-parallel domain structure with numerous domain walls. Since the dipole-dipole interaction is long-range in nature, we tested the convergence behavior of our calculation with respect to the number of terms included in the summation in Eq. (4.8). As shown in Sec. 4.3 the energy convergence is obtained for all relevant temperatures with a cutoff-radius of eight times the lattice constant. For illustration, a long-range dipole-dipole interaction between $\mathbf{P}(\mathbf{r}_i)$ at position $\mathbf{r}_i$ and $\mathbf{P}(\mathbf{r}_j)$ at position $\mathbf{r}_j$ within the cut-off radius R is sketched in Fig. 4.4.

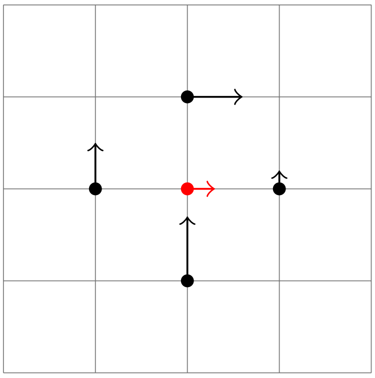

FIGURE 4.5 *Illustration of the polarization gradient. Due to the polarization gradient, there exists the extra energy contribution, i.e.,the domain wall energy.*

The presence of domain walls introduces additional energy, due to the energy gain by forming the polarized ground state and the elastic strain [60]. Similar to the phase-field theory, the domain wall energy H_{gr} is assumed to be proportional to $||\nabla\mathbf{P}||^2$. In Fig. 4.5 it shows the presence of the polarization gradient schematically, which leads to the existence of a domain wall energy. For the current 2D case, the following component form is used [163, 164],

$$\begin{aligned} H_{\text{gr}} &= S_J V_0 \sum_i \Big[g_1 \big[P_{x,x}^2(\mathbf{r}_i) + P_{y,y}^2(\mathbf{r}_i) \big] \\ &+ g_1' P_{x,x}(\mathbf{r}_i) P_{y,y}(\mathbf{r}_i) + g_2 \big[P_{x,y}(\mathbf{r}_i) + P_{y,x}(\mathbf{r}_i) \big]^2 \\ &+ g_2' \big[P_{x,y}(\mathbf{r}_i) - P_{y,x}(\mathbf{r}_i) \big]^2 \Big], \end{aligned} \tag{4.9}$$

where the double subscripts denote derivatives with respect to the coordinate, S_J is a gauge coefficient, and the constants g_1, g_1', g_2, g_2' allow anisotropic contribution of the gradient term. The gradient energy enlarges the domain size and suppresses domain walls. The gauge coefficient S_J can be given various values to study its influence on domain structure and material properties such as transition temperature, hysteresis and electrocaloric effect. In the transverse Ising model, this energy term is ignored [44].

Finally, the electrostatic energy H_{e} is given as:

$$H_{\text{e}} = -V_0 \sum_i \Big[\mathbf{P}(\mathbf{r}_i) \cdot \mathbf{E}^{ex} \Big], \tag{4.10}$$

where $\mathbf{E}^{ex}$ is the external electric field, as illustrated in Fig. 4.6.

In the potential energy additional density terms can be added to take other physics into account, for instance the mechanical coupling. However, in the current thesis, for simplicity the mechanical contributions are not addressed.

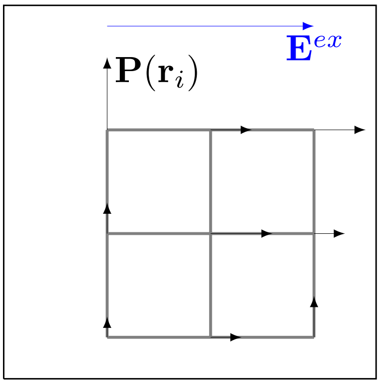

FIGURE 4.6 *Illustration of the polarization under the electric field, which brings about the electrostatic energy.*

4.3 Monte-Carlo Algorithm Development

Given the effective Hamiltonian and by placing the sample in a proper thermodynamical ensemble, the physical properties of the studied material, including the domain structure, the hysteresis and the electrocaloric effect, can be evaluated using the corresponding algorithms.

In statistical mechanics, several thermodynamical ensembles, including the canonical (NVT), microcanonical (NVE), grand canonical (μVT), and isothermal-isobaric (NPT) ensembles, can be applied to derive material properties [165]. The canonical ensemble (VT) describes a system with a fixed number of particles (N) and a fixed volume (V) in equilibrium with an infinitely large heat bath at a given temperature (T). In the microcanonical ensemble (NVE), the number of particles (N) and the volume (V) are fixed, while the total energy of the system (H^*) is constant. The grand canonical ensemble (μVT) is a system which can exchange energy and particles with a reservoir, but has a fixed chemical potential (μ), volume (V). When it comes to the isothermal-isobaric ensemble (NPT), the number of particles (N), the pressure (P), and the temperature are constant.

The electrocaloric effect results from an entropy change in a Carnot-type cycle by application and removal of the external electric field to a system under adiabatic conditions [5]. The ferroelectric materials used to generate the electrocaloric effect are prepolarized during this Carnot-type cycle. Therefore, the sample is first kept at a given temperature to reach its equilibrium configuration, and then is poled from this equilibrium state for sufficiently long time. Afterwards, the poling electric field is removed, and the sample is assumed to be fully relaxed. One can simulate the electrocaloric effect by first equilibrating the lattice-based model system in a canonical Monte-Carlo simulation at a given temperature. During the application of the external field, it is switched to a microcanonical ensemble using Creutz algorithm with constant total energy and measure the temperature variation directly from the demon energy. The total energy of the system H^* involves the thermal energy H^{k} and the potential energy H:

$$H^* \quad = \quad H^{\mathrm{k}} + H. \tag{4.11}$$

For the calculation of the potential energy, the effective Hamiltonian outlined in the previous subsection can be used.

4.3.1 Canonical Ensemble and Its Implementation

The details of the canonical ensemble and its implementation in Monte-Carlo codes can be found in Refs. [165–168]. Here only the key contents are summarized.

In a canonical ensemble, the probability that a system is found in a microstate β with energy H_β is given by

$$\varrho_\beta = \frac{1}{Z} \exp\left(-H_\beta / k_B T\right), \tag{4.12}$$

where k_B is the Boltzmann constant, T is the temperature, and Z is the partition function with

$$Z = \sum_{i=1}^{\infty} \exp\left(-H_\beta / k_B T\right). \tag{4.13}$$

We are interested in a system at equilibrium. Therefore, the detailed balance condition

$$\varrho_\beta \pi_{\beta\gamma} = \varrho_\gamma \pi_{\gamma\beta} \tag{4.14}$$

must be fulfilled, where $\pi_{\beta\gamma}$ and $\pi_{\gamma\beta}$ are the transition probability from state β to γ and from state γ to β, respectively. The transition probability $\pi_{\beta\gamma}$ can be calculated with the relation

$$\pi_{\beta\gamma} = \mathbb{M}_{\beta\gamma} \mathbb{A}_{\beta\gamma}, \tag{4.15}$$

where the transition matrix $\mathbb{M}_{\beta\gamma}$ determines the probability for performing a trial move from β to γ, and $\mathbb{A}_{\beta\gamma}$ is the acceptance probability of this trial move.

The transition matrix is symmetric in the Metropolis algorithm. Hence, one popular way in Monte-Carlo simulations is to set the acceptance probability as follows

$$\mathbb{A}_{\beta\gamma} = \min\left[1, \frac{\varrho_\gamma}{\varrho_\beta}\right] = \min\left[1, \exp\left(-\frac{H_\gamma - H_\beta}{k_B T}\right)\right]. \tag{4.16}$$

In order to decide whether to accept or reject the state γ, one generates a random number *Rnd* within [0,1], and compares this with $\mathbb{A}_{\beta\gamma}$. Clearly, the probability that *Rnd* is not bigger than $\mathbb{A}_{\beta\gamma}$ is equal to $\mathbb{A}_{\beta\gamma}$. Therefore, the transition from the state β to γ is accepted if $Rnd \leq \pi_{\beta\gamma}$, and otherwise is rejected. This rule guarantees that the probability of a transition from state β to γ is equal to $\pi_{\beta\gamma}$.

In the specific case of the lattice-based Monte-Carlo simulations of the ferroelectric materials, the state β represents $\left[\mathbf{P}(\mathbf{r}_1), ..., \mathbf{P}(\mathbf{r}_\mathrm{N})\right]$. One or several lattice sites can be randomly selected, and randomly assigned with possible switchings, with variation in both the magnitude and the orientation of the polarization. Now the new state is γ with $\left[\mathbf{P}'(\mathbf{r}_1), ..., \mathbf{P}'(\mathbf{r}_\mathrm{N})\right]$. The acceptance probability $\mathbb{A}_{\beta\gamma}$ is then calculated using the Eq. 4.16, and by comparison with *Rnd* we can decide whether this transition is accepted or not. This process is repeated until the domain structure reaches its equilibrium state. The canonical Monte-Carlo algorithm (also called the Metropolis algorithm) used in this thesis is illustrated in Fig. 4.7.

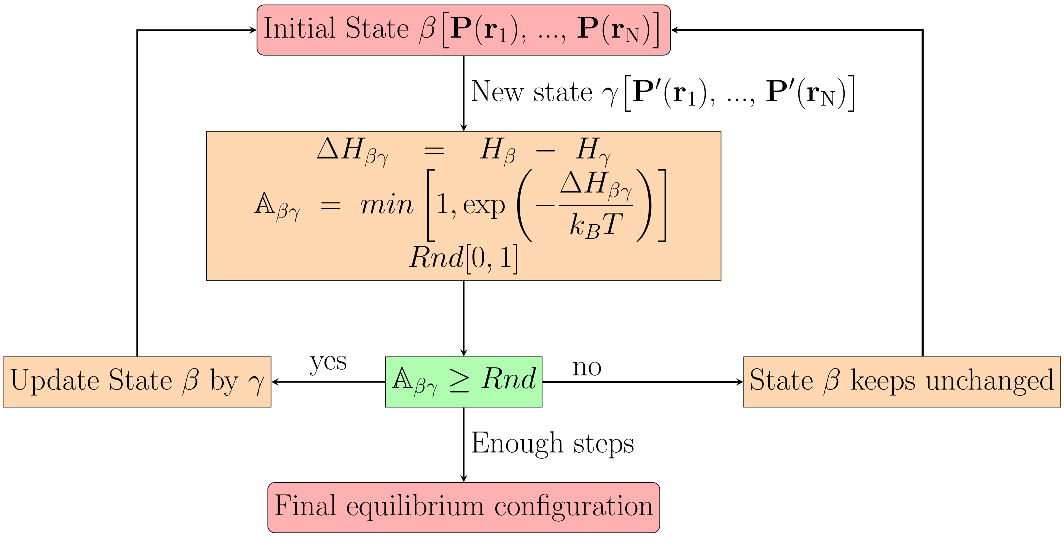

Figure 4.7 *The canonical Monte-Carlo algorithm.*

4.3.2 Microcanonical Ensemble and Its Implementation

For studying the electrocaloric effect under adiabatic conditions, the microcanonical ensemble is required, since in the microcanonical ensemble (NVE) the number of particles (N), the volume of the system (V), and the total energy are constant. In order to obtain a constant total energy as defined in Eq. (4.11), the concept of the demon energy is introduced, which represents the thermal energy [49, 169]. Either one single demon or a whole battalion of demons can be introduced to perform this conserved energy simulation [49, 50]. For a single demon, the configuration is taken from a thermalized ensemble and is no longer a representative for a thermalized ensemble [170]. However, it is not strictly microcanonical if this single demon is introduced, and the initial value of this single demon has to be chosen cautiously. Too large initial values lead to a deviation from the microcanonical condition, while too small initial values make the flipping unduly difficult [165]. The energy of a single demon has an exponential distribu-

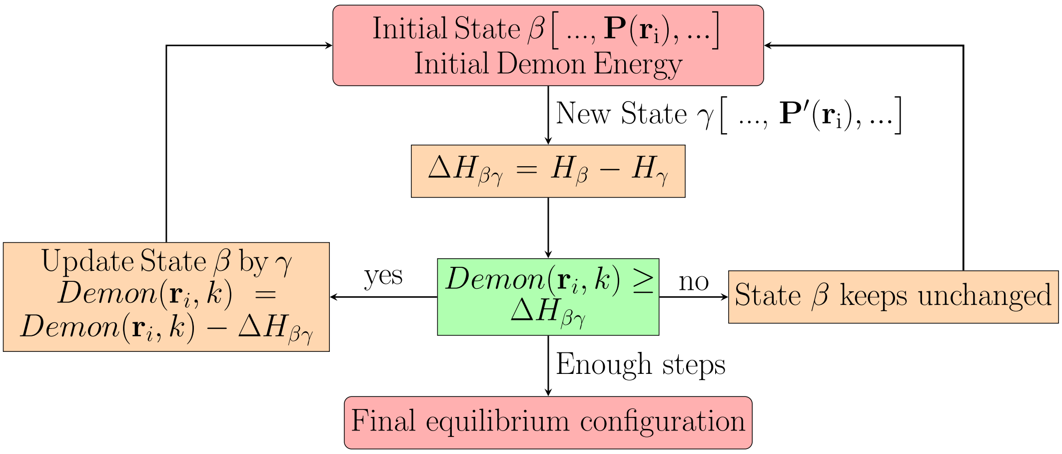

Figure 4.8 *The microcanonical Monte-Carlo algorithm.*

tion [49]. In the case of the multi-demon approach, an approximation is usually required since only integer number of demons can be considered. For instance, Ponomareva and Lisenkov [48] used 8 demons for the thermal energy per unit cell of $15k_BT/2$, which is the smallest integer number after the real number 15/2. In this way they approximated the contribution of the thermal energy into the heat capacity per unit cell by $8\,k_B\,T$.

In this virtue, one introduces the demon energy $Demon(\mathbf{r}_i,k)$ as the thermal energy of the two degrees of freedom carried by the k-th demon at site i. The value of $Demon(\mathbf{r}_i,k)$ must be positive, since the thermal energy is positive definitely. The demon energy in this sense signifies the thermal energy in the system, i.e.

$$H^{\mathrm{k}} = \sum_{i,k} Demon(\mathbf{r}_i,k) = \frac{f}{2} N k_B T. \tag{4.17}$$

In microcanonical Monte-Carlo simulations one demon $Demon(\mathbf{r}_j,k)$ is randomly selected from multiple demons. Similar to that in the canonical ensemble, the polarization $\mathbf{P}(\mathbf{r}_i)$ at a randomly chosen site $\mathbf{r}_i$ is signed with a random switching. If $\Delta H_{\beta\gamma} < 0$ or $Demon(\mathbf{r}_j,k) > \Delta H_{\beta\gamma}$ the new state is approved, and the demon energy is updated:

$$Demon(\mathbf{r}_j,k) = Demon(\mathbf{r}_j,k) - \Delta H_{\beta\gamma}. \tag{4.18}$$

Otherwise, the new configuration is rejected. In this fashion we can guarantee that the total energy is constant. This algorithm is illustrated in Fig. 4.8. Five demons are introduced, since each unit cell contains five atoms, which leads to 10 degrees of freedom per site in 2D model.

In fact, one can also choose the polarization and the demon at the same site during the calculations. Our simulation results show that both approaches lead to the same results. After the system reaches the equilibrium state, a sufficient number of Monte-Carlo steps will be further carried out to evaluate the thermal energy distribution. The temperature for the equilibrium configuration is then determined by the most probable thermal energy per site with details explained [169].

4.3.3 Convergence Test and Parallel Computation

For the given Hamiltonian, it is obligatory to test how the cutoff radius R affects the accuracy of our simulations. The convergence test is conducted with canonical Monte-Carlo calculations for the case with $S_J = 2.0$. Thereby the temperature dependence of the potential energy of the system is documented for various sets of the cutoff radius R with the same lattice size. The results are shown in Fig. 4.9. The potential energy is relatively small in the low temperature region, and large in the high temperature region. At a certain temperature, which corresponds to the Curie temperature, the potential energy increases steeply. It can be explained by the sharp increase of the correlation length. This temperature dependency agrees with the analytical solution of the Ising model in two dimensions [171]. As shown in Fig. 4.9, the convergence of the potential energy is observed as R increases. When $R \geq 8$, good convergence results can be obtained.

There is also a size effect as illustrated in Fig. 4.10. When $L = 16$ and $L = 32$ it can be seen that the average potential energy per site is unstable at the low temperature range ($100\,\mathrm{K} \leq T \leq 300\,\mathrm{K}$). The values of the potential energy for the case with $L = 63$ is almost identical to $L = 120$. It can be concluded that the size effect is trivial when $L \geq 63$. To retain the validity and simultaneously to avoid the high computation cost, the sample with $L = 63$ and $R = 8$ is used for the simulations in this thesis.

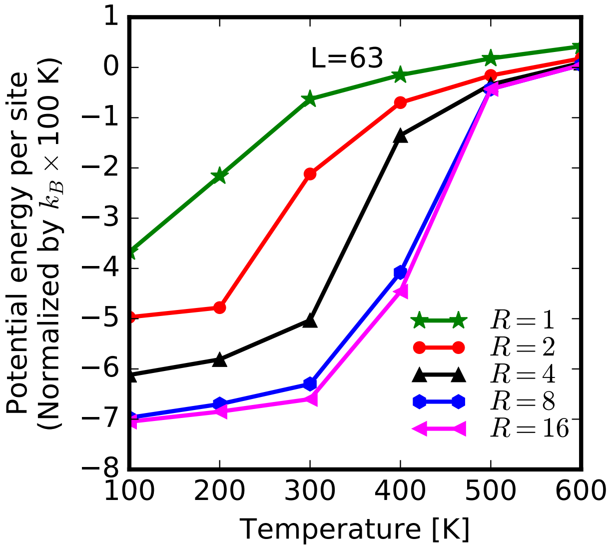

FIGURE 4.9 *Convergence test for the cutoff radius R of the dipole-dipole interaction with the same lattice size L, indicated by the potential energy. It is shown that the cutoff radius $R = 8$ is sufficient.*

Due to the presence of the long-range dipole-dipole interaction, the computation cost is fairly high. Therefore, a parallel scheme is used for both the canonical and microcanonical Monte-Carlo simulations. The system is divided into m^2 blocks, each of which has $(R+1) \times (R+1)$ sites. Thus, the total length of the sample becomes $L = m(R+1)$. Assume one site i in the first block with the dimensionless coordinates (j, k) is randomly chosen for the current Monte-Carlo step. The corresponding sites in all the blocks with dimensionless coordinates $(j + n(R+1), k + l(R+1)), n, l = 0, 1, ..., (m-1)$ can be picked simultaneously. In this fashion any two of these picked sites are far away enough from each other, so that the distance between these two sites is beyond the cutoff radius of the long-range dipole-dipole interaction. Hence, m^2 Monte-Carlo steps can be conducted parallelly by using m^2 threads of the computer.

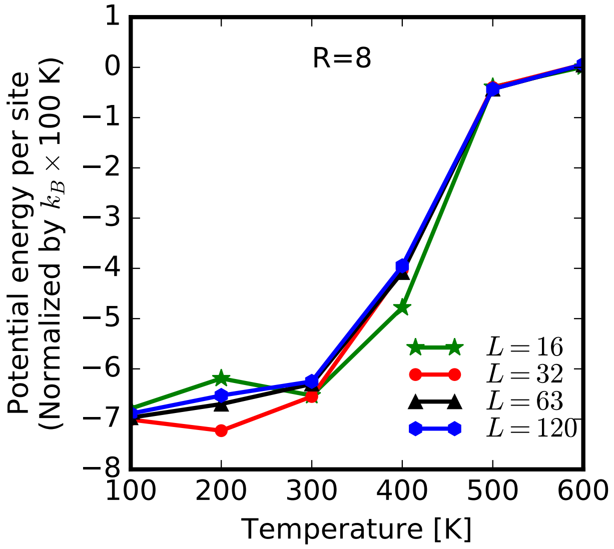

Figure 4.10 *The influence of the simulation box size on the potential energy (cutoff radius $R = 8$). The size effect proves to be insignificant when $L \geq 63$.*

4.4 Benchmark Tests for Conventional Ferroelectrics

Using the Ginzburg-Landau type effective Hamiltonian and the canonical/microcanonical algorithms outlined in the last two sections, dielectric and electrocaloric properties can be studied. For the verification of the model on relaxor ferroelectrics, simulation results on the behavior of the prototype ferroelectric material $BaTiO_3$ are presented in this subsection.

The following parameters are used for barium titanate. The lattice constant is set to $l_0 = 4$ Å. Based on first-principles results with zero strain and no non-soft-mode eigenmode amplitudes [159] the coefficients $a = 13.7128 \times 10^8\,\mathrm{J\,m\,C^{-2}}$, $b = 28.908 \times 10^9\,\mathrm{J\,m^5\,C^{-4}}$ are used in the Landau energy, while the sixth order term is ignored. Different values of the high-frequency permittivity ϵ_r can be found in literature, varying from 6.0 to 15.0 [153, 172, 173]. In the following simulations, we choose $\epsilon_r = 12.0$. For simplicity, the anisotropies of the permittivity and of the gradient energy are ignored. The coefficients $g_1 = g_1' = g_2 = g_2' = 2.0 \times 10^{-11}\,\mathrm{J\,m^3\,C^{-2}}$ are chosen for the gradient terms. To single out the influence of random fields, the above parameters are also used for the relaxor ferroelectrics.

In the following Monte-Carlo simulations, several assumptions are made. Firstly, the case of a single crystal is studied and the influence of grain boundaries is ignored. Secondly, simulations are merely associated with the cubic and the tetragonal phases. Similar to other studies [144, 164], the unit cell distortion during the phase transition is ignored, and the electrostrictive energy as well as the elastic energy is neglected. Thirdly, since this work focuses on the influence of bulk rather than surface forces, periodic boundary conditions are applied, and the depolarization effect on the exterior surface is disregarded. Finally, results are restricted to two-dimensional lattices in order to lower the computational cost. This should be, however, sufficient to reveal the underlying physics.

For evaluating the electrocaloric effect, canonical and microcanonical Monte-Carlo simulations are applied sequentially. The temperature range lies within the region where the equipartition theorem holds. The total thermal energy of a system is given as in Eq. (4.17). Thereby one considers merely the translational degrees of freedom. In a 2D model, it is apparent that the number of degrees of freedom f per site is taken as 10 since in the real perovskite structure there are 5 atoms per lattice site described in our model. For 10 degrees of freedom per site considered in this paper the contribution of the thermal energy to the heat capacity per site is $5k_BT$. The total number of demons in the system equals to 5 times the number of the lattice sites. In 3D, the number of degrees of freedom f per site is 15. Therefore, in our 2D case the heat capacity is underestimated, and the temperature change can be expected to be higher than in reality.

A sample with $N = L \times L$ sites is simulated ($L = 63$). For the long-range dipole-dipole interaction, a cutoff radius of R sites is employed. The cutoff radius influences the accuracy of the calculation and can be determined by convergence tests. The computation cost of the long-range dipole-dipole interaction is high. Therefore, a parallel computational scheme is proposed for the simulation. The convergence test and the parallelization method are described in Subsec. 4.3.3.

4.4.1 Phase Transition and Hysteresis of BaTiO$_3$

Experimentally, a ferroic material undergoes a significant thermal change near a ferroic phase transition when its order parameter is modified by the conjugate applied field [7]. Therefore, the phase transition and the polarization switching affect the electrocaloric effect, and need to be studied in detail.

We first consider an order-disorder phase transition [174], where the polarization is still present above the Curie temperature, but no long-range order exists.

For determining the phase transition temperature, canonical Monte-Carlo simulations for different given temperatures have been performed in absence of an external electric field. A statistical average polarization value $\langle P \rangle$ is calculated from the spontaneous polarization at each site through the following form

$$\langle P \rangle = \frac{1}{NM} \sum_i \sqrt{\Big[\sum_{k=1}^{M} P_x^k(\mathbf{r}_i)\Big]^2 + \Big[\sum_{k=1}^{M} P_y^k(\mathbf{r}_i)\Big]^2}. \tag{4.19}$$

Here M is the number of Monte-Carlo steps after reaching the equilibrium state, $P_x^k(\mathbf{r}_i)$ and $P_y^k(\mathbf{r}_i)$ are the Cartesian components of the polarization at site i for the k-th Monte-Carlo step.

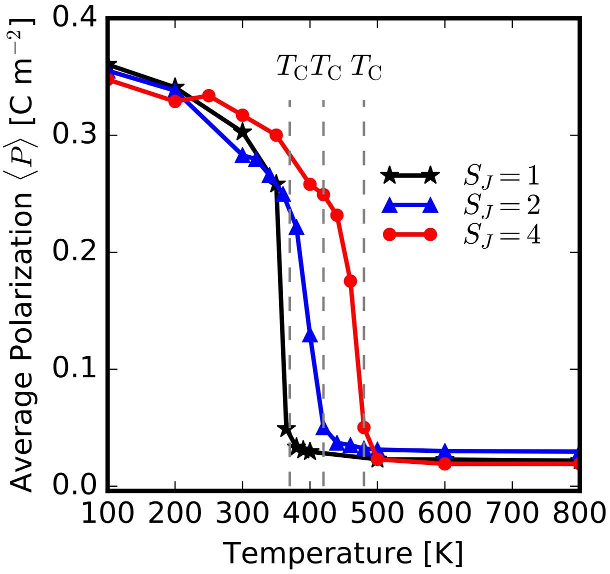

Figure 4.11 *Influence of the domain wall energy on the ferroelectric-to-paraelectric phase transition at the Curie temperature T_C, which is demonstrated by the change of the statistically averaged polarization with temperature. The domain wall energy is characterized by the prefactor S_J of the gradient energy term. T_C shifts to a higher temperature when the domain wall energy becomes greater.*

The phase transition behavior can be studied through the dependence of $\langle P \rangle$ on temperature, as shown in Fig. 4.11.

For all cases with different S_J sharp drops of $\langle P \rangle$ are visible as the temperature increases. The temperature, at which the drop appears, is the ferroelectric-to-paraelectric phase transition temperature. Since no random fields are involved, the simulation reproduces the phase transition behavior in a typical ferroelectric material. When the gradient energy becomes larger, i.e. S_J increases, the phase transition temperature rises. The predicted phase transition temperature is around 370 K, 420 K, and 480 K for $S_J = 1.0, 2.0, 4.0$, respectively. This is due to the fact that in the disordered state there are a lot of domain walls. The domain wall energy suppresses the number of domain walls. At the same temperature, a bigger S_J enlarges the domain size, and the sample stays in a more ordered state at the equilibrium state. Therefore more thermal energy is required to achieve the disorder state when S_J increases. The phase transition temperature of $BaTiO_3$ is known to be around 400 K, and thus a value $S_J = 2.0$ should be reasonable.

It is notable in Fig. 4.11 that the polarization $\langle P \rangle$ in the disordered phase does not vanish. This is due to the definition of the statistical value based on Eq. (4.19). Similar results can be found in the analysis of the order parameter using the Ising model for magnetics [175].

Domain switching driven by sinusoidal external electric fields at a constant temperature below the phase transition temperature is further investigated. During the canonical Monte-Carlo simulations, the increase of the external field is supposed to be so slow that the system has enough time to relax to an equilibrium state. Our simulation results on domain switching show that the coercive field increases with S_J as shown in Fig. 4.12. This influence of the domain wall energy has also been found by Liu *et al.* [164] and can be explained by the fact that the energy barrier for reversing the polarization increases with the domain wall energy. Therefore, it is more difficult for the sample to be switched, and a higher external field is needed. The dipole-dipole interaction favors an anti-parallel arrangement of the polarizations. Hence, when the domain wall energy is sufficiently small ($S_J = 1$), an antiferroelectric-type hysteresis is visible. According to the measurements by Gaynutdinov *et al.* [176], the coercive field is around 70 kV mm^{-1} for BaTiO$_3$ thin films with a thickness of 20 nm. The simulated sample size is 25.2 nm^2 in the present work, and for $S_J = 2$ the coercive field is about 120 kV mm^{-1}, which is in good agreement to the experimental value. Since no defects or grain boundaries are considered these values are considerably higher than what is typically found in experiments.

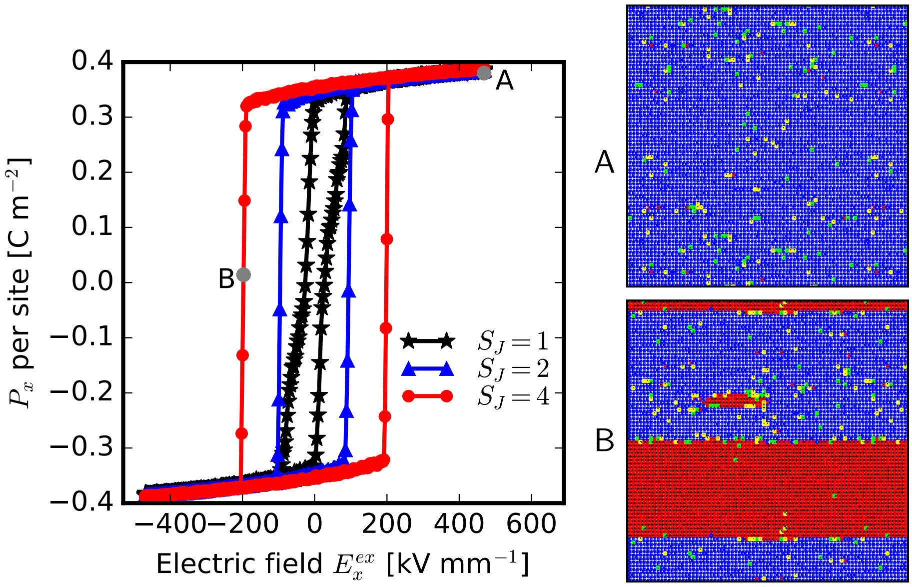

FIGURE 4.12 *Influence of the domain wall energy on dielectric hysteresis of ferroelectrics at $T = 300\,K$. P_x is the average polarization per site in the x direction. The external field is applied in the x direction as well. The coercive field increases with S_J, thus with the domain wall energy.*

4.4.2 Electrocaloric Effect of BaTiO$_3$

The electrocaloric effect of BaTiO$_3$ is simulated by first equilibrating the sample at constant temperature in a canonical ensemble using the Metropolis Monte-Carlo algorithm. During this stage a field is switched on and off to prepole the sample. After the poling electric field is removed, the sample is assumed to be fully relaxed. Then a constant external electric field parallel to the poling field is applied and the temperature change in this stage is calculated from the change of demon energy in a microcanonical ensemble using Creutz algorithm.

At each Monte-Carlo step of the microcanonical ensemble the values of the temperature changes at all sites can be calculated. After a sufficient number of Monte-Carlo steps are performed, an occurrence probability diagram of the values can be calculated. An example for $BaTiO_3$ is given in Fig. 4.13. This occurrence probability resembles a Gaussian distribution. The variance increases with temperature. This result agrees well with the analytical result for fluctuations of the temperature in the absence of pressure and volume change [177].

The most probable temperature change from the probability diagram is chosen to determine the temperature change at the given initial temperature. Thus, in the following context, the temperature change means the most probable temperature change. It can also be seen from Fig. 4.13 that by application of an external electric field, the temperature of the sample elevates.

From experiments it was concluded that in $BaTiO_3$ films of 20 nm thickness the coercive field is around $70\,\mathrm{kV\,mm^{-1}}$ [176]. Hence, for the ideal crystal, in order to recognize the physical phenomena clearly, it is essential to apply a very high external field in the simulation for the sample with size $25.2\,\mathrm{nm}^2$.

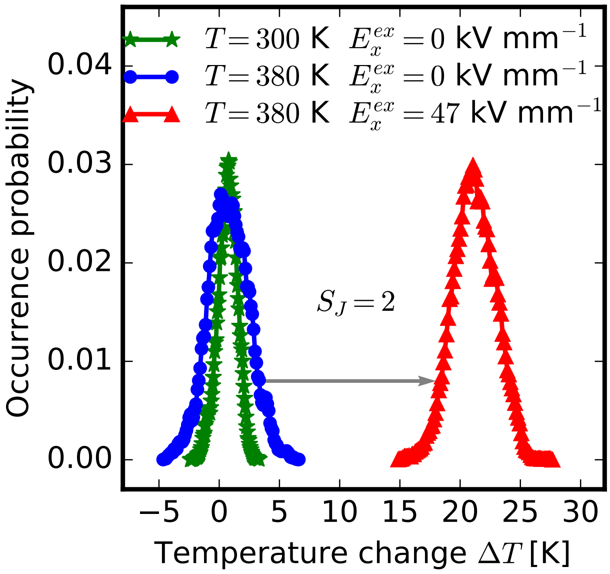

FIGURE 4.13 *Occurrence probabilities of the temperature changes and the influence of applying external electric fields. The distribution variance increases with temperature, and the most probable temperature change is used to evaluate the electrocaloric effect. The external electric field increases the temperature of the sample.*

In Fig. 4.14 the maximum electrocaloric effect appears at the Curie temperature, which can be seen by comparing with Fig. 4.11. This is because at the phase transition there is the largest variation of configurational energy and thus heat. In Fig. 4.14 the influence of the external field on electrocaloric effect in ferroelectrics is revealed as well. A higher field has more ability to change the extent of ordering. Thus, the electrocaloric effect increases with the magnitude of the external electric field. This feature is most apparent at the phase transition. The experimental results by Bai *et al.* [69], for comparison, exhibit a giant electrocaloric effect in a $BaTiO_3$ film, having 63 layers with the thickness of $3\,\mathrm{mm}^{-6}$ for each layer. Under an electric field of $80\,\mathrm{kV\,mm^{-1}}$, a temperature change of 7.1 K was achieved at 353 K. By comparison, the temperature change is 8.2 K at 360 K under $47\,\mathrm{kV\,mm^{-1}}$ in our simulation. The discrepancy

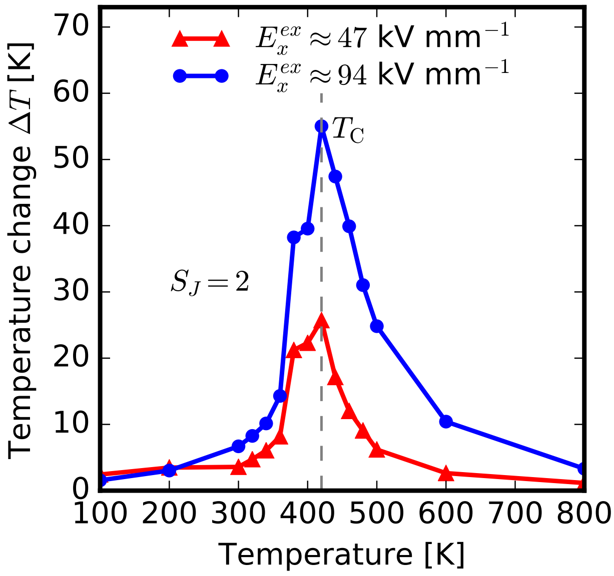

FIGURE 4.14 *Electrocaloric effect of* $BaTiO_3$ *at different initial temperatures for two different external electric fields.* ΔT *peaks appear at the Curie temperature, and the electrocaloric effect increases with external fields.*

may result from several aspects. Firstly, not all energy terms are taken into consideration, e.g. elastic energy. Moreover, defects and grain boundaries are ignored in the simulation, and the 2D simplification may also lead to a higher temperature change due to the underestimation of the heat capacity.

4.5 Summary

In this Chapter, a statistical lattice-based Monte-Carlo method is developed to investigate the electrocaloric effect. Four distinctive energy terms that significantly influence the material behavior are taken into account, namely a Landau double well ground state energy based on the first principles results, a long-range dipole-dipole interaction energy, an electrostatic energy describing the coupling of the local polarization to the external field and to random fields in Chap. 8 for relaxors. The evaluation of the phase transition temperature in ferroelectrics and the hysteresis is conducted at constant temperature in a canonical ensemble by using a Metropolis Monte-Carlo algorithm [165–168]. By contrast, the electrocaloric effect is evaluated directly under adiabatic conditions in a microcanonical ensemble within the scope of Creutz multi-demon algorithm [48, 49, 169]. In comparison with the First-Principles-based effective Hamiltonian, it allows flexible parameter studies and requires lower computation cost. Moreover, the combined canonical and microcanonical Monte-Carlo algorithm allows us to evaluate the electrocaloric effect directly without using Maxwell relations.

In oder to validate the model, a prototypic ferroelectric $BaTiO_3$ is investigated. The results show large size domains and sharp phase transition in the ferroelectric phase. Furthermore, as the domain wall energy density increases, the transition point becomes higher (see Fig. 4.11), since more thermal energy is required to achieve the disorder. With respect to the domain switching behavior (see Fig. 4.12), the domain wall movement can be visualized by the snapshot of the domain structure, and a big remnant polarization is demonstrated. Additionally, the higher domain wall energy promotes a fatter hysteresis loop, and a bigger coercive field can be obtained. Finally, the electrocaloric effect is investigated, which reveals that the electrocaloric effect increases with the external field, and at the phase transition temperature the ΔT peak appears due to the phase transition (see Fig. 4.14). This model serves as a basic model, and is modified later in the corresponding chapters for specific problems. For reducing the computation cost, two-dimensional model is applied, which leads to the underestimation of the heat capacity and the overestimation of the temperature change.

Chapter 5

Enhanced Electrocaloric Effect by Field Reversal

Secs. 5.1 and 5.2 are based on the publications “Y.-B. Ma, N. Novak, K. Albe, and B.-X. Xu, Appl. Phys. Lett. 109, 202906 (2016)” and “ Y.-B. Ma, N. Novak, J. Koruza, T. Yang, K. Albe, and B.-X. Xu, Phys. Rev. B 94, 100104(R) (2016)”, respectively.

Much progress has been made in exploring materials exhibiting large electrocaloric effects and also in designing corresponding device concepts, while the question, how to optimize the electrocaloric cycle has only been marginally addressed in the past. In a conventional electrocaloric cycle, the cooling effect is obtained by removing the previously applied electric field. Basso *et al.* [178] demonstrated that the electrocaloric cooling of a ferroelectric polymer can be enhanced if a negative electric field is applied to an initially positively poled sample in polymer ferroelectrics. Experimental and theoretical studies of adiabatic loading cycles in PZT [32, 179, 180] showed the occurrence of an inverse electrocaloric under a reversed electric field, and indicated that a reversed electric field should also increase the cooling effect. Recently, using a direct method, Dr. Nikola Novak and Dr. Jurij Koruza at TU Darmstadt measured the temperature change of $Pb(Mg_{1/3}/Nb_{2/3})_{0.71}Ti_{0.29}O_3$ with the thermistor. Their results show that there is indeed an optimal reversed electric field, corresponding to a position around the shoulder of the dielectric hysteresis, where the electrocaloric cooling effect reaches its maximum (also see Fig. 5.1). Experimental details can be found in [181] and are also summarized in Subsec. 5.1.4.

Therefore, it is of interest to understand this optimal reversed electric field in more detail. In literature [182], the electrocaloric cycle is considered to be reversible, which implies that the total entropy is constant under adiabatic conditions. This assumption leads to the conclusion that the maximal cooling takes place, if P=0, since at this point the dipolar entropy is at its maximum (see Model I). This conclusion deviates, however, from experimental observations.

In order to reveal the underlying mechanisms and to explore the maximal caloric effect induced by field reversal, the thermodynamical analytical model (Sec. 5.1) and lattice-based Monte-Carlo simulations (see Sec. 5.2) are applied. Both approaches signify the necessity of considering the entropy contribution from irreversible processes. The theoretical and experimental results are compared and show fairly good qualitative agreement.

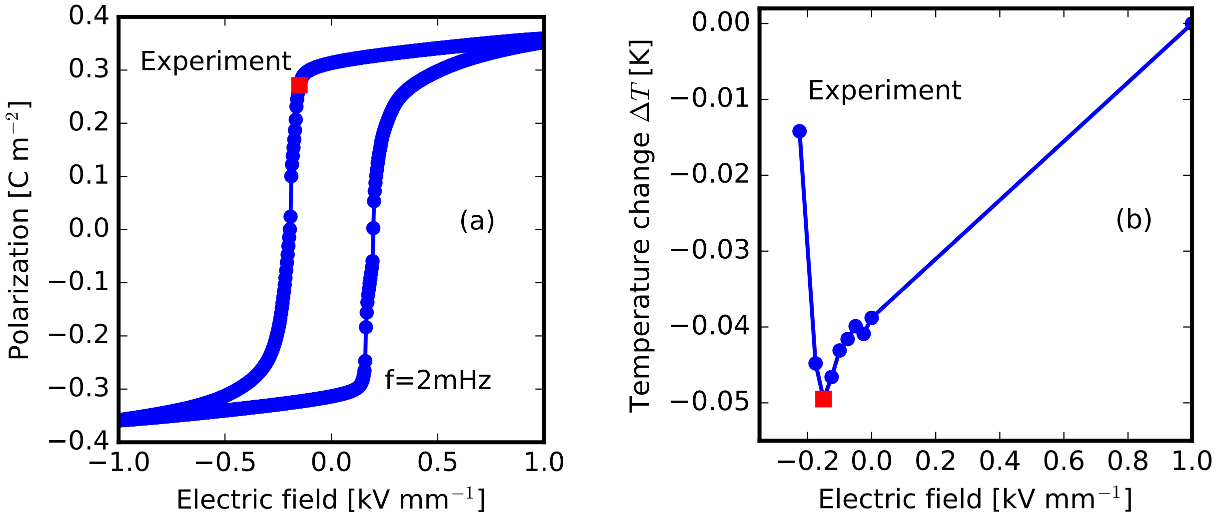

FIGURE 5.1 *Direct electrocaloric measurements on single crystals of* $Pb(Mg_{1/3}/Nb_{2/3})_{0.71}Ti_{0.29}O_3$ *(PMN-29PT) at 303.0 K. The maximum cooling is obtained after field reversal.*

5.1 Analytical Model of Entropy Changes

The conventional Carnot cycle is unipolar, and the process is nearly reversible [2,5,7,8,11,12, 15,46,182–185]. It follows that the total entropy remains constant during the reversible process. However, when a sesquipolar loading with a certain reversed field is applied, irreversible contributions in the process can increase significantly. In this case, adiabatic conditions, which mean constant energy, do not necessarily imply a constant total entropy.

In fact, the total entropy change ΔS_{total} should satisfy this relation

$$\Delta S_{\text{total}} = \Delta S_{\text{dip}} + \Delta S_{\text{vib}} \begin{cases} = 0 & \text{in reversible process,} \\ \neq 0 & \text{in irreversible process,} \end{cases}$$

where ΔS_{dip} and ΔS_{vib} are the dipolar and the vibrational entropy changes, respectively. If a reversed electric field is applied, irreversible contributions to the total entropy change become significant and result in a work loss W_{loss} [186]. Since the typically applied Maxwell relations are only valid for thermodynamically reversible processes [17,22,187], modeling the electrocaloric effect typically requires direct methods, like Monte-Carlo and Molecular-Dynamics simulations [39,48,181,187–189]. Monte-Carlo simulations will be described in the next section.

In this section an analytical method for describing entropy changes in a ideal ferroelectric with an open hysteresis loop is presented. The model takes into account irreversible processes and allows to derive the optimal reversed electric field for maximizing the electrocaloric cooling effect. The total entropy change induced by irreversible processes is calculated from the work loss (see Model II for ideal materials in Subsec. 5.1.2 and Model III for a more realistic scheme in Subsec. 5.1.3).

As starting point of the entropy analysis, one has to calculate the dipolar entropy. As introduced in Eq. (4.1), the dipolar mean field free energy density F_{dip} for one-dimensional case can be expressed as

$$F_{\text{dip}} = F = F_0 + \frac{1}{2}aP^2 + \frac{1}{4}bP^4 + \frac{1}{6}cP^6 - EP. \tag{5.1}$$

For simplicity, the sixth order-term and the temperature-dependence of b are neglected, while the parameter a has the typical temperature dependence $a = a_0(T_{\text{A}} - T_{\text{C}})$ with T_{A} and T_{C} as the initial temperature and the Curie temperature, respectively. If not specified, the initial temperature T_{A} is set to 0.7 in reduced units. According to Kutnjak *et al.* [182], the following normalized parameters are chosen: $a_0 = 1$, $T_{\text{C}} = 1$, and $b = 1/3$. The dipolar entropy S_{dip} can be derived from as $S_{\text{dip}} = -\partial F_{\text{dip}}/\partial T_{\text{A}} = -\frac{1}{2}a_0P^2$. Therefore, the change of dipolar entropy, ΔS_{dip}, from state A with polarization P_{A} to another state with polarization P can be simply expressed as

$$\Delta S_{\text{dip}} = -\frac{1}{2}a_0P^2 + \frac{1}{2}a_0{P_{\text{A}}}^2. \tag{5.2}$$

The change of vibrational entropy, ΔS_{vib}, can be approximated as [182]

$$\Delta S_{\text{vib}} = \int_{T_{\text{A}}}^{T} \frac{C_{\text{ph}}}{T} dT \cong C_{\text{ph}} \ln(T/T_{\text{A}}), \tag{5.3}$$

where T is the current temperature, and C_{ph} is the specific heat capacity of the non-polar degrees of freedom, which is taken as $C_{\text{ph}} = 15$ in reduced units according to Ref. [182].

In the following three different scenarios are considered to determine the optimal magnitude of the reversed field.

5.1.1 Model I: Reversible Process

For comparison with Model II and III, the optimal reversed field is also determined if the irreversible process is ignored. Assuming a reversible process under adiabatic conditions implies $\Delta S_{\text{total}} = 0$, and thus $\Delta S_{\text{vib}} = -\Delta S_{\text{dip}}$. With Eq. (5.2) and (5.3) we arrive at [182]

$$T = T_{\text{A}} \exp\left[\left(\frac{1}{2}a_0P^2 - \frac{1}{2}a_0{P_{\text{A}}}^2\right)/C_{\text{ph}}\right]. \tag{5.4}$$

For a state between point A and E, one can determine the corresponding temperature change by Eq. (5.4) and then the entropy changes. The derivatives of these changes with respect to the polarization can also be obtained thereafter. Results are shown in Fig. 5.2. It is seen that the maximal temperature drop happens at the point $P = 0$. This is due to the fact that Eq. (5.4) depends on P^2. When the polarization equals to 0, there appears the highest disorder of polarization, i.e., a maximum of S_{dip} and a corresponding minimum of S_{vib} since the total entropy is constant. In other words, ignoring the irreversible contribution leads to the conclusion that the maximum electrocaloric cooling appears at $P = 0$. This deviates from the previous experimental [178, 181] and numerical observation [181].

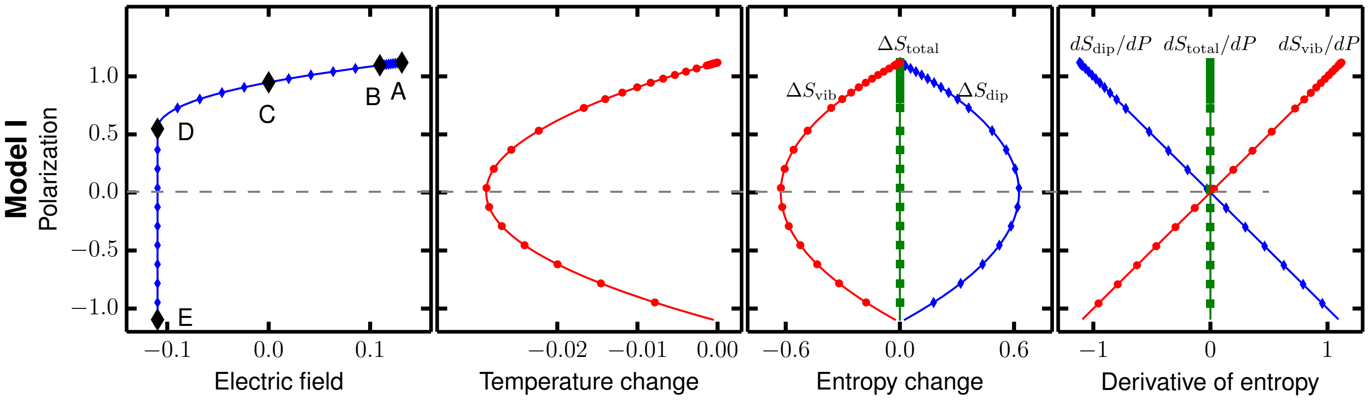

FIGURE 5.2 *Model I: Determination of the optimal reversed field with maximal cooling. The results are based on Model I. Gray horizontal lines indicate the positions with maximal cooling, which are always the points where* $dS_{\mathrm{total}}/dP = dS_{\mathrm{dip}}/dP$.

5.1.2 Model II: Irreversible Process

Considering the irreversible contribution, the total entropy change is related to the change of the work loss:

$$dS_{\mathrm{total}} = \frac{dW_{\mathrm{loss}}}{T} \approx \frac{dW_{\mathrm{loss}}}{T_{\mathrm{A}}}. \tag{5.5}$$

Since the temperature change is rather small compared to the initial temperature, we can safely assume that $T \approx T_{\mathrm{A}}$. Through integration of Eq. (5.5) one arrives at

$$\Delta S_{\mathrm{total}} = \frac{W_{\mathrm{loss}}}{T_{\mathrm{A}}} = \Delta S_{\mathrm{dip}} + \Delta S_{\mathrm{vib}}. \tag{5.6}$$

Inserting Eq. (5.2) and (5.3) into Eq. (5.6) leads to

$$T = T_{\mathrm{A}} \exp\left[(W_{\mathrm{loss}}/T_{\mathrm{A}} - \Delta S_{\mathrm{dip}})/C_{\mathrm{ph}}\right]. \tag{5.7}$$

This relation is reduced to Eq. (5.4), if $W_{\mathrm{loss}} = 0$. The work loss W_{loss} in irreversible process can be evaluated from the difference between the work done in the actual process and that in the reversible process under the same electric field E. Thus one can first decompose the polarization into irreversible and reversible parts. Setting the first derivative of the Landau free energy density $\partial F_{\mathrm{dip}}/\partial P$ to zero, one obtains a relation between the polarization and the actual electric field E:

$$E = aP + bP^3. \tag{5.8}$$

This corresponds to the S-shaped curve in the P-E plane below the Curie temperature, as it is shown in Fig. 5.3. Through snap-through construction of D-E and F-B, one obtains the ideal

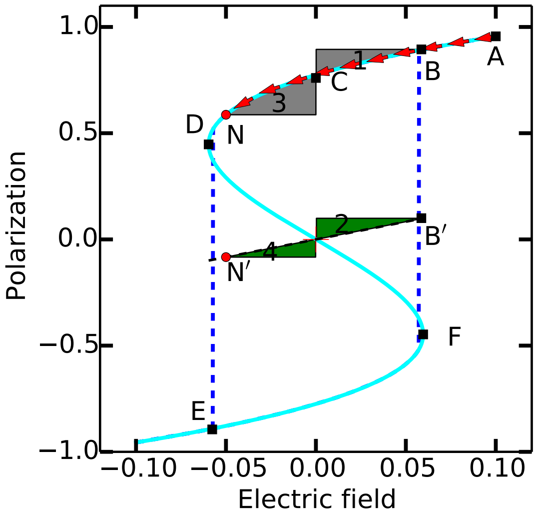

Figure 5.3 *Decomposition of the polarization into reversible and irreversible contributions.*

P-E loop. One chooses now point A as the initial state with saturation polarization P_A, initial temperature T_A and the electric field E_A. Point C corresponds to the case of zero electric field, and point D describes the inflection point of the S-shaped curve. Between A and B the process is fully reversible, while between B and E irreversibility is involved. Bolten *et al.* [186] pointed out that in a ferroelectric P-E loop, the reversible part can be described by a straight line without any hysteretic heat loss. Correspondingly, we take the tangent at point B as representative for the reversible polarization behavior. The slope is $\left.\frac{\partial E}{\partial P}\right|_{P=P_B} = a + 3bP_B{}^2$, where $E_B = aP_B + bP_B^3$. Then the reversible polarization P_r is given by

$$E = (a + 3bP_B{}^2)P_r. \tag{5.9}$$

From Eq. (5.8) and (5.9), it follows that

$$aP + bP^3 = (a + 3bP_B{}^2)P_r. \tag{5.10}$$

In this way the reversible part of the polarization P can be expressed by

$$P_r(P) = \frac{aP + bP^3}{a + 3bP_B{}^2}. \tag{5.11}$$

The work loss W_{loss} now can be calculated from the difference between the work done in the actual process and that in the reversible process under the same electric field E. For any point located between B and D, the work loss is given through the difference of two integrals:

$$\begin{aligned} W_{loss1}(P) &= W_{actual} - W_r \\ &= \int_{P_B}^{P} E dP - \int_{P_{B'}}^{P_r} E_r dP_r \end{aligned}$$

$$
\begin{aligned}
&= \frac{1}{2}aP^2 + \frac{1}{4}bP^4 - \left(\frac{1}{2}a{P_{\mathrm{B}}}^2 + \frac{1}{4}b{P_{\mathrm{B}}}^4\right) \\
&- \frac{1}{2}a{P_{\mathrm{r}}}^2 - \frac{3}{2}b{P_{\mathrm{B}}}^2{P_{\mathrm{r}}}^2 + \frac{1}{2}a{P_{\mathrm{B'}}}^2 + \frac{3}{2}b{P_{\mathrm{B}}}^2{P_{\mathrm{B'}}}^2 ,
\end{aligned} \tag{5.12}
$$

where $P_{\mathrm{B'}} = P_{\mathrm{r}}|_{P=P_{\mathrm{B}}} = \dfrac{aP_{\mathrm{B}} + bP_{\mathrm{B}}^3}{a + 3b{P_{\mathrm{B}}}^2}$. For point N illustrated in Fig. 5.3, the work loss Eq. (5.12) can be alternatively evaluated from the area difference $(V_2 - V_1) + (V_3 - V_4)$ with V_i being the area of the region i shown in Fig. 5.3. For any point between D and E, one has to go through the vertical snap-through line, which represents the hysteretic path. In this way, we obtain the work loss in the following form

$$
W_{\mathrm{loss2}}(P) \quad = \quad W_{\mathrm{loss1}}|_{P=P_{\mathrm{D}}} + (P - P_{\mathrm{D}})E_{\mathrm{D}}. \tag{5.13}
$$

As a result, we end up with

$$
W_{\mathrm{loss}} = \begin{cases} W_{\mathrm{loss1}} & \text{for points between B and D ,} \\ W_{\mathrm{loss2}} & \text{for points between D and E .} \end{cases}
$$

After W_{loss} is determined through Eq. (5.12) or (5.13), the temperature can be calculated by Eq. (5.7) for the irreversible process. The results based on this model are presented in Fig. 5.4. Different from model I, the maximum electrocaloric cooling occurs at a field, where the polarization does not vanish (see the gray dashed line) because of the entropy contribution of the irreversible process. From B to C, it is an almost reversible process, and this brings about a steady decrease of temperature. Within the region C-D, W_{loss} and $\Delta S_{\mathrm{total}}$ increase steadily with decreasing polarization, which leads to a weaker variation of the temperature change compared to the strong decrease within A-C. In the region D-E the irreversible process dominates, and

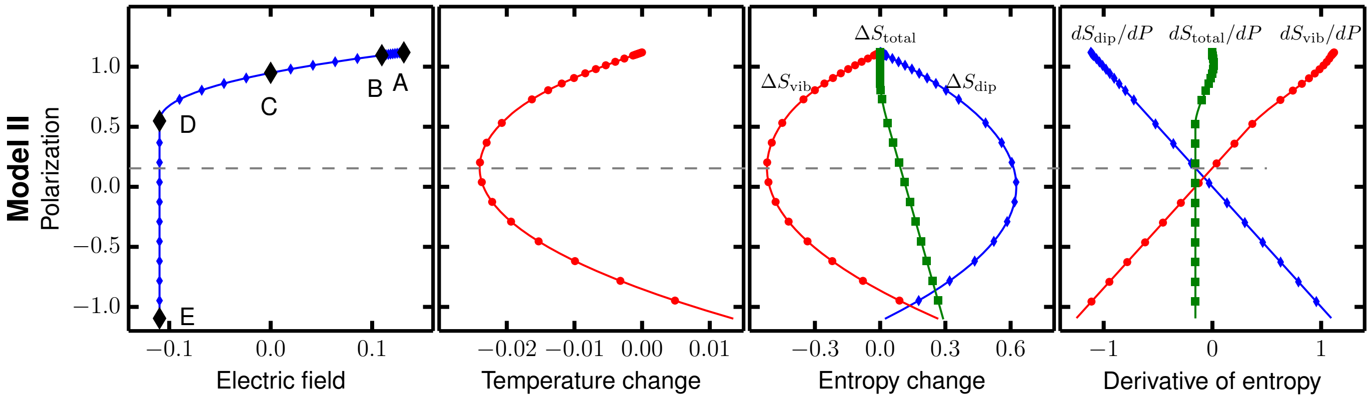

FIGURE 5.4 *Model II: Determination of the optimal reversed field with maximal cooling. The results are based on Model II. Gray horizontal lines indicate the positions with maximal cooling, which are always the points where* $dS_{\mathrm{total}}/dP = dS_{\mathrm{dip}}/dP$.

thus W_{loss} and ΔS_{total} increase, significantly. While the polarization decreases in this region, the increase of S_{total} gradually overtakes that of S_{dip}, which results in weaker temperature changes. Finally, at the point where dS_{total}/dP is equal to dS_{dip}/dP, a maximum electrocaloric cooling effect is reached (see the gray dashed line). Afterwards, dS_{total}/dP becomes larger than dS_{dip}/dP, and the cooling effect becomes weaker and can even be switched to heating.

This analysis demonstrates that the entropy contribution of irreversible processes shifts the conditions for a maximal electrocaloric effect to a state with positive polarization. However, the shift is still far away from point D, determined as optimal condition, experimentally.

5.1.3 Model III: Corrected Irreversible Process

As temperature increases and approaches T_C, the hysteresis becomes slimmer, and the polarization switching is more moderate around the coercive field. The ideal scheme of the P-E loop considered in model II, where at the coercive field the polarization is assumed to switch immediately from one direction to another, is inappropriate. In order to consider the P-E loop in a more realistic scheme, a temperature-dependent factor α is introduced to correct W_{loss} in Eq. (5.7),

$$T = T_A \exp\left[(\alpha W_{\text{loss}}/T_A - \Delta S_{\text{dip}})/C_{\text{ph}}\right], \tag{5.14}$$

where α is the factor between the work loss obtained considering a non-ideal P-E loop and the one used in model II. Since in the real case, the work loss is larger than that evaluated in model II, the condition $\alpha > 1$ holds. Meanwhile, α increases with temperature. However, the exact relation between α and the temperature is not available in literature. Nonetheless, it is known that at higher temperature the polarization switching within the metastable state by the Landau approach deviates further from that in real materials. In other words, the work loss is significantly underestimated within the metastable state at higher temperatures, if Eq. (5.7) is utilized. The radius of curvature R_D of the S-shaped curve at point D can serve as a measure for this purpose. From the Landau free energy density Eq. (5.1), one can obtain this relation for the radius: $R_D = 1/\sqrt{-12ab}$. At 0 K, the radius of curvature at point D is $R_0 = 1/\sqrt{12a_0 T_C b}$. Since the work loss is related to the area enclosed by the hysteresis, we assume that α is proportional to a normalized R_D^2 in the following fashion

$$\alpha = \lambda R_D^2/R_0^2 = \lambda T_C/(T_C - T_A). \tag{5.15}$$

The factor λ should be independent of temperature and reflects the work loss due to other factors, e.g., the presence of switchable defects and complex domain wall movements. In the following we use $\lambda = 2.0$. The resulting temperature and entropy changes are depicted in Fig. 5.5. In comparison with model II, the work loss in model III is corrected. Hence, the

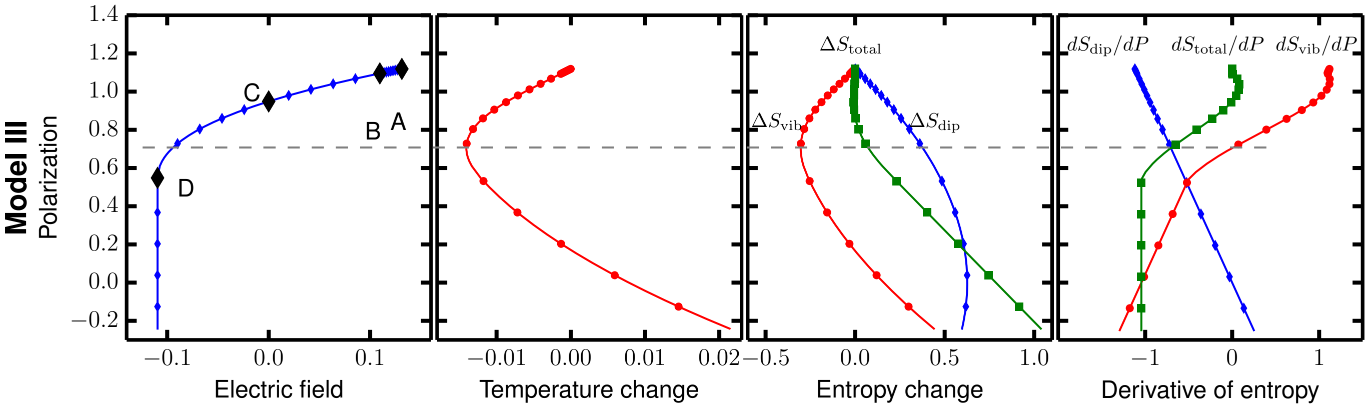

FIGURE 5.5 *Model III: Determination of the optimal reversed field with maximal cooling. The results are based on Model III, respectively. Gray horizontal lines indicate the positions with maximal cooling, which are always the points where* $dS_{\mathrm{total}}/dP = dS_{\mathrm{dip}}/dP$.

maximum electrocaloric cooling point is further shifted away from zero polarization towards point D, which is agreement with the experimental results [178, 181].

The exact position is also defined as the point where dS_{total}/dP catches up with dS_{dip}/dP (see the gray dashed line). The explanation provided in the model II remains valid here. The polarization change is predominantly reversible when the loop exhibits a relatively linear slope between the maximum polarization and the polarization state with the maximal cooling. Therefore, within this range, upon cycling the losses can be ignored, and there is a negligible difference in electrocaloric response, since the reversibility of the electrocaloric cycle is not influenced. However, total entropy increases sharply if the reversed field is becoming even larger and the electrocaloric is massively reduced.

5.1.4 Influence of Initial Temperature

Based on model III (see Fig. 5.6), the impact of initial temperature is examined. Results show that with increasing initial temperature, the optimal electric field for the maximum electrocaloric cooling decreases, and shifts closer to the coercive field. The maximal electrocaloric cooling also decreases.

For the experimental verification, direct electrocaloric measurements by Dr. Novak and Dr. Koruza on PMN-29PT single crystals were compared. Experiments are done on a platelet-shaped PMN-29PT single crystal, cut perpendicular to the [001] direction and polished. The geometry of platelet was $3.69\times4.35\times0.8\ \mathrm{mm}^3$. Surfaces were covered by sputtered silver electrodes on which copper contact wires were attached with electrically conducting silver paste. In addition, a thermistor was attached on one side of the sample with electric non-conducting varnish to perform direct electrocaloric measurement. Prior to measurement the sample was heated up to 450 K for 10 min and then stabilized within 1 mK at the target temperature. In the polarization hysteresis-loop measurements, the electric field is slowly cycled linearly with the frequency

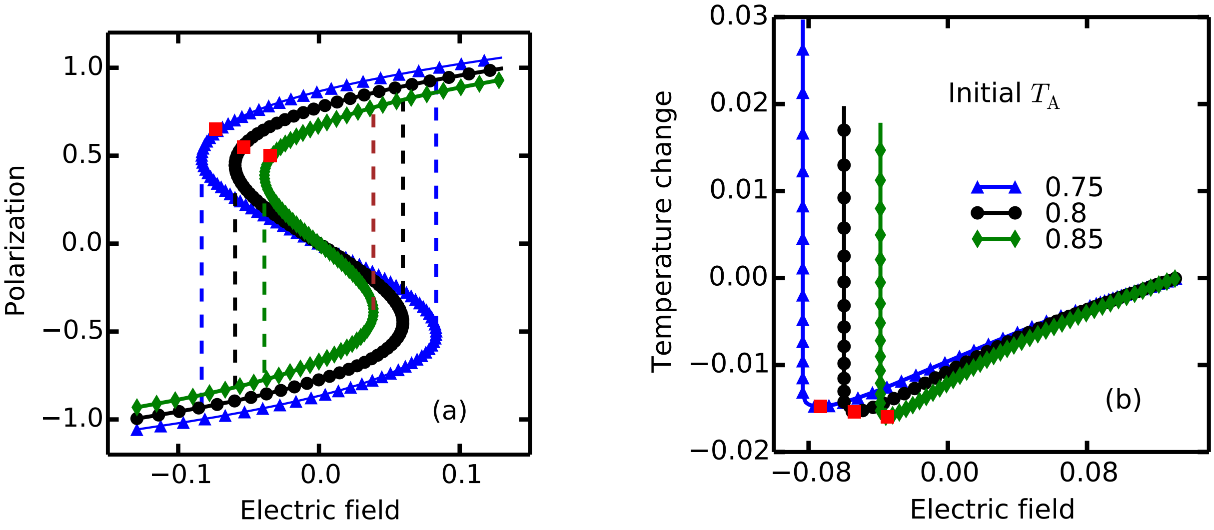

Figure 5.6 *Influence of the initial temperature on the electrocaloric effect.*

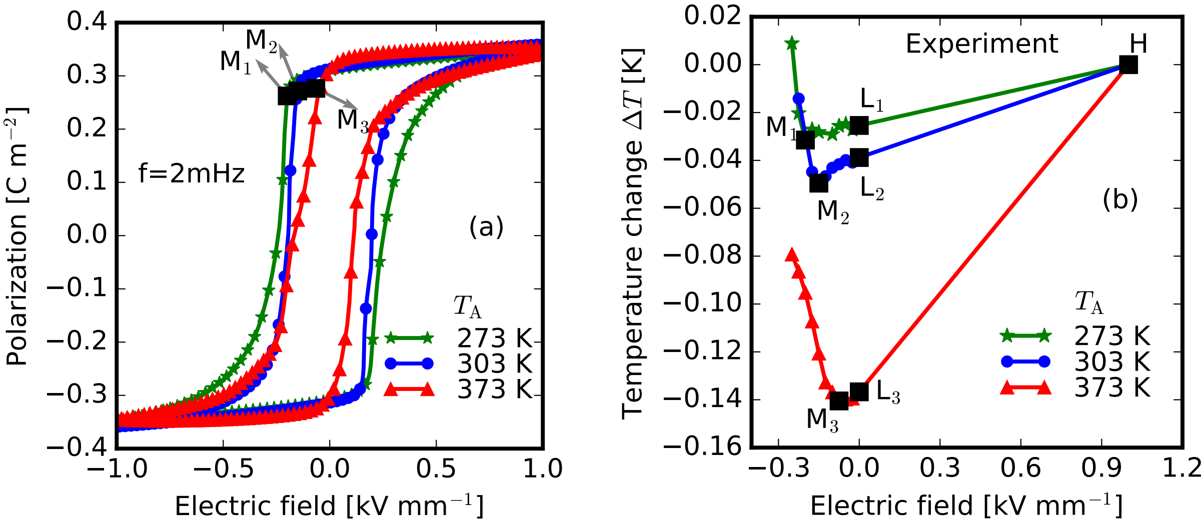

Figure 5.7 *Influence of the initial temperature on the electrocaloric effect, from experimental work on the single crystal of* $Pb(Mg_{1/3}/Nb_{2/3})_{0.71}Ti_{0.29}O_3$ *(PMN-29PT).*

of 0.002 Hz between ±1 kV mm^{-1}. The corresponding polarization charge was measured by a Keithley 6517B electrometer. The electrocaloric temperature change in PMN-29PT [001] was measured via a direct electrocaloric method [190, 191]. Each electrocaloric measurement consists of two parts, i.e., a heating part when the electric field is applied and a cooling part when the electric field is removed instantaneously. The actual electrocaloric temperature change ΔT was determined from the cooling part. The position of the maximum cooling effect is labeled with M$_1$, M$_2$ and M$_3$.

The phenomena in the experiments agree with those revealed in the theoretical analysis, qualitatively. As can be seen from the experimental results in Fig. 5.7, with increasing the initial temperature from 273 K to 303 K and 373 K, the optimal reversed field with maximum electrocaloric cooling decreases. At a given initial temperature the electrocaloric cooling is

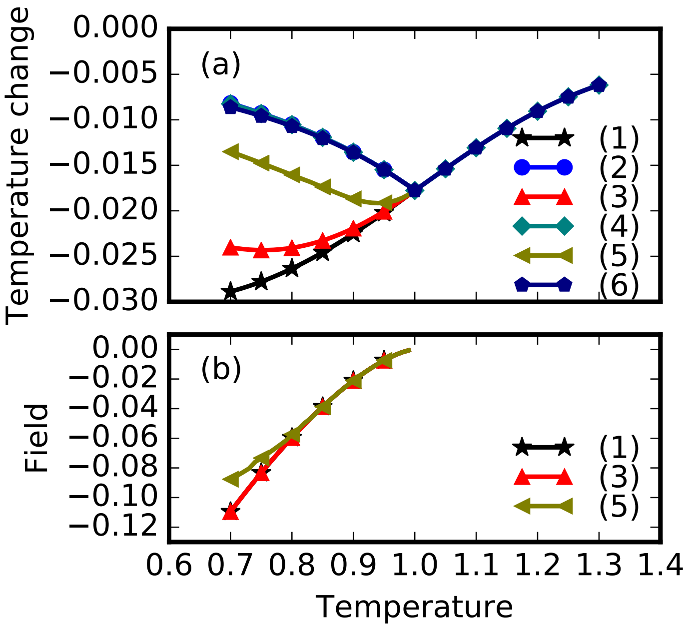

FIGURE 5.8 *For three cases, in (a) the temperature change is shown when reversing (case (1),(3),(5)) or simply removing (case (2), (4), (6)) the field. In (b), the optimal reversed field with the maximum electrocaloric cooling is presented. Model I corresponds to case (1) and (2). Model II corresponds to case (3) and (4). Model III corresponds to case (5) and (6).*

firstly enhanced by increasing the reversed field from point L to M and subsequently reduced, if the reversed field is further increased. It should be noted that there is no phase transition in the temperature regime studied here, since PMN-29PT does only exist in the rhombohedral phase between 273 and 373 K.

Analytical results have also been obtained for even higher temperature and are shown in Fig. 5.8. Above T_C Eq. (5.1) has one single extremum, and the process is nevertheless reversible. Hence, by applying the reversed field the polarization becomes more ordered, and S_{dip} decreases. Accordingly, S_{vib} and the temperature increase. In other words, the inverse electrocaloric effect cannot be observed. Therefore, the reversed field is applied only at the temperature below T_C.

In case of the field removal, there is one electrocaloric peak at the phase transition temperature $T = 1.0$. Additionally, the temperature changes are similar in all three models. Actually, the curve of the temperature changes of the three models almost overlap with each other. The underlying reason can be referred to the established arguments previously: the total entropy change in the case of field removal is fairly close to zero in all three models.

However, in the case of the field reversal, there are distinctive phenomena in the three models. In Model I, the maximum electrocaloric cooling appears when the polarization equals to zero at the coercive field. At lower initial temperature, the polarization is bigger at the same positive electric field. Therefore, when the initial temperature decreases and the magnitude of the corresponding coercive field increases, the electrocaloric cooling is continuously enhanced more greatly since a larger polarization change is expected. However, in experiments, it was observed that the magnitude of the maximum temperature is smaller at a lower temperature [181]. Hence, the results in Model I deviate from reality due to the missing work loss in presence of the irreversible polarization contribution. In Model II, with decreasing the initial temperature, electrocaloric cooling is firstly enhanced greatly, but the enhancement is weaker. These phenomena still deviate from the experimental and simulated observation [181] since hereby the work loss is highly underestimated in ideal materials. For the same reason, the maximum electrocaloric cooling appears with a small positive polarization, but still at the negative coercive field. Therefore, in Model II the optimal field with the maximum electrocaloric cooling is similar to that in Model I. In Model III, the situation is very different from that in Model I and II. The magnitude of the maximum temperature drop is lower when the initial temperature is lower, which agrees with the experimental results, qualitatively. The reason is that the work loss is corrected as in Eq. (5.14) to represent real material systems. The magnitude of the optimal electric with the maximum electrocaloric cooling is apparently different from the magnitude of the coercive field.

5.2 Latticed-based Monte-Carlo Simulation

In order to disclose the influence of field reversal on electrocaloric effect at the domain structure level, Monte-Carlo simulations based on the Ginzburg-Landau effective Hamiltonian and the microcanonical ensemble were also carried out. The prototypic ferroelectric $BaTiO_3$ is considered, and the energy terms and the algorithms used in this section are identical to those applied in Section 4.4.1.

The electrocaloric effect results from an entropy change during a Carnot-like cycle by application and removal of the external electric field to a system under adiabatic conditions [5]. The ferroelectric materials used to generate the electrocaloric effect are prepolarized as shown in Fig. 5.9 during this Carnot-like cycle. Therefore, the sample is first kept at a given temperature to reach its equilibrium configuration, and then is poled from this equilibrium state for sufficiently long time. Afterwards, the poling electric field is removed, and the sample is assumed to be fully relaxed. The electrocaloric effect is simulated by first equilibrating the lattice based model system in a canonical Monte-Carlo run at a given temperature. During the application of the external field, it is switched to a microcanonical ensemble using Creutz algorithm as explained in Subsec. 4.3.2 of Chap. 4 and measure the temperature variation directly from the demon energy.

An electrocaloric cycle contains the following four steps: isothermal heat absorption, adiabatic heating, isothermal heat release, and adiabatic cooling. In the following the temperature changes obtained for three distinct scenarios are compared, which are depicted in Fig. 5.9(a,b). Contrary to existing studies [32, 179, 180], here we are probing a sequence of isothermal and adiabatic steps as they would occur in a cooling device. The first case corresponds to a conven-

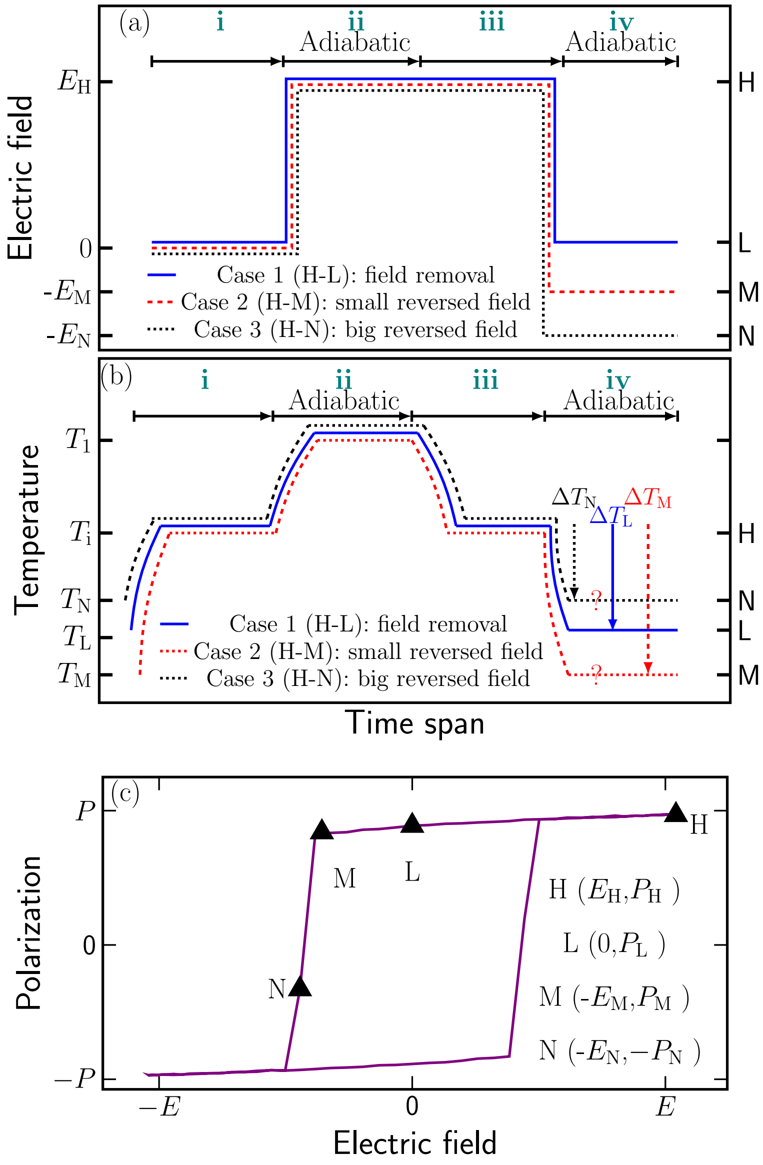

FIGURE 5.9 *The loading history (a), the possible temperature change (b) and the corresponding polarization change (c) are sketched for three different cases. The cooling procedure, i.e., the temperature drop from step* **iii** *to step* **iv**, *is of interest to the current work. For case 1, at step* **iv** *after removing the field the macroscopic polarization decreases (H to L in (c)). Hence, the electrocaloric cooling is achieved with the temperature drop ΔT_L (see (b)). For case 2, a small reversed electric field is applied (H to M), while for case 3 a high field is applied (H to N). The resultant temperature drop might be enhanced (ΔT_M) or degenerated (ΔT_N), which is judged by the simulation.*

tional electrocaloric cycle, where the cooling effect is obtained by removing the applied field. In the P-E loop, this corresponds to the change of polarization from the poled state H to the remnant state L shown in Fig. 5.9(c). In the other two cases, we study the influence of a small and large reversed field, respectively. As it is illustrated in Fig. 5.9(c), the small reversed field lies in the range between point L and M, where no significant polarization switching takes place, while the large reversed field E_N corresponds to the state N, where macroscopic polarization switching has started.

5.2.1 Influence of Field Reversal

The initial temperature is $T_\mathrm{i} = 320\mathrm{K}$ in all simulations and samples were poled by a field of $65.8\,\mathrm{kV\,mm^{-1}}$. Thus, all cases start with an identical fully-poled configuration.

Results of the temperature and the polarization changes are presented in Fig.5.10. As shown in Fig. 5.10(a), a temperature drop by $\Delta T = -5.0\,\mathrm{K}$ is observed for the case of field removal (H → L). An additional temperature drop leading to $\Delta T = -8.9\,\mathrm{K}$ can be achieved, if a small reversed field $|E_\mathrm{M}| \leq 28.2\,\mathrm{kV\,mm^{-1}}$ is applied (H → M). This indicates an enhanced electrocaloric cooling due to this reversed field, which is attributed to the inverse electrocaloric effect.

On the other hand, if a large reversed field of $|E_\mathrm{N}| \geq 37.6\,\mathrm{kV\,mm^{-1}}$ is applied, there is no temperature drop. Instead, a temperature increase relative to the starting temperature by $\Delta T = 6.1\,\mathrm{K}$ is observed (H → N).

The schematic domain patterns for the initially poled state H, the remnant state L, the state M under small reversed field, and the switching state N are shown in inset of Fig. 5.10(b). An increase of polarization disorder can be detected from H to L, as well as from L to M. Correspondingly, the polarization decreases slightly in both processes (see Fig.5.10(b)). These two processes are predominantly reversible. Thus, the total entropy $S_\mathrm{total} = S_\mathrm{dip} + S_\mathrm{vib}$, including the dipolar entropy S_dip and the vibrational entropy S_vib, stays constant. Due to the elevated polarization disorder, S_dip increases continuously from H to L and to M. It can be hence inferred that S_vib decreases gradually. Thus, T decreases from H to L, and further from L to M. (see Fig. 5.10(a)).

If we increase the field and move from H to N, the polarization switches significantly under the influence of the strong reversed field (see also Fig.5.10(b)). This indicates an irreversible adiabatic process, which leads to a giant upsurge of total entropy, and an increase of both S_vib and S_dip. Therefore, a deterioration of the electrocaloric effect is expected (see Fig. 5.10(a)). Around the coercive field S_dip is maximal, and the macroscopic polarization is zero. However, due to the irreversibility-induced increase of the total entropy, S_vib does not take its minimum. In fact, from $S_\mathrm{vib} = S_\mathrm{total} - S_\mathrm{dip}$, one concludes that the minimum of S_vib, i.e., the maximal temperature drop, occurs at the reversed electric field, which satisfies

$$\frac{dS_\mathrm{vib}}{dE} = \frac{dS_\mathrm{total}}{dE} - \frac{dS_\mathrm{dip}}{dE} = 0.$$

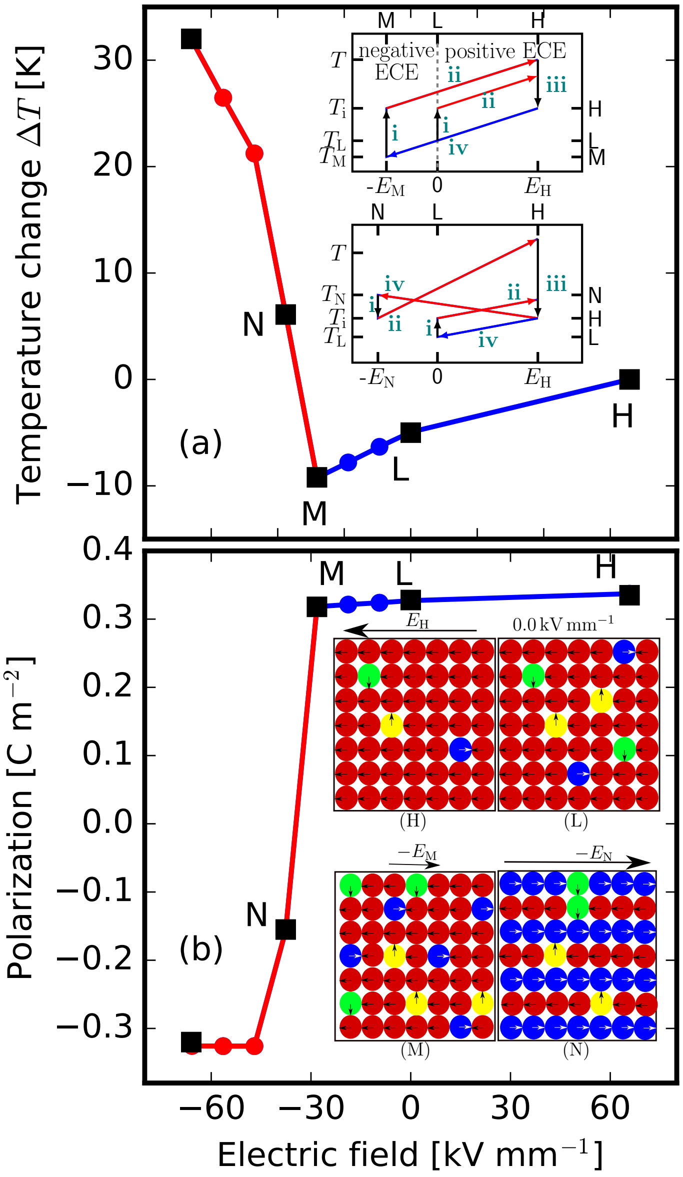

FIGURE 5.10 *The prepoled field E_H=65.8 kV mm^{-1} is kept constant for all cases, and the same polarization configuration can be assured. The temperature change (a) and the polarization (b) are depicted with respect to different reversed fields. With increasing the magnitude of the reversed field, the electrocaloric cooling is initially enhanced, but later degenerated. The phenomena at points H, L, M and N in (a) and (b) are explained by the schematic domain patterns in the inset of (b). At point H, the external field directs to the left, while at points M and N the reversed field directs to the right. From H to L and M the polarization disorder decreases, and the dipolar entropy S_dip increases. This reveals that the application of the reversed field leads to the further decrease of the temperature. However, from M to N, there is a sharp change of the polarization, and thus it is an irreversible adiabatic process. This leads to a huge increase of the total entropy and simultaneously the temperature. The cooling and heating phases are mapped separately in blue and red colors. The inset in (a) shows that compared with the conventional cycle (the interior cycle) the same inverse electrocaloric effect (the exterior cycle) can be utilized to enhance both the cooling and heating effect. Symbols* **i**, **ii**, **iii** *and* **iv** *represent the same steps as described in Fig. 5.9.*

This optimal reversed electric field should be smaller than the coercive field. This conclusion contrasts with the old report [179], in which the Maxwell relation that is only valid for the reversible process was utilized for a process with considerable irreversibility.

It is noted that the same inverse electrocaloric effect can be also utilized to enhance the heating effect. More specifically, by removing the reversed electric field, the temperature can be increased, as it is illustrated in the inset of Fig. 5.10(a). Since the loops exhibit a relatively linear slope between the maximum polarization and the polarization state just before coercive field (before point M), the polarization change is predominantly reversible. Therefore, the losses can be ignored, and there is a negligible difference in electrocaloric response when switching back and forth between the positive and negative field. However, the corresponding difference is big in the cases where the irreversibility of the polarization change is high, and the total entropy increases sharply (after point M).

5.2.2 Influence of Initial Temperatures

In order to understand the influence of the initial temperatures T_i on the phenomenon of electrocaloric enhancement, results for three initial temperatures, T_i = 300 K, 320 K and 340 K, are also compared. (see Fig. 5.11(a)) Note that all three initial temperatures are far below the Curie temperature 393 K, where only the tetragonal phase is present.

At lower temperature, the coercive field is higher which has been confirmed by the simulated P-E loops shown in Fig. 5.11(c). Therefore, by increasing the initial temperature from 300 K to

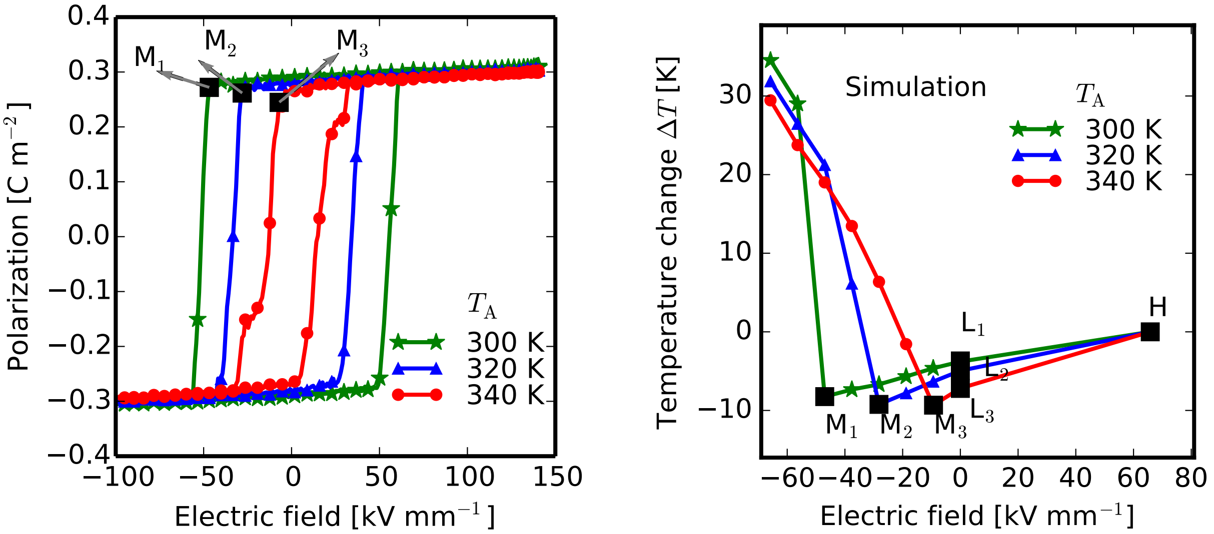

Figure 5.11 *Firstly, the simulation asserts that with increasing the magnitude of the reversed field, the electrocaloric cooling is initially enhanced, and later deteriorated. Secondly, with increasing the initial temperature T_i, the coercive field decreases. Therefore, the optimal reversed field with maximum temperature drop decreases. The position of the maximal cooling effect is labeled with M_1, M_2 and M_3. The corresponding hysteresis loops for the simulation are shown.*

320 K and 340 K, the optimal reversed field with maximum electrocaloric cooling decreases. It should be noted that the field reversal is only enhancing the electrocaloric effect if the material is in its ferroelectric state, since in the paraelectric configuration irreversible contributions are missing.

Compared with the experimental results in Fig. 5.7, agreements can be found at least in two aspects. Firstly, electrocaloric cooling is enhanced by applying a reversed field, and secondly, the optimal reversed electric field strength decreases with increasing initial temperature.

It should be noted that a quasistatic loading scenario is considered in both, simulations and measurements. This assumption is justified, since the characteristic polarization switching time [192] is on the order of 10^{-6} s and thus much faster than the typical electrocaloric measurement time scale of seconds [14, 193]. In the Monte-Carlo simulations the magnitude of the applied electric field and the obtained temperature variation are higher than those obtained by the experimental results. This quantitative discrepancy is related to the fact that the simulation is performed with a 2-dimensional model of single crystalline defect-free $BaTiO_3$, while the experiments are done for the bulk single crystal of PMN-29PT. However, the underlying physics is maintained, i.e., the electrocaloric effect can be enhanced by a proper magnitude of reversed field, thanks to the inverse electrocaloric effect.

5.3 Summary

The change of dipolar and vibrational entropies upon adiabatic application/removal electric fields manifests itself in heating/cooling of the electrocaloric material. Traditionally, the cooling effect is achieved by instantaneous removal of the electric field due to the increase of dipolar entropy. In contrast, applying a negative field on a positively poled ferroelectric sample can enhance the electrocaloric cooling and is a promising method to optimize the electrocaloric cycle. Experimental measurements show that the maximal cooling is not obtained, when the electric field is removed, but reversed to a value corresponding to the shoulder of the hysteresis loop (see Fig. 5.1). By comparing results from computer simulations using Monte-Carlo algorithms and experiments using direct electrocaloric measurements, we find that the electrocaloric cooling efficiency can be enhanced by more than 20% in standard ferroelectrics and also relaxor ferroelectrics, since the variation in dipolar entropy is further increased. However, the optimal reversed field cannot be predicted if a constant total entropy is assumed under adiabatic conditions. Thus, a thermodynamical analytical model of entropy changes based on work loss is proposed, which takes the entropy contribution of irreversible processes into account. In this analytical work, the total polarization is decomposed into the reversible and irreversible parts (see Fig. 5.3). Based on the experimental observations [194], the reversible part of the polarization is assumed to a straight line without any work loss passing though the center of the hysteresis. In this way, the difference of the work done by the reversible and irreversible polarization is obtained, and the entropy-related work loss in irreversible processes is calculated. The optimal reversed field determined by this approach agrees with the experimental observations (see Fig. 5.5). Our study signifies the importance of considering irreversible process in electrocaloric cycles.

It can be concluded from both theoretical and experimental results in this chapter that in ferroelectric materials, exhibiting a broad square-like isothermal hysteresis loop, the electrocaloric cooling can be greatly enhanced by field reversal (see Figs. 5.7 and 5.11). In contrast, irreversible adiabatic processes dominate in electrocaloric cycles in ferroelectric materials with slim hysteresis and thus an enhancement of the electrocaloric effect can be hardly observed. Therefore, the concept of applying a proper reversed field to enhance the electrocaloric cooling might be especially beneficial for thin-films, which have a square-shaped P-E loop.

Chapter 6

Inverse Electrocaloric Effect in the Presence of Defect Dipoles

The manuscript for Sec. 6.1 is being prepared. Sec. 6.2 is based on the publication "Y.-B. Ma, A. Grünebohm, K.-C. Meyer, K. Albe, and B.-X. Xu, Phys. Rev. B 94, 094113 (2016)".

In acceptor doped perovskite ferroelectrics, the A site or B site ions can be substituted by ions with a lower valence, e.g., Ti ions in $BaTiO_3$ are substituted by Mn as illustrated in Fig. 2.5. The associates of the acceptors and the compensating oxygen vacancies form non-switchable defect dipoles [70, 72–74], which shift or pinch the dielectric hysteresis [57, 70, 81–100], and might affect or even enhance the electrocaloric effect significantly. In this chapter, the thermodynamical analytical model of entropy changes is utilized to investigate the influence of defect dipoles on the electrocaloric effect in Sec. 6.1, and the statistical lattice-based Monte-Carlo simulations are applied to reveal the mechanism on the domain structure level in Sec. 6.2.

Both approaches show that the electrocaloric effect can be strongly influenced by the presence of defect dipoles. In particular, due to the delicate interplay of the external field and the internal field-induced by defect dipoles, the transition between the conventional and inverse electrocaloric effect can occur. Moreover, modified electrocaloric cycles, which make use of the inverse electrocaloric effect in the presence of defect dipoles, are proposed to enhance the electrocaloric effect.

6.1 Analytical Model of Entropy Changes

By extending the analytical model of entropy changes in Sec. 5.1, in this section the electrocaloric effect in samples with defect dipoles is investigated. Thereby, the entropy contribution of the irreversible process is taken into account. The details of the analytical model can be found in Subsec. 6.1.1. The influence of the defect polarization and of the strength of the external field are shown in Subsecs. 6.1.2 and 6.1.3, respectively. Using the obtained knowledge of the influential factors, the electrocaloric effect is tailored by defect engineering and shows a considerable enhancement (see Subsec. 6.1.4).

6.1.1 Model

When the fixed defect dipoles are considered, the dipolar mean field free energy density F_{dip} can be expressed as

$$F_{\mathrm{dip}} = F_0 + \frac{1}{2}aP^2 + \frac{1}{4}bP^4 + \frac{1}{6}cP^6 - EP - JPP_{\mathrm{d}}, \tag{6.1}$$

where P_{d} is the polarization induced by the defects, and J is the coupling strength between P and P_{d}. Hereby for simplicity, the sixth order-term and the temperature-dependence of b is abandoned while $a = a_0(T_{\mathrm{A}} - T_{\mathrm{C}})$ with T_{A} and T_{C} as the initial temperature and the Curie temperature. Apparently, the resultant bias field-induced by defect dipoles has the expression,

$$E_{\mathrm{d}} = 2JP_{\mathrm{d}}. \tag{6.2}$$

According to Kutnjak *et al.* [182], the following normalized parameters are chosen: $T_{\mathrm{C}} = 1$, $b = 1/3$, and $a_0 = \partial a/\partial T_A = 1$. The coupling strength between P and P_{d} is assumed to be $J = 3.0$.

Even though the theory presented here is general, only anti-parallel defect dipoles, which lie anti-parallel to the positive direction of the external electric field, are considered, as illustrated in Fig. 6.1.

The total entropy can be written as the sum of two contributions, i.e., the dipolar entropy S_{dip} and the vibrational entropy S_{vib}. The entropy changes satisfy

$$\Delta S_{\mathrm{total}} = \Delta S_{\mathrm{dip}} + \Delta S_{\mathrm{vib}}. \tag{6.3}$$

The dipolar entropy can be given in $S_{\mathrm{dip}} = -\partial F_{\mathrm{dip}}/\partial T_{\mathrm{A}} = -\frac{1}{2}a_0P^2$. Thus, the change of S_{dip} from state A with (P_{A}, E_{A}, T_{A}) to another state with (P, E, T) can be simply expressed as

$$\begin{aligned}\Delta S_{\mathrm{dip}} &= S_{\mathrm{dip}}(P) - S_{\mathrm{dip}}(P_{\mathrm{A}}) \\ &= -\frac{1}{2}a_0P^2 + \frac{1}{2}a_0{P_{\mathrm{A}}}^2.\end{aligned} \tag{6.4}$$

The change of S_{vib}, i.e., $\Delta S_{\mathrm{vib}} = S_{\mathrm{vib}}(T) - S_{\mathrm{vib}}(T_{\mathrm{A}})$, can be approximated as

$$\Delta S_{\mathrm{vib}} = \int_{T_{\mathrm{A}}}^{T} \frac{C_{\mathrm{ph}}}{T} dT \cong C_{\mathrm{ph}} \ln(T/T_{\mathrm{A}}), \tag{6.5}$$

where C_{ph} is the specific heat capacity of the non-polar degrees of freedom, which is assumed to be temperature-independent. In a purely reversible process, since $\Delta S_{\mathrm{total}} = 0$, the resultant temperature can be straightforwardly calculated.

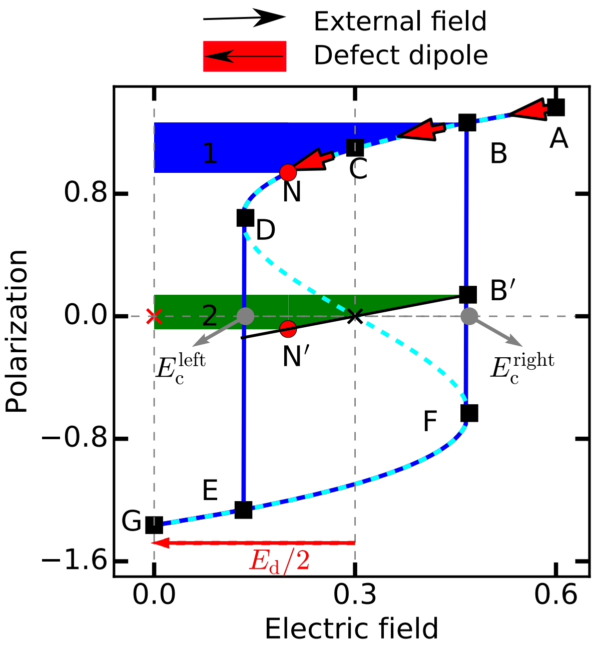

FIGURE **6.1** *The schematic P-E loop shifted by defect dipoles. Within A-B and B-E the process is reversible and irreversible, respectively. In the irreversible process B-E the total polarization can be separated into two parts: the reversible and irreversible polarization. The reversible polarization with respect to the electric field within B-E is assumed as the one to have the same slope as the tangent line to the S-shaped P-E loop at point B with* (E_B, P_B) *(see black line). The reversible process crosses the center of the hysteresis. The example of calculating the work loss* W_{loss1} *can be explained as following. The blue Area 1, and green area 2 are firstly designated as* V_1*, and* V_2*. Therefore, when the field is removed from B to N point, the actual work* W_{actual} *is* $-V_1$*, and* $-V_2$ *represents the work in a reversible process* W_r*. Consequently,* W_{loss1} *equals to* $-V_1 + V_2$*, which is a negative work loss.*

Similar to Subsec. 5.1.2, the change of total entropy is calculated from the work loss,

$$\Delta S_{\mathrm{total}} = \frac{W_{\mathrm{loss}}}{T_A}. \tag{6.6}$$

As shown in the following context, the work loss will be calculated from the difference of the work done by reversible and irreversible polarizations.

From Eqs. (6.3) and (6.4), (6.6), ΔS_{vib} can be formulated and then used in Eq. (6.5). One arrives at

$$T = T_A \exp\left[(W_{\mathrm{loss}}/T_A - \Delta S_{\mathrm{dip}})/C_{\mathrm{ph}}\right] \tag{6.7}$$

This indicates that the final temperature can be expressed by the work loss and the dipolar entropy change. The dipolar entropy can be expressed directly from the polarization variation, while the work loss can be obtained based on the reversal and irreversible contributions of the polarization. Eq. (6.7) can be simplified to Eq. (5.4) if the process is reversible with $W_{\mathrm{loss}} = 0$.

In ferroelectric materials, due to the presence of the hysteresis below the Curie temperature, during the polarization switching the polarization can be separated into two parts: the reversible and irreversible contribution [186, 194, 195]. Until now, much less is known on the irreversible process in the electrocaloric effect. W_{loss} can be evaluated by decomposition of the polarization within the Landau theory. Setting the first derivative of the Landau free energy density $\partial F_{\mathrm{dip}}/\partial P$ to be zero, one obtains a relation between the polarization and the actual electric field E:

$$E \quad = \quad aP + bP^3 - JP_{\mathrm{d}}. \tag{6.8}$$

Below T_{C} the corresponding S-shaped P-E loop is sketched in Fig. 6.1. At point A the polarization is saturated. Between point B and E Eq. (6.1) has multiple local extrema, and point N locates within point A and E. At point C the electric field equals to 0 if no defects exist, and D is the inflection point of this S-shaped curve. Between point A and B the process is reversible, and the electrocaloric effect can be studied using Eq. (5.4). However, since between B and E Eq. (6.1) has multiple local extrema, the process is metastable. Therefore, between point B and E the total polarization has two contributions, i.e., the reversible and irreversible polarization. In the ferroelectric P-E loops, the reversible process should be a straight line passing through the center of the hysteresis without any hysteretic heat loss since the contribution mainly arises from the ionic and electronic polarization [194].

The tangent line to the S-shaped P-E loop at point B with $(E_{\mathrm{B}}, P_{\mathrm{B}})$ is assumed to be the same as the tangent line of the reversible contribution part passing through the black crossing (see the black line $\mathrm{B}'\mathrm{N}'$ in Fig. 6.1). The slope is $\frac{\partial E}{\partial P}\,|_{P=P_{\mathrm{B}}} = a + 3bP_{\mathrm{B}}{}^2$, where $E_{\mathrm{B}} = aP_{\mathrm{B}} + bP_{\mathrm{B}}^3 - JP_{\mathrm{d}}$. Then the reversible polarization P_{r} and the corresponding field E satisfy the relation

$$E + E_{\mathrm{d}}/2 = (a + 3bP_{\mathrm{B}}{}^2)P_{\mathrm{r}}$$

or

$$E = aP_{\mathrm{r}} + 3bP_{\mathrm{B}}{}^2P_{\mathrm{r}} - JP_{\mathrm{d}}. \tag{6.9}$$

The work loss W_{loss} is termed as the difference between the work done in the reversible process and that in the actual process, under the same electric field E. Substitution of Eq. (6.8) into (6.9), one obtains the relation:

$$aP + bP^3 - JP_{\mathrm{d}} \quad = \quad aP_{\mathrm{r}} + 3bP_{\mathrm{B}}{}^2P_{\mathrm{r}} - JP_{\mathrm{d}}.$$

In this way the reversible polarization can be expressed as

$$P_{\mathrm{r}} \quad = \quad \frac{aP + bP^3}{a + 3bP_{\mathrm{B}}{}^2}.$$

For any point located between B and D, the work loss is given through the difference of the integrals

$$\begin{aligned} W_{\mathrm{loss1}}(P) &= W_{\mathrm{actual}} - W_{\mathrm{r}} \\ &= \int_{P_{\mathrm{B}}}^{P} E dP - \int_{P_{\mathrm{B'}}}^{P_{\mathrm{r}}} E dP_{\mathrm{r}} \\ &= \frac{1}{2} a P^2 + \frac{1}{4} b P^4 - (\frac{1}{2} a {P_{\mathrm{B}}}^2 + \frac{1}{4} b {P_{\mathrm{B}}}^4) + \frac{1}{2} a {P_{\mathrm{B'}}}^2 \\ &+ \frac{3}{2} b {P_{\mathrm{B}}}^2 {P_{\mathrm{B'}}}^2 - (\frac{1}{2} a {P_{\mathrm{r}}}^2 + \frac{3}{2} b {P_{\mathrm{B}}}^2 {P_{\mathrm{r}}}^2) \\ &- J P_{\mathrm{d}} (P - P_{\mathrm{B}} - P_{\mathrm{r}} + P_{\mathrm{B'}}), \end{aligned} \tag{6.10}$$

where $P_{\mathrm{B'}} = P_{\mathrm{r}}|_{P=P_{\mathrm{B}}} = \dfrac{a P_{\mathrm{B}} + b P_{\mathrm{B}}^3}{a + 3b {P_{\mathrm{B}}}^2}$.

For any point between D and E, one has to go through the vertical snap-through line, which represents the hysteretic path. In this way, we obtain the work loss in the following form

$$W_{\mathrm{loss2}}(P) = W_{\mathrm{loss1}}|_{P=P_{\mathrm{D}}} + (P - P_{\mathrm{D}}) E_{\mathrm{D}}. \tag{6.11}$$

In summary,

$$W_{\mathrm{loss}} = \begin{cases} W_{\mathrm{loss1}} & \text{for points between B and D ,} \\ W_{\mathrm{loss2}} & \text{for points between D and E .} \end{cases}$$

Alternatively, the work loss can be determined from the shaded areas in Fig. 6.1. One can shift the green area by $(0, P_{\mathrm{B}} - P_{\mathrm{B'}})$ and obtain Fig. 6.2. The amount of the work loss and the work in the reversible process can be represented by the area of the gray and green area, respectively. And the actual total work is equivalent to the sum of the green and gray area. It should be noted that the area corresponding to the work loss can be negative or positive, depending on its position with respect to the electric field axis.

With increasing temperature the hysteresis becomes slimmer. Meanwhile, the bias field can shift the center of the hysteresis. Below the Curie temperature, at the inflection point D, the polarization $P_{\mathrm{D}} = \sqrt{-\dfrac{a}{3b}}$, and according to Eq. (6.8) the coercive field on the left side of the hysteresis can be calculated

$$E_{\mathrm{c}}^{\mathrm{left}} = \frac{2}{3} a \sqrt{-\frac{a}{3b}} - J P_{\mathrm{d}}. \tag{6.12}$$

At a certain temperature, $E_{\mathrm{c}}^{\mathrm{left}} = 0$, and this characteristic temperature is denoted by ${T_{\mathrm{A}}}'$ and can be expressed as:

$${T_{\mathrm{A}}}' = T_{\mathrm{C}} - (J P_{\mathrm{d}})^{2/3} (27b/4)^{1/3} / a_0. \tag{6.13}$$

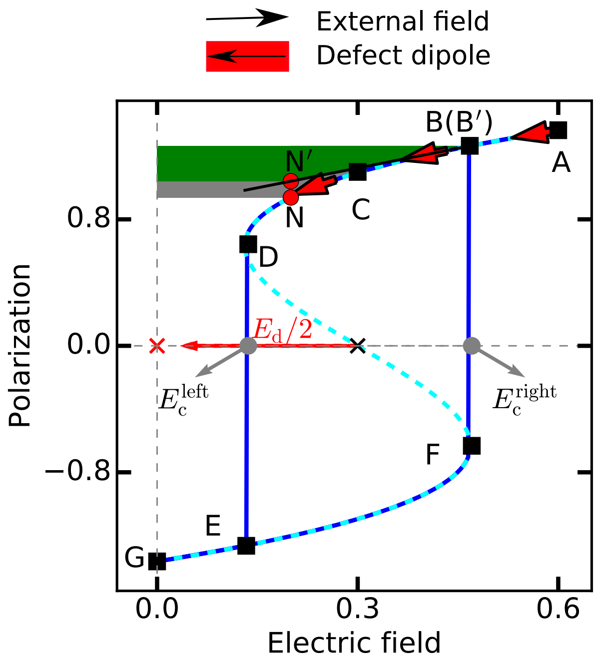

Figure 6.2 *Alternative way to represent the work loss. In order to show the work loss straightforwardly, the green area in Fig. 6.1 is shifted up by (0, $P_B - P_{B'}$). In this way, the green and gray area represent the work in the reversible process and the work loss, respectively. As a result the total work is the sum of the green and gray area.*

For the given P_d, this left coercive field is negative if $T \leq T_A^{'}$, while positive if $T_A^{'} \leq T \leq T_C$. In the case of no defect dipole, $T_A^{'} = T_C$. Figure 6.3 illustrates the change of the left coercive field with respect to temperature and the shift of this quantity by the defect dipole. It also highlights the characteristic temperature $T_A^{'}$.

In Sec. 6.1.2 and 6.1.3, the field removal case is concerned, namely the external field changes from E_{init} to 0. In Sec. 6.1.4, modified field application is proposed to optimize the electrocaloric effect. The external field changes from E_{init} to E_{end}, and E_{end} can be positive or negative, depending on initial temperature.

It is worth mentioning another characteristic temperature $T_A^{''}$, at which the applied external field E_{init} equals exactly the left coercive field. By forcing E_c^{left} in Eq. (6.12) equal to E_{init} and considering the temperature dependence of the coefficient a, one has

$$T_A^{''} \quad = \quad T_C - (E_{\text{init}} + JP_d)^{2/3}(27b/4)^{1/3}/a_0. \tag{6.14}$$

When the external field is equal to the internal field-induced by the defects, $T_A^{''}$ reaches its extremum, i.e., T_C.

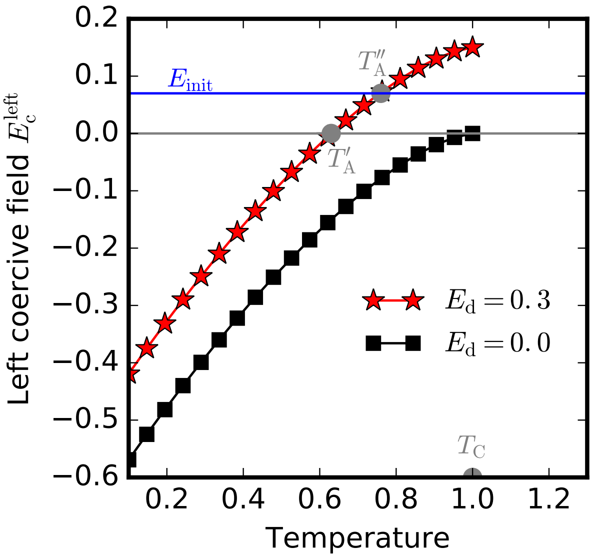

FIGURE 6.3 *Variation of the left coercive field with temperature* $E_{\rm c}^{\rm left}$. $T_{\rm A}^{'}$ *indicates the temperature at which* $E_{\rm c}^{\rm left} = 0$ *and* $T_{\rm A}^{''}$ *is the temperature at which* $E_{\rm init} = E_{\rm c}^{\rm left}$, *illustrated for a special case of* $E_{\rm init} = 0.07$.

6.1.2 Influence of Defect Polarization

In this subsection, the electrocaloric effect under field removal from a given strength of the external field $E_{\rm init} = 0.2$ is studied. In particular, the influence of the defect polarization on the electrocaloric effect over the whole temperature range is analyzed.

Four different anti-parallel defect dipole cases are considered: 1) without defect polarization $P_{\rm d} = 0.0$, 2) $P_{\rm d} = -0.01$, 3) $P_{\rm d} = -0.033$, and 4) $P_{\rm d} = -0.1$. The results are presented in Figs. 6.4 to 6.7, respectively. In each case, the temperature change ΔT, the corresponding work loss $W_{\rm loss}$, the total entropy change $\Delta S_{\rm total}$, the vibrational entropy change $\Delta S_{\rm vib}$ and the dipolar entropy change $\Delta S_{\rm dip}$ are shown at different initial temperatures. Hysteresis curves are plotted as well for the explanations of the corresponding electrocaloric behavior. In the hysteresis curves, the black dots indicate the starting point and the end point of the adiabatic stages, and the red arrows describe the corresponding loading history. The black and red crossings represent the center of the hysteresis with and without defect dipoles, respectively. The characteristic temperature $T_{\rm A}{'}$ is equal to $T_{\rm C} = 1.0$ in case 1, and $T_{\rm A}{'}$ is 0.873, 0.718, 0.413 in case 2, 3, and 4, respectively.

In all these four cases when the temperature is below $T_{\rm A}{'}$, there is no sign change of the polarization during field removal. Generally, after removing the field, the slope $|dP/dE|$ increases when the polarization drops from the saturation polarization to the zero polarization point. In other words, crossing the center of the hysteresis from the left to right, the slope $|dP/dE|$ increases. Since the center of the hysteresis is shifted to the right by the internal bias field $JP_{\rm d}$, polarization change and $\Delta S_{\rm dip}$ increases, when the defect polarization becomes stronger.

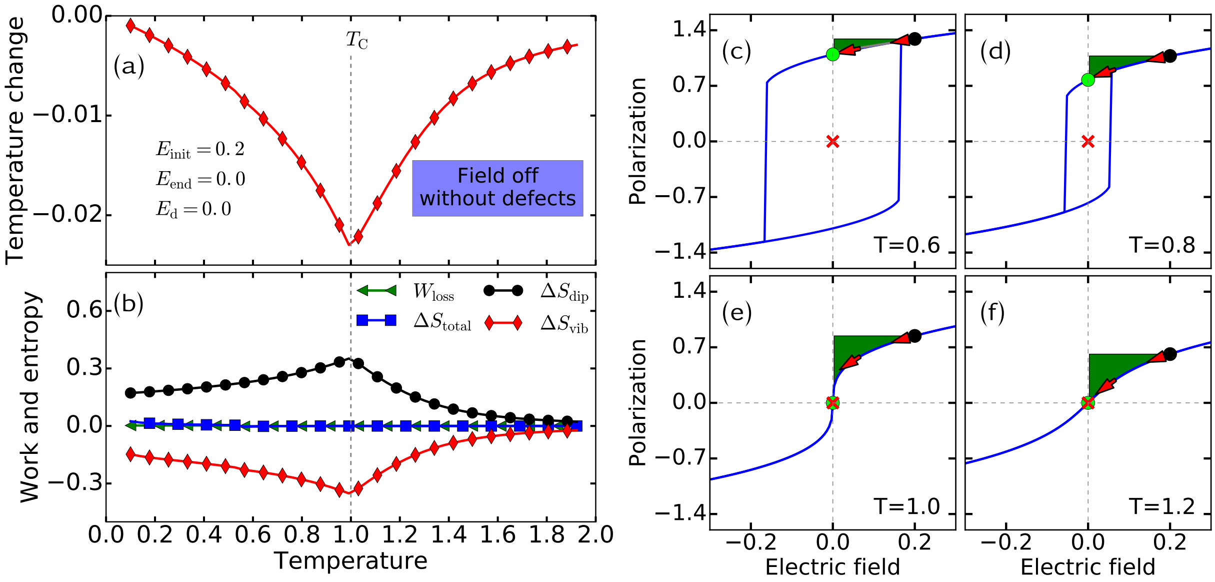

Figure 6.4 *Electrocaloric effect for the case without defects. The temperature change, the corresponding work loss and the entropy change are shown with the external field $E_{\text{init}} = 0.2$. Two hysteresis curves are illustrated as well. In this case, there is no sign change of the polarization before and after removing the field. The work loss is negligible, and the influence of the total entropy change is almost zero. Thus, the dipolar entropy change dominates the materials behavior. The polarization has the sharpest change at the Curie temperature, and thus the increase of the dipolar entropy is largest. Due to the above reason, at the Curie temperature the decrease of the vibrational entropy is sharpest, and there is one single valley of the electrocaloric temperature change.*

As a result, at $T < T_A^{'}$ the electrocaloric cooling becomes stronger when increasing the defect concentration. In the following, the phenomena above $T_A^{'}$ are mainly discussed.

In case 1, defect-free ferroelectric materials with $P_d = 0.0$ are studied, as shown in Fig. 6.4. As can be observed in the hysteresis curves, there is no sign change of polarization, and the contribution from the work loss is negligible (see the fairly small gray area). Hence, in this case our results, taking the irreversible process into account, are almost identical to those in the simplified case of ignoring the irreversibility, as has been done by other researchers [182]. The sharpest polarization change appears at the Curie temperature where the phase transition happens, which leads to the biggest change of ΔS_{dip}, ΔS_{vib} and ΔT. Therefore, one single electrocaloric cooling peak is observed.

In case 2 with $P_d = -0.01$, defect dipoles induce an internal bias field $E_d = -0.06$, which is much smaller than the external field. As it is shown in Fig. 6.5, the temperature change remains negative in the whole temperature range. However, the phenomena are greatly changed, and a bizarre W-shaped curve of the temperature change can be observed. As discussed previously, two different ranges can be distinguished: $T < T_A^{'} \approx 0.873$, and $T > T_A^{'}$. The phenomenon in the first range has been discussed. In the second range, by contrast, above $T_A^{'}$ the polarization changes the sign. Due to the partial cancellation of P^2, as shown in Eq. 6.4, ΔS_{dip} decreases

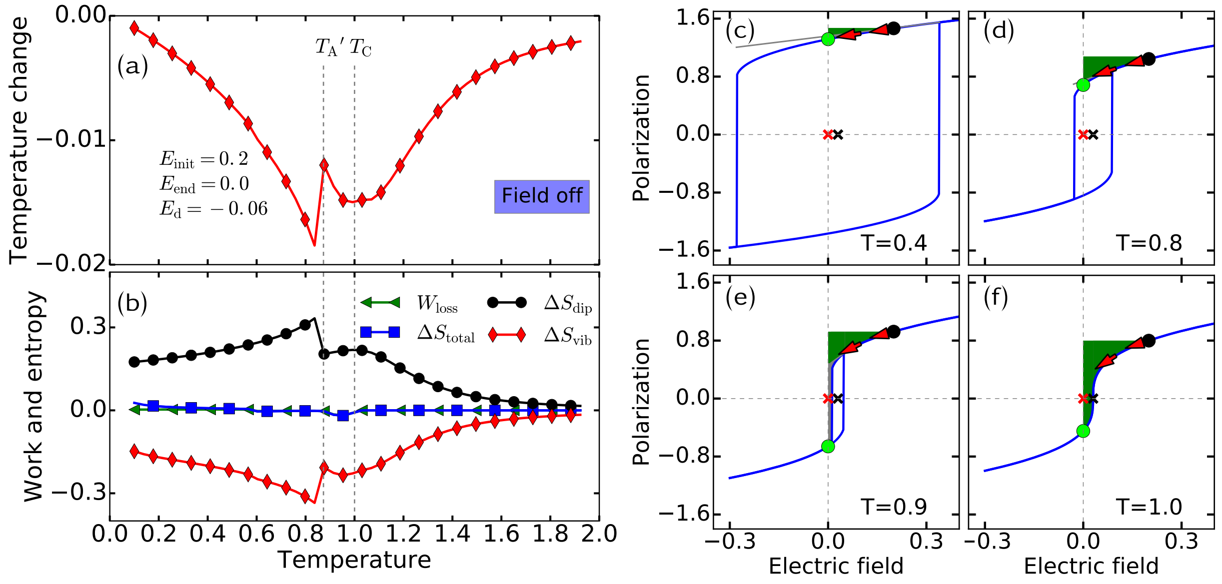

FIGURE 6.5 *Electrocaloric effect for the case with bias field* $E_{\mathrm{d}} = -0.06$ *induced by the fairly small magnitude of defect polarization.* E_{d} *shifts the hysteresis to the right, and the polarization change is bigger than in the case without defects. The temperature change is still negative, but shows a bizarre W-shape. Two different ranges can be observed, depending on whether there is a sign change before and after removing the field. When* $T < T_{\mathrm{A}}{}'$*, there is no sign change, and thus the dipolar entropy change, i.e., the temperature change, is bigger than that without defects. When* $T > T_{\mathrm{A}}{}'$*, there is a sign change. Therefore, the dipolar entropy change, i.e., the temperature change, is smaller than that without defects.*

greatly. But the magnitude of the initial polarization is still bigger than that of the final polarization. Hence, ΔS_{dip} still has a positive sign. As a result, the electrocaloric cooling still persists, but is weakened.

In case 3 moderate magnitude of defect polarization $P_{\mathrm{d}} = -0.033$ is concerned, and correspondingly one has the characteristic quantities $E_{\mathrm{d}} = -0.2$, $T_{\mathrm{A}}{}' = 0.718$. Compared with case 2, the curve of the temperature change is still W-shaped, but more irregular, as shown in Fig. 6.6. Three different ranges can be distinguished: $T < T_{\mathrm{A}}{}'$, $T_{\mathrm{A}}{}' < T < T_{\mathrm{C}}$, and $T > T_{\mathrm{C}}$. In the first range with $T < T_{\mathrm{A}}{}'$ the electrocaloric cooling increases with the initial temperature. In the second and third range, the polarization has the same magnitude, but opposite signs before and after the field removal. Hence, ΔS_{dip} is zero. In the second range, part of the process is irreversible, and W_{loss}, i.e., $\Delta S_{\mathrm{total}}$, is dominant in materials behavior. W_{loss} can be evaluated quantitatively as the area of the gray color in the hysteresis, while the area of the green color equals to the reversible work. Thus, W_{loss} is negative, and with increasing the temperature, the magnitude of W_{loss} increases firstly (compare the gray area in the hysteresis for $T = 0.72$ and $T = 0.9$), and then decreases (compare the gray area in the hysteresis for $T = 0.9$ and $T = 0.95$). Correspondingly, the temperature drop increases first, but then decreases. Hence, the temperature change shows a valley-like curve. However, in the third range with $T > T_{\mathrm{C}}$, the

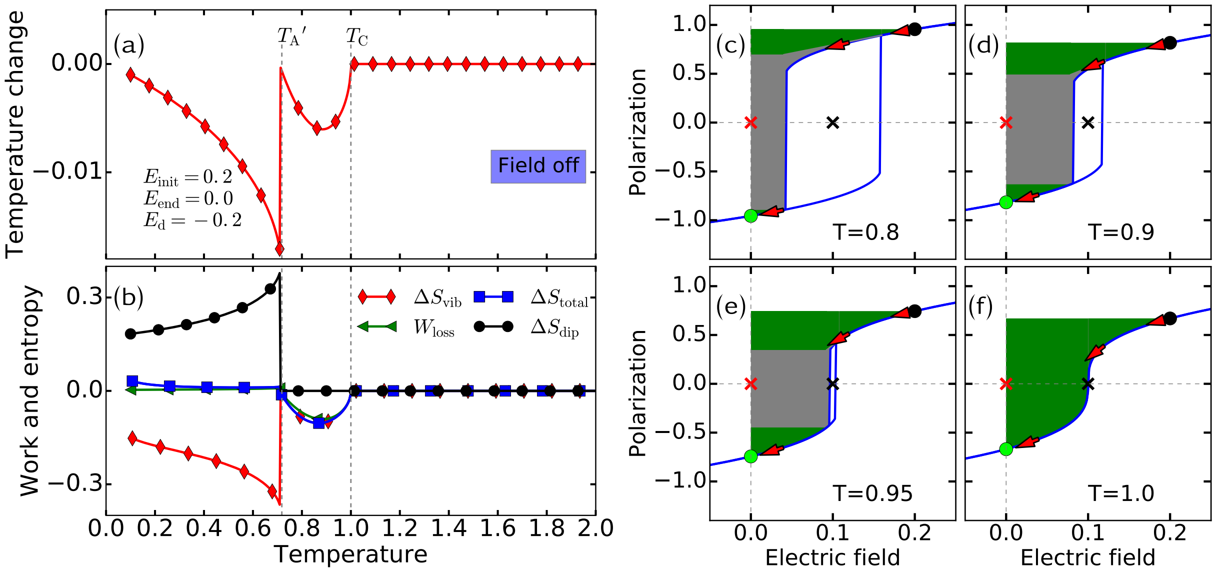

Figure 6.6 *Electrocaloric effect for the case with bias field* $|E_\mathrm{d}| = 0.2 = E_\mathrm{init}$ *induced by medium magnitude of defect polarization. Three different ranges can be distinguished with* $T < T_\mathrm{A}^{'}$, $T_\mathrm{A}^{'} < T < T_\mathrm{C}$ *and* $T > T_\mathrm{C}$*. In the first range, the electrocaloric cooling increases with the temperature. With* $T_\mathrm{A}^{'} < T$*, the polarization has the same magnitude but opposite sign before and after field removal. In the second range, the magnitude of the negative* W_loss *increases first, but then decreases, which leads to the same tendency of* ΔT*. In the third range for the reversible process,* ΔT *equals to 0.*

process is totally reversible. As a result, the change of the dipolar, vibrational and total entropy are zero as well as the temperature change.

In the cases 1-3, the internal bias field is not stronger than the external field. While in case 4 the defect dipole $P_\mathrm{d} = -0.1$ is much stronger, which results in $E_\mathrm{d} = -0.6$. It overruns the strength of the external field $E_\mathrm{init} = 0.2$. It also gives rise to $T_\mathrm{A}^{'} \approx 0.413$. Two different ranges can be distinguished: $T < T_\mathrm{A}^{'}$ and $T > T_\mathrm{A}^{'}$. With the same mechanism as in the above mentioned cases, in the first range with $T < T_\mathrm{A}^{'}$, there is a negative temperature change. By contrast, in the second range with $T > T_\mathrm{A}^{'}$, the temperature change is positive. This is due to the shift of the hysteresis, which leads to no sigh change of the polarization before and after removing the external field. The magnitude of the initial polarization is smaller than the final polarization, which results in a more ordered system after removing the field. Meanwhile, W_loss and ΔS_total change slightly within this range. Correspondingly, ΔS_dip is negative and ΔS_vib is positive, leading to the so-called inverse electrocaloric effect. By comparison, in case 1, 2 and 3 there exists only the conventional electrocaloric effect. Interestingly, the peak of the temperature change within this range deviates from the Curie temperature, even though there is a peak of the vibrational entropy change at the Curie temperature. This arises from the influence of the initial temperature, referring to Eq. (6.7).

In summary, the temperature change is highly influenced by the magnitude of defect dipoles. In case 1 without defects, there is no sign change of the polarization before and after removing

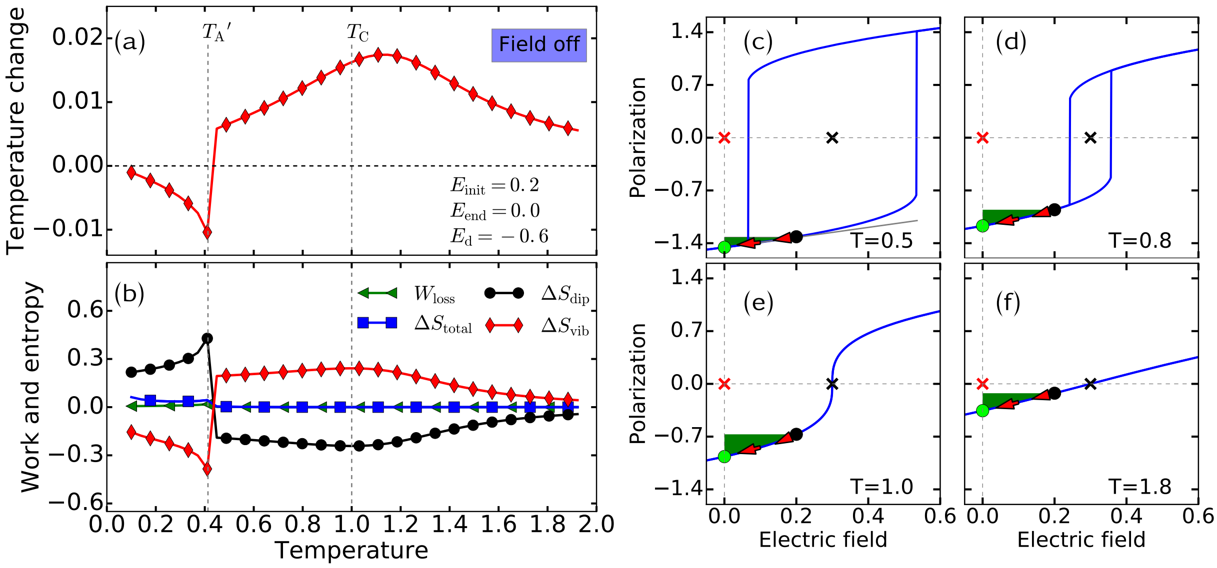

FIGURE 6.7 *Electrocaloric effect for the case with bias field* $|E_{\mathrm{d}}| = 0.6 > E_{\mathrm{init}}$ *induced by fairly large defect polarization with* $T_{\mathrm{A}}{}'$. *Different from the case with low and medium magnitude of defect polarization, there exists a positive temperature change. Two different ranges can be distinguished with* $T < T_{\mathrm{A}}{}'$ *and* $T > T_{\mathrm{A}}{}'$. *In the first range, the negative temperature change increases with the temperature. In the second range with insignificant work loss, the temperature change presents a positive sign. The change of the polarization increases firstly, and then decreases, leading to the corresponding entropy changes and a single peak of the temperature change.*

the field. The initial polarization is bigger than the final one, which leads to a negative temperature change, i.e., a conventional electrocaloric effect. However, in case 2 with low, and 3 with medium magnitude of defect polarizations, when the temperature is above $T_{\mathrm{A}}{}'$, the sign of the polarization changes before and after the field is removed. Therefore, ΔS_{dip} is reduced due to the partial cancellation of P^2 (referring to Eq. 6.4), even though in some cases the negative work loss contributes to the electrocaloric cooling. Hence, there is weaker electrocaloric cooling when $T > T_{\mathrm{A}}{}'$, compared with the range that the temperature is slightly below $T_{\mathrm{A}}{}'$. With increasing the magnitude of defect dipoles, the center of the hysteresis is shifted more by the internal bias field. Hence, stronger cancellation of P^2 exists (referring to Eq. 6.4), which leads to smaller ΔS_{dip}, i.e., weaker electrocaloric cooling. When the magnitude of the defect polarization is so high (see case 4), at $T > T_{\mathrm{A}}{}'$, there is no sign change of the polarization. However, different from case 1, the magnitude of the polarization decreases, which leads to a positive temperature change, i.e., an inverse electrocaloric effect.

6.1.3 Influence of External Field Strength

In this subsection, the influence of the strength of the external field is investigated, while the defect dipole is fixed $P_{\mathrm{d}} = -0.1$, with the characteristic quantities $E_{\mathrm{d}} = -0.6$ and $T_{\mathrm{A}}{}' \approx 0.413$.

Five different cases are shown: 1) $E_{\text{init}} << |E_{\text{d}}|$, 2) $E_{\text{init}} = |E_{\text{d}}|/2$, 3) E_{init} is slightly larger than $|E_{\text{d}}|/2$, 4) $E_{\text{init}} = |E_{\text{d}}|$, 5) $E_{\text{init}} > |E_{\text{d}}|$.

Case 1 has been already discussed in Fig. 6.7, since it is similar to the case 4 in Subsec. 6.1.2.

In case 2 with $E_{\text{init}} = |E_{\text{d}}|/2$ two ranges can be found, as shown in Fig. 6.8: $T < T_{\text{A}}^{'}$ and $T > T_{\text{A}}^{'}$. In case 1 and 2 there is a negative temperature change in the first range, while a positive temperature change in the second range. However, the polarization change is bigger in case 2 than in case 1. Hence, the inverse electrocaloric effect is stronger in case 2. Additionally, the peak position in case 2 is at the Curie temperature, while in case 1 the temperature of the peak position is slightly lower than the Curie temperature.

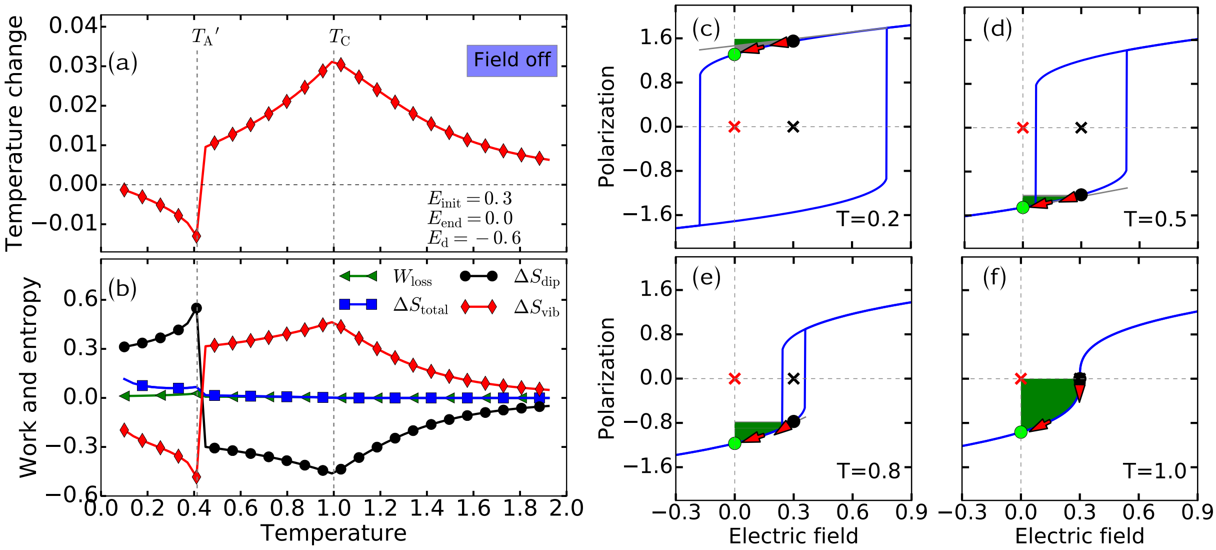

FIGURE **6.8** *Electrocaloric effect for the case with bias field* $E_{\text{d}} = -0.6$ *under external field* $E_{\text{init}} = 0.3$ *with* $T_{\text{A}}^{'} \approx 0.413$. *Sharing the same mechanism as the case with* $E_{\text{init}} << |E_{\text{d}}|$, *two ranges can be distinguished, with* $T < T_{\text{A}}^{'}$ *and* $T > T_{\text{A}}^{'}$. *The negative and positive temperature change appears in the first and second range, respectively.*

In case 3 the external field $E_{\text{init}} = 0.33$ is slightly higher than $|E_{\text{d}}|/2$. The phenomena change significantly, as shown in Fig. 6.9. Two characteristic temperatures $T_{\text{A}}^{'} \approx 0.413$ and $T_{\text{A}}^{''} \approx 0.873$ are influential. Correspondingly, four different ranges can be observed: $T < T_{\text{A}}^{'}$, $T_{\text{A}}^{'} < T < T_{\text{A}}^{''}$, $T_{\text{A}}^{''} < T < T_{\text{C}}$ and $T > T_{\text{C}}$. In the first range with $T < T_{\text{A}}^{'}$, the negative temperature change exists with a stronger cooling effect than $E \leq |E_{\text{d}}|/2$, however, sharing the same mechanism as with $E \leq |E_{\text{d}}|/2$. In the second range with $T_{\text{A}}^{'} < T < T_{\text{A}}^{''}$, the positive temperature change exists, and there is more contribution from the irreversible process in this case than that with $E \leq |E_{\text{d}}|/2$. Again, the same mechanism applies in this case and that with $E \leq |E_{\text{d}}|/2$. Strikingly, the temperature change varies from positive to negative when transferring from the second range to the third one. In the third range the negative and positive temperature change coexist. The underlying reason for this phenomenon arises from the competition between ΔS_{dip} and ΔS_{total}. In this range the polarization switches from positive with a small magnitude to negative with a big magnitude sharply. Hence, ΔS_{dip} is always negative with a large magnitude. Simultaneously,

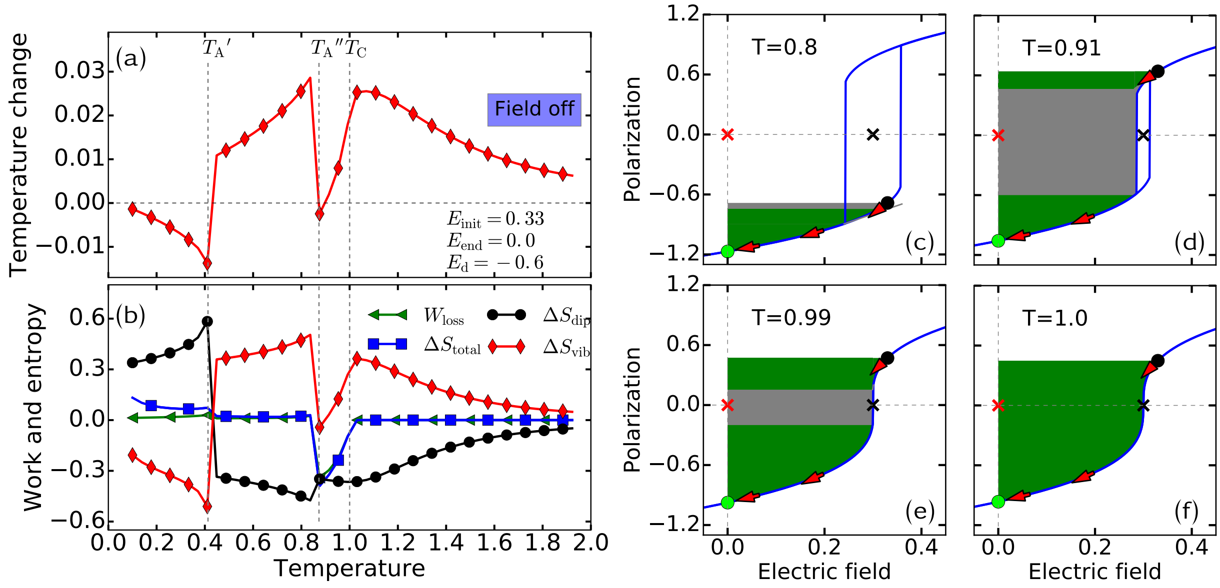

Figure 6.9 *Electrocaloric effect for the case with bias field $E_{\mathrm{d}} = -0.6$ induced by defect polarization under the external field $E_{\mathrm{init}} = 0.33$. Four ranges can be distinguished, with $T < T_{\mathrm{A}}^{'}$, $T_{\mathrm{A}}^{'} < T < T_{\mathrm{A}}^{''}$, $T_{\mathrm{A}}^{''} < T < T_{\mathrm{C}}$ and $T > T_{\mathrm{C}}$. In the first range, the electrocaloric cooling increases with the temperature. In the second range, with the same mechanism as the case with $E_{\mathrm{init}} \leq |E_{\mathrm{d}}|/2$, the positive temperature change appears, while the electrocaloric heating effect is stronger than the case with $E_{\mathrm{init}} \leq |E_{\mathrm{d}}|/2$. In the third range the positive and negative temperature change coexist. In this range the sign of the polarization switches from positive to negative before and after removing the field. During the polarization switching, the work loss and the total entropy transfers from negative with a considerable large value to almost 0 upon increasing the initial temperature (see the gray area in hysteresis for $T = 0.91$ and $T = 0.99$). However, the dipolar entropy change is always large. Due to the competition effect of the total and dipolar entropy, the temperature change transfers from an insignificant negative value to a considerable positive value. In the fourth range with $T > T_{\mathrm{C}}$, the paraelectric phase exists, and the temperature change decreases when increasing the temperature.*

in this range the negative W_{loss} with a large magnitude, i.e., $\Delta S_{\mathrm{total}}$, changes to almost 0. Since $\Delta S_{\mathrm{vib}} = \Delta S_{\mathrm{total}} - \Delta S_{\mathrm{dip}}$, the temperature change varies gradually from a small negative value to a large positive value. In the fourth range with $T > T_{\mathrm{C}}$, similar to the case with $E \leq |E_{\mathrm{d}}|/2$, the materials are in the paraelectric state. Hence, the temperature change decreases with increasing initial temperature.

The phenomena with $E_{\mathrm{init}} = |E_{\mathrm{d}}|$ in case 4 (see Fig. 6.10) are identical to those observed in Fig. 6.6, and they share the same explanation. Hence, the details for this case are not discussed.

In case 5 the external field $E_{\mathrm{init}} = 0.8$ is larger than $|E_{\mathrm{d}}|$, and it means that above $T_{\mathrm{A}}^{'}$, the polarization changes its sign before and after the field removal. The related results are shown in Fig. 6.11. Similar to case 4, three different ranges can be distinguished here: $T < T_{\mathrm{A}}^{'}$, $T_{\mathrm{A}}^{'} < T < T_{\mathrm{C}}$ and $T \geq T_{\mathrm{C}}$. As in all the other cases, there is a negative temperature change in the first range with $T < T_{\mathrm{A}}^{'}$. In the second range with $T_{\mathrm{A}}^{'} < T < T_{\mathrm{C}}$, the temperature change is negative, similar to case 4 but contrary to cases 1-3. Due to the same mechanism, the

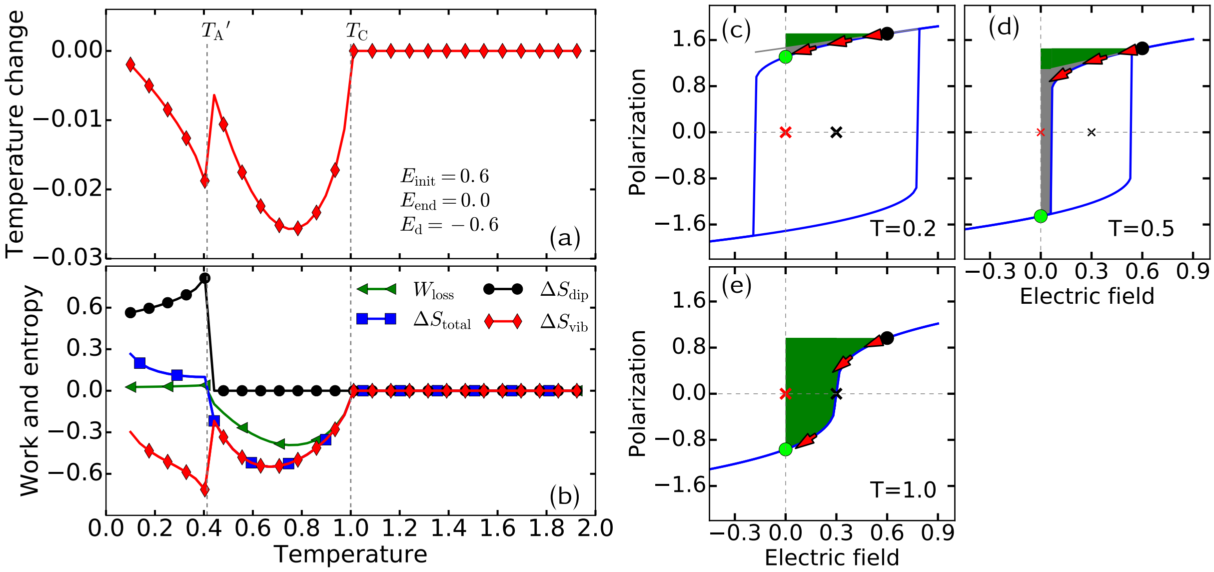

FIGURE 6.10 *Electrocaloric effect for the case with bias field* $E_d = -0.6$ *induced by defect polarization under the external field* $E_{init} = 0.6$*. The same explanation can be referred to Fig.* 6.6

explanation of the first and second range can be referred to these discussions for Fig. 6.6. In the third range with $T \geq T_C$, the temperature change is negative. By contrast, the temperature change is positive in case 1-3 and a zero value in case 4. This phenomenon has a straightforward explanation. The polarization changes the sign before and after removing the external field, and the magnitude of the initial polarization is bigger than the final polarization. It signifies that after removing the field, the system becomes more disordered, and ΔS_{dip} is positive. At the same time, above T_C the process is reversible, and no work loss, i.e., zero ΔS_{total}, is involved. Hence ΔS_{vib} and the temperature change are negative.

In summary, at $T < T_A{}'$, the temperature change is always negative, i.e., with the conventional electrocaloric effect. At $T \geq T_A{}'$, depending on the strength of the external field and of the induced bias field, three different phases can be found. Firstly, with $E_{init} \leq |E_d|/2$, the temperature change is positive, i.e., with the inverse electrocaloric effect. Secondly, with $|E_d|/2 < E_{init} < |E_d|$, there is a coexistence of the positive and negative temperature change, i.e., with both the conventional and inverse electrocaloric effect. Thirdly, with $E_{init} > |E_d|$, the temperature change is negative, i.e., with the conventional electrocaloric effect.

6.1.4 Improved Electrocaloric Cycle

Based on the gained knowledge on the influence of defect dipoles and the external field, a strategy to tailor the electrocaloric effect by defect engineering is considered in this subsection. The results are shown in Fig. 6.12, and are compared with the electrocaloric cycle without defect and the case with defects but without modification.

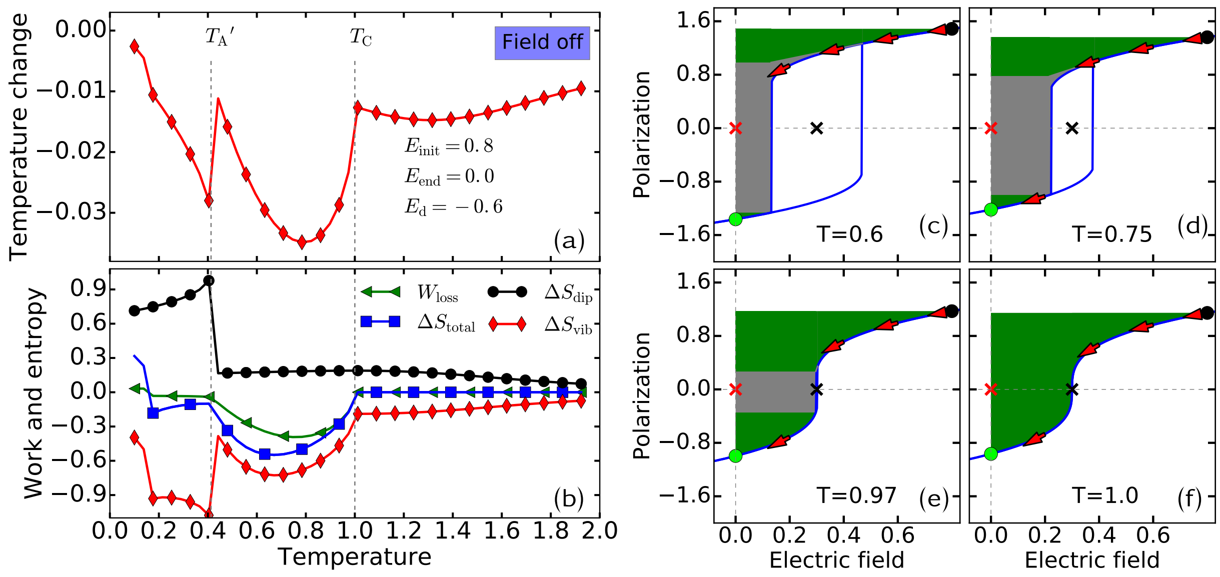

Figure 6.11 *Electrocaloric effect for the case with bias field* $E_{\mathrm{d}} = -0.6$ *induced by defect polarization under the external field* $E_{\mathrm{init}} = 0.8$. *It should be noted that hereby the external field is more than two times bigger than the induced internal field. Again, three different ranges can be distinguished, with* $T < T_{\mathrm{A}}'$, $T_{\mathrm{A}}' < T < T_{\mathrm{C}}$ *and* $T \geq T_{\mathrm{C}}$. *In this case, there is only the negative temperature change in all three ranges. For the first and second range, the mechanism can be referred to the case with* $E = 2|E_{\mathrm{d}}|$. *In the third range for the reversible process, there is a negative temperature change. The polarization changes from positive with a large magnitude to negative with a small magnitude, which leads to disordering of the material.*

Three ranges are addressed separately: $T < T_{\mathrm{A}}'$, $T_{\mathrm{A}}' < T < T_{\mathrm{C}}$ and $T > T_{\mathrm{C}}$. Here the characteristic temperature is $T_{\mathrm{A}}' \approx 0.413$. In the first and second range, the bias field $E_{\mathrm{d}} = -0.2$ induced by defects is half of the external field $E_{\mathrm{init}} = 0.2$. In the first range with $T < T_{\mathrm{A}}'$, the electric field is simply removed. Due to the shift of the center of the hysteresis, the polarization change in Fig. 6.12 is bigger than the defect-free case. Hence, the temperature change is bigger. The electrocaloric effect may be further enhanced by small reversed field, and the consideration will be similar to the previous chapter. In the second range with $T_{\mathrm{A}}' < T < T_{\mathrm{C}}$, a modified loading history is applied. Conventionally, as shown in the hysteresis with $T = 0.7$, the field is removed to be zero (see the black dot on the left). However, in this conventional cycle, the polarization changes the sign totally. ΔS_{dip} decreases due to the cancellation of the square of the polarization (referring to Eq. 6.4). And the electrocaloric cooling is degenerated. Due to this apparent drawback, a modified cycle is utilized. Instead of removing the field to be zero (see the black dot on the left), the field is partly removed to fulfill that the polarization to be zero (see the red dot). Through this modification, ΔS_{dip} is larger than that in the conventional cycle. Meanwhile, the negative work loss, i.e., $\Delta S_{\mathrm{total}}$, is considerably large, which contributes additionally to the decrease of the vibrational entropy as a superposition effect. As a consequence of the large polarization change and the considerable negative work loss, in parts of the second range the electrocaloric cooling effect proves to be stronger than in the case without defects. In the

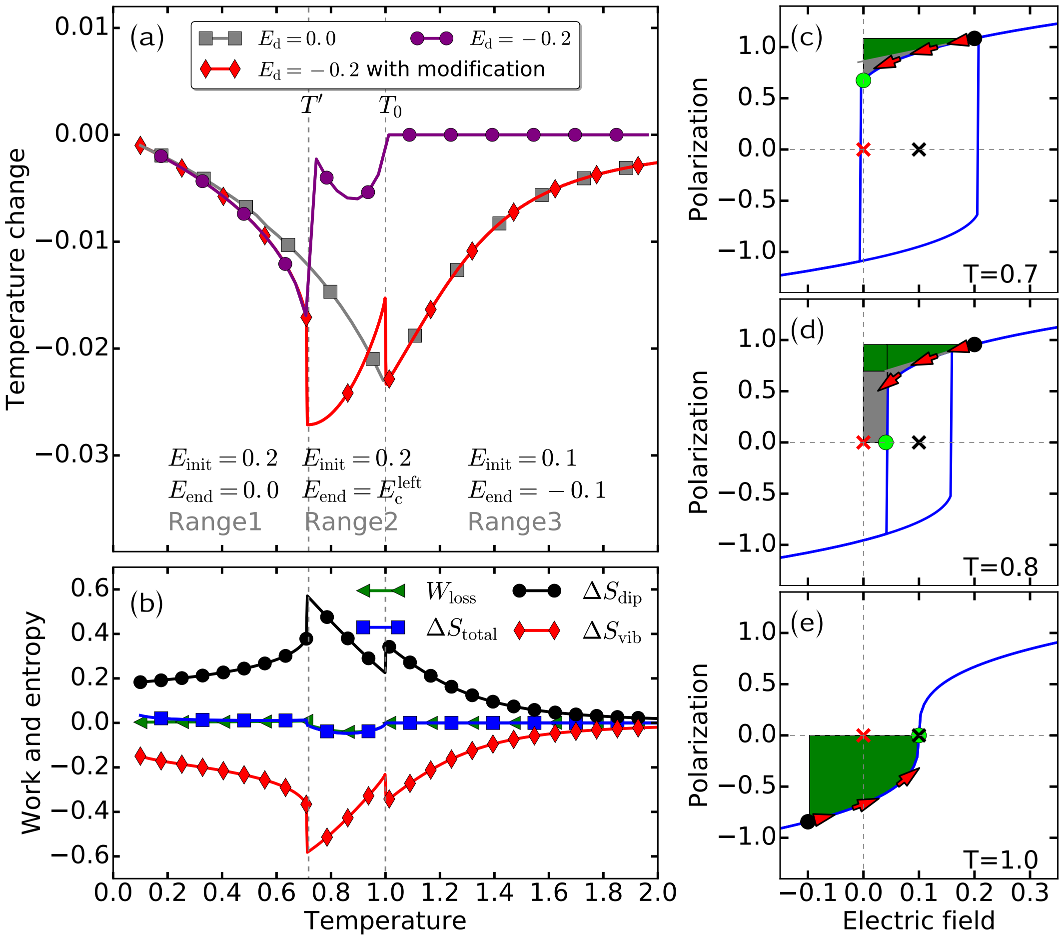

FIGURE 6.12 *Modified electrocaloric cycle. Different loading paths are applied in three ranges with* $T < T_A^{'}$, $T_A^{'} < T < T_C$ *and* $T > T_C$, *respectively. In the first range, the electric field is fully removed to be 0, which is the same as in Fig. 6.10. In the second range, the loading path is modified, and the electrocaloric cooling can be improved in part of this range. As shown in the hysteresis for* $T = 0.5$, *instead of removing the field fully (see the left black dot), the field is partly removed to fulfill that the polarization to be zero (see the red dot). Through this modification, the increase of the dipolar entropy is larger than the way in Fig. 6.10. Simultaneously, there appears considerable negative work loss, which contribute additionally to the temperature decrease. In the third range, the electric field changes from* $E_{init} = -0.3$ *to* $E_{end} = 0.3$. *Through this way, the same change of polarization as in the defect-free case can be obtained, which leads to the same temperature drop as well.*

third range with $T > T_C$, the process is reversible with $\Delta S_{total} = 0$. Hence, the only contribution to ΔS_{vib} is ΔS_{dip}, i.e., the polarization change. In the conventional cycle, if $E_{init} = 0.2 = |E_d|$, the magnitude of the polarization is the same before and after removing the field, but the sign is opposite. There will be no temperature change. Therefore, in this third range, the cycle should be modified as well. Hereby, in the modified cycle, a reversed field $E_{init} = -0.1$ is firstly applied so that the magnitude of the initial polarization is big, and the system is in a highly ordered state. Then a positive field $E_{end} = 0.1$ is applied so that the polarization becomes zero, and the system is in a highly disordered state. Through this modification, ΔS_{dip}, ΔS_{vib}, and the temperature change are the same as in the case without defects.

6.2 Latticed-based Monte-Carlo Simulation

In the previous section, using the analytical model, the influence of fixed defect dipoles on the electrocaloric effect was investigated. In this section, the influence of defect dipoles on the electrocaloric effect in acceptor doped $BaTiO_3$ is further studied by means of lattice-based Monte-Carlo simulations using a Ginzburg-Landau type effective Hamiltonian. Comparing with the analytical model, this approach preserves more physically related energy terms, and reveals the underlying mechanism on the microscopic domain structure level. Oxygen vacancy-acceptor associates are described by fixed local dipoles with orientation parallel or anti-parallel to the external field.

For the sake of completeness the model and the simulation setup are shortly described in Sec. 6.2.1. In Sec. 6.2.2 and Sec. 6.2.3 the influence of different arrangements of defect dipoles on the electrocaloric effect was investigated via Monte-Carlo simulations, for field-on and field-off case, respectively. Results show that the electrocaloric effect at high temperature can be increased in the presence of defect dipoles oriented parallel to the external field (parallel defect dipoles). An inverse electrocaloric effect and a double-peak behavior can be induced by defect dipoles which are anti-parallel to the external field (anti-parallel defect dipoles).

In order to show that the obtained abnormal features are physical and independent of the simulation methods, in Sec. 6.2.4 the Monte-Carlo simulation results are compared with the corresponding results of Molecular-Dynamics simulations. It proves that even though the Molecular-Dynamics model includes strain coupling and the Monte-Carlo model does not, the obtained results show good qualitative agreement. In Sec. 6.2.5 strategies to tailor the electrocaloric effect cycle by defect engineering are discussed. By additionally applying a reversed electric field during cooling an enhanced temperature drop is observed.

6.2.1 Model and Simulation Setup

The impact of fixed parallel and anti-parallel defect dipoles on the electrocaloric effect are investigated by directly calculating the adiabatic temperature change in lattice-based Monte-Carlo simulations with a box size of 63×63 (two-dimensional) and periodic boundaries. defect dipoles are introduced as fixed non-switchable polarizations on certain lattice sites and are shown in Fig. 6.17(a). Defect dipoles with different orientations are investigated, namely pointing parallel to $\mathbf{E}^{\text{ex}}$ and anti-parallel to $\mathbf{E}^{\text{ex}}$. The local polarization of defect dipoles [196] is approximated as $P_{\text{D}} = ql/V_0$, where the charge of the neutral defect dipole in $BaTiO_3$ is $q = +2e$, l is half of the lattice constant l_0 and V_0 is the lattice volume. Therefore, the local polarization for the defects is assumed as $1.0\,\mathrm{C\,m^{-2}}$. Defect dipoles generate internal electric and strain fields, and especially the internal electrical field $\mathbf{E}_\mathrm{i}$ has a large impact on the accessible dipolar (configurational) entropy S_conf.

The reason for aging in poled materials is due to the alignment of defect dipoles along the external field over time [80]. Since the orientation of defect dipoles follows the spontaneous polarization on time scales of days to months depending on temperature [73], we make the simplifying assumption of a static dipole orientation. This is reasonable since a typical electrocaloric effect cycle is operating on time scales of seconds or below. Experimentally, defect dipoles with unidirectional orientation can be introduced, for example, by a long-time poling process [93, 197]. Samples with rather large defect concentrations can be synthesized, e.g., $\mathrm{Ba(Ti_{0.93}Fe_{0.07})O_3}$ [198] and $\mathrm{Ba(Ti_{0.95}Mn_{0.05})O_3}$ [199] thin films. Accordingly, defect concentrations up to 6% were considered in our simulations.

As elaborated in Sec. 4.2 the potential energy H is described by a Ginzburg-Landau type expression which includes four contributions, i.e., $H = H_\mathrm{D} + H_\mathrm{dip} + H_\mathrm{gr} + H_\mathrm{e}$. During one Monte-Carlo step all lattice sites are visited in a random order and the polarization switching is allowed according to the Metropolis Monte-Carlo scheme. The change of the temperature is calculated via the modified Creutz algorithm, as it is explained in Sec. 4.3. The used parameters for simulating $\mathrm{BaTiO_3}$ are identical to those shown in Sec. 4.4.

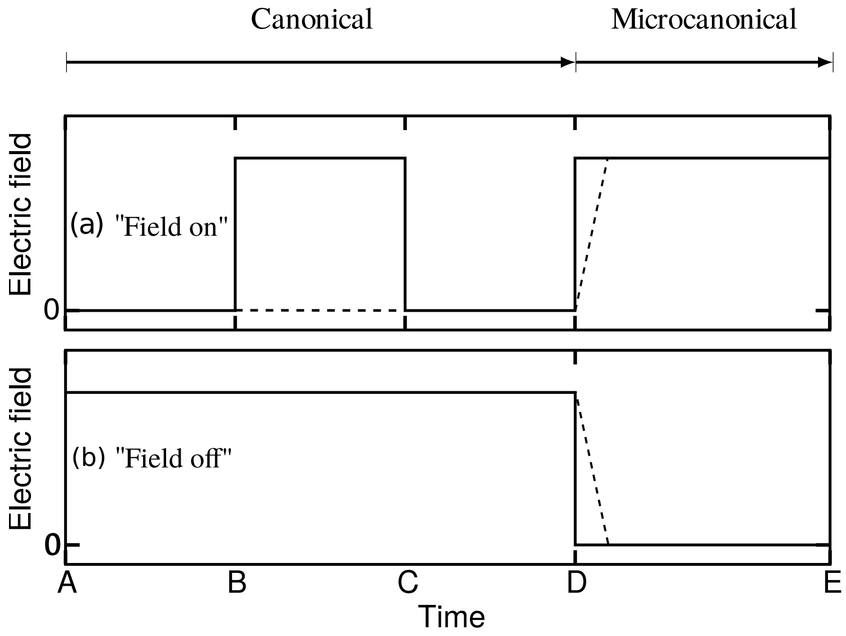

Figure 6.13 *Loading history in the (a) "Field off" and (b) "Field on" case for a Monte-Carlo (full line) and a Molecular-Dynamics (dashed line) simulation. Prepoling is neglected in the "Field on" case in the Molecular-Dynamics simulations, because at high defect concentrations the prepoled and unpoled sample are very similar. In the Monte-Carlo simulations the field is switched on or off instantaneously and in the Molecular-Dynamics simulations it is ramped.*

The electrocaloric effect temperature change can be obtained either by removing an external field ("Field off") or by switching the electrical field on ("Field on"), see Fig. 6.13. In both cases the system is equilibrated at a fixed temperature and fixed electrical field in the canonical ensemble. After the adiabatic removal or application of the electrical field the temperature change is calculated in a microcanonical ensemble.

The loading history for Monte-Carlo simulations is sketched by the solid lines in Fig. 6.13. For the "Field on" case prepoling is needed for samples with small internal fields (low defect concentration, weak defect dipoles) to avoid a non-collinear alignment between the external field and the local domains. For this purpose the external field is switched on and off with two additional equilibration runs, as can be seen in Fig. 6.13(a). For the "field off" case, the electric field is switched off instantaneously, as can be seen in Fig. 6.13(b).

6.2.2 Abnormal Electrocaloric Effect of the "Field On" Case

In the following, we discuss the influence of defect dipoles aligned parallel and anti-parallel to the external field within the Monte-Carlo simulations for the "field on" case.

The influence of the concentration of parallel defect dipoles on the electrocaloric effect is illustrated in Fig. 6.14(a). For pure $BaTiO_3$ the maximum $\Delta T/E$ is 5.7×10^{-7} K m/V which is comparable with the experimental result by Moya *et al.* [193] (8.3×10^{-7} K m/V). With increasing defect concentration, the ΔT peak decreases, and the maximum shifts to higher temperatures, due to the fact that the internal fields induced by defect dipoles stabilize the tetragonal phase. However, the interesting feature shown in Fig. 6.14(a) is that for initial temperatures above T_C samples containing parallel defect dipoles exhibit a larger temperature change than the defect-free sample. In addition, the obtainable electrocaloric effect is enhanced when $\mathbf{E}^{\text{ex}}$ is increased (see Fig. 6.14(b)) since a higher $\mathbf{E}^{\text{ex}}$ can increase the order of the system. Similar results have been reported by Rose and Cohen in crystals without defects [39]. It can be concluded that the electrocaloric effect can be enhanced either by application of higher fields or by incorporation of parallel defect dipoles.

For clarification of the observed effects, we investigate the domain configurations at different stages of the electrocaloric cycle. First, we concentrate on the maximum electrocaloric effect without defects, see point I in Fig. 6.14(a). The prepoled sample is in a multi-domain state with high dipolar entropy (Fig. 6.15(a)). It can clearly be seen that, when a field is applied, the number of domains decreases (Fig. 6.15(b)), which reduces the dipolar entropy and therefore the temperature is increased under adiabatic conditions.

If we now compare with the case, where defect dipoles in parallel orientation to $\mathbf{E}^{\text{ex}}$ are present, the situation changes (see point II in Fig. 6.14(a) and Fig. 6.15(c) and (d)). In the initial state the configurational space is reduced as compared to the defect free sample (see Fig. 6.15(a) and (b)), since defect dipoles induce internal fields that locally stabilize the domain structure

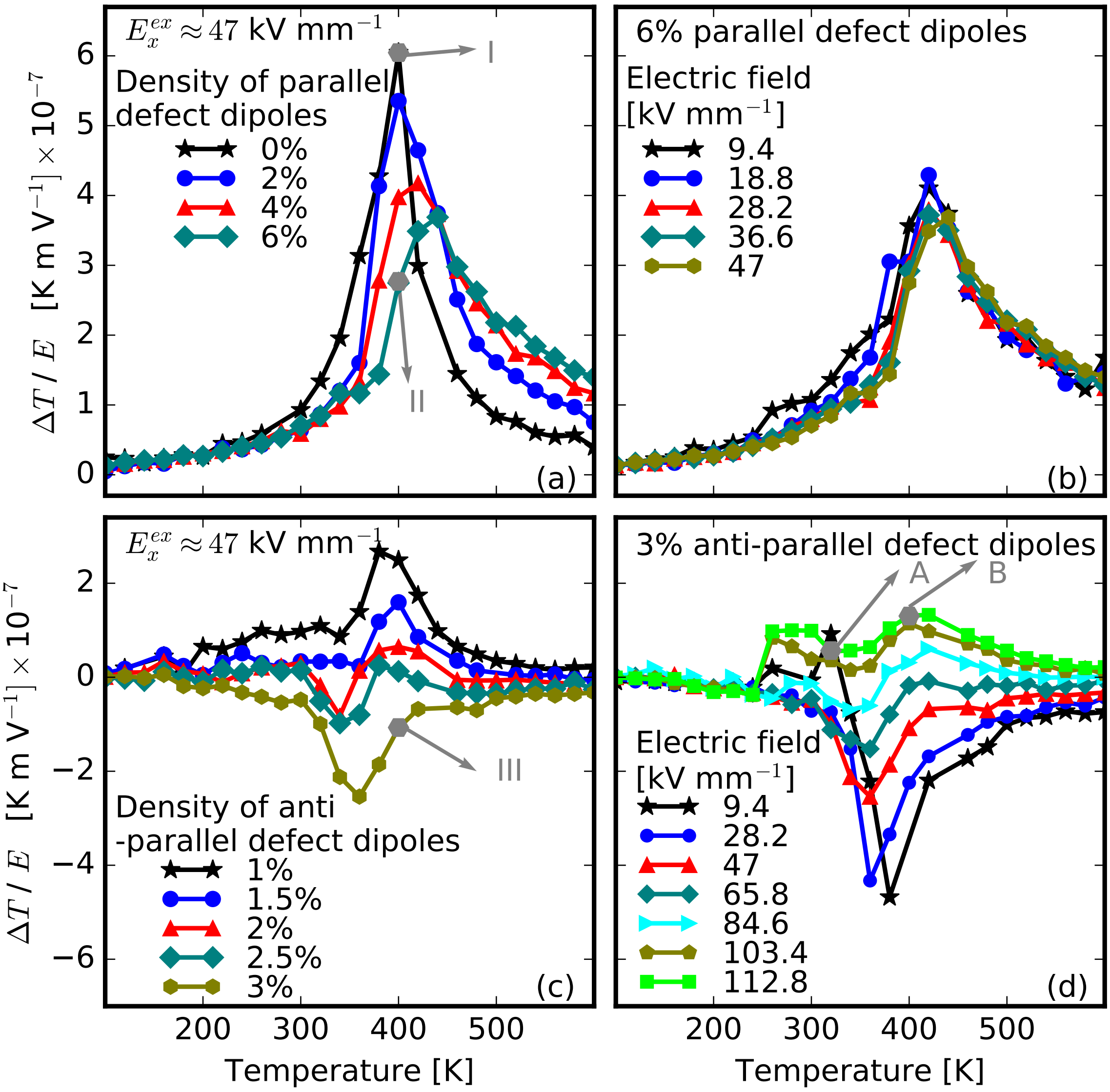

Figure 6.14 *Positive and inverse electrocaloric effect studied via Monte-Carlo for the "field on" case. (a) electrocaloric effect in the presence of parallel aligned defect dipoles. Different defect concentrations are considered under a given external field* $\mathbf{E}^{\mathrm{ex}}$*. (b) electrocaloric effect as a function of* $\mathbf{E}^{\mathrm{ex}}$ *for a defect concentration of 6%. (c) Positive and inverse electrocaloric effect in presence of anti-parallel dipoles. When the defect density exceeds a critical value, the resultant internal anti-parallel field overcomes* $\mathbf{E}^{\mathrm{ex}}$ *and a negative temperature change is observed (inverse electrocaloric effect). (d) Influence of* $\mathbf{E}^{\mathrm{ex}}$*, while anti-parallel defect dipoles with a concentration of 3% are present. When* $\mathbf{E}^{\mathrm{ex}}$ *surpasses the internal field-induced by the anti-parallel defect dipoles, an inverse electrocaloric effect appears only at lower temperatures, while a conventional electrocaloric effect dominates at higher temperatures, see the olive line (84.6 kV mm*$^{-1}$*). The above phenomena are explained by the domain structures at the points I, II, III, A and B in Fig. 6.15.*

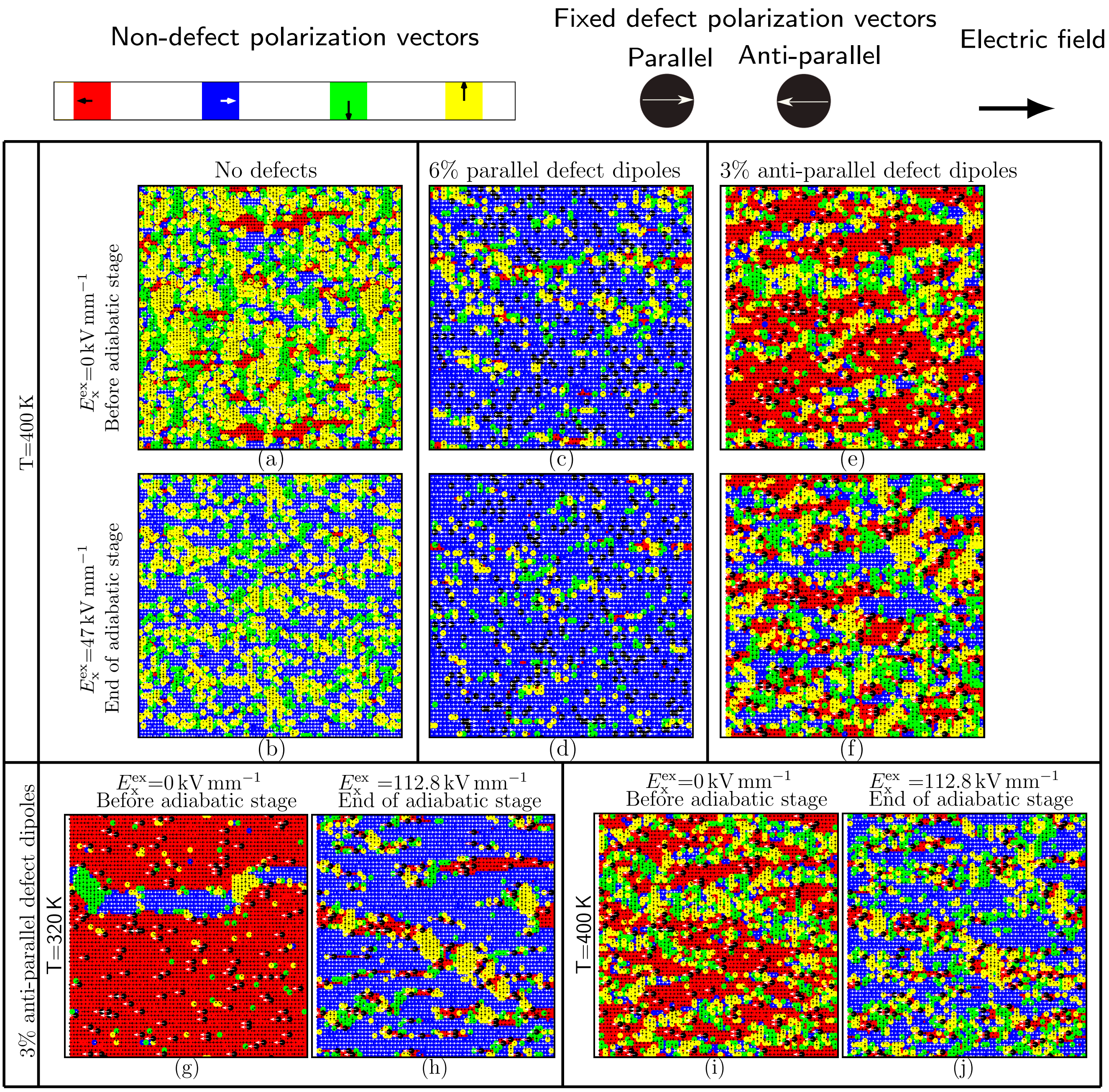

Figure 6.15 *Domain configurations at different points I, II, III, A and B marked in Fig. 6.14. The external field* $\mathbf{E}^{ex}$ *is applied in the horizontal direction and points to the right. (a) and (b) are the domain structure snapshots before and after the adiabatic stage for point I; (c) and (d) for point II; (e) and (f) for point III; (g) and (h) for point A; (i) and (j) for point B. The black dots with white arrows represent defect dipoles which are either parallel or anti-parallel to* $\mathbf{E}^{ex}$*. The red, blue, green and yellow dots represent the dipoles pointing to the left, to the right, to the bottom and to the top, respectively.*

against thermal fluctuations. If $\mathbf{E}^{\mathrm{ex}}$ is now switched on, the change in dipolar entropy S_{conf} is smaller than in the defect-free case and thus a weaker temperature variation is possible which explains the dependence of the electrocaloric effect on the defect concentration. In contrast to the low temperature range, at higher temperatures the electrocaloric effect is elevated by the existence of the parallel defects.

A different scenario occurs, if defect dipoles are pre-aligned in anti-parallel direction (Fig. 6.14(c)): a situation which can be created by poling the sample on extended time scales before reversing the field direction. For defect concentrations above 2% the electrocaloric effect turns from conventional to inverse and becomes more pronounced with increasing defect concentration. This can be explained again from the characteristic domain structure with 3% anti-parallel defect dipoles at point III in Fig. 6.14(c), shown in Fig. 6.15(e) and (f). Initially, the system is close to a single domain configuration with orientation parallel to defect dipoles and thus has a small S_{conf} because of the large average internal field of $\langle \mathbf{E}_{\mathrm{i}} \rangle = -87.2\,\mathrm{kV\,mm^{-1}}$. If now an external field of $\mathbf{E}^{\mathrm{ex}} = 47.0\,\mathrm{kV\,mm^{-1}}$ is switched on, the internal fields $\mathbf{E}_{\mathrm{i}}$ are partly compensated and the material can switch to a multi-domain configuration with increased S_{conf} (see Fig. 6.15(f)). Therefore, an inverse electrocaloric effect appears.

However, when the magnitude of $\mathbf{E}^{\mathrm{ex}}$ is comparable with that of $\mathbf{E}_{\mathrm{i}}$ both the conventional and inverse electrocaloric effect start to coexist (see Fig. 6.14(d)). For low fields, we observe mainly an inverse electrocaloric effect and for large fields a conventional electrocaloric effect. For large fields additionally a double peak behavior can be observed. This can be again explained by inspecting the domain structures for the case of a high field $\mathbf{E}^{\mathrm{ex}} = 112.8\,\mathrm{kV\,mm^{-1}}$ at point A and B in Fig. 6.14(d).

It can be seen that at point A with $T = 320\,\mathrm{K}$ in Fig. 6.15(g) and Fig. 6.15(h) the domain structure, and therefore S_{conf}, are similar. However, since the direction of the polarization changes entirely and a significant work loss ΔW_{work} occurs the total entropy increases from Fig. 6.15(g) to Fig. 6.15(h) because of the additional entropy term $\Delta S_{\mathrm{work}} = \Delta W_{\mathrm{work}}/T$. Accordingly, the vibrational entropy, i.e. the temperature, increases. At temperatures around 300 K, the work loss is larger and therefore the increase of the total entropy is bigger which leads to the first peak.

When the initial temperature is increased further, $\Delta T/E$ in Fig. 6.14(d) shows a second maximum (around 400 K under $112.8\,\mathrm{kV\,mm^{-1}}$). This second peak behavior can be attributed to a temperature induced ferroelectric to paraelectric phase transition in the initial state without a field. As can be seen from the domain configuration in Fig. 6.15(i) of point B in Fig. 6.14(d), only local domains have formed and the system has taken a multi-domain configuration in the initial prepoled sample. At this temperature the thermal fluctuations are strong enough to destroy the domains in the vicinity of the anti-parallel defect dipoles. Since the work loss decreases close to the phase transition and the change in the configuration entropy decreases the vibrational entropy goes up again. Thus, ΔT increases again. In short, at high initial temperatures no long-range order exist despite the dipole defects and the material behaves like a regular ferroelectric material.

6.2.3 Abnormal Electrocaloric Effect of the "Field Off" Case

Physically, it is also interesting to investigate the "field off" case, which mainly applies for the cooling effect in the conventional electrocaloric effect cycles. In this section, we investigate the "Field off" case at low and high electric fields with 3% anti-parallel defect dipoles, respectively.

For the “Field off" case under a weak field the electrocaloric effect curve obtained by Monte-Carlo simulations shows an inverse electrocaloric effect with a single peak as shown in Fig. 6.16(c). The underlying physics for this peak behavior has been explained in the discussion of Fig. 6.14(c) and (d).

For the “Field off" case under high fields the electrocaloric effect shows two extrema: at the maximum around 200-250 K we find an inverse electrocaloric effect and near the minimum at 400-450 K we find a conventional electrocaloric effect which is captured in the Monte-Carlo simulations (see Fig. 6.16(e).

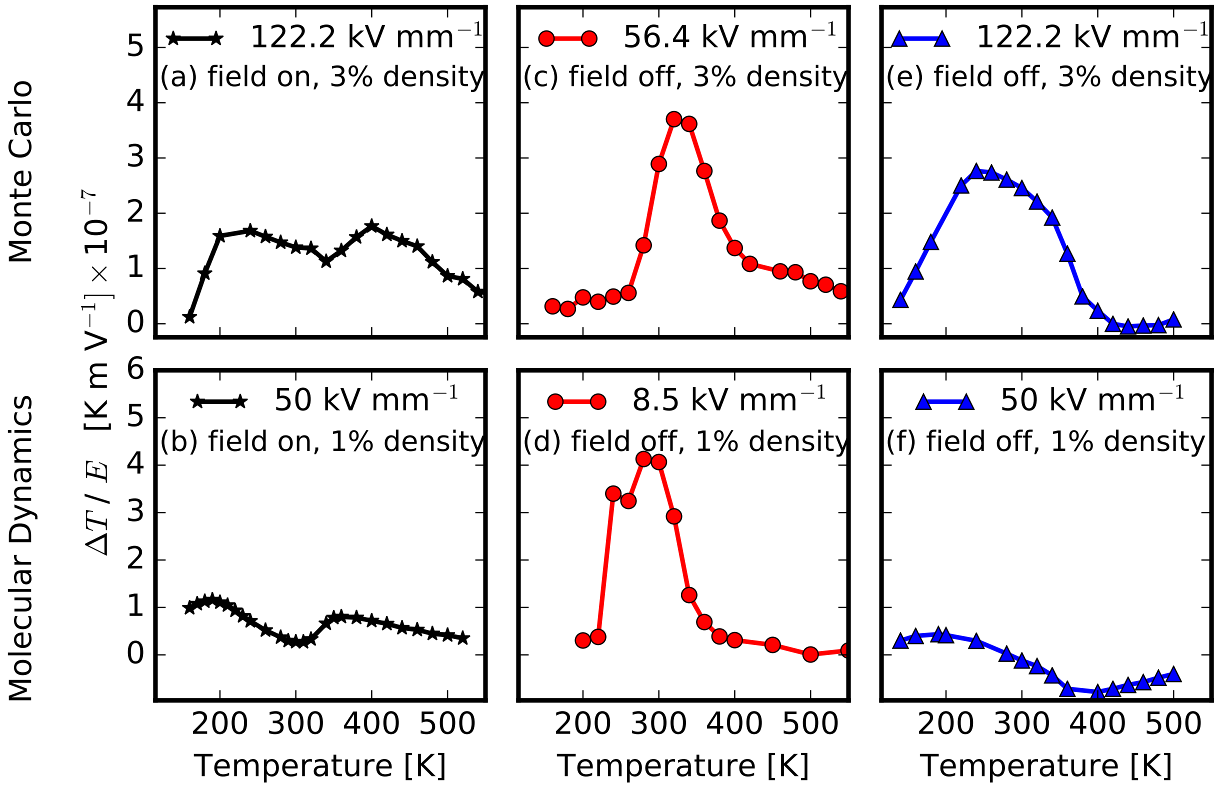

FIGURE 6.16 *Comparison of $\Delta T/E$ over T obtained from the Monte-Carlo simulations with 3% anti-parallel defect dipoles (top row) with the results of Molecular-Dynamics simulations with 1% anti-parallel defect dipoles (bottom row). (a) and (b) are “Field on" cases, while (c), (d), (e) and (f) are “Field off" cases. A qualitative agreement between the Monte-Carlo and Molecular-Dynamics simulations is clearly visible.*

At the initial temperature around 200-250 K an electric field induces disorder in the system. When the field is removed the polarization aligns with the defects and thus the entropy decreases and the temperature increases.

The minimum in $\Delta T/E$ around 400 K is the conventional electrocaloric effect and appears at the ferroelectric-paraelectric phase transition for the defect doped material because thermal fluctuations destroy the domains of the initial state when no field is applied.

6.2.4 Comparison with Molecular-Dynamics Results

The Monte-Carlo simulations are two-dimensional and has no strain coupling. In order to verify that the abnormal electrocaloric features presented in the last two subsections are physical and independent from the simulation methods and the model simplification, corresponding results by 3D Molecular-Dynamics simulations with full strain coupling are compared here.

The Molecular-Dynamics simulations were implemented by Dr. Anna Grünebohm in University of Duisburg-Essen and Kai-Christian Meyer in Technische Universität Darmstadt. Molecular-Dynamics simulations were performed deploying the feram code [126] (http://loto.sourceforge.net/feram/), based on an effective Hamiltonian,

$$\begin{aligned} H^{\text{eff}} = {} & \frac{M^*_{\text{dipole}}}{2} \sum_{\boldsymbol{R},\alpha} \dot{u}^2_\alpha(\boldsymbol{R}) + \frac{M^*_{\text{acoustic}}}{2} \sum_{\boldsymbol{R},\alpha} \dot{w}^2_\alpha(\boldsymbol{R}) + V^{\text{self}}(\{\boldsymbol{u}\}) + V^{\text{dpl}}(\{\boldsymbol{u}\}) + V^{\text{short}}(\{\boldsymbol{u}\}) \\ & + V^{\text{elas, homo}}(\eta_1, \ldots, \eta_6) + V^{\text{elas, inho}}(\{\boldsymbol{w}\}) + V^{\text{coup, homo}}(\{\boldsymbol{u}\}, \eta_1, \cdots, \eta_6) + V^{\text{coup, inho}}(\{\boldsymbol{u}\}, \{\boldsymbol{w}\}), \end{aligned}$$

with $\boldsymbol{u}$ being the local ferroelectric displacement vector and $\boldsymbol{w}$ the local acoustic displacement vector. This Hamiltonian includes the self energy of the ferroelectric soft mode, the long- and short-range dipole-dipole interaction energy, the elastic energy and the energy due to the coupling between the local soft modes and the strain. Details can be found in Refs. [126, 159, 160]. Only the three degrees of freedom of the polarization vector $\boldsymbol{u}$ are explicitly taken into account (the acoustic strain is optimized for each step, but not used as degree of freedom). Thus, the specific heat is reduced by a factor of 3/15 (actual number of degrees of freedom divided by the total degrees of freedom in a single $BaTiO_3$ unit cell). As the electrocaloric temperature change $\Delta T \sim T\Delta S_{\text{vib}}/c$ is inversely proportional to the specific heat c, the adiabatic temperature change, which is recorded from the kinetic energy averaged over space and time, is overestimated in Molecular-Dynamics simulations, where S_{vib} is the vibrational entropy [200]. Thereby, ΔT is rescaled according to the discussion given in Ref. [38]. Periodic boundary conditions and a 3D cell size of 38.4 nm×38.4 nm×38.4 nm (96×96×96 sites) are used, with a time step of $\Delta t = 1$ fs. For simulations in the canonical ensemble (NPT) the Nosé-Poincaré thermostat is applied [201]. Defects are modeled by freezing the local soft mode on random positions to approximately $0.5\,\text{C}\,\text{m}^{-2}$. In the following a defect concentration of 1% is used and the arrange-

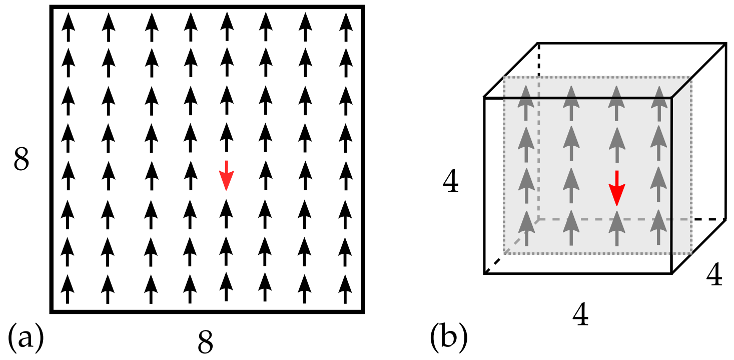

Figure 6.17 *Visualization of a simulation box with a fixed defect dipole (red) in the (a) 2D Monte-Carlo case and (b) 3D Molecular-Dynamics case (only one layer shown). Both simulations boxes have different sizes (8x8 and 4x4x4, respectively), but same concentrations (1/64). As can be seen, the distances between defect dipoles for the Monte-Carlo case are larger than for the Molecular-Dynamics case.*

ment is depicted in Fig. 6.17(b). For higher defect concentrations the prepoling is omitted in the Molecular-Dynamics runs. A ramping rate of 10^{-4} kV mm^{-1}fs^{-1} is used in Molecular-Dynamics. Although these switching rates are very fast compared to real switching time scales the results are in good qualitative agreement with slower switching rates [187].

A few differences can be noted between the Monte-Carlo and Molecular-Dynamics models. The first difference between the Monte-Carlo and Molecular-Dynamics models is that the coupling of the polarizations to the elastic strain is not considered directly in the Monte-Carlo simulations. In order to investigate the influence of this simplification on the obtained electrocaloric effect Molecular-Dynamics simulations (which include the strain coupling) are performed for comparison. Another important difference between the models lies in the dimensions. The lattice of the Monte-Carlo model is only 2D and in the Molecular-Dynamics model the lattice extends over 3D. Therefore, for a certain defect concentration (percentage of sites occupied by defects), the mean distance between defect dipoles in the Monte-Carlo simulation is larger than in the Molecular-Dynamics simulation (compare Fig. 6.17(a) and (b)). The effect of this difference can be seen when looking at the change of the total energy when a single defect dipole is introduced into aligned polarizations (red and gray arrows in Fig. 6.17). The change of the total energy in each case is small. However, the ratio of the total energy differences $\Delta E^{\mathrm{MD}}_{\mathrm{total}}/\Delta E^{\mathrm{MC}}_{\mathrm{total}}$ between Molecular-Dynamics and Monte-Carlo is about 400%. Thus, the influence of the defects is stronger in the Molecular-Dynamics model and therefore the concentration in the Molecular-Dynamics simulations has to be smaller as in the Monte-Carlo simulations. In addition, because of the different energy terms used in the Hamiltonians of the Monte-Carlo and Molecular-Dynamics models, the coupling of external field and dipoles is different. For this reason, the strength of the electric field and the polarization of the defect have to differ between the simulations of the Monte-Carlo and Molecular-Dynamics as well. It should also be noted that the phase transition from the ferroelectric to paraelectric state in Monte-Carlo lies around 400 K. However, with the effective Hamiltonian used for the Molecular-Dynamics simulations the ferroelectric-paraelectric phase transition temperature is systematically underestimated (300 K) compared to the 400 K found in experiment [126]. When large internal fields are present (high defect concentration, strong defect dipoles), the domains are oriented collinear to the external field and the prepoling can be neglected. By ramping the field and long equilibration times in the Molecular-Dynamics the system can overcome possible energy barriers due to domain switching.

In spite of these differences in methods, impressive agreements can be found in the electrocaloric results obtained from the Monte-Carlo and Molecular-Dynamics simulations.

Three scenarios are regarded to study the electrocaloric effect at different loading histories and field strengths to make sure that the Monte-Carlo and Molecular-Dynamics simulations are comparable for a broad range of applications. First, we determine ΔT in a "Field on" simulation at rather high field, which is similar to what we already studied in Sec. 6.2.2. Second and third, we investigate the "Field off" case at low and high electric fields like in Sec. 6.2.3, respectively. Like in the Monte-Carlo simulations, for the “Field on" case under a high field the Molecular-Dynamics simulations demonstrate a double-peak electrocaloric effect behavior with the same reason, as it is seen in Fig. 6.16(b). Simultaneously, for the “Field off" case under a weak field the electrocaloric effect curve obtained by Molecular-Dynamics simulations show an inverse electrocaloric effect with a single peak as shown in Fig. 6.16(d), which agrees with the Monte-Carlo result qualitatively as shown in Fig. 6.16(c) and the underlying physics for this peak behavior can be explained in the same fashion. For the “Field off" case for high fields, with the same mechanism as in Fig. 6.16(e), in Molecular-Dynamics simulations of Fig. 6.16(f) the electrocaloric effect shows two extrema; at the maximum around 200-250 K we find an inverse electrocaloric effect and near the minimum at 400-450 K.

In summary, the Monte-Carlo and Molecular-Dynamics simulations show similar abnormal electrocaloric features in all the three loading cases. Both Monte-Carlo and Molecular-Dynamics simulations reveal three important electrocaloric effect features: 1) double-peak electrocaloric effect for the “Field on" case under a high field, 2) single peak inverse electrocaloric effect for the “Field off" case under a weak field, 3) two extrema electrocaloric effect for the “Field off" case under high field. This agreement between the Monte-Carlo and Molecular-Dynamics results, despite of their difference in dimensionality and Hamiltonian, indicates strongly that the obtained abnormal electrocaloric effect behavior is an intrinsic property.

6.2.5 Defect Engineering for Electrocaloric Application

As an example to make use of the gained knowledge in the previous subsections for electrocaloric application, a strategy to tailor the electrocaloric effect by defect engineering is proposed. Fig. 6.14(a) indicates that at high temperature the samples with defect dipoles can generate a higher electrocaloric effect than those without defects under a parallel external field.

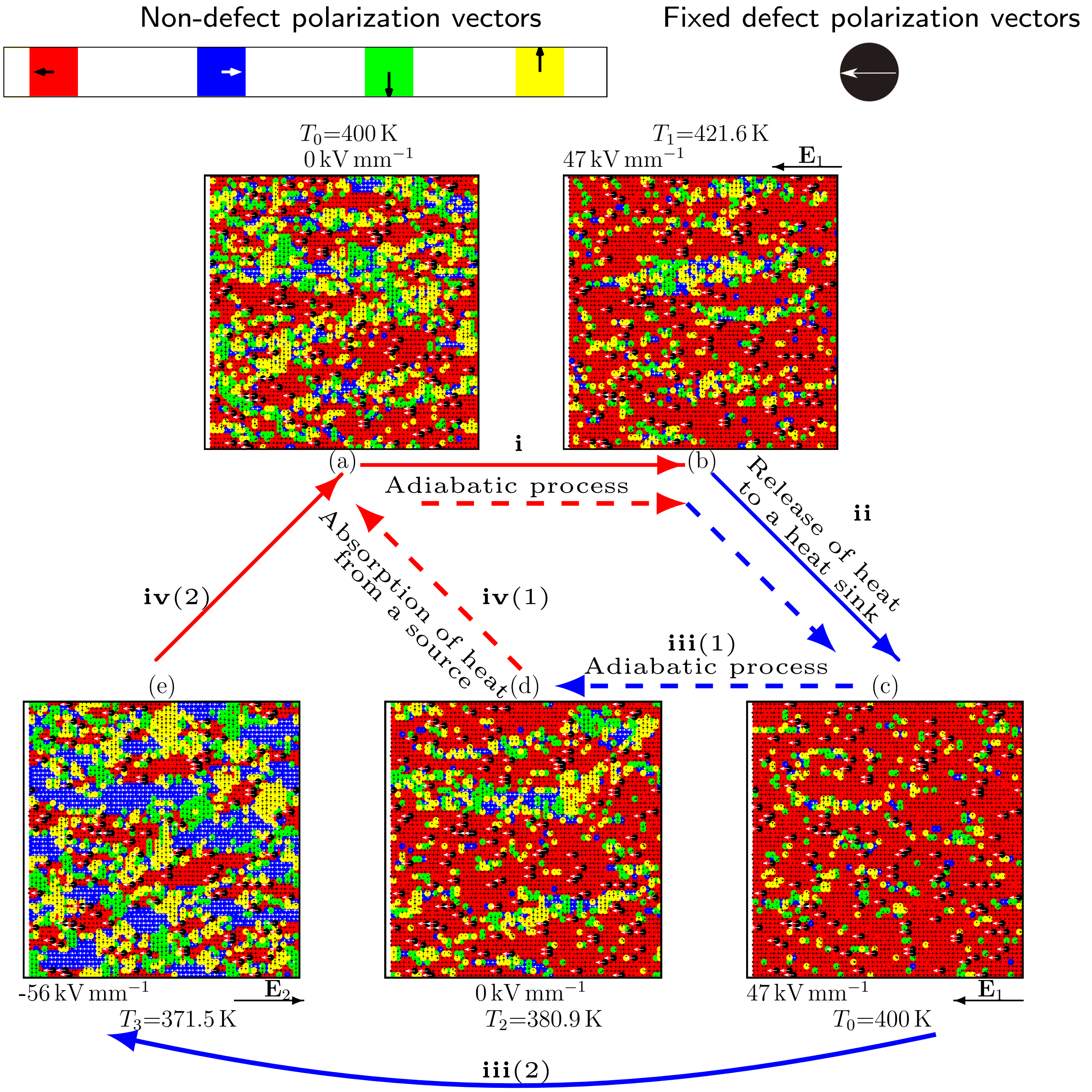

Figure 6.18 *Proposed modified electrocaloric effect cycle to enhance the resultant* ΔT *of a sample containing defect dipoles. The conventional cycle involves a-b-c-d-a (dashed arrows), and the new proposed one includes a-b-c-e-a (solid arrows). Under adiabatic condition a field is applied rapidly parallel to defect dipoles, taking the initial state (a) at* T_0 *to a state (b) with lower dipolar entropy at* T_1*. By transferring heat to a heat sink, the state (b) transforms to the state (c) with further lower dipolar entropy at* T_0*. Removing the field rapidly under adiabatic conditions, from state (c) the system is cooled to state (d) at* T_2*. By comparison, applying a field anti-parallel to defect dipoles the system is cooling further from state (c) to state (e) (*$T_3 < T_2$*). It should be noted that the magnitude of the external field should not be greater than the magnitude of the average internal field-induced by defect dipoles. Finally, by absorbing heat from a load, the system warms up to the state (a). The relation of the involved temperatures can be summarized as* $T_3 < T_2 < T_0 < T_1$*. It can seen be that by introduction of defect dipoles an enhancement of the electrocaloric cooling is achieved.*

For example, the temperature change at 460 K for the sample with 2% parallel defect dipoles is 12.1 K while only 7.2 K for the sample without defects. In other words, the parallel defect dipoles have a potential for high temperature applications. More importantly, the design of a novel electrocaloric cycle can be stimulated by utilizing the conventional-inverse electrocaloric effect transition. As an example, we propose in the following a modified Carnot-like Cycle with a reversed external field which provides the possibility to improve the cooling efficiency of the electrocaloric device. A cycle with 3% defect dipoles at an initial temperature $T_0 = 400\,\mathrm{K}$ is illustrated in Fig. 6.18. In the classical concept the electrocaloric effect cycle [5] includes four states “a-b-c-d-a" (see dashed arrows), while the new concept contains the route ’a-b-c-e-a’ (see solid arrows). Compared with the state (d), the new state (e) involves a reversed electric field which induces a further temperature drop due to the inverse electrocaloric effect indicated in Fig. 6.14(d).

The red and blue arrows represent the heating and cooling processes, respectively. Process **i** is an adiabatic process from state (a) with $T_0 = 400\,\mathrm{K}$ to (b) with $T_1 = 421.6\,\mathrm{K}$ which decreases the dipolar entropy and increases the temperature by applying the field $\mathbf{E_1}$. Hereby $\mathbf{E_1}$ is parallel to defect dipoles. **ii** is a process from stage (b) to (c) with $T_0 = 400\,\mathrm{K}$, in which the temperature decreases by releasing the heat to a heat sink. Process **iii**(1) from state (c) to (d) with $T_2 = 380.9\,\mathrm{K}$ and **iii**(2) from state (c) to (e) with $T_3 = 371.5\,\mathrm{K}$ are both adiabatic processes. In process **iii**(1) the dipolar entropy increases by removal of a field while in process **iii**(2) by application of a reversed field $\mathbf{E_2}$. Namely, the direction of $\mathbf{E_2}$ is opposite to $\mathbf{E_1}$. By application of this reversed field the vibrational entropy decreases more than in process **iii**(1). The temperature drop in **iii**(2) is 28.5 K, which is higher than 19.1 K in **iii**(1). Process **iv**(1) from state (d) to (a) and **iv**(2) from state (e) to (a) are both processes, in which the temperature increases through adsorption of heat from a heat source. The example shows that the incorporation of defect dipoles and application of a reversed field can enhance the cooling effect by around 50%.

6.3 Summary

Through acceptor doping, dopants and the oxygen vacancies form associate defect dipoles with preferred orientation parallel to the spontaneous polarization. Since defect dipoles influence the domain evolution significantly, they affect the electrocaloric effect as well, which is investigated in this Chapter. The strategy of using defect engineering to enhance the electrocaloric effect is also explored. Here for simplicity, non-switchable defect dipoles are prescribed in the whole interested temperature range. In reality, it is true only at low temperatures due to the high activation barrier of oxygen vacancy migration. On contrary, defect dipoles are fairly mobile or even disappear at high temperatures.

In Sec. 6.1, an analytical model based on the entropy change calculation is utilized for the "field off" case in the presence of defect dipoles anti-parallel to the external field. In this analytical model the entropy change due to irreversible processes is considered as in Sec. 5.1. As an important characteristic temperature, $T_A^{'}$ represents the temperature where the coercive field at the left side is equal to zero. Below $T_A^{'}$, independent of the strength of the defect polarizations, the temperature change is always negative. For $T > T_A^{'}$, the defect polarizations influence the electrocaloric effect significantly. Different phenomena are observed, depending on competition of the external field and the defect-induced internal field. (1) When the external field is much weaker than the internal field, only the inverse electrocaloric effect persists (see Fig. 6.8). (2) When the external field is moderately weaker than the internal field, the conventional and inverse electrocaloric effects (heating after removing the field) coexist (see Fig. 6.9). (3) When the external field is stronger than the defect-induced internal field, there exists the conventional electrocaloric effect, i.e., electrocaloric cooling after removing the field (see Fig. 6.10). Based on the obtained knowledge, distinctive strategies are posed to optimize the electrocaloric effect for different temperature ranges (see Fig. 6.12). More specifically, (1) below $T_A^{'}$ the external field is fully removed, (2) between $T_A^{'}$ and T_C the electric field is partly removed to promise the final polarization to be zero with maximum polarization disordering, and (3) above T_C an initial negative field and a final positive field are given to promise a big polarization disordering.

In Sec. 6.2, lattice-based Monte-Carlo simulations developed in Chap. 4 are utilized to reveal the mechanism on the domain structure level. Additionally, for comparison, Molecular-Dynamics simulations with an effective Hamiltonian are performed by our cooperators. Our results by Monte-Carlo simulations (see Fig. 6.14) show that the incorporation of defects parallel to the external field shifts the peak of the electrocaloric effect to higher temperatures but decreases the achievable temperature change. In the presence of anti-parallel defect dipoles the sign of the electrocaloric effect varies from conventional to inverse when increasing the density of defect dipoles. Moreover, a transition from the inverse to conventional electrocaloric effect can be observed at a given density of anti-parallel dipoles when the external field increases. More specifically, in presence of strong defect dipoles for the "field on" case, there are (1) the inverse electrocaloric effect under weak external fields, (2) the coexistence of the conventional and inverse electrocaloric effects under moderate external fields, and (3) the double peak behavior under strong fields. For the "field off" case, there are (1) the inverse electrocaloric effect under weak external fields, and (2) the coexistence of the conventional and inverse electrocaloric effects under strong external fields. These transitions can be interpreted by the delicate interplay between the internal and external fields, and are explained by the domain structure evolution. The results are compared to those obtained by Molecular-Dynamics simulations employing an ab initio based effective Hamiltonian, which shows a qualitative agreement (see Fig. 6.16). Finally the inverse electrocaloric effect in the presence of defect dipoles is utilized to modify the electrocaloric cycle, and a significant enhancement of the electrocaloric effect can be achieved.

In short, the results from the analytical solution, the lattice-based Monte-Carlo simulations and the Molecular-Dynamics show the transition from the conventional to inverse electrocaloric effect due to the competition of defect-induced internal fields and external fields. This can be utilized to modify the electrocaloric cycling and to enhance the electrocaloric effect.

Chapter 7

State Transition and Electrocaloric Effect of Relaxors: $BaZr_xTi_{1-x}O_3$

This Chapter is based on the publication "Y.-B. Ma, C. Molin, V. V. Shvartsman, S. Gebhardt, D. C. Lupascu, K. Albe, and B.-X. Xu, J. Appl. Phys. 121, 024103 (2017)".

As one of the most simple relaxors and environment-friendly electrocaloric effect materials, the solid solution system $BaZr_xTi_{1-x}O_3$ has attracted great interest [139,145]. Many experimental observations suggest that $BaZr_xTi_{1-x}O_3$ is a promising candidate for electrocaloric cooling. However, the origin of the electrocaloric effect in $BaZr_xTi_{1-x}O_3$ is still not fully understood, since the related relaxor behavior and state transition in $BaZr_xTi_{1-x}O_3$ is still under debate even though a number of experimental [105,109,129–140] and theoretical investigations [141–144] have been done, as it has been reviewed in Secs 2.3. In this chapter, a systematic study is implemented on the relation of the electrocaloric effect and the relaxor state transition of $BaZr_xTi_{1-x}O_3$ using Monte-Carlo simulations in comparison with experiments.

The basic model presented in Chap 4 is modified for the solid solution system $BaZr_xTi_{1-x}O_3$ in Sec. 7.1, particularly by taking multi-well or single well Landau potentials for Ti or Zr sites and a composition-dependent dipole-dipole interaction strength into account.

7.1 Modification to Effective Halmiltonian

For the Monte-Carlo simulations of $BaZr_xTi_{1-x}O_3$, lattices with corresponding sites of Zr cells and Ti cells are generated, depending on the Zr concentration. For the energy calculation, the Ginzburg-Landau type effective Hamiltonian for $BaTiO_3$ presented before is revised. In particular, different ground state Landau-type terms are introduced for unit cells containing Zr or Ti. A multi-well Landau term is used for describing Ti displacements, while a single-well Landau term is applied for modeling Zr-containing unit cells. Moreover, the dipole-dipole interaction term becomes also dependent on the nature of the two involved dipoles. This aspect is considered in the model by adjusting the high-frequency permittivity parameters in the dipole-dipole energy.

The static ground state energy H_D for a 2-dimensional system can be expressed as

$$H_D = \quad V_0 \sum_i \left[\frac{a_i}{2} \left[P_x^2(\mathbf{r}_i) + P_y^2(\mathbf{r}_i) \right] \right.$$

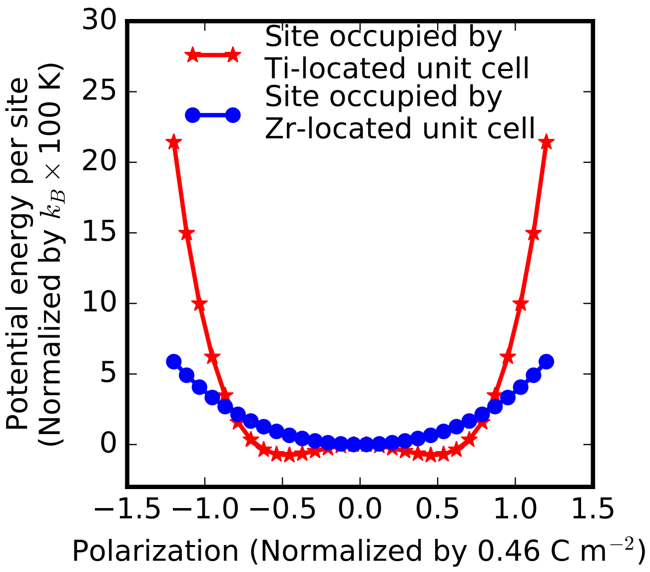

Figure 7.1 *A multi-well Landau-type term is applied for the sites occupied by Ti-containing unit cells, and a single well type for Zr-containing unit cells.*

$$+ \quad \frac{b_i}{4}\left[P_x^4(\mathbf{r}_i)+P_y^4(\mathbf{r}_i)\right]+\frac{c_i}{6}\left[P_x^6(\mathbf{r}_i)+P_y^6(\mathbf{r}_i)\right]\Bigg], \tag{7.1}$$

where $V_0 = l_0^3$ is the volume per site with l_0 being the lattice constant. The parameters a_i, b_i, c_i are material-dependent coefficients, $\mathbf{r}_i$ is the coordinate of site i, and $P_x(\mathbf{r}_i)$, $P_y(\mathbf{r}_i)$ are the Cartesian components of the polarization vector $\mathbf{P}(\mathbf{r}_i)$ at site i. It is assumed that the lattice constant $l_0 = 4$ Å is independent of the Zr content, since the lattice constants change insignificantly after Zr substitution.

$BaTiO_3$ is a ferroelectric material while $BaZrO_3$ is paraelectric. Therefore, for unit cells containing Ti, H_D is interpreted as a Ginzburg-Landau multi-well energy term, while a single-well energy term is used when Zr-ions occupy the B-site. This concept for the site dependent Landau-type term is illustrated in Fig. 7.1. Based on first-principles results with zero strain and soft-mode eigenmode amplitudes [159], only, the necessary coefficients can be obtained for an expansion in fourth order: $a_i = -13.7128 \times 10^8\,\mathrm{J\,m\,C^{-2}}$, $b_i = 28.908 \times 10^9\,\mathrm{J\,m^5\ C^{-4}}$ for Ti-located unit cells; $a_i = 6.112 \times 10^8\,\mathrm{J\,m\,C^{-2}}$, $b_i = 1.4454 \times 10^9\,\mathrm{J\,m^5\ C^{-4}}$ for Zr-located unit cells.

The dipole-dipole interaction energy [60] is given by

$$\begin{aligned} H_{\mathrm{dip}} &= V_0^2\frac{1}{8\pi\epsilon_0}\sum_{i,j}\frac{1}{\epsilon_{ij}}\left[\frac{\mathbf{P}(\mathbf{r}_i)\cdot\mathbf{P}(\mathbf{r}_j)}{|\mathbf{r}_i-\mathbf{r}_j|^3}\right. \\ &- \left.\frac{3\left[\mathbf{P}(\mathbf{r}_i)\cdot(\mathbf{r}_i-\mathbf{r}_j)\right]\left[\mathbf{P}(\mathbf{r}_j)\cdot(\mathbf{r}_i-\mathbf{r}_j)\right]}{|\mathbf{r}_i-\mathbf{r}_j|^5}\right], \end{aligned} \tag{7.2}$$

where ϵ_0 is the vacuum permittivity. The high-frequency relative permittivity ϵ_{ij} depends on the Zr concentration. Different values for $BaTiO_3$ were given in literature, varying from 6 to

15 [153, 172, 173]. In the present paper, we choose $\epsilon_{ij} = 12$ for the case when both sites, i and j, are occupied by Ti-centered unit cells.

The relative permittivity of $BaZrO_3$ is chosen as $\epsilon_{ij} = 144$. While the value of high-frequency permittivity for $BaZrO_3$ reported from first-principles calculations [202] is close to the value of $BaTiO_3$. We use a higher permittivity for $BaZrO_3$ for the following reasons. Experiments [107, 136, 203] showed that the real part of permittivity becomes smaller with increasing Zr content in $BaZr_xTi_{1-x}O_3$. It is theoretically known that the decrease of high frequency permittivity leads to an increase of the real part. Thus, experimental results [107, 136, 203] indicate that higher permittivity values should be used for $BaZr_xTi_{1-x}O_3$ than for $BaTiO_3$. To ensure that $BaZrO_3$ becomes paraelectric, the high frequency permittivity of $BaZr_xTi_{1-x}O_3$ must adapt a sufficiently high value in our model. Since no additional data for the high permittivity of $BaZr_xTi_{1-x}O_3$ is available in literature, the composition-dependent permittivity of $BaZr_xTi_{1-x}O_3$ is simply approximated by the linear interpolation of the two ends, i.e., pure $BaTiO_3$ and $BaZrO_3$. In result, ϵ_{ij} is chosen as

$$\epsilon_{ij} = \begin{cases} 12 & \text{if i=Ti and j=Ti,} \\ 144 & \text{if i=Zr and j=Zr,} \\ 12(1-x) + 144x & \text{if (i=Zr and j=Ti)} \\ & \text{or if (i=Ti and j=Zr) ,} \end{cases} \tag{7.3}$$

where x is the Zr concentration in $BaZr_xTi_{1-x}O_3$. It should be noted that this concept of a concentration-dependent high-frequency permittivity is similar to the random-bond concept proposed by Pirc and Blinc [118].

Moreover, in the calculation of the gradient energy the associated polarizations on neighboring sites, either Zr or Ti cell, should be considered. The parameters for the domain wall energy is set to be the same as these for $BaTiO_3$. Since the size-difference between Ti^{4+} and Zr^{4+} is small, the related elastic energy and the electrostrictive interaction should be negligible. This simplification does not have a qualitative influence on the calculated entropy variations.

Other energy terms in the effective Hamiltonians, i.e. the electrostatic energy and the thermal energy term, and also the canonical and microcanonical algorithms remain the same as elaborated for $BaTiO_3$ in Chap 4.

7.2 Electrocaloric Effect

For the electrocaloric simulations, samples are first prepoled in an isothermal canonical assemble, before an external field of $E^{ex} = 47.0\text{kV mm}^{-1}$ is applied to the system in an adiabatic stage described by a microcanonical Monte-Carlo simulation. Details about the loading history and the algorithms can be found in Ref. [188].

The corresponding simulation result for $BaTiO_3$, $BaZr_{0.12}Ti_{0.88}O_3$ and $BaZr_{0.2}Ti_{0.8}O_3$ are shown in Fig. 7.2(b). It is noticeable that the peak of the temperature variation drops significantly. This change can be interpreted by the corresponding domain patterns. The domain pattern at each peak is shown in Fig. 7.3. In the initial state (the prepoled sample), the dipolar entropy S_{dip} is apparently higher in $BaTiO_3$ than in $BaZr_{0.12}Ti_{0.88}O_3$. Nonetheless, at the end of the adiabatic stage, the domain patterns are similar for both, $BaTiO_3$ and $BaZr_{0.12}Ti_{0.88}O_3$, and S_{dip} is comparable. In short, the variation of S_{dip}, i.e., the variation of the temperature, in $BaTiO_3$ is bigger than in $BaZr_{0.12}Ti_{0.88}O_3$. The sites occupied by Zr-centered unit cells are energetically unstable sites, and their neighbor sites become more fluctuating since mutual short- and long-interactions are present. Due to the long-range interaction, for compositions of $0.1 \leq x \leq 0.2$ the effective number of sites contributing to configurational variations increases more than linearly with increasing Zr-content, which signifies the sharp declination of the temperature variation. In short, with increasing Zr content, the peak is lowered and appears at lower temperature.

For comparison, experimental results on the electrocaloric effect in this subsection and the dielectric hysteresis in the next subsection of ceramics samples of $BaZr_xTi_{1-x}O_3$ with 0 mol%, 12 mol% and 20 mol% Zr content are used. The experiments were performed by Christian Molin and Dr. Sylvia Gebhardt in Fraunhofer Institute for Ceramic Technologies and Systems. The samples were synthesized using a mixed oxide route, and in the electrocaloric effect measurement sheath thermocouples were utilized. For hysteresis measurements, electrodes of silver conductive pastes were painted and fired at 800 °C for 20 min. The hysteresis loop measurements were carried out at 5 Hz, using a Sawyer Tower circuit with an analog input and digital I/O module (Measurement Computing, USB-1616HS-4). More details on the experimental background can be found in the publication [204].

The measured electrocaloric effect strength $\Delta T/\Delta E$, is plotted in Fig. 7.2(a). At the temperature where the tetragonal phase transforms to the cubic phase in $BaTiO_3$ (398.45 K), $BaZr_{0.12}Ti_{0.88}O_3$ (352.45 K) and $BaZr_{0.2}Ti_{0.8}O_3$ (316.19 K) or the orthorhombic phase transforms to the tetragonal phase in $BaTiO_3$ (295.9 K), the peaks appear. Figure 7.2(a) further demonstrates that with increasing Zr-content the peak drops quickly, and the peak shifts to lower temperature. Comparison between the simulated and experimental results in Fig. 7.2(a) and (b) shows a good qualitative agreement.

Nevertheless, there are notable discrepancies between the measured and calculated temperature changes and the applied electric field. These discrepancies can be explained as follows. Firstly, only one ΔT peak occurs in the simulation results for pure $BaTiO_3$ in Fig. 7.2(a), whereas the experimental data show two maxima. This is due to the fact that in the simulation only the transition from the tetragonal to the cubic phase is considered. Secondly, the samples used in the simulation don't contain defects and correspond to single crystalline thin film materials, while the samples in the measurements are polycrystalline ceramics. Hence, the applied

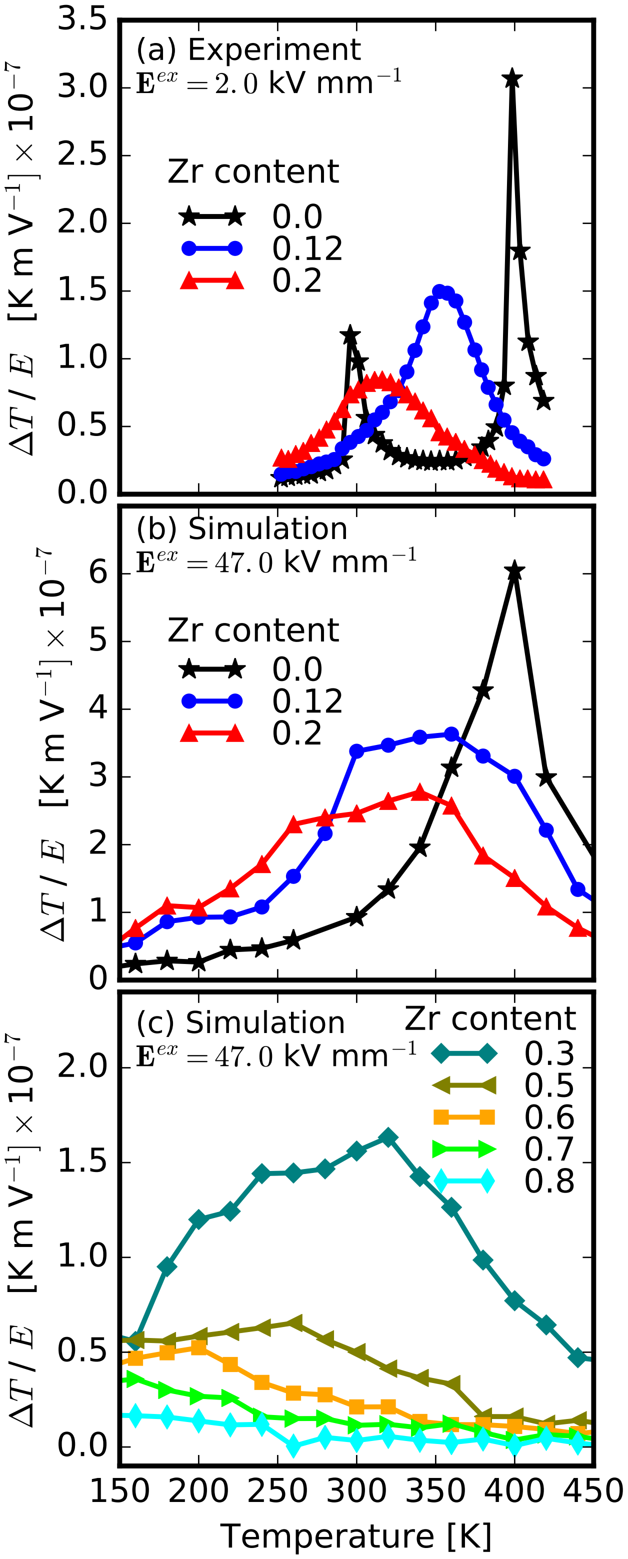

FIGURE 7.2 *Measurement (a) and simulation (b)-(c) of the electrocaloric effect. Both, in experiment (a) and simulation (b), the temperature and Zr-content dependence of the electrocaloric effect was studied for* $BaZr_xTi_{1-x}O_3$ *with* $0 \leq x \leq 0.2$*. When the Zr content is slightly increased, a sharp decrease of the electrocaloric effect can be observed. With respect to this point, the experimental results agree with the simulated conclusion qualitatively. In the simulation (c), the temperature and Zr-content dependence of the electrocaloric effect was studied for* $BaZr_xTi_{1-x}O_3$ *with* $x \geq 0.3$*. Two phases of electrocaloric effect can be distinguished: a moderate decrease for* $0.3 \leq x \leq 0.7$*, and vanishing peaks for* $x \geq 0.8$*.*

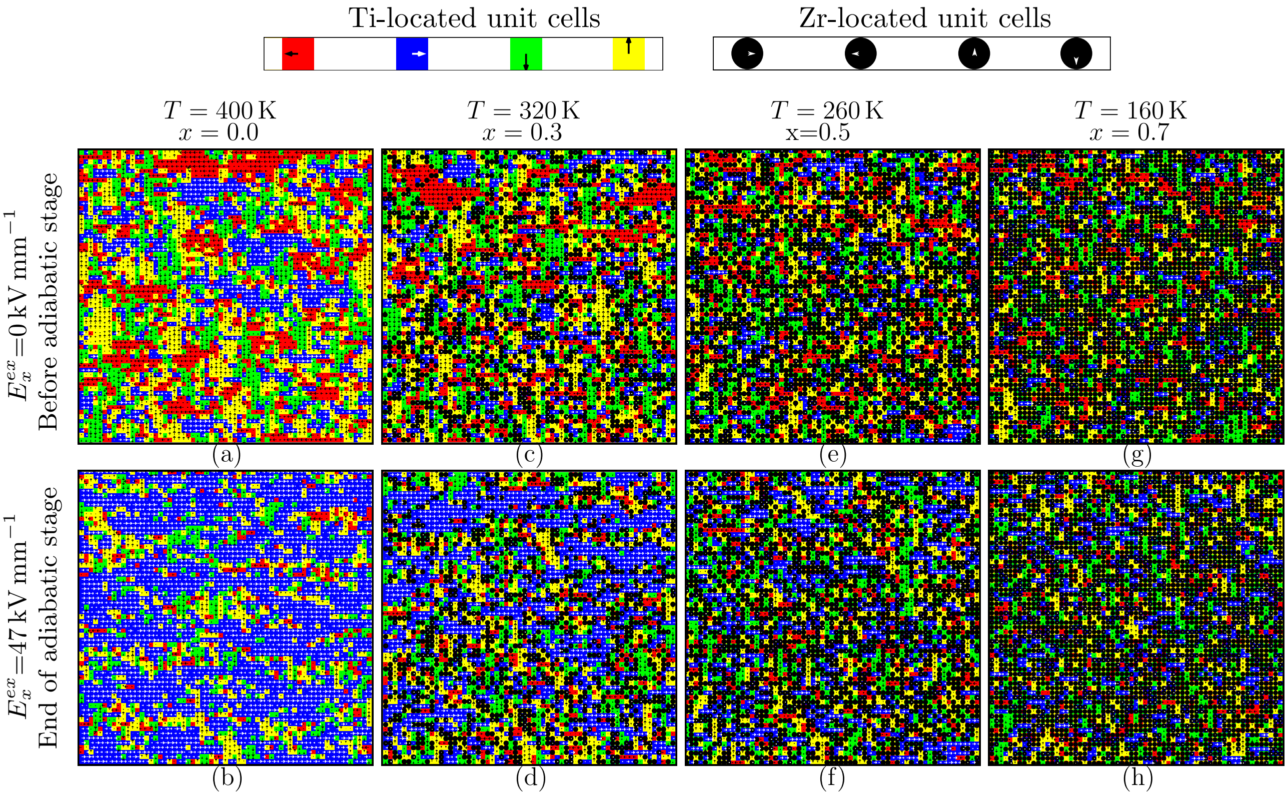

FIGURE 7.3 *Influence of the Zr content in $BaZr_xTi_{1-x}O_3$ on the domain configurations. For compositions $0 \leq x \leq 0.2$, e.g. (a) and (b), the number of sites which switch polarization is large. This results in the sharp drop of the ΔT peak within this compositional range. For $0.3 \leq x \leq 0.7$, as shown in (c)-(h), the number of switching sites is gradually reduced with increasing Zr content. Therefore, the value of the ΔT peak decreases more and more moderately. The red, blue, yellow and green squares represent the dipoles pointing to the left, right, top and bottom, respectively. The black dots represent the sites occupied by Zr-located unit cells.*

external field and the electrocaloric effect in the simulation is much higher than in the experiments. Reported experimental values for the electrocaloric effect in thin film $BaZr_{0.2}Ti_{0.8}O_3$ (7 K temperature variation under 19.5 kV mm^{-1}) [139] are therefore much closer to the simulation result. Thirdly, the simulations are describing a 2-dim. system and thus underestimate the heat capacity. Therefore, the temperature variation is larger than in a 3-dim. setup. Fourthly, at the ΔT peak of $BaTiO_3$, the calculated $\Delta T / \Delta E$ is equal to $0.59 \times 10^{-6}\,\mathrm{K \cdot V^{-1}\,m}$, which is 1.8 times of the experimental value of $0.32 \times 10^{-6}\,\mathrm{K \cdot V^{-1}\,m}$. However, experimental electrocaloric effect measurements were not carried out under adiabatic conditions. That is why the temperature variation is smaller. The major heat leaks are the steel sheath of the used sheath thermocouples and electrical contacts by copper wires.

Cooling systems can have different working temperatures. Therefore, it is also of interest to discuss the temperature dependence of the electrocaloric effect. Fig. 7.2(a) and Fig. 7.2(b) reveal that the electrocaloric effect of $BaZr_{0.12}Ti_{0.88}O_3$ and $BaZr_{0.2}Ti_{0.8}O_3$ is significantly higher than for pure $BaTiO_3$. As can be seen in Fig. 7.2(a) a significantly stronger electrocaloric effect can be observed in $BaZr_{0.12}Ti_{0.88}O_3$ within 311 K and 388 K, and in $BaZr_{0.2}Ti_{0.8}O_3$ below 290 K or within 306 K and 374 K. This might provide an application potential for the micro cooling system.

Further simulations were carried out for $BaZr_xTi_{1-x}O_3$ with $0.3 \leq x \leq 0.7$, as shown in Fig. 7.2(c). In the compositional range of $0.3 \leq x \leq 0.7$, the electrocaloric effect is weakened gently due to the fact that effective number of switching sites does not increase as much as in the range of $0.1 \leq x \leq 0.2$. With further increasing Zr concentration there is a saturation. Therefore, the value of the ΔT peak decreases slightly. In the concentration range of $x \geq 0.8$, there is no ΔT peak within the investigated temperature range. This can be explained by the full saturation of number of switchable sites. In addition, the temperature variation drops with increasing temperature.

7.3 State Transition

The electrocaloric properties of $BaZr_xTi_{1-x}O_3$ are closely related to the state transition and polarization switching of the material, which is investigated in detail in the following sections.

7.3.1 Temperature-dependence of Polarization

In Fig. 7.4, it can be seen that for pure $BaTiO_3$ the average polarization changes sharply around $T = 400$ K, which corresponds to the transition temperature from the tetragonal to cubic phase. For $BaZr_xTi_{1-x}O_3$, since the sites occupied by Zr are weakly polar or even nonpolar, less thermal energy is required to induce the transformation from the ordered to disordered phase.

With increasing Zr content in $BaZr_xTi_{1-x}O_3$, the temperature where the average polarization becomes almost zero shifts to a lower temperature. Meanwhile, higher Zr concentration leads to a more moderate change of the temperature-induced polarization. Additionally, at the same temperature the average polarization is lower when more sites occupied by Zr are introduced. For a better understanding of this phenomenon, the corresponding domain structures at 300 K, are visualized in Fig. 7.5 and discussed in the following subsection.

7.3.2 Domain Structure

In combination of the canonical Monte-Carlo simulations and the piezoresponse force microscopy measurements by Dr. Vladimir V. Shvartsman and Prof. Doru C. Lupascu in University of Duisburg-Essen, Zr-concentration dependent domain structure is studied in this subsection.

In Fig. 7.5 equilibrium domain patterns recorded by Piezoresponse Force Microscopy measurements at room temperature are shown in Fig. 7.5 (a$'$)-(c$'$) and compared to the simulation results (a)-(e). In Fig. 7.5(f), the internal electric field on each site has been evaluated and

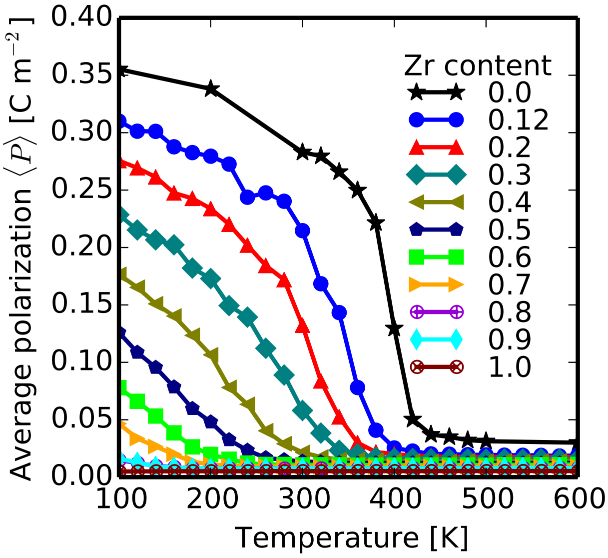

FIGURE 7.4 *Temperature-dependence of the average polarization calculated for different Zr concentrations of* $BaZr_xTi_{1-x}O_3$*. The legend presents the Zr content x. The more sites are occupied by Zr and thus weakly polar unit cells are introduced, the more the change of the polarization becomes moderate with respect to temperature, and the polarization becomes fairly small even at low temperature.*

analyzed, based on the simulated spatial distribution of the polarization. The long-range correlated Ti-Ti sites are interrupted by Zr occupied cites [107] which are weakly polar or nonpolar. Hence, in general, the miniaturization of the domains is due to the increasing Zr concentration.

In Fig. 7.5(a′), (b′), (c′), (a), (b), and (c) $BaTiO_3$, $BaZr_{0.12}Ti_{0.88}O_3$ and $BaZr_{0.2}Ti_{0.8}O_3$ are investigated.

At room temperature, $BaTiO_3$ has a narrow distribution of large internal fields as can be seen in Fig. 7.6, which bring out a high order in the samples. As expected, the stripe-like regular domain patters are observed for $BaTiO_3$ in Fig. 7.5(a′). A similar kind of domains can be observed in the simulation (see Fig. 7.5(a)).

In $BaZr_{0.12}Ti_{0.88}O_3$ and $BaZr_{0.2}Ti_{0.8}O_3$ the distribution of the internal fields is broad, and no apparent peaks can be observed (see Fig. 7.6), which is due to the disorder in the samples. Therefore, instead of regular domains only mosaic-like domain patters exist in $BaZr_{0.12}Ti_{0.88}O_3$ and $BaZr_{0.2}Ti_{0.8}O_3$ (see Fig. 7.5(b′) and (c′)). The domains in $BaZr_{0.12}Ti_{0.88}O_3$ are larger than those in $BaZr_{0.2}Ti_{0.8}O_3$. A similar observation can be made in the simulated domain patterns (see Fig. 7.5(b) and (c)). In short, the decrease of domain size with increasing Zr content reflects the crossover from the ferroelectric state to the relaxor state due to the presence of random fields. These random fields can arise from the breakdown of long-range correlation of Ti-Ti sites due to the presence of nonpolar or weakly polar sites occupied by Zr [107]. Moreover, the correlation strength between sites occupied by Ti and Zr is weakened with increasing Zr content, which leads to additional contributions to random fields. The high-frequency permittivity is composition-dependent so that the correlation strength between sites can be both composition- and position-dependent (see Eq. 7.2).

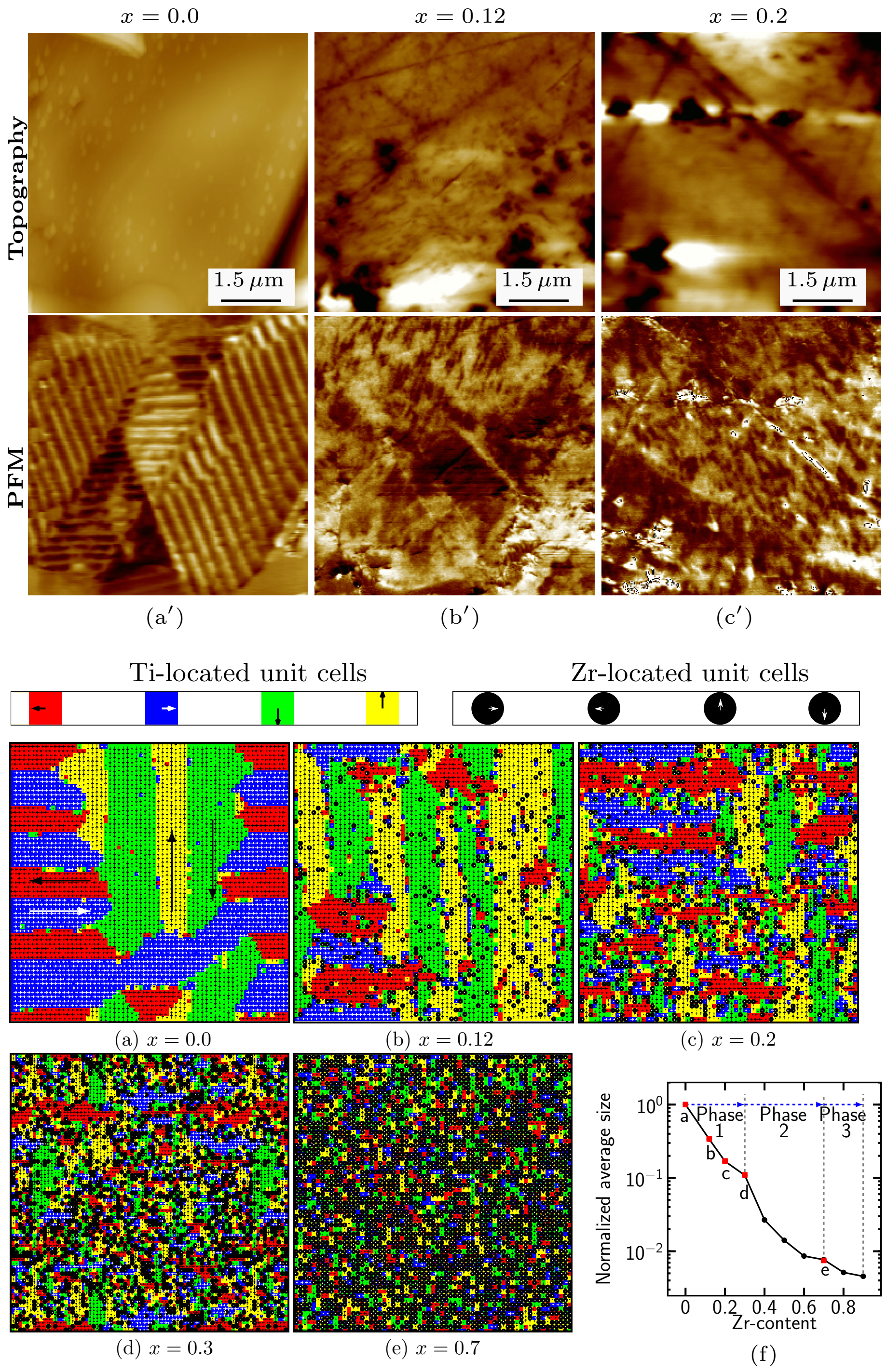

(a′) (b′) (c′)

(a) $x = 0.0$ (b) $x = 0.12$ (c) $x = 0.2$

(d) $x = 0.3$ (e) $x = 0.7$ (f)

Figure 7.5 *(a′)-(c′) topography and Piezoresponse Force Microscopy images , (a)-(e) the simulated domain patterns at room temperature, and (f) the normalized domain size. Topography and Piezoresponse Force Microscopy images for* $BaTiO_3$*,* $BaZr_{0.12}Ti_{0.88}O_3$ *and* $BaZr_{0.2}Ti_{0.8}O_3$ *are shown. Multiple regular ferroelectric domains are observable in* $BaTiO_3$*. However, in* $BaZr_{0.12}Ti_{0.88}O_3$ *and* $BaZr_{0.2}Ti_{0.8}O_3$ *instead of the regular domains the mosaic-like domain patterns are observed. With increasing Zr content, the domain size decreases, which suggests the crossover from the ferroelectric state to the relaxor state and supports the claim in the simulation. In the simulation, the domain patterns are shown for* $BaZr_xTi_{1-x}O_3$ *from (a) to (e).*

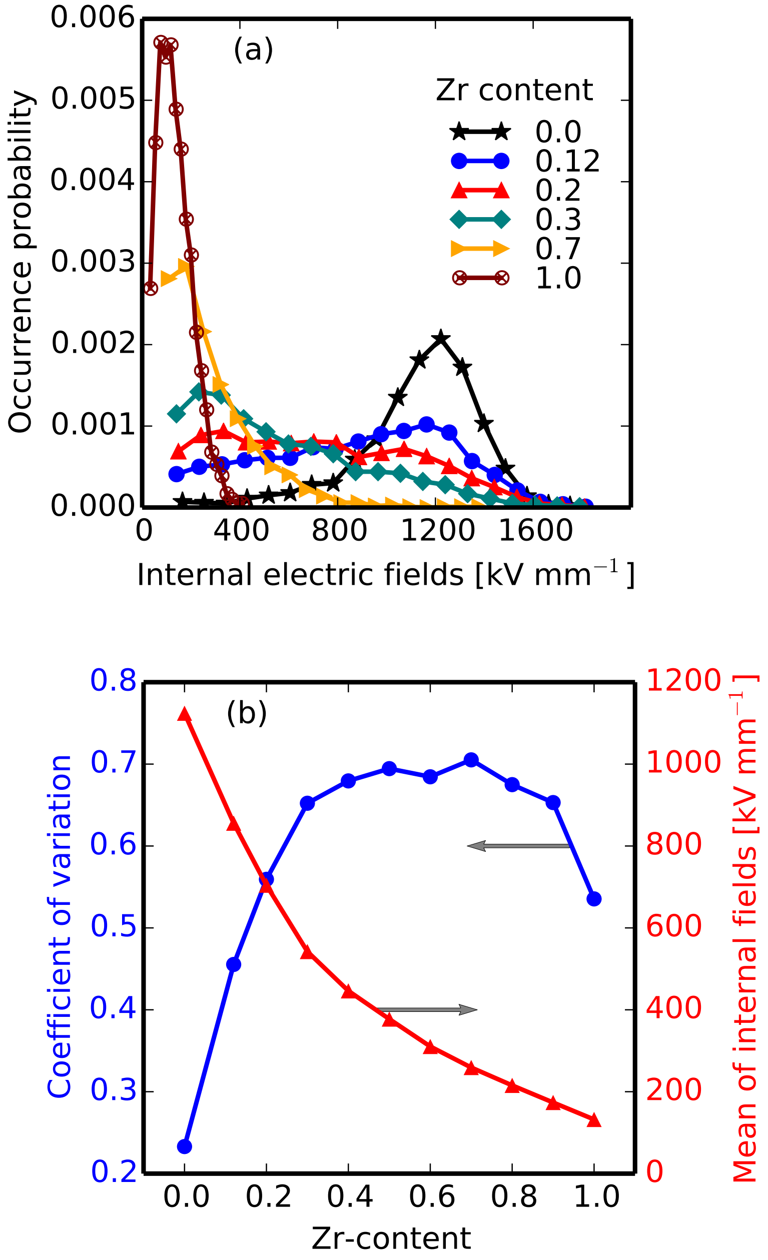

Figure 7.6 *(a) Occurrence probability distribution, and (b) coefficient of variation of the absolute internal electric fields. In the simulation, based on the spatial distribution of the polarizations in Fig. 7.5, the magnitude of the internal electric fields imposed on each site can be calculated. (a) shows that the distribution peak shifts to lower field with more Zr substitution. (b) presents that the internal fields are most random for* $BaZr_xTi_{1-x}O_3$ *with* $0.3 \leq x \leq 0.9$*. The appearance of the relaxor behavior relies mainly on the coefficient of variation rather than the magnitude of the internal fields. Namely, with a big coefficient of variation, the relaxor behavior shows up even under a high magnitude of the internal fields. The current investigation on* $BaZr_xTi_{1-x}O_3$ *reveals the indispensable role of the random fields in understanding of relaxor ferroelectrics. Hence, as shown as following, in Chap. 8 a generic model based on random field theory is proposed to study the relaxor behavior.*

Additionally, several composition dependent regimes can be distinguished in the simulated domain patterns in Fig. 7.5(a)-(e). In the range of $0 \leq x \leq 0.2$ the domain size is comparably large due to the large proportion of ferroelectric Ti-containing cells. In the range of $0.3 \leq x \leq 0.6$ more Zr is incorporated and induces random fields. These arise mainly for two reasons: 1) the incompatibility of the multi-well Landau potential for Ti^{4+} sites and single well potential for Zr^{4+} sites, and 2) the random correlation length between sites due to the composition-dependent dipole-dipole interaction. Therefore, the domain patterns are unstable and resemble polar nanoregions when approaching $x = 0.3$, which hints towards the onset of the relaxor behavior. When the Zr content is above 0.3, enough sites are occupied by Zr and dominate the material behavior. Therefore, the long-range order is vanishing. In the composition range of $0.7 \leq x \leq 0.9$, $BaZr_xTi_{1-x}O_3$ can be interpreted as nonpolar Zr containing matrix with some polar Ti-sites. These dipolar clusters are almost isolated from each other, and thus no relaxor-like behavior can be observed. Finally, in the case of pure $BaZrO_3$ no dipolar clusters exist because it is a paraelectric material. From the domain patterns the domain sizes were analyzed as shown in Fig. 7.5(f). The domain sizes shown are normalized to the average domain size in pure $BaTiO_3$. Again, the various composition ranges mentioned above can be also identified in this plot.

Fig 7.6(a) shows the occurrence probability distribution of the magnitude of the internal fields for different Zr contents. It is obvious that the peak of the occurrence probability shifts to lower fields upon increasing Zr content. The coefficient of variation (CV) and the mean value of the fields are also presented in Fig. 7.6(b). The CVs forms a vault-like curve with increasing Zr concentration, while the mean value decreases gradually. For pure $BaTiO_3$, Fig. 7.6(a) shows that the occurrence probability distributes narrowly and in the high field range, which is compatible with the well small CV and a big mean value in Fig. 7.6(b). This indicates that an apparent ferroelectric domain pattern can be formed in presence of a well distributed internal field, which keeps coherent to Fig. 7.5(a). For $BaZr_{0.12}Ti_{0.88}O_3$ and $BaZr_{0.2}Ti_{0.8}O_3$, the occurrence probability distributes wider than pure $BaTiO_3$. However, for $BaZr_{0.12}Ti_{0.88}O_3$ and $BaZr_{0.2}Ti_{0.8}O_3$ the field distributes most probably in the high field region, and the CVs are still smaller than $BaZr_xTi_{1-x}O_3$ with $x \geq 0.3$. It can be inferred that the domains undergo a miniaturization, but $BaZr_{0.12}Ti_{0.88}O_3$ and $BaZr_{0.2}Ti_{0.8}O_3$ are still ferroelectric. Fig. 7.5(b) and (c) substantiates this inference. For $0.3 \leq x \leq 0.6$ in $BaZr_xTi_{1-x}O_3$, CVs possess a large value while the mean value of fields is moderate. It can be concluded that the internal fields are large and random, which dominate the materials behavior. In other words, it leads to the relaxor states with polar nanoregions (see Fig. 7.5(d)). For $BaZr_{0.8}Ti_{0.2}O_3$ and $BaZr_{0.9}Ti_{0.1}O_3$, CVs are still large, and simultaneously the mean value of fields are quite small. It suggests that the fields are small and random, which corresponds to the appearance of dipolar clusters (see Fig. 7.5(e)). For pure $BaZrO_3$, the CV are sharply drops to a small value with a small mean value of fields. It stands for a state with small and narrow distributed fields, which results in the paraelectric phase, where no domains structures can be observed.

7.3.3 Hysteresis

The P-E loops of $BaZr_xTi_{1-x}O_3$ with Zr contents of $x = 0.0$, $x = 0.12$ and $x = 0.2$ were investigated both experimentally and theoretically at different temperatures, as can be seen in Fig. 7.7 and Fig. 7.8.

In $BaTiO_3$ the tetragonal phase transforms to the orthorhombic phase around 293.15 K, which is indicated by a peak of the electrocaloric effect in Fig. 7.2(a). Therefore, there is a sudden drop of the saturation polarization P_{sa} and the remnant polarization P_r between 293.15 K and 313.15 K (see Fig. 7.7). In the simulation, only the transition from the cubic to tetragonal phase is considered. Hence, this sudden drop cannot be observed (see Fig. 7.8). Above 313.15 K the results for $BaTiO_3$ in Fig. 7.7 agree with the simulation results qualitatively (see Fig. 7.8). Similarly, the sharp variations of P_{sa} and P_r in $BaTiO_3$ from 393.15 K to 413.15 K, in $BaZr_{0.12}Ti_{0.88}O_3$ from 353.15 K to 373.15 K and in $BaZr_{0.2}Ti_{0.8}O_3$ from 313.15 K to 333.15 K indicate the transition from the tetragonal to cubic phase, which is responsible for the ΔT peak in Fig. 7.2(a).

In a sinusoidal external electric field, the polarization switching process can be studied by canonical Monte-Carlo simulations (see Fig. 7.8). It can be seen that the hysteresis loops become smaller when the temperature or the Zr concentration increases, more exactly, P_{sa}, P_r and the coercive field E_c decrease. As the temperature increases, higher thermal energy promotes the thermal fluctuation of the polarization, which eliminates the necessity of high electric fields to achieve domain switching.

Experimental data [129, 205] shows a decrease of P_{sa}, P_r and E_c with increasing temperature, which agrees with our simulation qualitatively. As for the influence of Zr concentration, it

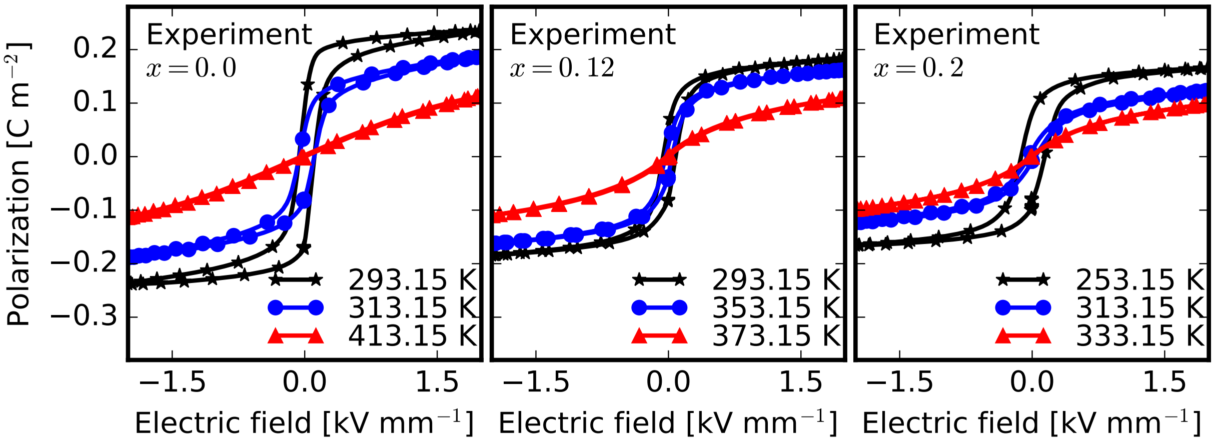

FIGURE 7.7 *The measured dielectric hysteresis at different temperatures for $BaTiO_3$, $BaZr_{0.12}Ti_{0.88}O_3$ and $BaZr_{0.2}Ti_{0.8}O_3$. At higher temperature or with increasing Zr content, the hysteresis loops become slimmer.*

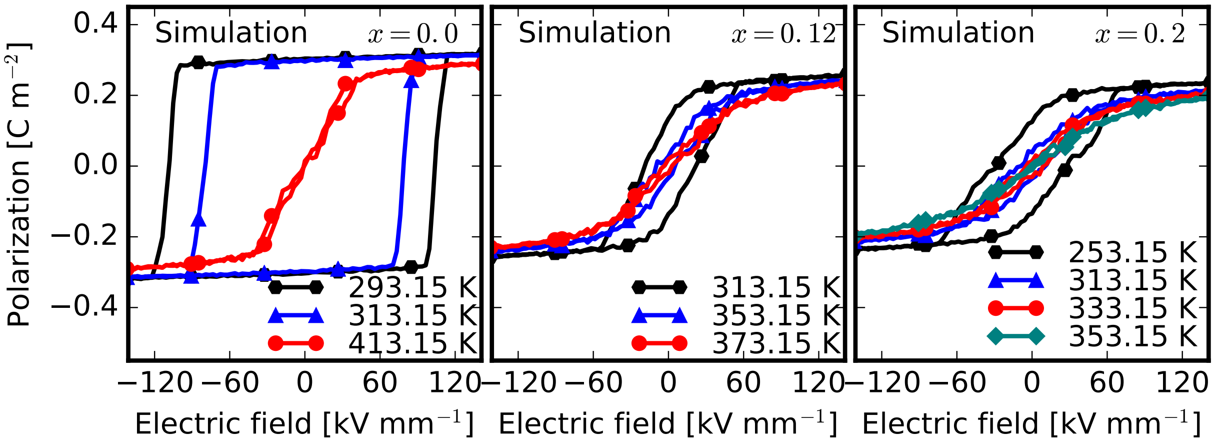

Figure 7.8 *The simulated dielectric hysteresis at various temperatures for* $BaTiO_3$, $BaZr_{0.12}Ti_{0.88}O_3$ *and* $BaZr_{0.2}Ti_{0.8}O_3$*. It shows that either by increasing the temperature or raising Zr content, the hysteresis loops become slimmer, i.e., with lower remnant and saturation polarization and smaller coercive field. These results agree with the experimental work in Fig. 7.7 qualitatively.*

can be reasoned that at weakly polar or nonpolar sites occupied by Zr it requires less effort to reverse the polarization, as compared with polar sites occupied by Ti.

For pure $BaTiO_3$ or $BaZr_xTi_{1-x}O_3$ with low Zr concentration ($x < 0.20$), the material is ferroelectric. Hence, the polarization switching is quite steep around E_c below the phase transition temperature. In the experimental study by Moura *et al.* [206], well saturated hysteresis loops with regular shape for $BaZr_{0.05}Ti_{0.95}O_3$, $BaZr_{0.1}Ti_{0.9}O_3$ and $BaZr_{0.15}Ti_{0.85}O_3$ were observed, which is typical for ferroelectric materials and supports our conclusion. Even by introducing only a small amount of Zr ($x = 0.12$) the coercive field is sharply reduced, since Zr-centered cells act as nucleation sites for reversed domains. In contrast, a moderate decrease of coercive field is observed upon further increasing Zr content.

Both, experiment and computer simulation, reveal that at higher temperatures or with increasing Zr content the hysteresis loops become smaller, and the slope around the coercive field becomes less steep. The saturation polarization in the simulation is higher than that in the experiment, since it is typical that the single crystal without defects has a higher saturation polarization than the polycrystalline ceramics.

Additionally, more compositions are investigated to reveal the influence of Zr content on the materials behavior (see Fig. 7.9). A relaxor-like hysteresis can be seen for compositions of $0.3 \leq x \leq 0.7$, even at $T = 100\,\mathrm{K}$. In the experimental study by Yu *et al.* [129], the relaxor-like hysteresis was also observed in $BaZr_{0.3}Ti_{0.7}O_3$ at a temperature of $T = 175\,\mathrm{K}$. At $T = 100\,\mathrm{K}$ and $x \leq 0.7$, P_r is still larger than zero while P_r is vanishing for $x \geq 0.8$. This phenomenon is in accordance with the observation shown in Fig. 7.4, i.e., the average polarization becomes almost zero only when $x \geq 0.8$ at $T = 100\,\mathrm{K}$. The same explanation can be extended to interpret the vanishing value of P_r at $T = 200\,\mathrm{K}$ for $x \geq 0.6$ and at $T = 300\,\mathrm{K}$ for $x \geq 0.4$. In $BaZr_xTi_{1-x}O_3$ with $x = 0.8$ and $x = 0.9$, only dipolar clusters exist. Merely, at quite low temperatures (e.g.,

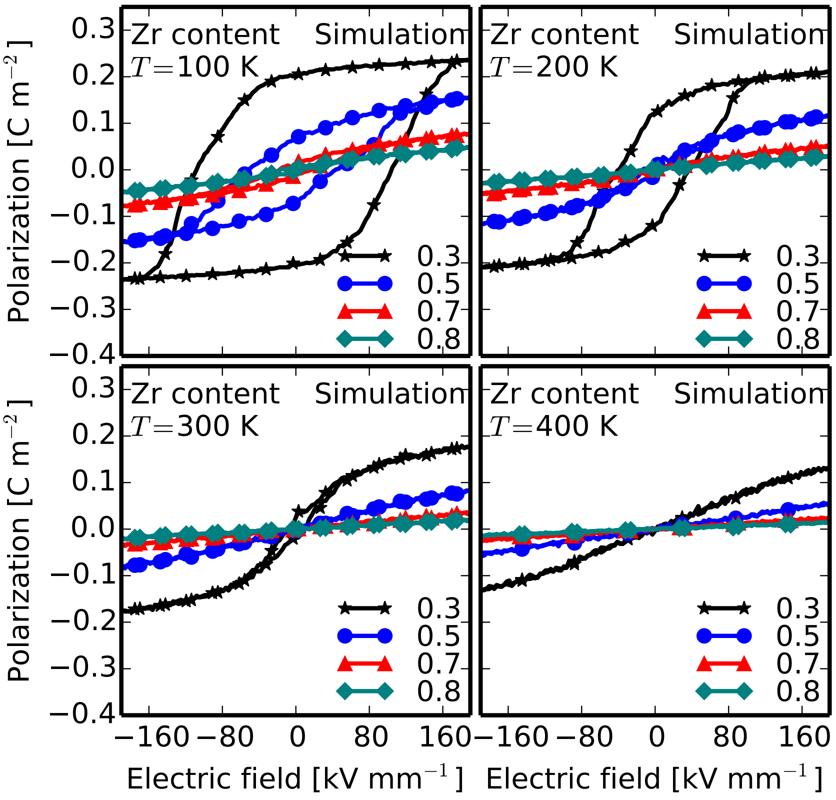

FIGURE 7.9 *The simulated dielectric hysteresis at various temperatures for* $BaZr_xTi_{1-x}O_3$ *with* $x \geq 0.3$. *For compositions of* $0.3 \leq x \leq 0.7$ *the relaxor-like hysteresis is present.*

$T = 100\,\mathrm{K}$), these dipolar clusters can be correlated. Therefore, the hysteresis can be solely observed at low temperature. At a higher temperature (e.g., $T = 200\,\mathrm{K}$), the weak mutual interaction of these dipolar clusters is superimposed by high thermal fluctuations. Hence, a linear type of dielectric response is expected. Furthermore, the hysteresis loops nearly overlap with each other for these two compositions.

7.4 Summary

In this chapter a simple solid solution $BaZr_xTi_{1-x}O_3$ is studied. We have modified the lattice-based Monte-Carlo scheme developed in Chap. 4 to evaluate directly the electrocaloric effect in $BaZr_xTi_{1-x}O_3$. A multi-well Landau-type term is applied for unit cells containing Ti, and a single well for Zr. The long-range dipole-dipole interaction strength is set to composition-dependent. Here the electrocaloric effect is studied as well as the origin of the relaxor behavior. For comparison, experiments were carried out for $BaZr_xTi_{1-x}O_3$ ($x = 0.0, 0.12, 0.2$) by our cooperators.

Both experiments and simulations (see Fig. 7.2) reveal a sharp drop of the electrocaloric effect with increasing the Zr content from 0% to 20%. With increasing Zr content, the ΔT peak also shifts to lower temperatures. Three distinct composition dependent regimes can be identified: a sharp drop of the peak for $0.0 \leq x \leq 0.2$, a moderate drop for $0.3 \leq x \leq 0.7$, a very weak peak or no peak existence for $x \geq 0.8$.

Domain patterns at room temperature were analyzed through Piezoresponse Force Microscopy. In $BaTiO_3$, a regular strip-like ferroelectric domain structure is present. In contrast, mosaic-like domain patterns are present in $BaZr_{0.12}Ti_{0.88}O_3$ and $BaZr_{0.2}Ti_{0.8}O_3$. In $BaZr_{0.12}Ti_{0.88}O_3$ the domain size is bigger than in $BaZr_{0.2}Ti_{0.8}O_3$. All these facts indicate a crossover from the ferroelectric to the relaxor ferroelectric state, which agrees with the simulation. Simulated domain patterns reveal several different phases, including the phase with big domain size, the phase with small domain size and dipolar clusters respectively (see Fig. 7.5). According to the above domain patterns the internal electric fields were calculated, and the probability distribution of the fields was analyzed (see Fig. 7.6). Especially, the vault-like coefficient of the variation of fields reveals several transitions step by step with increasing Zr content: ferroelectrics, relaxor ferroelectrics, dipolar clusters and paraelectrics. The results show that the appearance of the relaxor behavior relies mainly on the coefficient of variation rather than the magnitude of the internal fields. Namely, with a big coefficient of variation, the relaxor behavior shows up even under a high magnitude of the internal fields. The current investigation on $BaZr_xTi_{1-x}O_3$ reveals the indispensable role of the random fields in understanding of relaxor ferroelectrics.

The polarization switching behavior was additionally investigated by studying the hysteresis, experimentally and theoretically (see Figs. 7.7-7.9). The hysteresis reveals that with increasing Zr concentration or with increasing temperature, the remnant and saturation polarization and the coercive field decrease. Meanwhile, the simulations show that for $x \geq 0.3$ the hysteresis has a typical relaxor-type behavior. Finally, this work reveals that $BaZr_xTi_{1-x}O_3$ has a wider application temperature range than $BaTiO_3$, which is essential for cooling devices.

Chapter 8

Generic Model for Relaxors

In this chapter, Secs. 8.1 and 8.2 are based on the publications “Y.-B. Ma, K. Albe, and B.-X. Xu, Phys. Rev. B 91, 184108 (2015)” and “Y.-B. Ma, K. Albe, and B.-X. Xu, in ISAF (IEEE, Singapore, 2015), pp. 203-206”, respectively.

The origin of relaxor behavior is strongly material-dependent. As reviewed in Chap. 2, several models were proposed to interpret the relaxor behavior, including polar nanoregions [105], the dipole-glass model [102], the random field model [116, 117], and the spherical random bond-random field model [118]. However, in a generic sense they can all lead to internal random fields [116]. For instance, in the $BaZr_xTi_{1-x}O_3$ system, the compositional fluctuation gives rise to random field, as demonstrated in Fig. 8.9. For an explicit examination on the impact of random fields on the mesoscopic effects, a generic lattice-based Monte-Carlo model based on random field theory is developed in Sec. 8.1. As another possible source of random fields, random defect dipole configuration is also simulated and compared with the generic model of random field in Sec 8.2.

8.1 Relaxor Ferroelectrics with Random Field

In our Monte-Carlo simulations, the potential energy H is described by a Ginzburg-Landau type expression which includes four contributions: $H = H_{\mathrm{D}} + H_{\mathrm{dip}} + H_{\mathrm{gr}} + H_{\mathrm{e}}$. The former three energy terms, including H_{D}, H_{dip} and H_{gr}, are identical to these utilized in Sec. 4.2 of Chap. 4. The randomness of relaxors is described through random electric fields, which should enter the electrostatic energy. Thus, the electrostatic energy is modified accordingly. Static and dynamic random local electric fields are introduced to explain the absence of long-range ferroelectric order in relaxor ferroelectrics [207]. Here, only the static part of the random field is regarded, which does not change during the domain evolution. Both the external electric field $\mathbf{E}^{ex}$ and the random local electric field $\mathbf{E}^{rm}$ contribute to the electrostatic energy with the illustration shown in Fig. 8.1. Hence the electrostatic energy H_{e} is given as:

$$H_{\mathrm{e}} = -V_0 \sum_i \Big[\mathbf{P}(\mathbf{r}_i) \cdot \Big(\mathbf{E}^{ex} + \mathbf{E}^{rm}(\mathbf{r}_i) \Big) \Big]. \tag{8.1}$$

In the present work the external field is always applied in the x direction. The direction of $\mathbf{E}^{rm}$ is randomly distributed between 0° and 360°, and the magnitude between 0 and an allowed

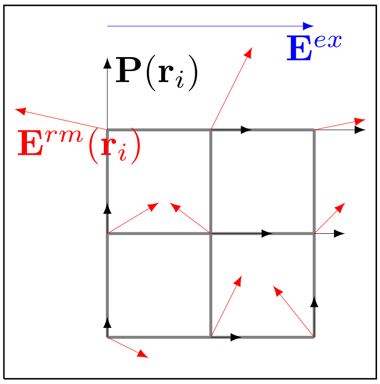

Figure 8.1 *Illustration of the electrostatic energy with the static random local electric fields.*

maximum value $|E^{rm}|$. In this way, the mean value of $\mathbf{E}^{rm}$ is almost zero, and thus the effective field caused by the random electric field is negligible.

The canonical and microcanonical algorithms for calculation of dielectric and electrocaloric results remain the same as in Chap. 4. To single out the influence of random fields, the parameters for $BaTiO_3$ are also used for the study in this subsection. In the following the influence of random fields, including their strength and density, on the relaxor ferroelectrics behavior and the electrocaloric effect is studied.

8.1.1 Nonergodic-to-Ergodic State Transformation and Hysteresis

In the following, we turn to the case of relaxor ferroelectrics and apply random fields [116] to mimic the characteristics of relaxor ferroelectrics.

There are various origins of random fields, e.g. the chemical disorder, defect dipoles and so forth. The strength of the electric field-induced by defect dipoles is chosen as upper bound for the random fields. A fixed defect dipole with a given magnitude of $0.63\,\mathrm{C\,m^{-2}}$ induces an electric field of $942.7\,\mathrm{kV\,mm^{-1}}$ on the nearest neighbor lattice sites, calculated through Eq. (4.8). Hence, this value is taken as the maximum value of random fields in our simulations.

In the presence of random fields, local polarization can be randomly pinned, while the short-range and the long-range interactions try to keep the system in an ordered state. When the random field is sufficiently high at site i, and the polarization at site i remains parallel to the random field. Therefore, more domain walls are produced and the size of the ordered clusters is smaller in the case with stronger random field (Fig. 8.2).

Fig. 8.3 and Fig. 8.4 demonstrate the influence of random fields on the temperature-induced polarization change and the nonergodic-to-ergodic state transformation, respectively. It can be seen that random fields make the temperature-induced polarization change moderate. At specific sites the presence of random fields may incur a very low electrostatic energy H_e. The flipping of this polarization will be difficult, since a sharp increment of H_e is required. At some high temperature, the necessary thermal energy for flipping may be still much higher

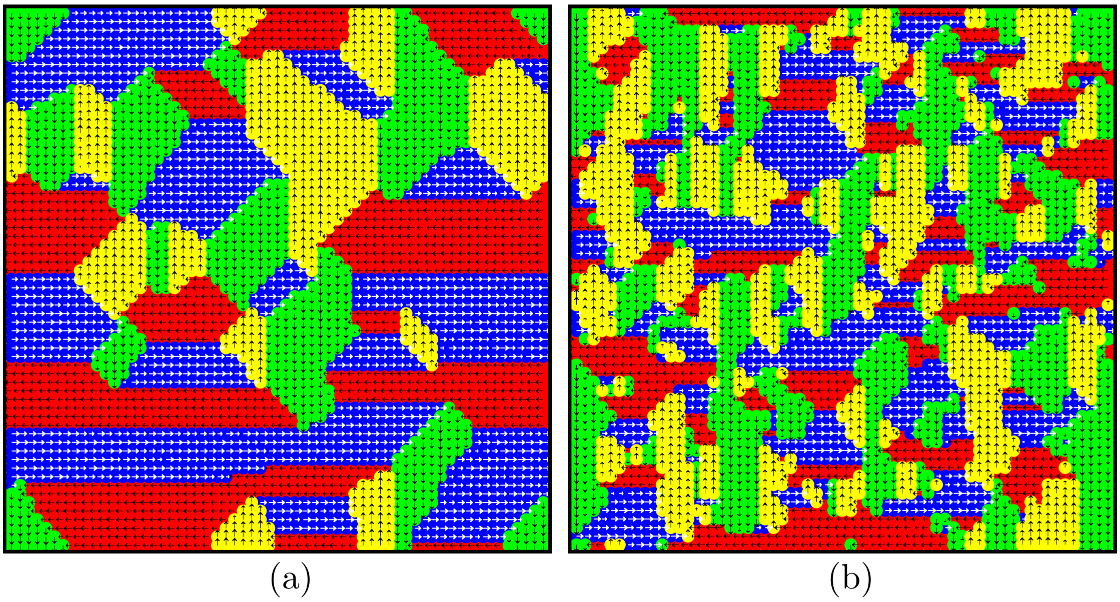
(a) (b)

FIGURE 8.2 *Equilibrium domain configurations with* $S_J = 2$ *and* $T = 100\,K$ *for: (a) ferroelectrics and (b) relaxor ferroelectrics with* $|E^{rm}| \approx 940\,kV\,mm^{-1}$. *The pinning effect of random fields makes the domain size smaller.*

than the current thermal energy. These dipoles can be pinned, and thus a distribution of local polarizations appears with an apparent nonzero mean value. Consequently, the temperature-induced polarization change becomes less sharp.

The average polarization has finite values within a broad temperature range in relaxor ferroelectrics. This feature agrees qualitatively well with the experimental observations in disordered $PbSc_{0.5}Ta_{0.5}O_3$ single crystal [110] and becomes more dominant when the random field is stronger.

The nonergodic state of relaxor ferroelectrics can be irreversibly transformed into ferroelectrics by applying a large external electric field while the ergodic phase has no such feature [108]. By comparing the polarization per site in the x direction of a virgin sample and that of a sample, which was first poled and then relaxed, the transition temperature from the nonergodic to ergodic state, i.e. the so-called freezing temperature, can be determined. In Fig. 8.4(a), the polarization for these two cases is depicted in combination with that of a poled sample without relaxation. In both samples a random field with $|E^{rm}| = 470\text{kVmm}^{-1}$ is present. At a high temperature the polarization in both samples is vanishing, while below a certain temperature around 340 K there is a noticeable remnant polarization in the relaxed sample. This indicates that prepoling has induced a transition to a ferroelectric state, and that the freezing temperature of this sample lies around 340 K. It is further shown by comparison between Fig. 8.4(a) and (b) that the freezing temperature decreases with the strength of the random field. Meanwhile, the freezing temperature increases with the domain wall energy, as the comparison between Fig. 8.4(b) and (c) demonstrates.

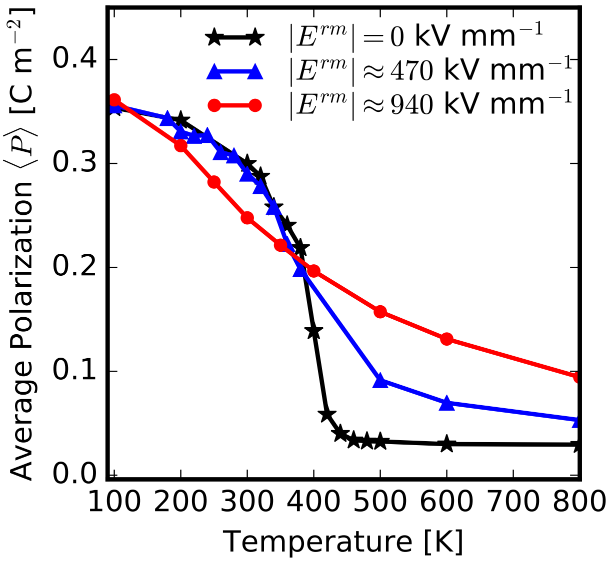

FIGURE 8.3 *Influence of random fields on temperature dependence of polarization, with* $S_J = 2$ *and no external field. Random fields lead to a moderate temperature-induced polarization change.*

In Fig. 8.5(a) the effective polarization of the simulated sample is plotted with respect to the external electric field. In absence of random fields, a ferroelectric type hysteresis is obtained. If the random field is rather small, the hysteresis is still of a ferroelectric type with the almost same remnant and saturation polarization, but the coercive field decreases. If the random field is rather strong, not only the hysteresis becomes slim, but also the remnant polarization and the saturation polarization decrease rapidly. If the random field is strong enough, the remnant polarization vanishes, and a relaxor ferroelectric type hysteresis is observed.

The change of the hysteresis with the random fields can be better explained through the domain evolution during application of an external field. Two snapshots of the domains are illustrated in Fig. 8.5. Domain walls are unlikely to move as a unit but rather through a nucleation-type mechanism [208–210]. In ferroelectrics the nucleation of the reversed domains is energetically more favorable near the domain wall than far away from the domain wall. Thus, domain wall movement in ferroelectrics is visible. This is confirmed by the snapshot of the domain structure shown in the left snapshot of Fig. 8.5(a).

However, if the strength of the random field is high enough, the electrostatic energy due to the random fields can influence the domain nucleation and the domain wall motion considerably. Random fields favor the polarization flip to the direction parallel to themselves. Thus, nucleation of reversed domains can already appear, before the external field reaches the reversed coercive field. Nucleation takes place not only near the domain wall. Instead, a random distribution of nucleation occurs, as the right snapshot of Fig. 8.5(a) shows. Hereby many sites with polarizations perpendicular to the external electric field can even survive. Similar phenomena has also been observed in Monte-Carlo simulation by Padurariu *et al.* [144], in which only the dipole-dipole interaction is taken into consideration. This domain structure remains, even after

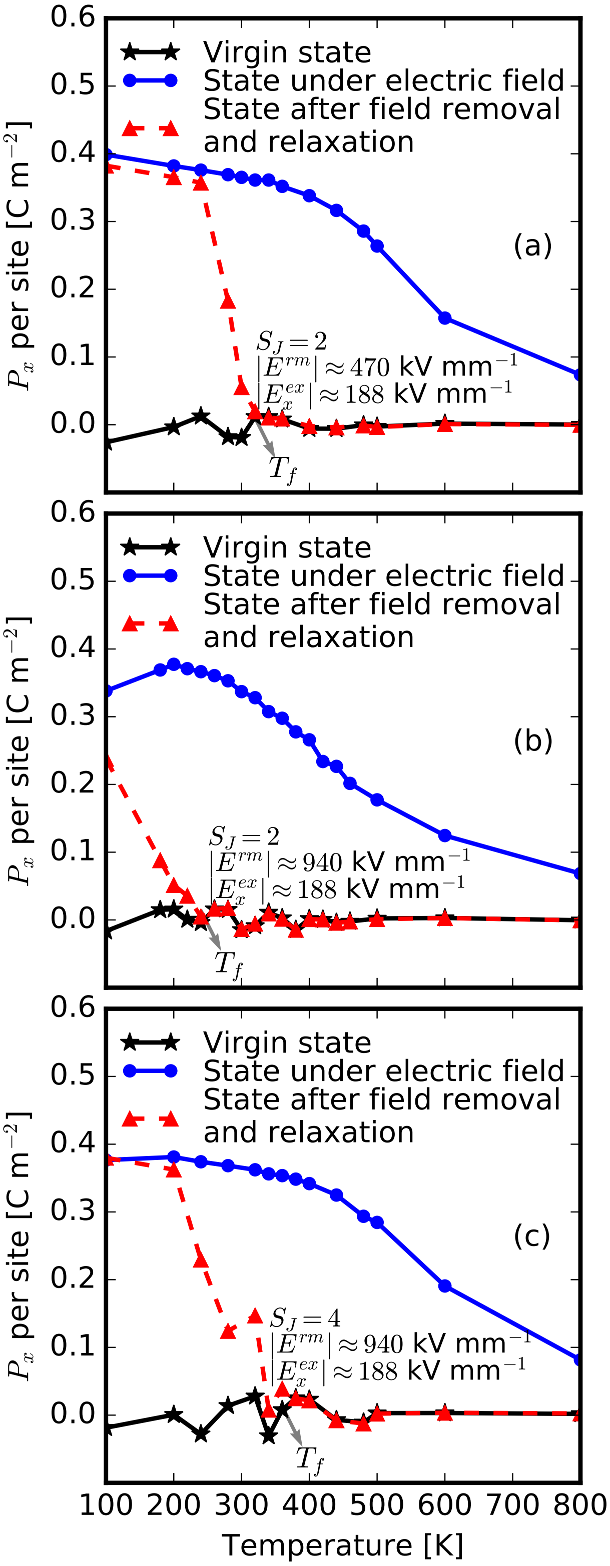

FIGURE 8.4 *Influence of random fields and the domain wall energy on the freezing temperature* T_f*, which can be determined by the polarization difference per site in the x direction between the fully relaxed sample and the virgin sample. (a)* $|E^{rm}| \approx 470\,\mathrm{kV\,mm^{-1}}$*,* $S_J = 2$*, (b)* $|E^{rm}| \approx 940\,\mathrm{kV\,mm^{-1}}$*,* $S_J = 2$ *and (c)* $|E^{rm}| \approx 940\,\mathrm{kV\,mm^{-1}}$*,* $S_J = 4$*.* T_f *decreases with increasing random fields. By contrast, the increasing domain wall energy promotes* T_f*.*

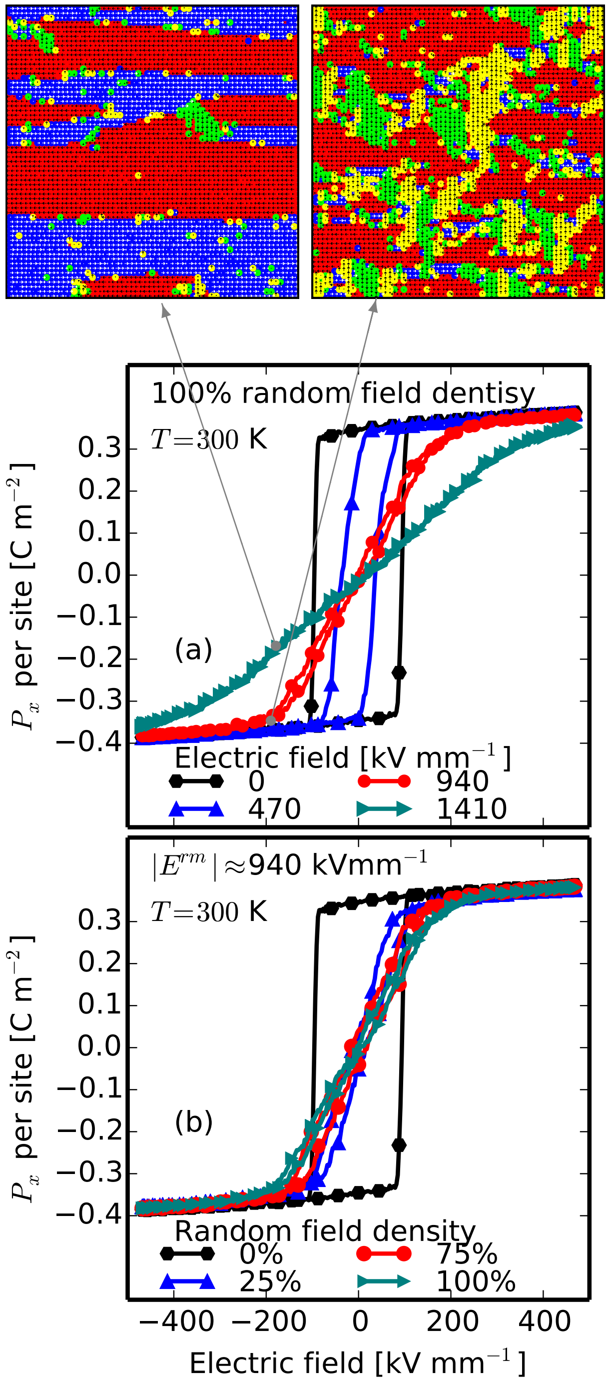

FIGURE 8.5 *Variation of hysteresis with (a) the strength of the random field $|E^{rm}|$ and (b) the density of the random field. P_x is the average polarization per site in the x direction. The external field is applied in the x direction as well. The two images on the top are the snapshots of the domain configuration during the reversal of the external electric field for the case without random field and the case with random field of $|E^{rm}| \approx 940\,kV\,mm^{-1}$, respectively. The pinning effect due to the presence of random fields is visible.*

the external field is removed. This can explain the decline of the remnant polarization. Furthermore, remnant polarization almost vanishes for ergodic relaxor ferroelectrics, when sufficiently far above the freezing temperature [211]. It is seen from Fig. 8.4 that the freezing temperature T_f is around 340 K for $|E^{rm}| \approx 470\,\mathrm{kV\,mm}^{-1}$, and around 260 K for $|E^{rm}| \approx 940\,\mathrm{kV\,mm}^{-1}$. In other words, at the given temperature $T = 300\,\mathrm{K}$, the material is at a nonergodic state, when $|E^{rm}| \approx 470\,\mathrm{kV\,mm}^{-1}$, while at an ergodic state, when $|E^{rm}| \approx 940\,\mathrm{kV\,mm}^{-1}$. Thus, the remnant polarization for the latter case is almost zero. Meanwhile, if the random field is large enough, the polarization can be pinned in the direction favored by the random fields. Hence the sample cannot be fully poled by the external field. Therefore, it leads to a decreased saturation polarization in the hysteresis, e.g. in the case of $|E^{rm}| \approx 1410\,\mathrm{kV\,mm}^{-1}$.

In addition, the effect of the number of sites with random fields is further analyzed. In the previous example the random fields are distributed over the whole simulated sample, i.e. the random field density is assumed to be 100%. Depending on the extent of disorder, the number of sites with random fields, i.e. the random field density, could also be different. For instance in Fig. 8.5(b), a given fraction of sites, are randomly selected. The magnitude of random fields on these selected sites is uniformly chosen between 0 and the maximum value of $940\,\mathrm{kV\,mm}^{-1}$, and the direction of random fields varies between 0° and 360°. Fig. 8.5(b) presents the hysteresis variation with the density of random fields, while the maximal value of the random fields is kept constant at $|E^{rm}| \approx 940\,\mathrm{kV\,mm}^{-1}$. It can be seen that the saturation polarization remains unchanged, while the remnant polarization decreases with increasing random field density.

8.1.2 Electrocaloric Effects

The electrocaloric effect depends on the strength of random fields as illustrated in Fig. 8.6(a). Compared with the case without random field, the ΔT peak is shifted to a lower temperature. When random fields become stronger, either through the strength or the density, the peak shifts further to the lower temperature. It is noticeable that the peaks occur at the corresponding freezing temperature. It implies that the potential change due to the nonergodic-to-ergodic transition contributes significantly to the thermal energy change under adiabatic conditions. Since the freezing temperature decreases with increasing random fields, as it has been demonstrated in Subsec. 8.1.1, the ΔT peak moves accordingly to a lower temperature.

Further, the range of temperatures with perceptible electrocaloric effect becomes wider, as random fields increase. It is due to a moderate change of the temperature-induced polarization. These features are in agreement with the experimental observation on $PbSc_{0.5}Ta_{0.5}O_3$ by Correia *et al.* [128].

However, Fig. 8.6(a) also shows that random fields lower the peak value of electrocaloric effect. This is due to the pinning effect of random fields. The mechanism is better explained by comparing the domain structures before and at the end of the adiabatic stage. In the loading

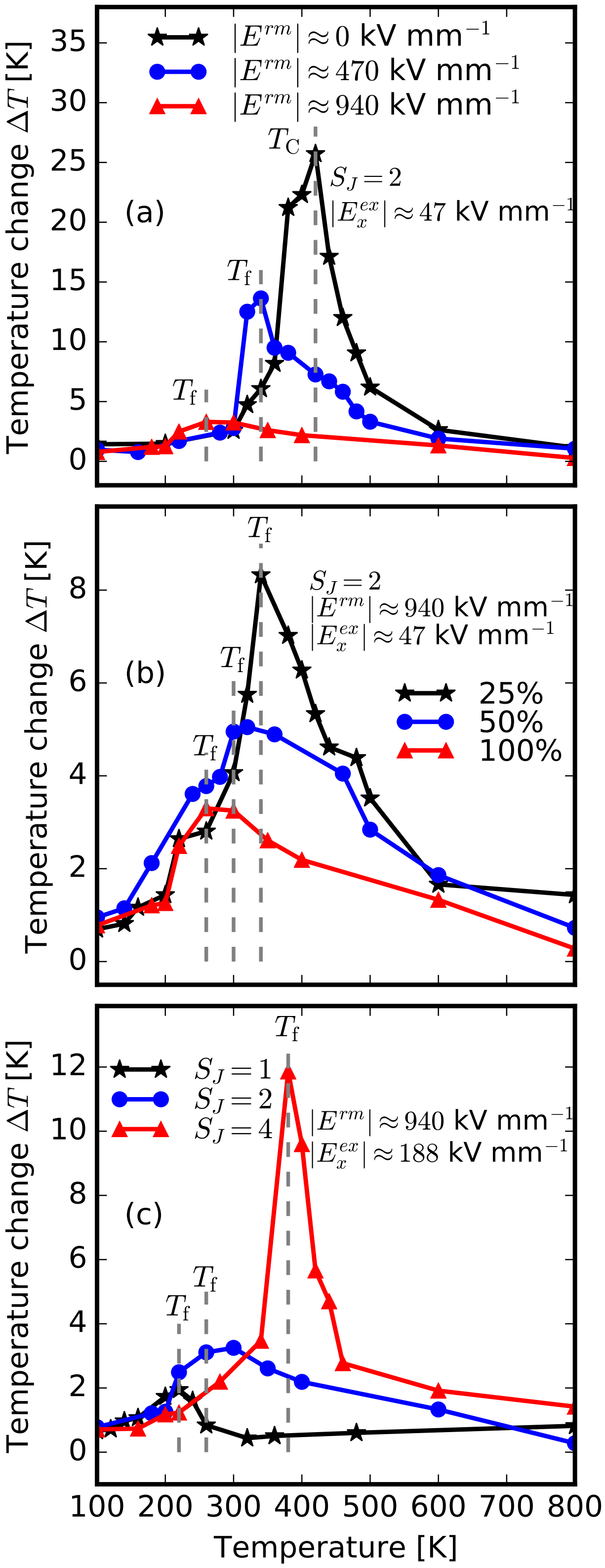

FIGURE 8.6 *Electrocaloric effect of relaxor ferroelectrics: Influence of (a) the strength of the random field $|E^{rm}|$, (b) the density of the random field, and (c) the domain wall energy. When the strength or the density of the random fields increases, the ΔT peak shifts to a lower temperature and the peak value becomes smaller. On the contrary, if the domain wall energy increases, the peak shifts to a higher temperature and the peak value becomes larger.*

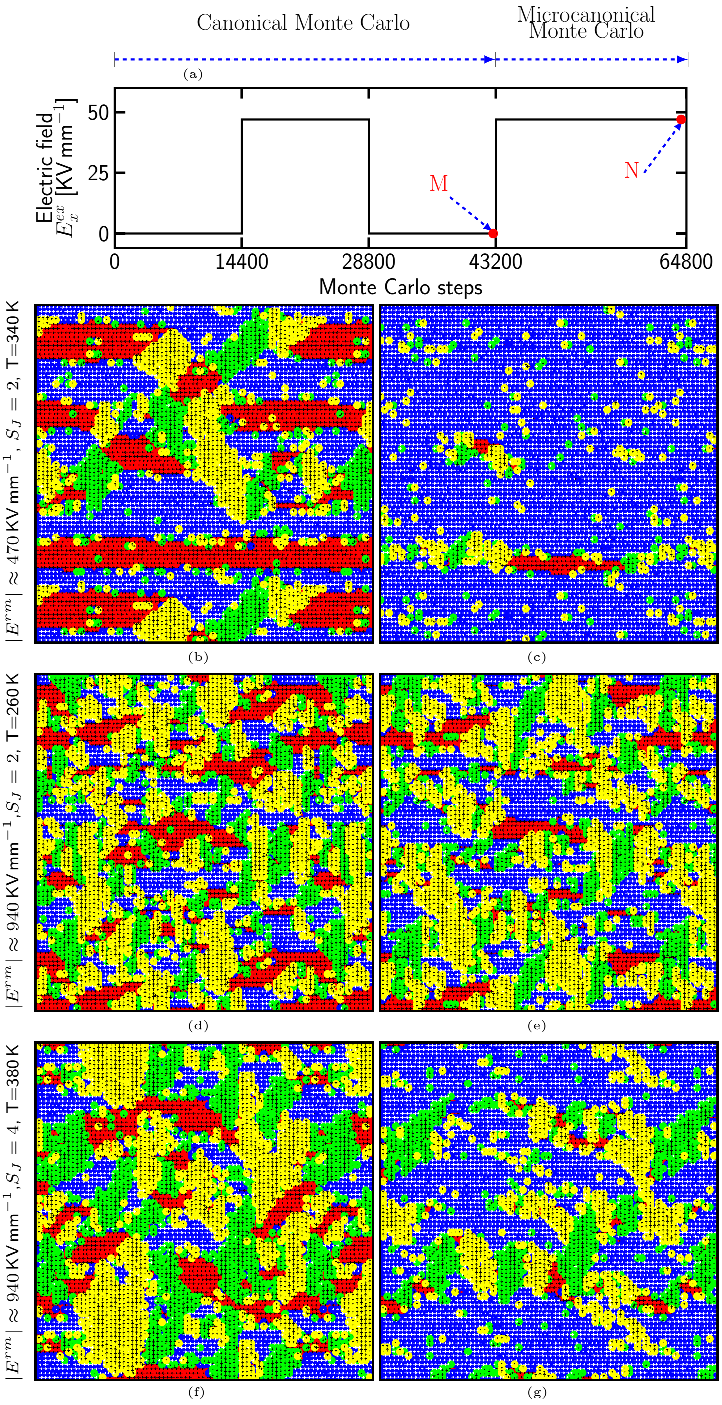

Figure 8.7 *Explanation to the electrocaloric effect influence of the random field and of the domain wall energy by domain structure. (a) shows the loading history for the canonical and microcanonical ensemble. Images (b), (d) and (f) show the domain structures before the adiabatic stage, i.e. the point M in the loading history curve (a). Images (c), (e) and (g) show the domain structures at the end of the adiabatic stage, i.e. the point N in the loading history curve (a). The change of the domain structure from (d) to (e) is less than that from (b) to (c), which implies that the pinning effect increases with the random fields, weakening the electrocaloric effect. On the contrary, the change of the domain structure from (f) to (g) is more than that from (d) to (e), which implies that the large domain wall energy lowers the pinning effect of the random fields, enhancing the electrocaloric effect.*

history of the Monte-Carlo simulations illustrated in Fig. 8.7(a), the point M indicates the time step right before the adiabatic stage, and the point N the time step at the end of the adiabatic stage. When $|E^{rm}| \approx 470\,\mathrm{kV\,mm^{-1}}$ and $S_J = 2$, the largest electrocaloric effect happens at $T = 340K$. For this case, Fig. 8.7 (b) and (c) shows the domain structures at the point M and N, respectively. When the strength of the random field is increased from $470\,\mathrm{kV\,mm^{-1}}$ to $940\,\mathrm{kV\,mm^{-1}}$ and S_J remains untouched, the largest electrocaloric effect appears at $T = 260K$. The corresponding domain structures at the point M and N are shown in Fig. 8.7 (d) and (e), respectively. It is noticeable that the change of the domain structure from Fig. 8.7(d) to (e) is less than that from Fig. 8.7(b) to (c). In other words, when the random field increases, more sites are pinned and cannot rotate to the direction parallel to that of the external field. It leads to less decrease of potential energy and thus less thermal energy change.

The density of random fields has similar influence on the electrocaloric effect as the strength, as shown in Fig. 8.6(b). For all cases in Fig. 8.6(a) random fields are prescribed on each lattice site, i.e. the density of the random field is 100%. When the number of sites with random fields decreases, i.e. the density of the random field decreases, the ΔT peak shifts to higher temperatures. At the same time the ΔT peak value becomes larger. It should be noted that the electrocaloric effect does not decrease linearly with the density. For instance, when the density changes from 0% (namely without random field) to 25%, the ΔT peak value decreases drastically from 27 K to 8 K. Whereas, when the density increases from 50% to 100%, the ΔT peak decreases slightly from 5.5 K to 3 K. This nonlinear phenomenon simply is due to the fact that the lattice sites are not isolated from each other, but rather interact in a short-range fashion due to the domain wall energy and a long-range fashion through the dipole-dipole interaction. The results on the density of the random field indicates that through adjusting the phase volume fraction in composites combining ferroelectrics and relaxor ferroelectrics, the operating temperature range of the electrocaloric effect can be optimized for the desired application.

On the contrary, the domain wall energy affects the electrocaloric effect in a different fashion. Fig. 8.6(c) demonstrates the temperature change in relaxor ferroelectrics for cases with different gradient energy prefactors S_J. In all cases, the external field and the random field remain the same: $|E^{ex}| \approx 47\,\mathrm{kV\,mm^{-1}}$ and $|E^{rm}| \approx 940\,\mathrm{kV\,mm^{-1}}$. It is noticeable in Fig. 8.6(c) that larger S_J leads to a higher peak value and shifts the ΔT peak to a higher temperature. It manifests the importance of ordering factors in electrocaloric effect. Higher ordering leads to a higher nonergodic-ergodic transition point and a higher peak of electrocaloric effect. Higher domain wall energy change leads to a greater potential change and thus more thermal energy change. Similarly, the influence of the domain wall energy can be more clearly explained by the domain structure change before and at the end of the adiabatic stage. As it has been mentioned, Figs. 8.7(d) and (e) show the corresponding domain structures at the loading history point M and N, for the ΔT peak in the case of $|E^{rm}| \approx 940\,\mathrm{kV\,mm^{-1}}$ and $S_J = 2$. When the gradient energy prefactor S_J is increased from 2 to 4, the corresponding domain structures at the loading point M and N are shown in Fig. 8.7 (f) and (g). The change of the domain structure from Fig. 8.7(d) to (e) is less than that from Fig. 8.7(f) to (g). It implies that when the domain wall energy increases, the pinning effect of the random field is counteracted. It leads to a higher potential energy change and thus more thermal energy change.

It can be seen that the effect by reducing the random fields and the effect by increasing the domain wall energy are alike. These results indicate that by adjusting the features of the random field (strength or density) and the domain wall energy, one may optimize the relaxor ferroelectrics in order to lower the operating temperature, broaden the operating temperature range and increase the ΔT peak value at the same time.

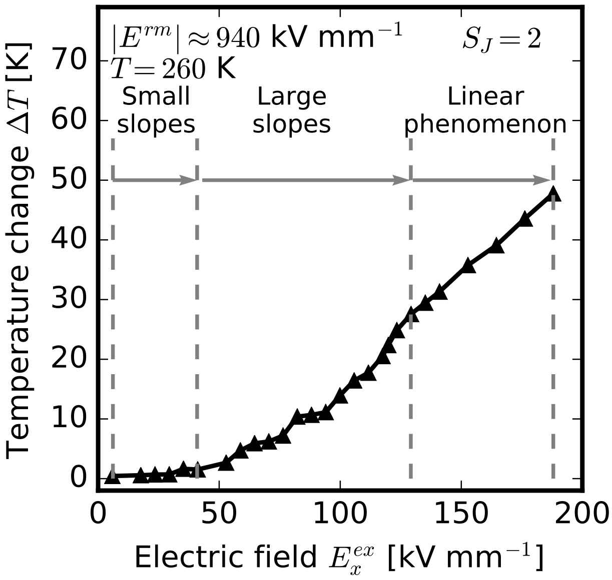

Figure 8.8 *Electrocaloric effect of relaxor ferroelectrics varies with the magnitude of the external electric field at the freezing temperature 260 K for the case with $|E^{rm}| \approx 940\,kV\,mm^{-1}$ and $S_J = 2$. Three different stages appear: 1) At very low field, ΔT is trivial. This is due to the fact that inconsiderable polarization switching is induced. 2) At sufficiently high field, ΔT increases significantly. The slope first increases and then decreases slightly. The big temperature variation can be explained by the remarkable change in potential energy induced by domain wall movement. 3) At very high field, ΔT increases linearly, which results from the monodomain configuration after prepoling.*

Higher external fields induce stronger electrocaloric effect, but the exact dependency is related to the initial temperature. [212] Here we study the case around the freezing temperature, since at this temperature the ΔT peak appears. Fig. 8.8 reveals the dependency of temperature variation on the external field around the freezing temperature 260 K. The temperature change ΔT increases with the field, but three different stages are visible. At the first stage when the external field is very small, the increase of ΔT is hardly noticeable. At the second stage, the temperature variation increases sharply with the external field. The slope first increases and then decreases slightly. At the third stage ΔT increases almost linearly with the field. Similar phenomena were also observed in the experimental work by Hagberg [212] and the theoretical work by Ponomareva and Lisenkov [48]. The reason for the different behavior at the three stages lies on the domain switching. At a sufficiently low field, miniature polarization switching happens, and only the magnitude of the polarization at most sites varies. Therefore, there is no significant change in the dipolar entropy, and thus a weak temperature variation with the electric field appears. When the field is high enough to promote the domain wall movement remarkably, a large change in the dipolar entropy is expected, and thus a strong temperature variation is obtained. Under a very high field, the whole sample is almost prepoled as a single domain before the adiabatic stage. In this way the potential energy change in the adiabatic stage is approximately linear under a linear increase of the external field.

8.2 Relaxors with Random Defect Dipoles

In the previous chapter, by introducing Zr into $BaTiO_3$ the random fields can be induced due to two reasons: two different types of Landau type term for sites occupied by Ti and Zr, and the composition-dependent dipole-dipole interaction strength. In this section, instead of doing that, random fields are induced to reproduce the relaxor behavior by incorporating the frozen random dipoles. In presence of denser frozen dipoles, the hysteresis is slimmer and the electrocaloric effect has a wider application temperature range but a weaker peak.

8.2.1 Model and Setups

Identical to that used in Sec. 4.2, we apply a lattice-based microcanonical Monte-Carlo scheme to directly calculate the electrocaloric effect [188]. This Hamiltonian consists of the potential energy H and the thermal energy H_k. The potential energy H is described by a Ginzburg-Landau type expression which includes four contributions: the Landau multi-well energy term H_D, the dipole-dipole interaction energy H_dip, the domain wall energy H_gr arising from short-range and elastic interactions [126] and the electrostatic energy H_e:

$$H = H_\mathrm{D} + H_\mathrm{dip} + H_\mathrm{gr} + H_\mathrm{e}. \tag{8.2}$$

Due to the presence of static and dynamic random local electric fields long-range ferroelectric order disappears in relaxors [207]. In the present work the external field $\mathbf{E}^{ex}$ is always applied in the x direction. Hereby, random fields $\mathbf{E}^{rm}$ are induced by the introduction of the frozen dipoles with four random directions. The local polarization for the frozen dipoles is assumed as $0.23\,\mathrm{C\,m^{-2}}$, and the sites where these frozen dipoles locate are randomly selected. These frozen dipoles can be assumed to be fully fixed during the process of simulation since the relaxation

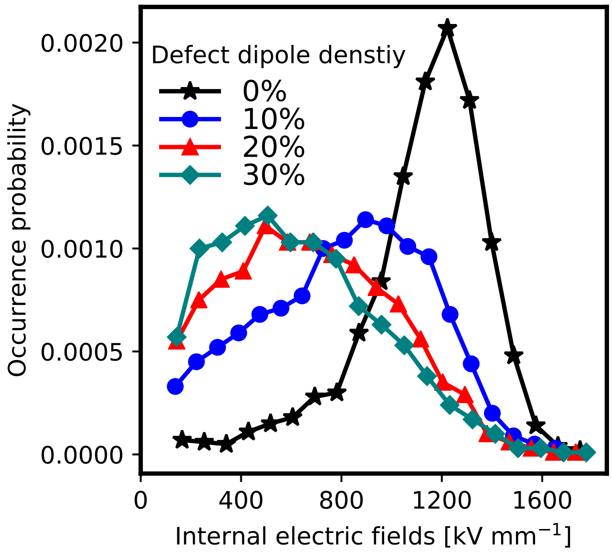

FIGURE 8.9 *Occurrence probability distribution of the absolute internal electric fields. Similar to Fig. 7.6, random fields are generated, however, from the source of random frozen dipoles.*

time for these frozen dipoles is much longer than normal dipoles. Static random fields are induced by these random frozen dipoles, following the equation,

$$\mathbf{E}_\mathrm{i} = V_0 \frac{1}{4\pi\epsilon_0\epsilon_r}\left[\frac{3\mathbf{r}_\mathrm{ij}[\mathbf{P}_\mathrm{d}(\mathbf{r}_j)\cdot\mathbf{r}_\mathrm{ij}]}{|\mathbf{r}_\mathrm{ij}|^5} - \frac{\mathbf{P}_\mathrm{d}(\mathbf{r}_j)}{|\mathbf{r}_\mathrm{ij}|^3}\right], \tag{8.3}$$

where $\mathbf{E}_\mathrm{i}$ is the internal field at site i induced by its neighboring defect dipole $\mathbf{P}_\mathrm{d}(\mathbf{r}_j)$, $\mathbf{r}_\mathrm{ij} = \mathbf{r}_\mathrm{i} - \mathbf{r}_\mathrm{j}$, ϵ_0 is the vacuum permittivity and ϵ_r is the relative high-frequency permittivity. Correspondingly, the occurrence probability distribution of the absolute internal fields can be calculated, as shown in Fig. 8.9. It should be noted hereby random frozen dipoles are an alternative source of random fields, comparing with Fig. 7.6. This further proves that it is reasonable to utilize random field theory to mimic the relaxor behavior as performed in the previous section.

Canonical and microcanonical Monto Carlo together with the simulation parameters utilized in the simulation as shown in Sec. 4.3. For simplicity, single crystal material is studied with periodic condition, and merely with the tetragonal and cubic phases in $BaTiO_3$.

8.2.2 Results and Discussion

At T =100, 200 or 300 K the dielectric hystereses are shown in Fig. 8.10, for $BaTiO_3$ with different frozen dipoles. Thermal fluctuation of the polarization becomes stronger when the temperature is higher. Simultaneously, at the sites close to the frozen dipoles, the induced internal field becomes random since these frozen dipoles sites and the direction of the frozen dipoles are randomly selected. Thus, under the sinusoidal external electric field, these frozen dipoles ease the difficulty of switching the dipoles to the direction of $\mathbf{E}^{ex}$, i.e. these frozen dipoles

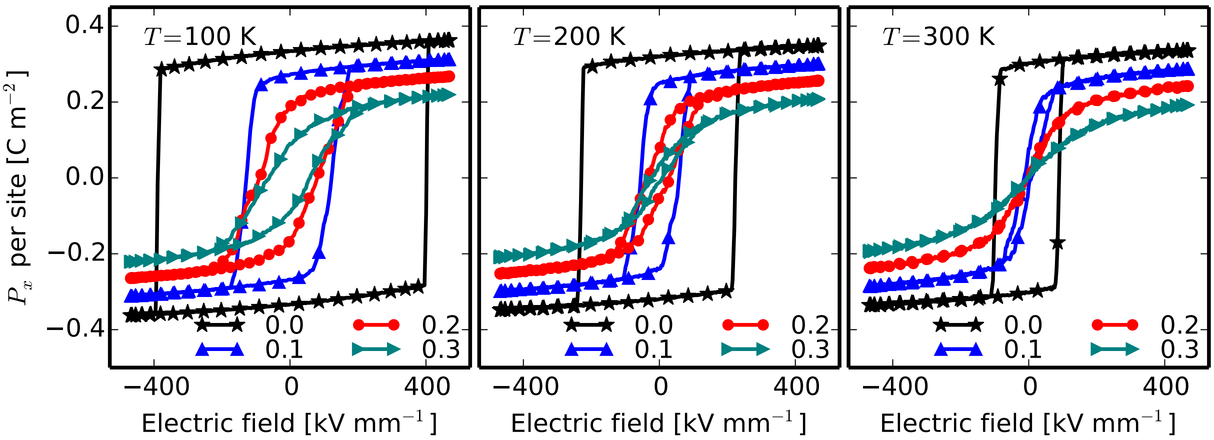

FIGURE 8.10 *The influence of the density of the frozen dipoles and the temperature on the dielectric hysteresis. By increasing the temperature or the density of the frozen dipoles, the hysteresis loops become thinner, i.e. with lower remnant & saturation polarization and smaller coercive field. Hereby, when the density is above 0.2, a typical relaxor-type hysteresis is present.*

act as the nucleation sources of reversed domains. As a result, by elevating the temperature or the density of the frozen dipoles, the hysteresis become slimmer, i.e. the saturation polarization P_s, the remnant polarization P_r and the coercive field E_c decrease. These results support the argument that defect dipoles can be responsible for the aging behavior of ferroelectrics.

For pure $BaTiO_3$ or $BaTiO_3$ with 10% density of the frozen dipoles, the hysteresis still remains a ferroelectrics-type with quite steep polarization switching around E_c. When the density of the frozen dipoles is increased to 20%, the hysteresis involves into a relaxor-type with small P_r and E_c. The values of P_r and E_c are finite at 200 K while almost 0 at 300 K, which indicates the transition from the nonergodic to ergodic state. If the density of the frozen dipoles increases further, the above phenomenon is even more prominent.

Fig. 8.11 reveals the influence of the density of the frozen dipoles on the electrocaloric effect at different temperatures. The transition temperature from the tetragonal to cubic phase or from the nonergodic to ergodic state appears at the point, where the extent of order changes sharply. In the case without the frozen dipoles or with low density of them, the extent of order, i.e. the potential energy, changes fairly sharply at the transition temperature. Correspondingly, high thermal energy, i.e. high temperature is required to achieve this sharp change of the extent of order. By contrast, in the case with high density of the frozen dipoles, the potential energy changes less sharply since the induced internal random fields increase the disorder of the structure. In other words, less thermal energy, i.e. lower temperature, is required to fulfill the phase or state transition. The ΔT peak appears at the transition point from the tetragonal to cubic phase or from the nonergodic to ergodic state. It is straightforward to deduce that upon increasing the density of the frozen dipoles, the ΔT peak is shifted to lower temperature.

Apart from the shift of the ΔT peak position, in Fig. 8.11 the ΔT peak value is observed to slump down with the increase of the frozen dipoles. Further explanation for this phenomenon

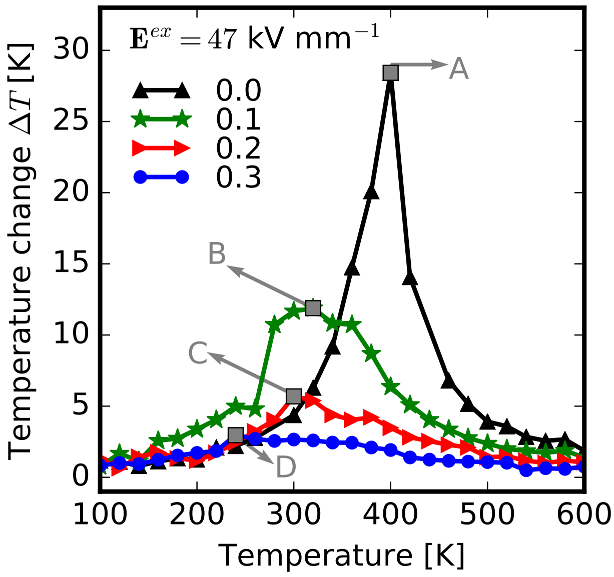

FIGURE 8.11 *Electrocaloric effect: influence of the density of the frozen dipoles. When the density of the frozen dipoles increases, the ΔT peak shifts to a lower temperature, the peak value becomes smaller and the operation temperature becomes wider. Domain structures for the ΔT peaks marked as A, B, C and D are illustrated in Fig. 8.12 for further explanation.*

is illustrated by the domain structures in Fig.8.12. In the initial state (the prepoled sample), the dipolar entropy S_{dip} is apparently higher in pure BaTiO$_3$ than in BaTiO$_3$ with 10% frozen dipoles (see Figs. 8.12(a) and (c)). Nonetheless, at the end of the adiabatic stage, similar domain structures and comparable S_{dip} are revealed for both cases (see Figs. 8.12(b) and (d)). Briefly, the variation of S_{dip}, i.e. the variation of the temperature, in BaTiO$_3$ is bigger than in BaTiO$_3$ with 10% frozen dipoles.

The frozen dipoles have four random directions, with equal probability in each direction. Among them only 25% of these dipoles lies in parallel to the external field in the adiabatic process. The polarization at other 75% of these sites is energetically unstable, and is more fluctuating under external field. Thus, the configurational space is mainly sampled in the neighbor sites of these frozen dipoles. For the presence of the long-range interaction, the number of the sites responsible for the configurational space N_{eff} increases much more than linearly with the increase of frozen dipoles (see Figs.8.12(b), (d), (f) and (h)). When the density of the frozen dipoles is not so high (≤ 0.3), it signifies the sharp declination of the temperature variation. N_{eff} might reach saturation, and the drop of the ΔT peak should be moderate by further increasing the density of the frozen dipoles, which is however beyond the current work.

Additionally, depending on the densities of the frozen dipoles different operation temperature ranges are present. A fairly narrow operation temperature range appears in pure BaTiO$_3$. With more frozen dipoles, the operation temperature range becomes wider and wider.

Through the incorporation of the random frozen dipoles, random fields are induced, which can represent the feature of the relaxors. It can be observed that upon increasing the density

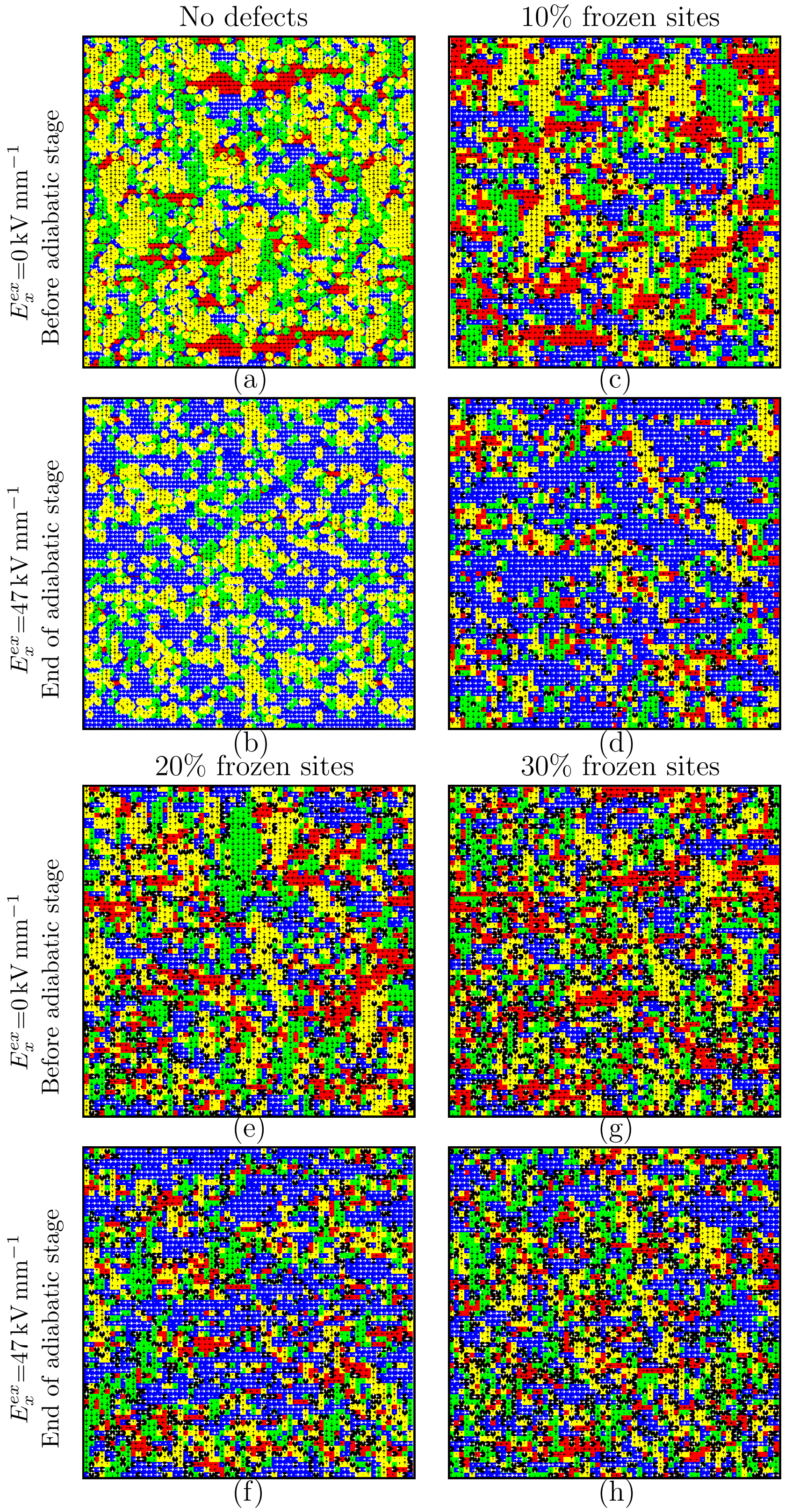

Figure 8.12 *Domain structure explanation of electrocaloric effect for the points A, B, C and D marked in Fig. 8.11. The external field is applied in the horizontal direction and points to the right. (a) and (b) are the domain structure snapshots before and after the adiabatic stage for the point A; (c) and (d) for point B; (e) and (f) for point C; (g) and (h) for point D. The black dots with white arrows represent the frozen dipoles. The red, blue, yellow and green dots represent the dipoles pointing respectively to the left, to the right, to the top and to the bottom.*

of the frozen dipoles, the hysteresis begins to show a relaxor-type. Furthermore, with higher density of the frozen dipoles, it can be observed that the ΔT peak position shifts to lower temperature, the peak value slumps down, and the operation temperature range becomes wider.

It should be noted that the frozen dipoles in the current model is non-switchable. A more realistic model with switchable frozen dipoles should be developed in the future.

8.3 Summary

In this chapter, by modifying the statistical Monte-Carlo model in Chap. 4 for $BaTiO_3$, we presented generic models on basis of Ginzburg-Landau free energy to study polarization switching and electrocaloric effect in relaxors.

In the first section, static random fields were introduced to characterize the effect of chemical disorder in the material. The paraelectric-to-ferroelectric transitions and the nonergodic-to-ergodic state transitions, which have strong influence on the electrocaloric effect, are naturally incorporated through the Monte-Carlo algorithm, and thus there is no need to prescribe the transition temperatures as in phenomenological models.

As influential factors of electrocaloric effect, the temperature-induced polarization change, the nonergodic-to-ergodic state transformation and the polarization switching in relaxor ferroelectrics are first studied. Our results show that in the presence of random fields the temperature-induced polarization change is moderate, rather than sharp as in the case of conventional ferroelectrics (see Fig. 8.3). It also lowers the freezing temperature (see Fig. 8.4). The introduction of random fields leads to miniaturization of domain size and a relaxor ferroelectrics type hysteresis (see Fig. 8.5). Our results also reveal that both the density and the magnitude of the random fields influence the hysteresis shape.

By means of microcanonical Monte-Carlo simulations, the electrocaloric effect in relaxor ferroelectrics was studied (see Fig. 8.6). Our results demonstrate that the higher the random field strength is, or the denser the random field distribution is, the lower the ΔT peak becomes. Thereby the point where the peak appears shifts to the lower temperature, due to the decrease of the freezing temperature. On the other hand, the gradient energy, i.e. the domain wall energy, elevates the ΔT peak value and the temperature where it appears. It can be concluded that the electrocaloric effect is favored by ordering, while suppressed by disordering originated from such as the paraelectric phase and the random fields. Finally, we show that the electrocaloric effect increases in three different stages with the strength of the applied external field.

In Chap. 7 for the investigation of $BaZr_xTi_{1-x}O_3$, random fields are induced by prescribing double/single well Landau type ground state energies to Ti/Zr located unit cells and the composition-dependent long-range dipole-dipole interaction strength. It was revealed that random fields might be responsible for the crossover from ferroelectrics, relaxors, dipolar clusters to paraelectrics. Alternatively, in the second section of this chapter, for simplicity random frozen defect dipoles were introduced, which, however, in reality should be switchable. In this way randoms field are induced (see Fig. 8.9), and the relaxor behavior is reproduced. Namely, the hysteresis becomes slimmer, the peak of the electrocaloric effect drops, the application temperature widens and the peak position shifts to a lower temperature due to the pinning effect (see Figs. 8.10-8.12). This agrees with the results in the first section.

Chapter 9

Conclusions and Outlook

9.1 Conclusion

In this thesis the electrocaloric effect was intensively investigated to reveal ways to optimize the role of entropy changes in the electrocaloric cycle, the influence of defect dipoles and the potential application of relaxors.

Due to the existing drawbacks of the indirect method, the direct method is utilized to investigate the electrocaloric effect. The corresponding lattice-based Monte-Carlo simulations with Ginzburg-Landau type effective Hamiltonian are developed in Chap. 4. By combining canonical and microcanonical Monte-Carlo algorithms the electrocaloric effect can be directly evaluated. The model describes the ferroelectric features like the ground Landau energy, the domain wall energy arising from short-range and elastic interactions, the long-range dipole-dipole interaction energy, and the electrostatic energy.

In Chap. 5 the analytical model of entropy changes with the information of work loss in the irreversible process and the Monte-Carlo simulations with the explanation on the domain structure level are utilized to optimize the electrocaloric cycle. The results reveal that the electrocaloric effect in ferroelectrics can be enhanced by a proper reversed electric field and the optimal reversed field is around the shoulder of the hysteresis. This finding signifies the importance of considering the total entropy change arising from the irreversible process under adiabatic conditions in the study of electrocaloric cycles. The theory, simulation and experiments show very good qualitative agreement.

Similarly, in Chap. 6 with the information of entropy changes and the explanation on the level of domain structures, the influence of defect dipoles on the electrocaloric effect is investigated. Internal fields are induced by defect dipoles arising from the associates of the acceptors and the oxygen vacancies, which act as “memory elements" and change the profile of the electrocaloric effect significantly. The ΔT peak is shifted to higher temperatures with lower peak values when introducing defect dipoles parallel to the external field. In contrast, the electrocaloric effect can transfer from the conventional to inverse when the internal fields induced by the anti-parallel defect dipoles are stronger than the external electric field. The cooling efficiencies of electrocaloric devices can be enhanced through delicately controlling the direction and the magnitude of defect dipoles and the external field.

From Chap. 7 to Chap. 8 the relaxor ferroelectrics are studied. Even though different models are utilized, all results prove that the origin of relaxor behaviors can be attributed to the existence of randoms fields.

In Chap. 7, the electrocaloric effect and the relaxor behavior of $BaZr_xTi_{1-x}O_3$ are investigated as function of Zr content, computationally and experimentally. In $BaZr_xTi_{1-x}O_3$ cells containing sites occupied by Ti are described by a multi-well Landau type as in $BaTiO_3$. However, different from $BaTiO_3$, sites occupied by Zr are described by a single-well Landau type in $BaZr_xTi_{1-x}O_3$. Simultaneously, in $BaZr_xTi_{1-x}O_3$ the high-frequency permittivity, which reflects the inverse of the dipole-dipole interaction strength, is assumed to be a composition-dependent parameter rather than is treated as a constant value as in $BaTiO_3$. In experiment, $BaTiO_3$, $BaZr_{0.12}Ti_{0.88}O_3$, and $BaZr_{0.2}Ti_{0.8}O_3$ ceramics are studied. The domain patterns are revealed by Piezoresponse Force Microscopy, together with the hysteresis and the electrocaloric effect at various temperatures.

Three distinct composition dependent regimes can be identified with increasing Zr content: the big domain size in the ferroelectric phase with $0.0 \leq x \leq 0.2$, the small domain size in relaxor ferroelectric phase with $0.3 \leq x \leq 0.7$, and dipolar clusters or paraelectric phase with $x \geq 0.8$. According to the polarization profile in the domain structures, the internal fields are calculated. It shows that the relaxor behavior is related to the magnitude of the average internal fields and the relative standard deviation of the internal fields distribution. Meanwhile, the shape of hysteresis changes from fat, slim to linear when transferring from ferroelectric, relaxor ferroelectric to the phase of dipolar cluster. Simultaneously, the peak of the electrocaloric effect experiences a sharp drop within the ferroelectric phase, a moderate drop within relaxor ferroelectric phase, and very weak peaks or no peak can exist within dipolar clusters or paraelectric phase. Also, the peak position of the electrocaloric effect shifts to lower temperature with increasing Zr content. The phenomena are interpreted explicitly by the domain patterns. It presents a good qualitative consistence between the phenomena observed in simulation and experiment.

In Chap. 8, a generic model is developed for relaxor ferroelectrics by incorporating the coupling of random fields to the polarization in the electrostatic energy. The case without and with static random local electric fields is utilized to present ferroelectrics and relaxor ferroelectrics concept individually. We investigate some significant factors, which influence the switching behavior and the electrocaloric effect in ferroelectrics and relaxor ferroelectrics. For ferroelectrics, firstly the higher gradient energy drives the phase transition point to a higher temperature, and it demonstrates a sharp phase transition around the phase transition temperature. Secondly, when polarization switches, it is apparent to visualize the domain wall moving and strong remnant polarization. In contrast, for relaxor ferroelectrics, it demonstrates a moderate temperature-induced polarization change, and the freezing temperature decreases with increasing random fields. Furthermore, we can observe the domain nucleation at random site and the weak remnant polarization. These phenomena become more prominent when the magnitude of random fields becomes larger or the density of random fields becomes higher. In the evaluation of the electrocaloric effect, for ferroelectrics or relaxor ferroelectrics, we observe the highest temperature change near the Curie temperature or the freezing temperature, and the higher magnitude of external electric field means higher temperature variation. For relaxor ferroelectrics, the higher magnitude or the higher density of random fields drives the peak of electrocaloric effect to a lower temperature range, and the peak value becomes smaller. On the contrary, if the domain wall energy increases, the peak shifts to a higher temperature, and the peak value becomes larger.

Simultaneously, in Chap. 8 through incorporation of the random frozen dipoles, random fields are introduced to represent the relaxor ferroelectrics due to the presence of long-range dipole-dipole interaction and short-range gradient energy term. A relaxor-type hysteresis appears upon introducing 20% density of frozen dipoles. Additionally, higher density of frozen dipoles results in the shifting of the peak position of the electrocaloric effect to a lower temperature, lowering the peak values, widening the operation temperature range.

In summary, our research reveals the importance of considering irreversible processes in electrocaloric cycles, the existence of the inverse electrocaloric effect tailoring by defect dipoles, the significant role of random fields to represent the relaxor behavior, and the important feature of the wide application temperature of relaxor ferroelectrics.

9.2 Outlook and Challenges

In short, the electrocaloric effect was investigated by us and other researchers from many aspects. However, there are still plentiful of unsettled questions and challenges, deserving more intense investigations [2].

For example, in antiferroelectrics the role of different contributions to the electrocaloric effect, e.g., the latent heat and the work done by external field, are not explicitly revealed yet. Also, the phenomena of the electrocaloric effect near the morphotropic phase boundary in some ferroelectric materials are complex, e.g., there exists inverse electrocaloric effect due to the phase-transition, and they need to be explained by theory succinctly.

At the same time, the simulation model should be further developed with more physically related energy terms so that the complex phenomena in the electrocaloric effect can be interpreted clearly, and more interesting phenomena can be properly predicted.

In this thesis, due to the high computational cost Monte-Carlo simulations are performed in 2-dimensional space to reveal some underlying physics in the electrocaloric effect, and a full 3-dimensional calculation should be put on schedule to present real material behavior. Due to the expensive computation cost for the long-range interaction, optimizing the parallel-computing codes will be a tough job, and a proper postprocessing code for the results in 3-dimensional space should be also developed.

Also, for simplification the mechanical coupling, which is a essential feature in ferroelectric materials, is ignored in this thesis. In order to investigate the mechanical related properties, the mechanical coupling should be introduced, and the model should be further developed. However, in most cases the stress/strain field is inhomogeneous in the materials, and the finite difference method is not a very suitable tool to solve complex mechanical problems, which might lead to some difficulties.

Moreover, in multiferroics there exists the multi-caloric effect, which has a high potential for wide application and deserves developing a new model to describe its behavior. Several impediment mights arise here, e.g., the inaccessibility of the material coefficients and the immature understanding on multiferroics.

Furthermore, from the aspect of the structure, the multi-layer capacitors represent a potentially ideal embodiment of the electrocaloric effect [2], which attracts the interest of the theoretical community, and poses new challenges as well since in general the material behavior at the inter-layer is well difficult to predict and understand.

At last, sooner or later the caloric effect should enter the application market. Hence, in order to predict the property of the final product, the multi-scale simulation, which covers the device scale and the materials scale, should be taken into consideration. There are some possible obstacles, e.g., the difficulty of constructing a reasonable multi-scale model and the increasing computation cost.

In summary, even though a lot of work has been done, more time and vigor should be given to deepen the understanding of the electrocaloric effect, and it might be still a long way to construct a device with considerable efficiency and bring the devices into the commercial markets.

Bibliography

[1] A. S. Mischenko, Q. Zhang, J. F. Scott, R. W. Whatmore, and N. D. Mathur, Science **311**, 1270 (2006).

[2] *Electrocaloric Materials*, edited by T. Correia and Q. Zhang (Springer-Verlag, Berlin, Heidelberg, 2014).

[3] O. V. Pakhomov, S. F. Karmanenko, A. A. Semenov, A. S. Starkov, and A. V. Es'kov, Tech. Phys. **55**, 1155 (2010).

[4] C. Zimm, A. Jastrab, A. Sternberg, V. Pecharsky, K. G. Jr, M. Osborne, and I. Anderson, in *Advances in Cryogenic Engineering*, edited by P. Kittel (Springer-Verlag, New York, 1998), pp. 1759–1766.

[5] J. Scott, Annu. Rev. Mater. Res. **41**, 229 (2011).

[6] P. Kobeko and J. Kurtschatov, Z. Physik **66**, 192 (1930).

[7] X. Moya, S. Kar-Narayan, and N. D. Mathur, Nat. Mater. **13**, 439 (2014).

[8] L. Mañosa, A. Planes, and M. Acet, J. Mater. Chem. A **1**, 4925 (2013).

[9] B. Neese, B. Chu, S.-G. Lu, Y. Wang, E. Furman, and Q. M. Zhang, Science **321**, 821 (2008).

[10] L. Liu, Y. Liu, B. Li, and J. Leng, Appl. Phys. Lett. **99**, 181908 (2011).

[11] M. Ožbolt, A. Kitanovski, J. Tušek, and A. Poredoš, Int. J. Refrig. **37**, 16 (2014).

[12] S. Qian, D. Nasuta, A. Rhoads, Y. Wang, Y. Geng, Y. Hwang, R. Radermacher, and I. Takeuchi, Int. J. Refrig. **62**, 177 (2016).

[13] S. Kar-Narayan and N. D. Mathur, Appl. Phys. Lett. **95**, (2009).

[14] S. Kar-Narayan and N. D. Mathur, J. Phys. D: Appl. Phys. **43**, 032002 (2010).

[15] S. Fähler, U. K. Rößler, O. Kastner, J. Eckert, G. Eggeler, H. Emmerich, P. Entel, S. Müller, E. Quandt, and K. Albe, Adv. Eng. Mater. **14**, 10 (2012).

[16] G. Akcay, S. P. Alpay, J. V. Mantese, and G. A. Rossetti Jr, Appl. Phys. Lett. **90**, 252909 (2007).

[17] G. Akcay, S. P. Alpay, G. A. Rossetti Jr, and J. F. Scott, J. Appl. Phys. **103**, 024104 (2008).

[18] J. H. Qiu and Q. Jiang, J. Appl. Phys. **103**, 034119 (2008).

[19] J. H. Qiu and Q. Jiang, Eur. Phys. J. B **71**, 15 (2009).

[20] J. Zhang, A. A. Heitmann, S. P. Alpay, and G. A. Rossetti, Integr. Ferroelectr. **125**, 168 (2011).

[21] Y. P. Shi and A. K. Soh, Acta Mater. **59**, 5574 (2011).

[22] J. Zhang, I. B. Misirlioglu, S. P. Alpay, and G. A. Rossetti Jr, Appl. Phys. Lett. **100**, 222909 (2012).

[23] N. Novak, B. Rožič, J. Holc, M. Kosec, R. Pirc, and Z. Kutnjak, Ferroelectrics **426**, 223 (2012).

[24] M. A. Hamad, J. Adv. Ceram. **2**, 308 (2013).

[25] J. Liu, W. Chen, B. Wang, and Y. Zheng, Materials **7**, 6502 (2014).

[26] Y.-B. Ma, N. Novak, K. Albe, and B.-X. Xu, Appl. Phys. Lett. **109**, 202906 (2016).

[27] B. Li, J. B. Wang, X. L. Zhong, F. Wang, Y. K. Zeng, and Y. C. Zhou, EPL **102**, 47004 (2013).

[28] B. Li, J. B. Wang, X. L. Zhong, F. Wang, B. L. Liu, and Y. C. Zhou, J. Nanopart. Res. **15**, 1427 (2013).

[29] Y. Liu, J. Wei, P.-E. Janolin, I. C. Infante, X. Lou, and B. Dkhil, Appl. Phys. Lett. **104**, 162904 (2014).

[30] J. Wang, M. Liu, Y. Zhang, T. Shimada, S.-Q. Shi, and T. Kitamura, J. Appl. Phys. **115**, 164102 (2014).

[31] J. Y. Lee, A. K. Soh, H. T. Chen, and L. Hong, J. Mater. Sci. **50**, 1382 (2015).

[32] Y. K. Zeng, B. Li, J. B. Wang, X. L. Zhong, W. Wang, F. Wang, and Y. C. Zhou, RSC Adv. **4**, 30211 (2014).

[33] H.-H. Wu, J. Zhu, and T.-Y. Zhang, Phys. Chem. Chem. Phys. **17**, 23897 (2015).

[34] H.-H. Wu, J. Zhu, and T.-Y. Zhang, Nano Energy **16**, 419 (2015).

[35] H.-H. Wu, J. Zhu, and T.-Y. Zhang, RSC Adv. **5**, 37476 (2015).

[36] S. Lisenkov and I. Ponomareva, Phys. Rev. B **80**, 140102 (2009).

[37] S. P. Beckman, L. F. Wan, J. A. Barr, and T. Nishimatsu, Mater. Lett. **89**, 254 (2012).

[38] T. Nishimatsu, J. A. Barr, and S. P. Beckman, J. Phys. Soc. Jpn. **82**, 114605 (2013).

[39] M. C. Rose and R. E. Cohen, Phys. Rev. Lett. **109**, 187604 (2012).

[40] E. Glazkova, C.-M. Chang, S. Lisenkov, B. K. Mani, and I. Ponomareva, Phys. Rev. B **92**, 064101 (2015).

[41] A. Grünebohm and T. Nishimatsu, Phys. Rev. B **93**, 134101 (2016).

[42] R. Pirc, Z. Kutnjak, R. Blinc, and Q. M. Zhang, J. Appl. Phys. **110**, 074113 (2011).

[43] L. J. Dunne, M. Valant, A.-K. Axelsson, G. Manos, and N. M. Alford, J. Phys. D: Appl. Phys. **44**, 375404 (2011).

[44] H.-X. Cao and Z.-Y. Li, J. Appl. Phys. **106**, 094104 (2009).

[45] R. Blinc, V. Smolej, B. Žekš, I. Levstek, and B. B. Lavrenčič, Ferroelectrics **7**, 203 (1974).

[46] Y. Liu, J. F. Scott, and B. Dkhil, Appl. Phys. Rev. **3**, 031102 (2016).

[47] A.-K. Axelsson, F. L. Goupil, L. J. Dunne, G. Manos, M. Valant, and N. M. Alford, Appl. Phys. Lett. **102**, 102902 (2013).

[48] I. Ponomareva and S. Lisenkov, Phys. Rev. Lett. **108**, 167604 (2012).

[49] M. Creutz, Phys. Rev. Lett. **50**, 1411 (1983).

[50] M. Creutz, A. Gocksch, M. Ogilvie, and M. Okawa, Phys. Rev. Lett. **53**, 875 (1984).

[51] J. Valasek, Phys. Rev. **17**, 475 (1921).

[52] K. C. Kao, *Dielectric Phenomena in Solids* (Academic Press, San Diego, 2004), pp. 213–282.

[53] A. Devonshire, Adv. Phys. **3**, 85 (1954).

[54] D. Damjanovic, Rep. Prog. Phys. **61**, 1267 (1998).

[55] G. H. Haertling, J. Am. Ceram. Soc. **82**, 797 (1999).

[56] E. Buixaderas, S. Kamba, and J. Petzelt, Ferroelectrics **308**, 131 (2004).

[57] M. Dawber, K. M. Rabe, and J. F. Scott, Rev. Mod. Phys. **77**, 1083 (2005).

[58] N. Setter, D. Damjanovic, L. Eng, G. Fox, S. Gevorgian, S. Hong, A. Kingon, H. Kohlstedt, N. Y. Park, G. B. Stephenson, I. Stolitchnov, A. K. Taganstev, D. V. Taylor, T. Yamada, and S. Streiffer, J. Appl. Phys. **100**, 051606 (2006).

[59] M. E. Lines and A. M. Glass, *Principles and Applications of Ferroelectrics and Related Materials* (OUP Oxford, New york, US, 1977).

[60] K. Rabe, C. Ahn, and J.-M. Triscone, *Physics of Ferroelectrics. A Modern Perspective* (Springer-Verlag, Berlin, Germany, 2008).

[61] A. Tagantsev, L. Cross, and J. Fousek, *Domains in Ferroic Crystals and Thin Films* (Springer, New York, 2010), pp. 521–711.

[62] W. P. Mason and B. T. Matthias, Phys. Rev. **74**, 1622 (1948).

[63] B. Matthias and A. von Hippel, Phys. Rev. **73**, 1378 (1948).

[64] A. Kontsos and C. M. Landis, J. Appl. Mech **77**, 041014 (2010).

[65] G. A. Samara, J. Phys.: Condens. Matter **15**, R367 (2003).

[66] D. Fu and M. Itoh, in *Ferroelectric Materials - Synthesis and Characterization*, edited by A. Peláiz-Barranco (InTech, Online, 2015).

[67] R. Meyer, L. Liebert, L. Strzelecki, and P. Keller, J. Phys. Lett. **36**, 69 (1975).

[68] Y. Bai, X. Han, X.-C. Zheng, and L. Qiao, Sci. Rep. **3**, 2895 (2013).

[69] Y. Bai, G.-P. Zheng, K. Ding, L. Qiao, S.-Q. Shi, and D. Guo, J. Appl. Phys. **110**, 094103 (2011).

[70] X. Ren, Nat. Mater. **3**, 91 (2004).

[71] R.-A. Eichel, J Electroceram **19**, 11 (2007).

[72] B. Jaffe, W. Cook, and H. Jaffe, *Piezoelectric Ceramics* (Academic, London, UK, 1971).

[73] P. Erhart, P. Träskelin, and K. Albe, Phys. Rev. B **88**, 024107 (2013).

[74] G. H. Jonker and P. V. Lambeck, Ferroelectrics **21**, 641 (1978).

[75] W. A. Schulze and K. Ogino, Ferroelectrics **87**, 361 (1988).

[76] D. M. Smyth, M. P. Harmer, and P. Peng, J. Am. Ceram. Soc. **72**, 2276 (1989).

[77] D. M. Smyth, Current Opinion in Solid State and Materials Science **1**, 692 (1996).

[78] C. Elissalde and J. Ravez, J. Mater. Chem. **11**, 1957 (2001).

[79] V. Gopalan, V. Dierolf, and D. A. Scrymgeour, Annu. Rev. Mater. Res. **37**, 449 (2007).

[80] Y. A. Genenko, J. Glaum, M. J. Hoffmann, and K. Albe, Mater. Sci. Eng. B **192**, 52 (2015).

[81] G. Arlt and H. Neumann, Ferroelectrics **87**, 109 (1988).

[82] W. L. Warren, K. Vanheusden, D. Dimos, G. E. Pike, and B. A. Tuttle, J. Am. Ceram. Soc. **79**, 536 (1996).

[83] Y. Yu and R. N. Singh, J. Appl. Phys. **94**, 7250 (2003).

[84] L. X. Zhang, W. Chen, and X. Ren, Appl. Phys. Lett. **85**, 5658 (2004).

[85] A. Picinin, M. H. Lente, J. A. Eiras, and J. P. Rino, Phys. Rev. B **69**, 064117 (2004).

[86] W. Zhang and K. Bhattacharya, Acta Mater. **53**, 199 (2005).

[87] P. J. Schorn, U. Böttger, and R. Waser, Appl. Phys. Lett. **87**, 242902 (2005).

[88] B. Li, G. Li, Q. Yin, Z. Zhu, A. Ding, and W. Cao, J. Phys. D: Appl. Phys. **38**, 1107 (2005).

[89] L. Zhang and X. Ren, Phys. Rev. B **73**, 094121 (2006).

[90] J.-M. Liu, S. T. Lau, H. L. W. Chan, and C. L. Choy, J Mater Sci **41**, 163 (2006).

[91] D. Lin, K. W. Kwok, and H. L. W. Chan, Appl. Phys. Lett. **90**, 232903 (2007).

[92] Z. Feng and X. Ren, Phys. Rev. B **77**, 134115 (2008).

[93] C. M. Folkman, S. H. Baek, C. T. Nelson, H. W. Jang, T. Tybell, X. Q. Pan, and C. B. Eom, Appl. Phys. Lett. **96**, 052903 (2010).

[94] H. Zhang, X. Deng, T. Li, W. Zhang, R. Chen, W. Tian, J. Li, X. Wang, and L. Li, Appl. Phys. Lett. **97**, 162913 (2010).

[95] S. Yun, J. Shi, and X. Qian, Mater. Chem. Phys. **133**, 487 (2012).

[96] Z. Feng, Z. Cheng, D. Shi, and S. Dou, AIP Adv. **3**, 062105 (2013).

[97] Y. Q. Tan, J. L. Zhang, and C. L. Wang, Adv. Appl. Ceram. **113**, 223 (2014).

[98] X. Zhao, W. Chen, L. Zhang, J. Gao, and L. Zhong, Appl. Phys. A **118**, 931 (2014).

[99] Y. Ichikawa, Y. Kitanaka, T. Oguchi, Y. Noguchi, and M. Miyayama, J. Ceram. Soc. Jpn. **122**, 373 (2014).

[100] N. V. Dang, N. T. Dung, P. T. Phong, and I.-J. Lee, Phys. B **457**, 103 (2015).

[101] J. Van Vechten, *Dielectic Refrigerator Using Orientable Defect Dipoles* (Google Patents, US, 1979), uS Patent 4,136,525.

[102] J. A. Smolenskii and V. A. Usupov, Zh Tekh Fiz **24**, 1375 (1954).

[103] L. E. Cross, Ferroelectrics **76**, 241 (1987).

[104] L. E. Cross, Ferroelectrics **151**, 305 (1994).

[105] A. A. Bokov and Z.-G. Ye, J. Mater. Sci. **41**, 31 (2006).

[106] L. E. Cross, *Piezoelectricity*, No. 114 in *Springer Series in Materials Science* (Springer, Berlin Heidelberg, 2008), pp. 131–155.

[107] V. V. Shvartsman, J. Zhai, and W. Kleemann, Ferroelectrics **379**, 77 (2009).

[108] A. A. Bokov and Z.-G. Ye, J. Adv. Dielect. **02**, 1241010 (2012).

[109] V. V. Shvartsman and D. C. Lupascu, J. Am. Ceram. Soc. **95**, 1 (2012).

[110] N. Setter and L. E. Cross, J. Appl. Phys. **51**, 4356 (1980).

[111] W. Kleemann, S. Miga, Z. K. Xu, S. G. Lu, and J. Dec, Appl. Phys. Lett. **104**, 182910 (2014).

[112] D. Viehland, M. Wuttig, and L. E. Cross, Ferroelectrics **120**, 71 (1991).

[113] C. Lei, A. A. Bokov, and Z.-G. Ye, J. Appl. Phys. **101**, 084105 (2007).

[114] Z. Ye, Key Eng. Mater. **155-156**, 81 (1998).

[115] V. Bobnar, Z. Kutnjak, R. Pirc, and A. Levstik, Phys. Rev. B. **60**, 6420 (1999).

[116] V. Westphal, W. Kleemann, and M. D. Glinchuk, Phys. Rev. Lett. **68**, 847 (1992).

[117] M. D. Glinchuk and R. Farhi, J. Phys.: Condens. Matter **8**, 6985 (1996).

[118] R. Pirc and R. Blinc, Phys. Rev. B **60**, 13470 (1999).

[119] R. Blinc, V. V. Laguta, B. Zalar, and J. Banys, J. Mater. Sci. **41**, 27 (2006).

[120] Y. Imry and S.-k. Ma, Phys. Rev. Lett. **35**, 1399 (1975).

[121] S. Semenovskaya and A. G. Khachaturyan, J. Appl. Phys. **83**, 5125 (1998).

[122] D. Wang, X. Ke, Y. Wang, J. Gao, Y. Wang, L. Zhang, S. Yang, and X. Ren, Phys. Rev. B **86**, 054120 (2012).

[123] M. Gröting, S. Hayn, and K. Albe, J. Solid State Chem. **184**, 2041 (2011).

[124] B. P. Burton, E. Cockayne, S. Tinte, and U. V. Waghmare, Phase Transit. **79**, 91 (2006).

[125] J. Paul, T. Nishimatsu, Y. Kawazoe, and U. V. Waghmare, Phys. Rev. Lett. **99**, 077601 (2007).

[126] T. Nishimatsu, U. V. Waghmare, Y. Kawazoe, and D. Vanderbilt, Phys. Rev. B **78**, 104104 (2008).

[127] D. Saranya, A. R. Chaudhuri, J. Parui, and S. B. Krupanidhi, Bull. Mater. Sci. **32**, 259 (2009).

[128] T. M. Correia, S. Kar-Narayan, J. S. Young, J. F. Scott, N. D. Mathur, R. W. Whatmore, and Q. Zhang, J. Phys. D: Appl. Phys. **44**, 165407 (2011).

[129] Z. Yu, C. Ang, R. Guo, and A. S. Bhalla, J. Appl. Phys. **92**, 2655 (2002).

[130] T. Maiti, R. Guo, and A. S. Bhalla, J. Appl. Phys. **100**, 114109 (2006).

[131] A. Dixit, S. B. Majumder, R. S. Katiyar, and A. S. Bhalla, *Frontiers of Ferroelectricity* (Springer, US, 2006), pp. 87–96.

[132] R.-h. Liang, X.-l. Dong, Y. Chen, F. Cao, and Y.-l. Wang, Ceram. Int. **33**, 957 (2007).

[133] S. Ke, H. Fan, H. Huang, H. L. W. Chan, and S. Yu, J. Appl. Phys. **104**, 034108 (2008).

[134] J. W. Xiong, B. Zeng, and W. Q. Cao, J. Electroceramics **21**, 124 (2007).

[135] N. K. Karan, R. S. Katiyar, T. Maiti, R. Guo, and A. S. Bhalla, J. Raman Spectrosc. **40**, 370 (2009).

[136] T. Maiti, R. Guo, and A. S. Bhalla, J. Am. Ceram. Soc. **91**, 1769 (2008).

[137] D. Ricinschi, C. E. Ciomaga, L. Mitoseriu, V. Buscaglia, and M. Okuyama, J. Eur. Ceram. Soc. **30**, 237 (2010).

[138] T. Maiti, R. Guo, and A. S. Bhalla, Ferroelectrics **425**, 4 (2011).

[139] H.-J. Ye, X.-S. Qian, D.-Y. Jeong, S. Zhang, Y. Zhou, W.-Z. Shao, L. Zhen, and Q. M. Zhang, Appl. Phys. Lett. **105**, 152908 (2014).

[140] W. Kleemann, J. Dec, and S. Miga, Phase Transit. **88**, 234 (2015).

[141] A. Bilić and J. D. Gale, Phys. Rev. B **79**, 174107 (2009).

[142] C. Laulhé, A. Pasturel, F. Hippert, and J. Kreisel, Phys. Rev. B **82**, 132102 (2010).

[143] D. Sherrington, Phys. Rev. Lett. **111**, 227601 (2013).

[144] L. Padurariu, C. Enachescu, and L. Mitoseriu, J. Phys.: Condens. Matter **23**, 325901 (2011).

[145] X.-S. Qian, H.-J. Ye, Y.-T. Zhang, H. Gu, X. Li, C. A. Randall, and Q. M. Zhang, Adv. Funct. Mater. **24**, 1300 (2014).

[146] L. D. Landau, Zh. Eksp. Teor. Fiz. **7**, 19 (1937).

[147] L. D. Landau, Zh. Eksp. Teor. Fiz. **7**, 19 (1937).

[148] L. Landau and E. Lifshitz, *Statistical Physics* (Elsevier Science, New York, US, 1996), No. v. 5.

[149] A. F. Devonshire, The London, Edinburgh, and Dublin Philosophical Magazine and Journal of Science **40**, 1040 (1949).

[150] A. F. Devonshire, The London, Edinburgh, and Dublin Philosophical Magazine and Journal of Science **42**, 1065 (1951).

[151] A. F. Devonshire, Philos. Mag. **2**, 1027 (1957).

[152] J. W. Cahn and J. E. Hilliard, J. Chem. Phys. **28**, 258 (1958).

[153] J. Hlinka and P. Márton, Phys. Rev. B **74**, 104104 (2006).

[154] H.-L. Hu and L.-Q. Chen, J. Am. Ceram. Soc. **81**, 492 (1998).

[155] L.-Q. Chen, J. Am. Ceram. Soc. **91**, 1835 (2008).

[156] J.-M. Liu, X. Wang, H. L. W. Chan, and C. L. Choy, Phys. Rev. B **69**, 094114 (2004).

[157] B. L. Li, X. P. Liu, F. Fang, J. L. Zhu, and J.-M. Liu, Phys. Rev. B **73**, 014107 (2006).

[158] Y. Tomita, T. Kato, and K. Hirota, J. Phys. Soc. Jpn. **79**, 023001 (2010).

[159] R. D. King-Smith and D. Vanderbilt, Phys. Rev. B **49**, 5828 (1994).

[160] W. Zhong and D. Vanderbilt, Phys. Rev. Lett. **74**, 2587 (1995).

[161] L. Hu, H. Li, and R. Tao, Phys. Rev. B **60**, 10222 (1999).

[162] J. M. Liu and X. Wang, Mater. Sci. Eng. B **106**, 282 (2004).

[163] W. Cao and G. R. Barsch, Phys. Rev. B **41**, 4334 (1990).

[164] B. Liu, Y. Huang, H. Jiang, S. Qu, and K. C. Hwang, Comput. Methods Appl. Mech. Eng. **193**, 1849 (2004).

[165] D. P. Landau and K. Binder, *A Guide to Monte Carlo Simulations in Statistical Physics* (Cambridge University Press, Cambridge, UK, 2005).

[166] The Canonical Ensemble, http://www.northeastern.edu/afeiguin/p4840/p131spring04/node132.html.

[167] R. K. Pathria and P. D. Beale, *Statistical Mechanics (Third Edition)* (Academic Press, Boston, 2011), pp. 39–90.

[168] D. Frenkel and B. Smit, *Understanding Molecular Simulation (Second Edition)* (Academic Press, San Diego, 2002), pp. 23–61.

[169] D. J. E. Callaway and A. Rahman, Phys. Rev. Lett. **49**, 613 (1982).

[170] E. T. Tomboulis and A. Velytsky, Phys. Rev. D **75**, 076002 (2007).

[171] L. Onsager, Phys. Rev. **65**, 117 (1944).

[172] J. L. Servoin, F. Gervais, A. M. Quittet, and Y. Luspin, Phys. Rev. B **21**, 2038 (1980).

[173] S. Nayak, B. Sahoo, T. K. Chaki, and D. Khastgir, RSC Adv. **4**, 1212 (2014).

[174] M. I. Marqués, Phys. Rev. B **71**, 174116 (2005).

[175] K. Binder, Rep. Prog. Phys. **60**, 487 (1997).

[176] R. Gaynutdinov, M. Minnekaev, S. Mitko, A. Tolstikhina, A. Zenkevich, S. Ducharme, and V. Fridkin, Jetp Lett. **98**, 339 (2013).

[177] L. Landau and E. Lifschitz, *Course of Theoretical Physics, Vol.5: Statistical Physics* (Pergamon Press Ltd., Oxford, UK, 1969).

[178] V. Basso, J.-F. Gerard, and S. Pruvost, Appl. Phys. Lett. **105**, 052907 (2014).

[179] P. D. Thacher, J. Appl. Phys. **39**, 1996 (1968).

[180] J. Wang, T. Yang, K. Wei, and X. Yao, Appl. Phys. Lett. **102**, 152907 (2013).

[181] Y.-B. Ma, N. Novak, J. Koruza, T. Yang, K. Albe, and B.-X. Xu, Phys. Rev. B **94**, 100104(R) (2016).

[182] Z. Kutnjak, B. Rožič, and R. Pirc, *Wiley Encycl. Electr. Electron. Eng.* (John Wiley & Sons, Inc., Hoboken, NJ, USA, 2015), pp. 1–19.

[183] S. Crossley, N. D. Mathur, and X. Moya, AIP Advances **5**, 067153 (2015).

[184] Y. Liu, J. F. Scott, and B. Dkhil, APL Mater. **4**, 064109 (2016).

[185] F. L. Goupil and N. M. Alford, APL Mater. **4**, 064104 (2016).

[186] D. Bolten, U. Böttger, T. Schneller, M. Grossmann, O. Lohse, and R. Waser, Appl. Phys. Lett. **77**, 3830 (2000).

[187] M. Marathe, A. Grünebohm, T. Nishimatsu, P. Entel, and C. Ederer, Phys. Rev. B **93**, 054110 (2016).

[188] Y.-B. Ma, K. Albe, and B.-X. Xu, Phys. Rev. B **91**, 184108 (2015).

[189] Y.-B. Ma, A. Grünebohm, K.-C. Meyer, K. Albe, and B.-X. Xu, Phys. Rev. B **94**, 094113 (2016).

[190] B. Rožič, B. Malič, H. Uršič, J. Holc, M. Kosec, B. Neese, Q. M. Zhang, and Z. Kutnjak, Ferroelectrics **405**, 26 (2010).

[191] N. Novak, R. Pirc, and Z. Kutnjak, Phys. Rev. B **87**, 104102 (2013).

[192] W. J. Merz, Phys. Rev. **95**, 690 (1954).

[193] X. Moya, E. Stern-Taulats, S. Crossley, D. González-Alonso, S. Kar-Narayan, A. Planes, L. Mañosa, and N. D. Mathur, Adv. Mater. **25**, 1360 (2013).

[194] D. Bolten, U. Böttger, and R. Waser, J. Appl. Phys. **93**, 2890 (2003), 00002.

[195] D. Bolten, U. Böttger, and R. Waser, J. Eur. Ceram. Soc. **24**, 725 (2004).

[196] R.-A. Eichel, Phys. Chem. Chem. Phys. **13**, 368 (2011).

[197] Y. Zhang, C. Wang, J. Li, M. Zhao, and J. Zhang, Phys. B **403**, 2822 (2008).

[198] F. Lin and W. Shi, Phys. B **407**, 451 (2012).

[199] Y. Shuai, S. Zhou, D. Buerger, H. Reuther, I. Skorupa, V. John, M. Helm, and H. Schmidt, J. Appl. Phys. **109**, (2011).

[200] R. Pirc, Z. Kutnjak, R. Blinc, and Q. M. Zhang, Appl. Phys. Lett. **98**, 021909 (2011).

[201] S. D. Bond, B. J. Leimkuhler, and B. B. Laird, J. Compu. Phys. **151**, 114 (1999).

[202] A. R. Akbarzadeh, I. Kornev, C. Malibert, L. Bellaiche, and J. M. Kiat, Phys. Rev. B **72**, 205104 (2005).

[203] R. Pantou, C. Dubourdieu, F. Weiss, J. Kreisel, G. Köbernik, and W. Haessler, Mater. Sci. Semicond. Process. **5**, 237 (2003).

[204] Y.-B. Ma, C. Molin, V. V. Shvartsman, S. Gebhardt, D. C. Lupascu, K. Albe, and B.-X. Xu, J. Appl. Phys. **121**, 024103 (2017).

[205] M. L. V. Mahesh, V. V. Bhanu Prasad, and A. R. James, J. Alloys Compd. **611**, 43 (2014).

[206] F. Moura, A. Z. Simões, B. D. Stojanovic, M. A. Zaghete, E. Longo, and J. A. Varela, J. Alloys Compd. **462**, 129 (2008).

[207] A. A. Bokov and Z.-G. Ye, Phys. Rev. B **74**, 132102 (2006).

[208] R. Landauer, J. Appl. Phys. **28**, 227 (1957).

[209] R. C. Miller and A. Savage, Phys. Rev. **115**, 1176 (1959).

[210] R. C. Miller and G. Weinreich, Phys. Rev. **117**, 1460 (1960).

[211] E. Sapper, N. Novak, W. Jo, T. Granzow, and J. Rödel, J. Appl. Phys. **115**, (2014).

[212] J. Hagberg, A. Uusimäki, and H. Jantunen, Appl. Phys. Lett. **92**, 132909 (2008).

Publications and Presentations

Publications

I) Y.-B. Ma, K. Albe, and B.-X. Xu, Lattice-Based Monte-Carlo Simulations of the Electrocaloric Effect in Ferroelectrics and Relaxor Ferroelectrics, Phys. Rev. B 91, 184108 (2015).

II) Y.-B. Ma, K. Albe, and B.-X. Xu, Monte-Carlo Simulations of the Electrocaloric Effect in Relaxor Ferroelectrics, in ISAF (IEEE, Singapore, 2015), pp. 203-206.

III) Y.-B. Ma, N. Novak, J. Koruza, T. Yang, K. Albe, and B.-X. Xu, Enhanced Electrocaloric Cooling in Ferroelectric Single Crystals by Electric Field Reversal, Phys. Rev. B 94, 100104(R) (2016).

IV) Y.-B. Ma, A. Grünebohm, K.-C. Meyer, K. Albe, and B.-X. Xu, Positive and Negative Electrocaloric Effect in $BaTiO_3$ in the Presence of Defect Dipoles, Phys. Rev. B 94, 094113 (2016).

V) Y.-B. Ma, N. Novak, K. Albe, and B.-X. Xu, Optimized electrocaloric effect by field reversal: Analytical model, Appl. Phys. Lett. 109, 202906 (2016).

VI) Y.-B. Ma, C. Molin, V. V. Shvartsman, S. Gebhardt, D. C. Lupascu, K. Albe, and B.-X. Xu, State transition and electrocaloric effect of $BaZr_xTi_{1-x}O_3$: Simulation and experiment, J. Appl. Phys. 121, 024103 (2017).

Conferences with Presentations and Posters

- 1st GAMM-Seminar on Phase Field Models, 2014, Darmstadt.
- Materials Science and Engineering-Congress, 2014 and 2016, Darmstadt
- International Symposium on the Applications of Ferroelectrics, 2015, Singapore; 2016, Darmstadt.
- European Meetings on Ferroelectricity, 2015, Portugal.
- German Physical Society Spring Meeting, 2016, Regensburg.
- Hysteresis Workshop, 2016, Dresden.

Curriculum Vitae

Personal

Yangbin Ma.
Born on December 8, 1986.
From Jiyuan City, Henan Province, China.

Educational background

Doctoral study in Materials Science
Technische Universität Darmstadt, Germany
Thesis: Electrocaloric Effect of Ferroelectrics and Relaxors
Superviser: Prof. Bai-Xiang Xu and Prof. Karsten Albe
February 2013 - October 2017

Master degree of Biomaterials and Composites
AGH University of Science and Technology, Cracow, Poland
October 2009 - June 2011
Thesis: Modeling of Electrodiffusion Problems using Matlab
Superviser: Prof. Robert Filipek

Polish training
Cracow University of Technology
October 2008 - July 2009

Bachelor degree of Materials Science and Engineering
University of Science and Technology Beijing (USTB), China
September 2004 - July 2008
Thesis: B_4C/TiB_2 Composites Derived from TiB_2 Powders by the Sol-gel Method
Superviser: Prof. Shiju Guo

Working experience

Associate Research Manager
Jiangsu Xujing New Energy Co., Ltd., China
Responsibility: Development of New Structure for Backsheet of Solar cells
September 2011 - October 2012

Honors

In Poland

Scholarship for Learning Achievements honored by AGH, 2010

Scholarship honored by China Scholarship Council, 2008 - 2011

In China

Excellent Undergraduate honored by USTB 2008

2nd Prize in Contemporary Undergraduate Mathematical Contest in Modeling (Beijing), 2007

People’s Scholarship 2005-2007

3rd Prize in Advanced Mathematical Contest held by USTB, 2005

Excellent Student in USTB, 2005